ABSTRACT

Title of Document:	LATCHING MICROELECTROMECHANICAL SHOCK SENSOR SYSTEMS: DESIGN, MODELING, AND EXPERIMENTS
	Luke J. Currano, Ph.D., 2010
Directed By:	Professor Balakumar Balachandran, Department of Mechanical Engineering Assistant Professor Miao Yu, Department of Mechanical Engineering

Latching shock sensors are acceleration threshold sensors that trigger when the acceleration level exceeds the designed acceleration threshold. The latching mechanism provides a mechanical memory, which keeps the sensor in a triggered, or latched, state until the sensor is reset. The attractive feature of this type of sensor is that it does not require power during monitoring; power is only needed to query and reset the sensor. Several devices have been presented in the literature, but with limited experimental data and models that provide little to no insight into the dynamics of the latching event. *The aim of this work is to further the understanding of the physics and design of micromechanical latching shock sensors by conducting a combination of careful experiments and development of original reduced-order*

models. These efforts enable one to obtain a detailed picture of the latching dynamics for the first time.

Latching shock sensors have been designed, fabricated, and experimentally evaluated in this work. The model predictions have been compared to the experimental results to verify the validity, including a quantitative comparison of the position of the shock sensor during a latching event captured via high-speed videography. *This is the first time a latching event has been imaged in this class of sensors, and the first time, the model predictions of position versus time histories have been validated through experiments*. The models have also been used to conduct detailed numerical studies of the shock sensor, amongst other things to predict a latch "bounce" phenomenon during an acceleration event. To understand more thoroughly how the various design parameters affect the latching threshold of the sensor, various parametric and optimization studies have also been conducted with the reduced-order models to guide designs of future latching acceleration threshold sensors.

LATCHING MICROELECTROMECHANICAL SHOCK SENSOR SYSTEMS: DESIGN, MODELING, AND EXPERIMENTS

By

Luke J. Currano

Dissertation submitted to the Faculty of the Graduate School of the
University of Maryland, College Park, in partial fulfillment
of the requirements for the degree of
Doctor of Philosophy
2010

Advisory Committee:
Professor Balakumar Balachandran, Chair and Advisor
Assistant Professor Miao Yu, Co-Advisor
Professor Shapour Azarm
Associate Professor Elisabeth Smela
Professor Inderjit Chopra, Aerospace Engineering, Dean’s Representative
Dr. Madan Dubey, U.S. Army Research Laboratory

Dedication

This dissertation is dedicated to my wife, Kim, for her steady patience and support throughout the last four years.

Acknowledgements

I would first like to thank my advisors, Dr. Miao Yu and Dr. Balachandran, and all the members of my committee, who have all helped focus my research and improve this dissertation in numerous ways. Many thanks to Danny Gee for help with fabricating and testing sensors at various points, and to Brian Isaacson for fabrication support. And thanks to the cleanroom support staff at ARL for keeping the cleanroom running smoothly and the equipment in good working order. I am deeply indebted to Romeo del Rosario and Kwok Tom for providing applications and transition pathways for this research. Thanks also to Madan Dubey for encouraging me to undertake this PhD, and to Brett Piekarski, Paul Amirtharaj, John Pellegrino, and all the management of ARL for their support and flexibility in accommodating my course schedule and research.

Table of Contents

List of Tables

List of Figures

1. Introduction

In this chapter the background and motivation for this work is provided, along with a review of the relevant prior work in the literature, the scope of the work and the organization of the dissertation.

1.1 __Background and Motivation__

Every synthetic system must ultimately fail. Buildings may withstand the ravages of the natural world for hundreds of years; a laptop might function for a few years; a tungsten filament light bulb might last a few hundred hours. Three very different systems, with very different fabrication techniques and orders of magnitude difference in expected lifetime, but each will eventually succumb. The causes of failure might include fatigue, flaws in the materials or fabrication, unexpected loading beyond the design limit, among others. The failure might be a gradual decay in performance or a sudden catastrophic cease of function. The consequences may be mild, such as the annoyance of the light going out; or severe, such as hydraulic failure on an airliner during flight. The inherent risk in a system can be evaluated according to the probability of failure and the severity of the consequences.

Devices with a high probability of failure and severe consequences are high risk, while low probability and low severity equate to low risk. In high risk systems it is desirable to know when and how failure is likely to occur, so steps can be taken to repair the system and avoid the severe consequences associated with unexpected failure. The function of predicting failure before it occurs is performed by a health monitoring system. The benefits of health monitoring go beyond avoiding the unexpected catastrophic failure, however. In a perfect health monitoring system, routine scheduled maintenance can be eliminated completely in favor of condition-based maintenance. This saves time, money, and reduces waste due to replacing components before the end of their useful life.

Health monitoring is becoming more cost effective due to the widespread availability of inexpensive, miniature, low-power sensors [1,2]. Two fundamental approaches to carry out health monitoring are as follows: i) monitoring of the system performance and ii) monitoring of the environment in which the system is located. Each of these approaches has its own benefits. On one hand, implementation of environmental monitoring is typically simple, with a handful of sensors and simple allowable thresholds. Performance monitoring generally requires many more sensors and sophisticated data analysis algorithms. On the other hand, performance monitoring is more directly linked to system health. Historically, specification sheets list allowable environmental conditions, and environmental monitoring can be used to determine if the allowed specifications are exceeded. Due to the ease of implementation and the available specifications, environmental monitoring is currently the more commonly used approach.

The more challenging applications of health monitoring are those with limited available power and space. Automobile companies have been very successful in integrating sensors in their vehicles because power and size are not major constraints. The result is that the average car today contains dozens of sensors, including accelerometers, gyroscopes, pressure sensors, temperature sensors, light sensors, and in some cases humidity sensors, rain sensors, and cameras [3]. When power and size are major factors, implementing health monitoring systems becomes more difficult and tradeoffs are necessary between the amount and precision of the data collected and the power consumed.

The present work is motivated by a need to monitor acceleration in environmental monitoring systems with a minimal amount of power. Power available for environmental monitoring systems is often severely limited, especially for small, long-life systems. Low-power sensors are critical to enabling embedded health monitoring where power is not readily available. For example, a piece of ammunition may be stored for ten years or more on a pallet in a warehouse before being required to perform its function with near-perfect reliability. For many (if not most) health monitoring applications, temperature, humidity, and acceleration are core environmental parameters that must be monitored. By way of example, the Military Standard Design Requirements for Standard Electronic Modules lists specific ranges for these parameters (along with a few other specialty environments rarely encountered in commercial applications) [4]. There are many other sensors needed for specific applications, but these three are needed in most cases, and may be sufficient by themselves in many cases. The sensor targeted by this work is the accelerometer, because acceleration alone of these three core parameters of interest is generally a quickly-changing quantity. For temperature and humidity sensing, power management is not a major factor because the sensor can have very low duty cycles, waking up for a millisecond every minute or hour to take a reading. Because the temperature and humidity environment generally change over much longer timescales, a good representation of the environmental history of each can be obtained by interpolating between measurements widely spaced in time.

Conversely, acceleration must be sampled at high frequencies because a damaging drop or impact may last only a few milliseconds. The acceleration sensor must therefore be constantly powered or a critical transient impulse might be missed. In addition, supporting circuitry such as signal conditioning electronics and analog to digital converters must be powered on to convert the sensor output into a form that the system can use. Together this can pose a significant drain on the power supply. An acceleration sensor that draws no power and requires no supporting electronics during monitoring is therefore ideal. The mechanical latching acceleration threshold sensor is one approach to meet this need at the expense of resolution - the information provided by each sensor is only whether the acceleration exceeded the threshold. If several sensors with different threshold levels are provided, the acceleration seen by the system can be classified into one of several bins, but the resolution will still be orders of magnitude lower than using a true accelerometer.

1.2 Acceleration Threshold Sensor Literature Review

Microelectromechanical system (MEMS) accelerometer technology is mature, with many different applications and hundreds of millions of dollars in annual sales [5]. MEMS acceleration threshold sensors have not enjoyed nearly as much interest as accelerometers because the potential applications are far more limited. In many cases, an exact acceleration level or profile is needed, and a threshold sensor alone will not give this information. Threshold accelerometers do have a niche in applications that either require ultra-low-power monitoring of acceleration or those that do not have a need for the high precision offered by a conventional accelerometer. No power monitoring of acceleration might be necessary in systems with a lifetime of many years or where the power source is very limited. The low-precision realm includes primarily systems where a simple go/no go acceleration level can be defined, such as automobile airbags, projectile launch systems, or simple health monitoring systems that monitor whether allowable ranges have been exceeded.

A handful of other acceleration threshold sensors have been studied by other researchers. They are all mechanical switches of one sort or another, where the switch changes state when the acceleration is exceeded. Some researchers use the name “inertial switch” or “g-switch,” but the function is the same.

There are two primary categories of acceleration threshold switch designs: contact between surfaces is broken following an acceleration (normally closed), or contact between surfaces is made following an acceleration (normally open). In either category, the response to the acceleration can be classified as “intermittent” (wherein the device reverts to its original state after the acceleration event is over) or “persistent” (wherein the device remains in the altered state after the acceleration event is over). An intermittent design is sufficient if the device is monitored constantly, such that the trigger event can be recorded as it occurs. A persistent design is generally more complex, but also has the flexibility of not requiring the constant power of monitoring electronics. The persistent nature of the device serves as a mechanical memory and is suitable for system architectures in which the electronics are powered up to query the sensors at regular intervals. This is the typical architecture for monitoring of temperature and humidity, and a persistent threshold accelerometer enables the same mode for acceleration monitoring.

Prior work on acceleration threshold sensors is mostly concentrated on intermittent, normally-open devices [6-13]. These devices generally consist of a spring, a mass, and a contact surface separated from the mass by a gap. Some use out-of-plane motion of the mass [6, 7, 10-12] and others use in-plane motion [8, 9], but each relies on the intermittent contact between the mass and another surface. Several of these previous designs array the switches such that many different acceleration levels can be detected. The very first micromechanical acceleration contact switch was reported in 1972 by Frobenius, Zeitman White, O'Sullivan and Hamel [6], and consisted of gold cantilevers above a gold stationary electrode, with only the mass of the cantilever providing inertial force (Figure 1.1). More recently, Yang *et al.* [12] introduced multiple springs and thick proof masses for low acceleration thresholds, as well as a compliant electrode to decrease bounce and protect against shock damage (Figure 1.2). Jia *et al.* [13] incorporated an electrode to

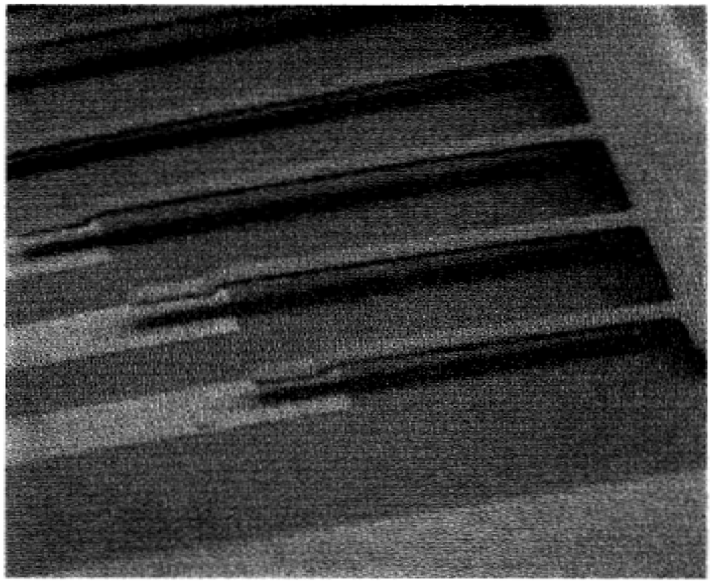

Figure 1.1. The first MEMS acceleration threshold switch by Frobenius *et al.* [6].

provide for electrostatic tuning of the threshold level and to hold the switch in the closed state (Figure 1.3). While this blurs the line between intermittent and persistent designs, the author considers this an intermittent device because electrical energy is required to hold the device in the closed state.

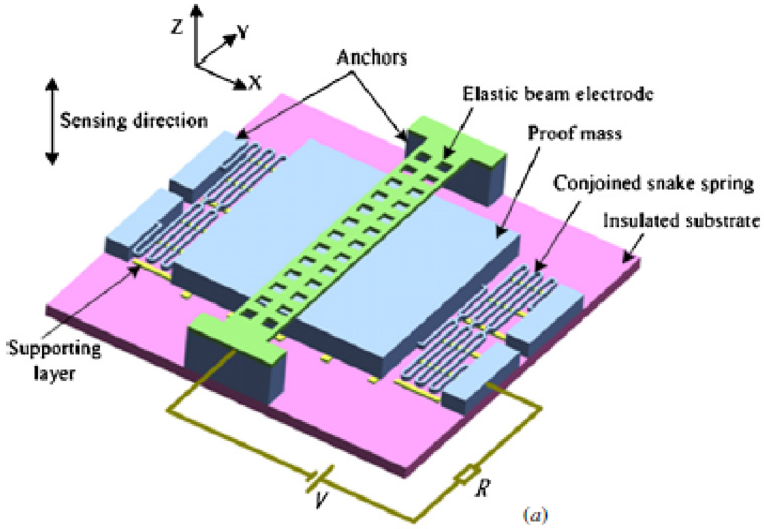

Figure 1.2. Out-of-plane intermittent acceleration threshold sensor design with compliant contact by Yang *et al.* [12].

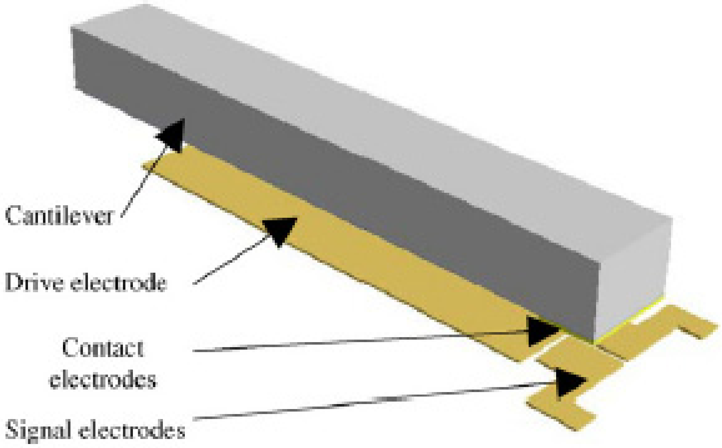

Figure 1.3. Intermittent acceleration threshold sensor with adjustable threshold and electrostatic hold-down by Jia *et al.* [13].

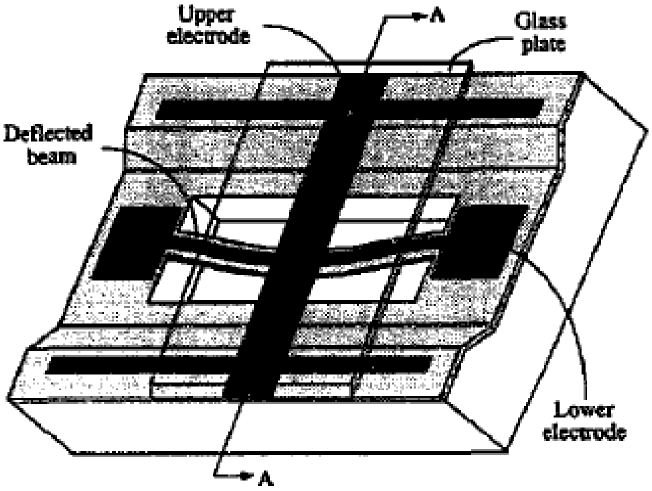

Figure 1.4. Bistable acceleration threshold sensor design based on prestressed bilayer beams by Go *et al.* [14].

A few persistent, normally open designs have been studied as well. Persistent contact has been achieved using bistable mechanisms [14-17] as well as physical locks or latches [18-24]. The first report of a bistable acceleration threshold switch was by Go, Cho, Kwak, and Park in 1996 [14], and it used a prestressed bimorph beam with out-of-plane contacts (see Figure 1.4). More recent work makes use of bistable geometries that can be easily defined lithographically [15-17].

The shock sensor that is the subject of this dissertation is a physically latching acceleration switch. This requires sliding contact between two surfaces, generally considered to be the most challenging of the four classes of MEMS devices (no moving parts, moving but no contact, contact but no sliding, and contact with sliding) from a design perspective because there are more potential failure modes [25]. Partly due to this complexity, and partly because of the wide availability of standard MEMS accelerometers, very few physically latching acceleration switches have been reported. However, there is a fundamental advantage; the physical latch allows the device and all associated circuitry to be completely powered off most of the time to save power, with the system waking up to query the sensor either at pre-programmed intervals or when a user instructs it to query by pressing a button, for instance.

The earliest acceleration threshold switch with a physical latching mechanism was reported by Ciarlo in 1992 [18], and consisted of two cantilevers perpendicular to each other with shaped ends to provide a locking mechanism (Figure 1.5). More recently, multiple suspension springs, large proof masses, and electro-thermal reset actuators have been included by Whitley, Kranz, Kesmodel, and Burgett [19], and Jean et al, [20-22] (Figure 1.6). Guo et al. [23, 24] presented a device that physically separates the mass from the latching mechanism and electrical contacts to reduce the chances of secondary shocks or vibration causing loss of contact after latching. All of the reports of physically latching acceleration switches have very limited experimental data (at most test results from one or two devices are reported). Each also relies on simplistic (often static) models to predict the threshold acceleration and/or response time that in every case neglect the interaction of the sensor with the latch.

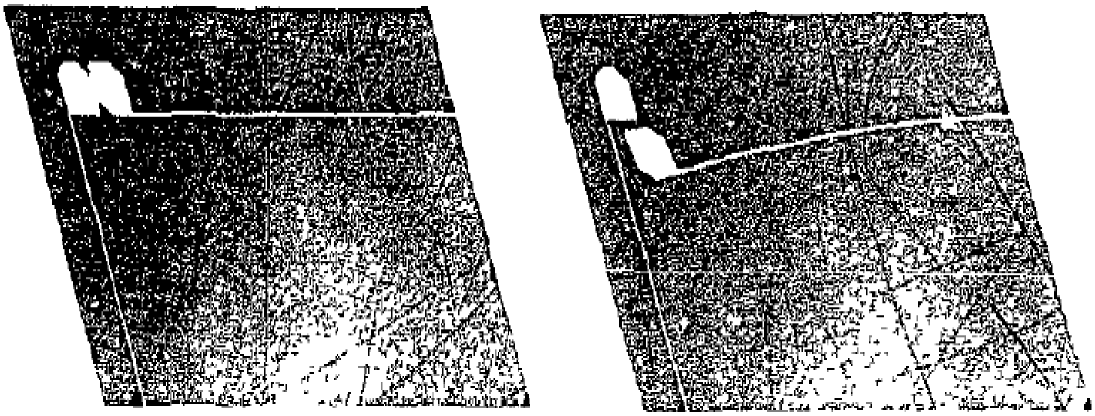

Figure 1.5. The first latching MEMS accelerometer by Ciarlo *et al.* [18].

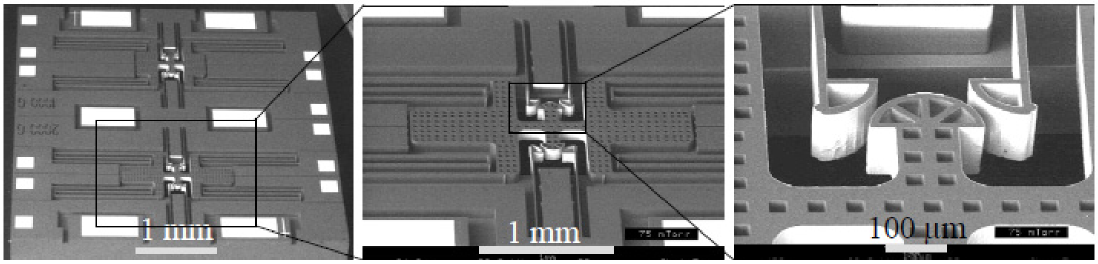

Figure 1.6. Latching acceleration threshold sensor design with multiple suspension springs by Jean [20].

1.3 Friction Measurements for MEMS Literature Review

From a design perspective, the most challenging MEMS are those that require surfaces with sliding contact between them. Accounting for friction and wear in the contacting surfaces introduces an added level of complexity in modeling and uncertainties in material properties. Although friction and wear are well understood and extensively characterized on the macroscale, the same is not true at the microscale.

The characterization of friction and determination of friction coefficients on the microscale has been carried out by using various techniques. Perhaps the most popular method is to scrape the tip of an atomic force microscope or a scanning probe microscope across the surface of a film and measure the normal and transverse forces by using the tip itself [26, 27]. This method can not be easily adapted to sliding contacts where the two surfaces are vertical rather than horizontal, as is the case in many MEMS. In addition, the friction properties may depend on the surface preparation conditions, with published friction coefficient values ranging from 0.01 to 0.8 for silicon/silicon nitride contact [28]. For these reasons, many MEMS have been used for friction measurements on both horizontal surfaces [29-31] and vertical surfaces [32-37]. All of these devices have relied on electrostatic actuation to generate the needed normal and tangential forces. The electrostatic actuators include parallel-plate and comb-drive type actuators. In this work, a design for making friction measurements by using MEM thermal actuators is detailed and presented along with the obtained experimental results. The advantages of using thermal actuators include far lower operating voltages, a much smaller footprint, and typically a much longer range of motion. Furthermore, in this design, one can create a wide range of forces by changing a single parameter, the offset angle of the V-beam actuator.

1.4 Scope of this Work

The focus of this work is to enable the development of an acceleration threshold sensor system with the following features: i) uni-axis, bi-directional acceleration threshold sensing (i.e. +/- accelerations in the y-axis must be detected and differentiated from each other); ii) a physical latching mechanism to serve as a mechanical memory of a threshold event; iii) electrical sensing of the latch closure; and iv) a reset function to use the sensor again after it has been triggered. The dissertation effort encompasses the design, modeling, fabrication and experimental study of this sensor system. The experimental study is used to learn more about the dynamics of this type of sensor and verify that the model is sufficiently representative of the sensor operation. The model is intended to serve as a framework for design of the sensors. As such, parametric studies and optimization codes are also included in the scope of the work.

Various parts of this dissertation have been adapted from journal and conference papers written through the course of this dissertation research. These are noted at the top of each chapter as applicable. Although some of these papers have several co-authors, the co-authors can be grouped into one of the following three categories: i) the author's advisors, who primarily guided the research directions, ii) collaborators who provided fabrication or testing support, wherein all of the underlying procedures have been developed by the author of this dissertation, and iii) collaborators on subjects related to the dissertation topic but not included in the dissertation, such as the development of a current ramp circuit to power the reset actuators discussed in reference [37]. This latter material, which is not a part of the author's contributions, is not included in this dissertation.

1.5 __Organization__

This dissertation is organized into six chapters, an appendix, and a bibliography section. In the first chapter, the background and motivation for this work is provided along with a review of prior work on MEMS shock sensors. In Chapter 2, the shock sensor design under consideration is presented and the fabrication process flow developed to realize the design is discussed. In Chapter 3, the experimental studies carried out with the sensor, reset actuators, and friction test structures are discussed. In Chapter 4, the author has discussed the development of models for the shock sensor and the reset actuators, as well as parametric and optimization studies undertaken with the models. In Chapter 5, comparisons between the model predictions and experimental results are made for the purpose of verification. In Chapter 6, the conclusions that can be drawn from the dissertation work are presented along with the author’s contributions and thoughts on future research directions. Appendix A is included to provide fabrication details and information related to the numerical studies.

2. Design and Fabrication

In this chapter, an overview of the shock sensor as a system is presented. The design and working principle of the shock sensor under consideration are introduced along with a novel rotational actuator developed during this work. The author has also presented the fabrication processes employed to make the devices found in the experimental portion of this work. Portions of this chapter have been adapted from the author's journal papers on the latching shock sensor [38] and the rotational thermal actuator [39].

2.1 Sensor Design

The sensor consists of a series of springs attached to the substrate at one end and the mass at the other, as shown in Figure 2.1. The pictured device makes use of a

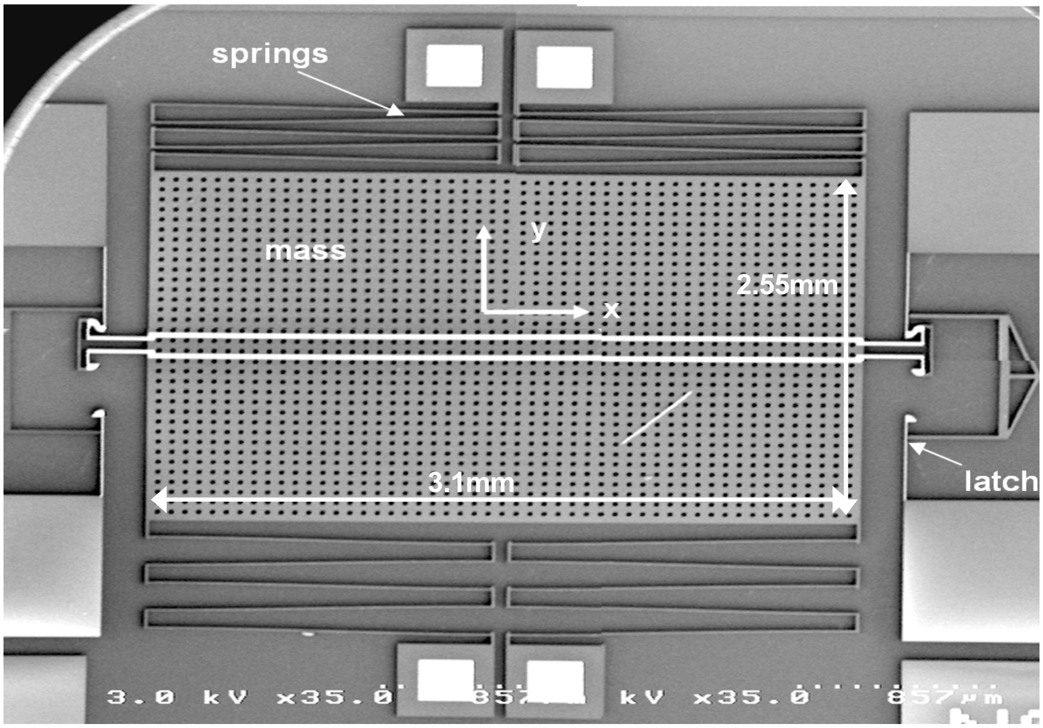

Figure 2.1. Shock sensor (shown in latched position). The mass is in the center, the springs are at the top and bottom, and the reset actuators are at the far left and far right.

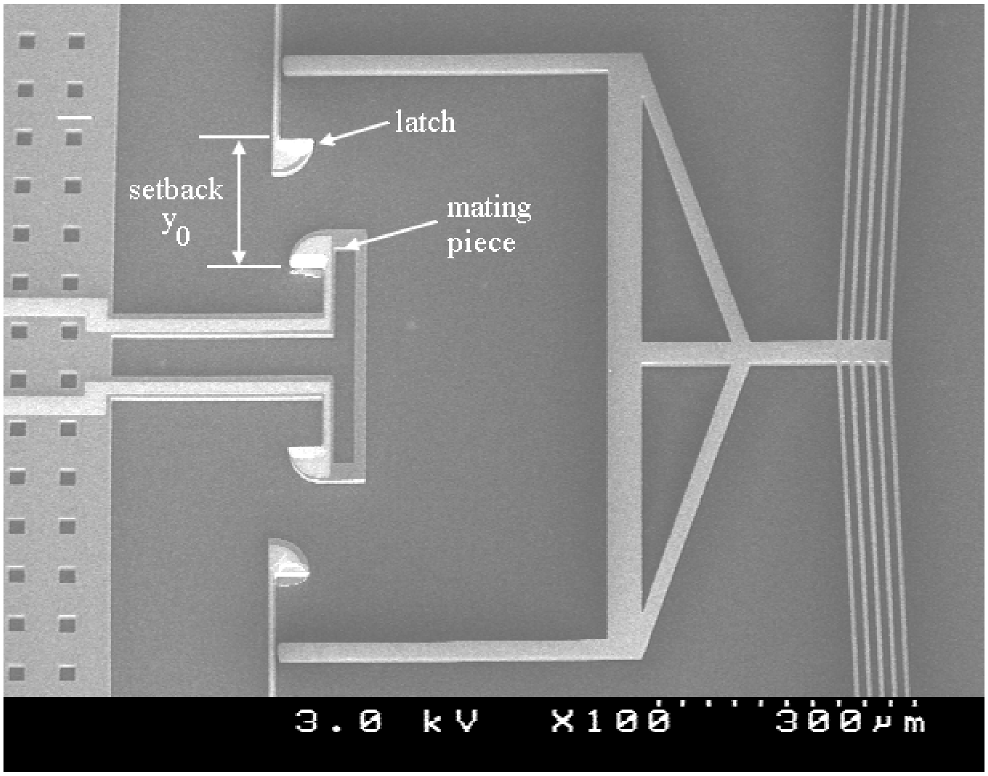

Figure 2.2. Close-up of the latch and release mechanism.

two-fold symmetric design with four springs to reduce the sensitivity to off-axis and rotational accelerations compared with single and dual-spring configurations. When the system undergoes acceleration along the y-axis, the motion of the mass forces two of the springs into compression and the other two springs into extension. The sensor incorporates latches anchored to the substrate, which engage the mating pieces attached to the mass after the sensor has traveled the designed setback distance (Figure 2.2). The latches are cantilevered so that they are stiff in the y-direction and less stiff in the x-direction. This allows them to move out of the way as the mass pushes past them. Four latches are used in this device with two of them meant for positive acceleration and the other two meant for negative acceleration along the same axis. Once the mass pushes past the latches, it may continue to move but will be prevented by the latches from returning to its resting state. As the acceleration dissipates, the mass comes to rest against the flat back surface of the latches. These flat surfaces are coated with metal, and when the mass touches both metal contacts, an electrical circuit is closed between the two latches. This serves as the shock-detection mechanism.

The sensor is reset following the detection and recording of the shock event by using thermal actuators (Figure 2.2). Here, V-beam style thermal actuators (also called bent-beam actuators) are used, since it is difficult to get sufficient force with U-beam style actuators (also called hot-beam/cold-beam actuators). The bent-beam actuators have been described in previous studies [6-8], and here, for clarity, a brief description of their operation is provided. The baseline actuator is a conductive beam divided into two segments that are rotated in-plane slightly by design to give the full beam a “V” shape. When current is driven through the beam, Joule-heating causes thermal expansion of each segment. Since the beam structures are fixed at the ends, the two segments push against each other and generate an in-plane motion in the direction they are pointed towards. Due to the shallow angle and slender beam profile required for thermal strain amplification of the V-beam structure, most of the generated force is not along the actuation direction. The force component that is not along the actuation direction axially compresses the V-beam structure. If this axial force component is large enough to cause buckling of the structure, the output force from the actuator can drop dramatically. However, multiple beam structures can be used in parallel to overcome this limitation.

In the present work, the required actuation force to reset the shock sensor necessitated the use of five parallel beam structures. For the chosen V-beam dimensions (5 µm width and 600 µm length), a minimum of five beams is required to reliably unlatch the device while avoiding buckling of the individual V-beams. The actuators here push against the latches to disengage them from the mass. It is worth noting that the reset actuators are not connected to the latches; there is a gap of 3 µm in between them and this gap can be seen in Figure 2.2.

2.1.1 Sensor Limitations and Failure Modes

The sensor design investigated here is limited to sensing of a single acceleration threshold along one axis. By having an array of multiple devices and rotating the orientation, two axes of sensing and multiple threshold levels can be incorporated onto a single chip. To provide a third sensing axis, a second chip would have to be made with a sensing axis oriented in a perpendicular direction to the first axis. The sensor also cannot be used to sense a second acceleration event after it has been latched and before it is reset – therefore, two (or more) events may be interpreted as a single event. There is also a finite delay in the sensor response, as the sensor must travel past the latch, and return to rest against the latch as the imposed acceleration dies out. For the designs discussed here, the delay is on the order of 1.5 to 3 ms. With design modifications that separate the electrical contacts from the latch, the dissipation of the acceleration is not required before electrical contact is established [19, 23]. These same design modifications prevent the loss of electrical contact due to vibration or secondary shocks occurring after the sensor is latched.

In the MEMS industry, there is a widely accepted characterization of devices into four classes based on the complexity of design and the number of potential failure modes [25]. Class 1 consists of devices with no moving parts, and this class is considered the simplest to design since it has the fewest failure modes. Class 2 consists of devices with moving parts, but no contact. Class 3 consists of devices with moving parts that make contact with other parts of the device or substrate, but no sliding is involved in the contact. Class 4 consists of devices that have moving parts that engage in sliding contact with other parts of the device or substrate. The shock sensor belongs to Class 4, as the mass slides past the latch during an acceleration event, and the latch slides out of the way of the mass during the reset operation. In addition to the failures modes for devices in Classes 1-3 (particle contamination, charging, electrostatic discharge, stiction, fatigue, creep, impact-induced cracking or fracture), the general failure modes for devices in Class 4 also includes the unique failure modes associated with friction-induced heating and wear.

For the specific shock sensor designs described in this work, the author has observed failure by stiction and shock-induced fracture of the latches, suspension springs, and reset actuators. Wear is observed in the contacting surfaces, including both the rounded side of the latch and the contact metallization on the flat side of the latch, but this has not been observed to cause failures when the devices have been tested up to 100 cycles.

Shock-induced fracture of the thin members usually occurs when the wafer is cleaved to separate individual devices. At least one thin member fractures during cleaving in approximately one out of every three or four devices. This failure mode has been observed during shock testing as well, but is far less common.

Stiction is the biggest problem with this design and this is by far the most common failure mode, due to the very large mass (2.5 mm x 3.1 mm), relatively compliant suspension springs, and small (2-4 μm) gap between the mass and the substrate. Stiction failures occur in fabrication if the released device is exposed to liquid, but this is relatively easy to avoid with a gas phase release process. They also occur in storage if the device is stored in a non-conductive plastic carrier, because the carrier collects charge from the air and attracts or repels the mass, eventually causing it to contact the substrate and stick in place. Stiction failures also occur in operation of the device, and the author hypothesizes that this is due to rubbing of the mass against the substrate, resulting in exchange of electrons and a buildup of charge similar to that what occurs during rubbing of a balloon against a wool sweater.

While not technically device failure, during shock testing, the mass does sometimes engage one latch but not both, resulting in a situation where the device needs to be reset but the circuit is not closed. This may be caused by slight asymmetries in the fabrication process, where one latch is stiffer than the other, for instance, or from an acceleration that is not applied exactly parallel to the sensing axis. This effect could be alleviated by designing a sensor with only one latch, by using a spring anchor as the second terminal for sensing the change in resistance when the switch closes.

The electrothermal reset actuators are also subject to overheating if the applied current is too large. Overheating can result in plastic deformation or fracture of the actuator beams. This can be avoided by using a reset signal with a defined pulsewidth. If the actuator beams are too narrow, too long, or the bend angle is too shallow, the actuators may also buckle before the device is reset. This can be addressed in the actuator design, ensuring that the output force generated is sufficient to reset the latch and the axial load on each beam does not exceed the Euler buckling load [40].

2.2 Rotational Actuator Design

Thermal actuators are often not given full consideration in MEMS because of their high power consumption relative to many electrostatic and piezoelectric actuators, but they do have certain advantages. They are useful in some MEMS devices because they can simultaneously provide large forces and large displacements. They also require relatively low voltage inputs (often less than 10 V [41-46]), especially when compared to electrostatic actuators. The focus of most research efforts on thermal actuators has primarily been on two types of actuators, namely, bent-beam or V-beam actuators (so called because of their shape) and hot-arm/cold-arm or u-beam actuators. Bent-beam actuators supply very large forces (typically hundreds of micronewtons to a few millinewtons) with translational deflections extending to 30 μm [41, 42]. Hot-arm/cold-arm actuators are generally limited to small forces (less than 10 μN) but can supply relatively large free displacement along an arc (up to 50 μm) [44].

The author therefore designed an offset-beam rotational thermal actuator, shown in Figure 2.3, to overcome the low force limitation of u-beam actuators while reducing the required power compared to V-beam actuators [39]. The offset beam actuator therefore provides the best of both worlds: free displacements approaching those of similarly sized U-beam actuators, and maximum output forces approaching those of similarly sized bent-beam actuators, with power consumption on the order of u-beam actuators. Output forces of up to 1.44 mN along with displacements greater

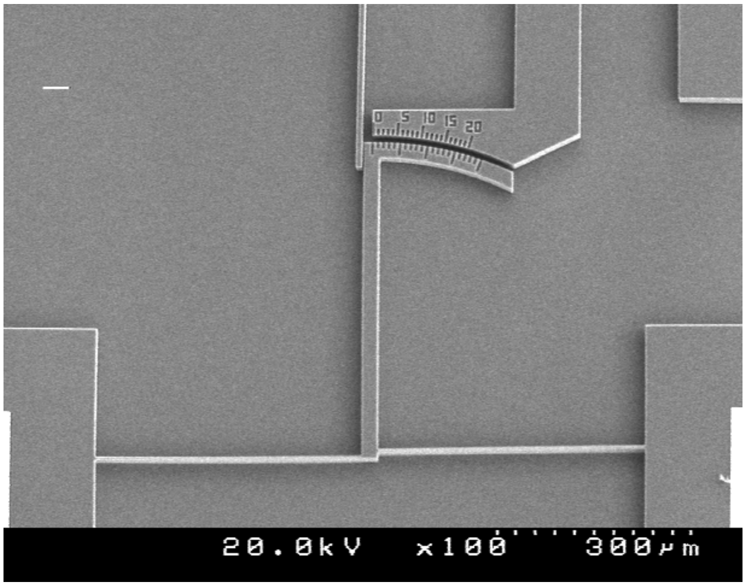

Figure 2.3. Rotational actuator test structure.

than 20 μm were achieved, indicating that these actuators provide better force-displacement performance than hot arm/cold arm style actuators. Although a direct comparison to bent beam actuators is difficult because the displacement profiles are different (rotational vs. translational), similar free deflections can be obtained from the offset-beam rotational actuators with about 40% less current and 40% less voltage (i.e., 64% less power).

The actuator under consideration (Figure 2.3) is fundamentally a rotational actuator, although it is not difficult to transform the output to near-linear translation over small angular stroke lengths. The actuator consists of two flexible beams connected to a central displacement amplification beam with an offset between their respective axes, as shown in Figure 2.4. As in other MEMS thermal actuators, current passing through the flexible beams generates joule heating and this causes each beam to expand. Due to the offset between the two actuator beams, the axial expansion is converted into a torque on the amplification beam about the point *P*, shown in Figure 2.4. The central beam then rotates according to the amount of torque applied and the

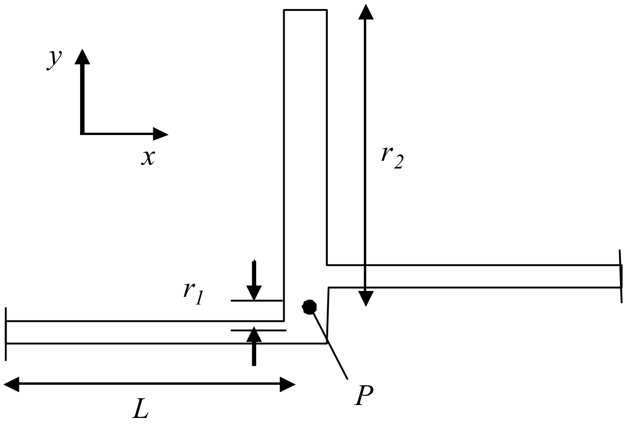

Figure 2.4. Rotational actuator conceptual drawing and parameter definition.

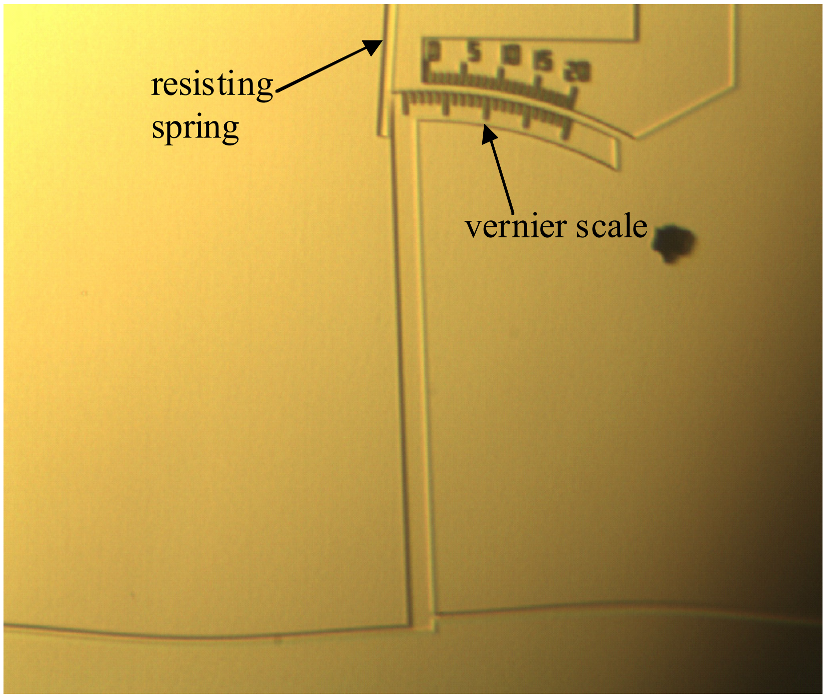

Figure 2.5. Deformed shape of actuator.

bending stiffness of each of the actuator beams. The length of the yoke or moment arm r_2 defines the amount of translation that can be derived from the resulting rotation. The deformed shape of the actuator is similar to the second bending modeshape of the complete system, as shown in Figure 2.5.

The intent in designing this actuator was to replace the V-beam reset actuators with these rotational actuators to achieve reset with lower power levels. In practice, the reset operation required stabilization of the actuator to prevent buckling of the slender beams, and this negated the expected performance improvements. However, the rotational actuator design, modeling, and testing is included here because it is likely to be a useful contribution for other applications. Also, independent from this work, Heo and Kim have also developed MEMS thermal actuators with the same operation principle around the same time [47].

2.3 Device Fabrication

The mass, spring, latches, and reset actuator of the sensor are made of low-resistivity silicon (1 to 3 mΩ-cm) to lower the voltage required by the actuators and the resistance of the sensor in the latched-state. The sensor is fabricated on a silicon-on-insulator (SOI) wafer with a 20 µm thick device layer, a 2µm buried oxide layer, and a 500µm thick, 1-10Ω-cm handle wafer. The fabrication process flow is shown in Figure 2.6, with further details on specific recipes and device settings given in Appendix A. 200/2000 Å of chrome gold (Cr/Au) is deposited first on the anchors of each of the springs, latches, and actuators via ebeam evaporation and patterned by liftoff (step a). These pads serve as wirebonding sites for connection to an electronic package. Gold-tin (AuSn 80/20 weight %) rings are then deposited via ebeam evaporation and patterned by liftoff around each of the anchors to provide for wafer-to-wafer bonding with a cap wafer later in the process (step b). Next, the complete device profile, including springs, mass, latches, and actuators, is patterned with contact photolithography and deep reactive ion etching (DRIE) is used to transfer the profile to the silicon device layer in a single step (step c). The wafer is re-patterned with a thick negative photoresist that allows patterning over features up to about 30μm and sputtered Cr/Au or aluminum is deposited on the mating sidewalls of the latches to lower the contact resistance (step d). The last patterning step on the device wafer is a backside DRIE of trenches about 375 μm deep and 100 μm wide in between the individual die to provide cleaving lines for die separation (step e).

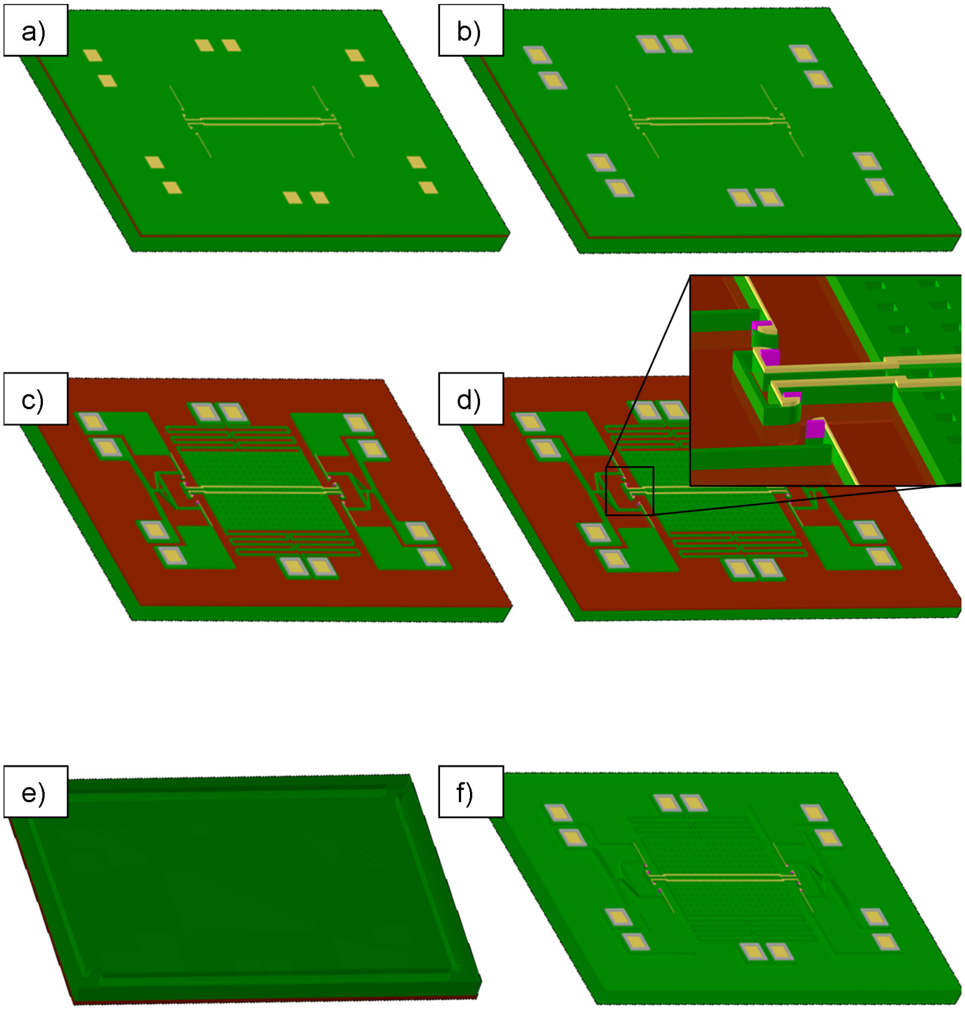

Figure 2.6. Shock sensor fabrication process flow. Individual steps are a) deposition of pads for wirebonding on SOI wafer, b) deposition of AuSn solder rings for wafer bonding, c) DRIE of device structure, d) deposition of patterned metal contacts on latch sidewall, e) DRIE of cleave assist lines, and f) final device release by oxide undercut.

Attempts to release the device in a standard liquid HF/supercritical drying process were found to be unreliable. Many of the devices adhered to the wafer during release due to the large mass and relatively compliant springs. Therefore, a vapor-phase HF release process was used (step f), performed in a Primaxx MEMS-CET etcher that provided good results with no stiction or residue; this etcher is also less aggressive in attacking the Cr adhesion layer under the bond pads.

Coating sidewalls with a lithographically-defined pattern (step d) is a challenging process step that merits additional detailed information. Spin-coating over deep topography causes significant thickness variations, with thicker photoresist layers forming inside wells and thinner layers forming on the mesas, and especially thin layers at the corner of the mesas (see Figure 2.7). The author developed this process by using a negative photoresist because the various thicknesses would cause features on the top of mesas to be over-exposed and the sidewalls to be under-exposed. With negative photoresist, the exposure and subsequent bake cause the resist to cross-link, which prevents exposed features from developing. Even if the resist is not fully exposed all the way through the thickness, the top surface will be cross-linked, impeding development underneath any exposed areas.

The photoresist used was Futurex NR5-8000, spun at 500rpm for 5 seconds, then 1000rpm for 40 seconds to yield a nominally 15 μm thick layer. The viscosity and slow spin speed allow the resist to fully coat the corners of mesas up to 20μm high (see Figure 2.7). Thinner resist or faster spin speeds can cause gaps in the resist coating at these corners, which will result in metal adhering during the liftoff process in undesired locations.

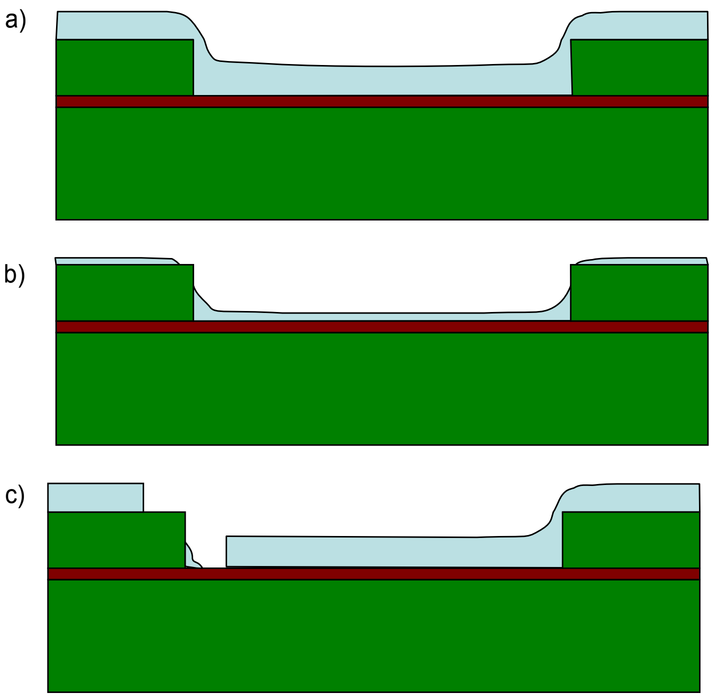

Figure 2.7. Spinning photoresist over topography: a) thick photoresist completely covers corners of mesas, while b) thin photoresist can leave corners uncoated. After development, c) there may be some residue left in the corner, but most of the sidewall is cleared for coating with metal.

Once a complete coating is achieved, an exposure dose about 15 percent higher than usual worked well with these devices. On a Karl Suss MA6 contact aligner, with dose of 1000mJ/cm^2, the best results were achieved with an exposure time of 7.8 seconds (on a silicon wafer with no topography, the exposure time is 6.8 seconds). The usual postbake procedure at 100 ºC for 120 seconds was used, and the resist was developed in Futurex RD6. Since it is difficult with standard microscopy equipment to view and monitor development on the sidewalls themselves, development was stopped when inspection revealed full development at both the top and bottom of the mesa edge. Some resist remains undeveloped where the resist pools at the bottom corner of the mesa (Figure 2.7 c), but the important part for this process is that part of

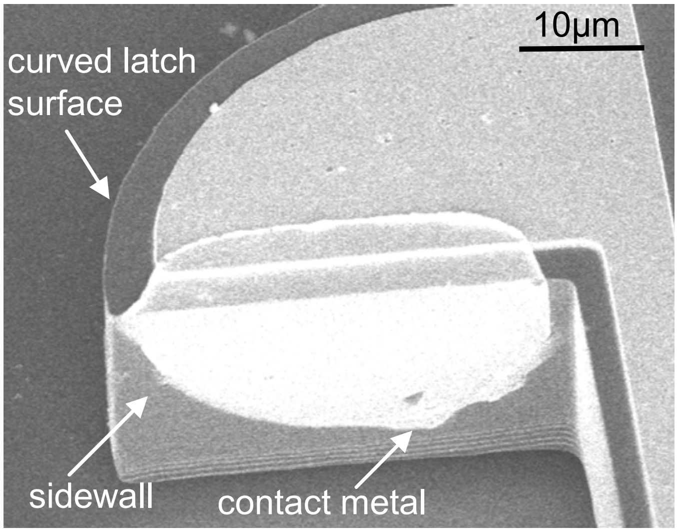

Figure 2.8. Sidewall contact metallization.

the sidewall is now free of resist, so an electrical connection can be made from the top of the mesa to the sidewall. The end result of the metal deposition and liftoff is shown in Figure 2.8.

2.4 Wafer Level Packaging Process

Vacuum packaging reduces the power required for the reset actuators dramatically, since the dominant loss mechanism is heat transfer through the air into the underlying substrate. This has been observed before for thermal actuators [6]. Vacuum probe station tests on the fabricated devices have shown that a sensor that resets at 15V/108mA in air at atmospheric pressure will reset at 7V/50mA at an air pressure of 140mT. Further characterization is needed to determine the pressure levels up to which the benefit of the low surrounding pressure can be utilized.

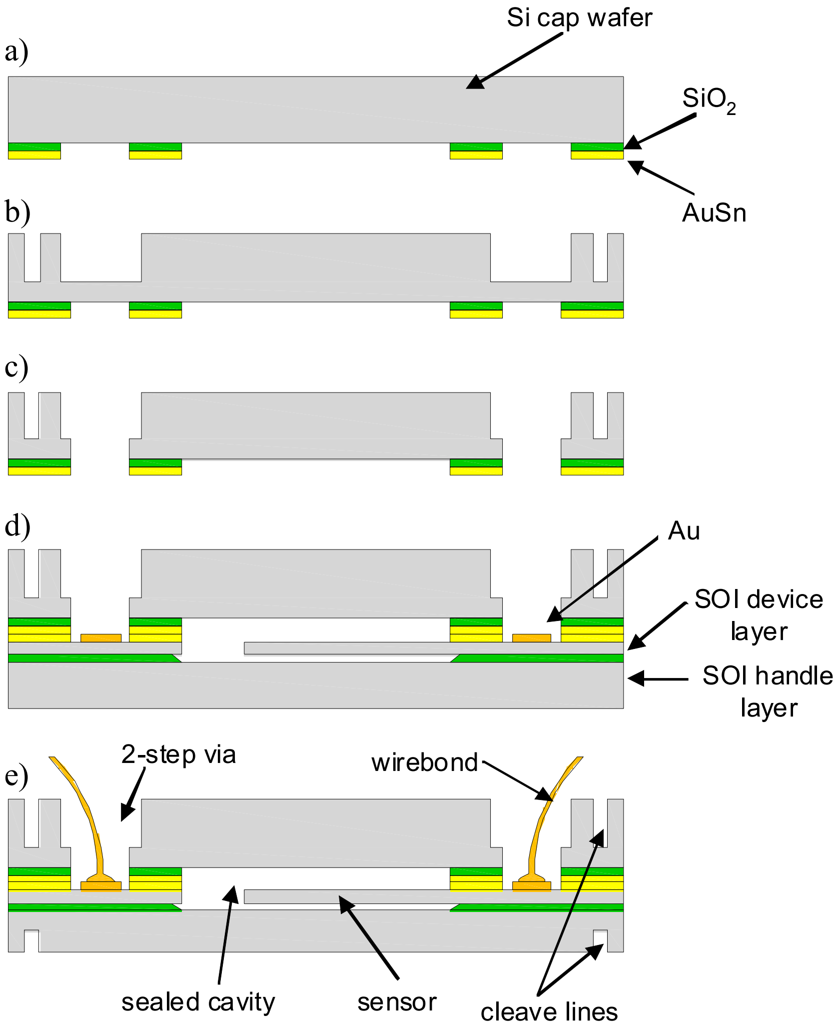

Figure 2.9. Wafer-level packaging process: a) deposition and patterning of oxide insulting ring and AuSn bond rings on cap wafer, b) 375 μm backside etch in cap wafer for cleaving lines and wide part of through hole, c) frontside etch of cap wafer to finish narrow part of through hole, d) bond cap wafer to device wafer using AuSn eutectic bond, and e) wirebond to electronic package.

The author developed a AuSn wafer-level vacuum packaging process to lower the reset actuator current and voltage (see Figure 2.9). The procedure for this process is as follows. First, a silicon dioxide layer 0.5μm thick is deposited on a second double-side-polished silicon wafer (standard, not SOI). Subsequently, AuSn rings matching those on the device wafer are deposited on top of the oxide layer via e-beam evaporation. The oxide layer is removed in the area inside the ring with an RIE etch.

On the opposite side of the cap wafer, cleaving lines and through holes are etched about 375μm deep by using DRIE. The cleaving lines match those in the device wafer. This first part of the through holes is substantially wider than the bond pads to accommodate a wire bonding capillary. These holes are then finished from the front side of the cap wafer with another DRIE; this part of the hole is smaller than the diameter of the AuSn ring. The cap wafer is then aligned and bonded to the device wafer with an AuSn eutectic bond, at a temperature of 300ºC in a 50T H_2N_2 atmosphere by using 1 psi bond pressure. The result of this packaging process is that the device bond pads are exposed to the environment so that electrical contact can be made, while the sensor is contained in a sealed chamber (see Figure 2.9). Electrical connection between the sensor and the bond pads is accomplished through the low-resistivity silicon device layer of the SOI wafer.

The wafer is either cleaved apart or diced, and the individual sensors are placed in an electronic package and wire bonded (Figure 2.10). It is worth noting that

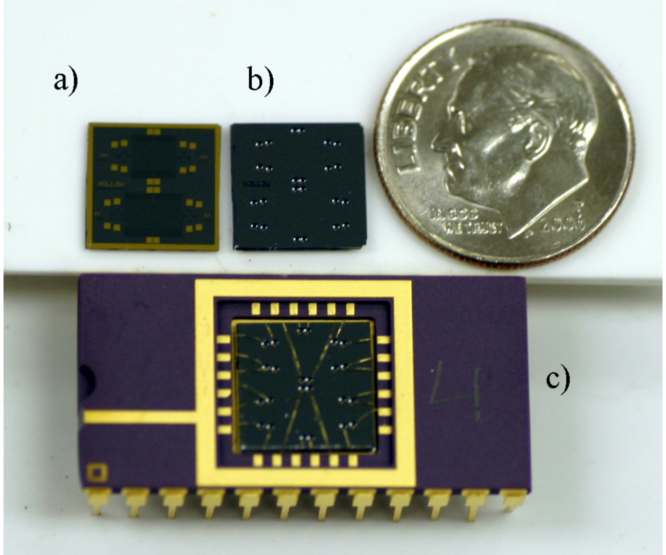

Figure 2.10. Electronic package: a) unpackaged die, b) wafer-bonded die, and c) wafer-bonded and wire-bonded shock sensor die. Each die has two sensors designed to latch at different acceleration threshold levels.

each of the springs is wire bonded to a pin-out on the package for diagnostic use. The resistance between each of the springs can be checked to determine if the spring is intact or broken. The typical spring-spring resistance in the fabricated devices is about 5 kΩ.

One issue encountered with the bonding process was that the Cr/Au bond pads sometimes showed discoloration and bubbles after bonding (see Figure 2.11). The author believes this to be due to pinholes in the bond pads, which allow the underlying chromium to be attacked by the vapor HF. The bond pads appeared undamaged after the release process, but when the wafer is heated above 275ºC, a reaction apparently takes place between the gold and the silicon substrate causing the bubbles and discoloration. Attempts to wire bond to the damaged bond pads failed, since the wire bond would not stick to the pad. By increasing the thickness of the gold

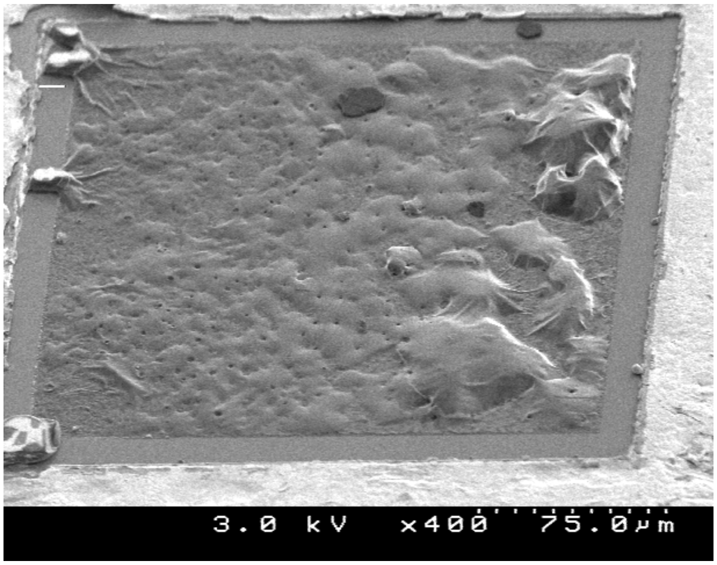

Figure 2.11. Damaged bond pad after wafer bonding, showing bubbles due to HF penetration through micropores in the bondpad and subsequent undercut of the chromium adhesion layer.

layer from 2000 Å to 4000 Å, it is found that the pinholes could be eliminated and the bond pads remained intact after bonding.

2.5 Summary and Author's Contributions

An overview of the sensor and reset actuator design and fabrication process has been presented in this chapter. While the details of the sensor design are unique, the device is functionally very similar to those presented in [19] and [16, 20]. The primary novel aspect of the sensor design is patterned coating of only the flat contact surfaces with metal, which eliminates false positive readings when the sensor is in contact with the latch but not yet fully latched. The rotational thermal actuator design presented in Section 2.2 is a novel actuator concept, although as mentioned above, Heo and Kim independently developed a very similar actuator around the same time [47]. In the area of fabrication, the author's main contributions are the process for patterning and liftoff of metal on the sidewalls, and the wafer-level packaging scheme, which eliminates the need for filled vias.

3. Experimental Studies and Results

This chapter contains a description of the experimental portion of this work. This includes shock testing of the sensor to determine the minimum acceleration required to latch, shock testing of already-latched sensors to investigate possible loss of contact, and high-speed imaging of the latching process to examine the physics and to compare with models developed in Chapter 3.4. Harmonic excitation of the shock sensors is carried out to obtain an indirect measurement of the stiffness of the springs and latches. Testing of both the V-beam style and rotational offset-beam thermal actuators is also presented, as is friction testing conducted by using the V-beam thermal actuators. Portions of this chapter have been adapted from the author's two journal papers [38, 48] and two conference papers on the shock sensor [49, 50], as well as his journal paper on the rotational thermal actuator [39] and conference paper on the friction test device [51].

3.1 <u>Sensor Testing</u>

Two different versions of the shock sensor have been fabricated and tested. They are denoted throughout the text as Design 1 and Design 2, and correspond to nominal acceleration thresholds of 50 g's and 100 g's. The dimensions for each design are summarized in Table 3.1. This work is limited to the study of two different designs because the detailed experimental characterization undertaken here takes considerable time, and an in-depth study of more designs would not be practical. Two devices is also a minimum number needed to begin a validation of the model prediction of the device response. Once a basic understanding of the fundamental physics of the device performance has been established through experiments and simulations of these two designs has been carried out, the reduced-order models can be used to explore the parametric design space and identify new designs to provide a more targeted study of trends and identified phenomena.

3.1.1 Shock Characterization

As the sensor is intended to be a shock sensor, the fundamental measure of performance is how the sensor responds to a sudden acceleration event. To characterize the magnitude of the acceleration required to latch the sensor, shock testing was performed. In this section, the author describes the shock testing methodology and the acceleration threshold results obtained for each of the two designs.

The shock table testing was performed on a GHI Systems Linear Shock Machine (LSM-100). This machine is a horizontal shock machine, so the initial velocity is produced purely through a compression of two springs. The shock itself occurs when the table hits a programmer and comes to rest. The LSM-100 produces pulse durations between 0.1 and 30 ms, with velocity change limits of 63.5cm/sec to 635cm/sec depending on the amount of spring compression (setback) and the hardness of the programmer stop. The programmer that produces the longest duration acceleration pulses was used for all testing except the high-speed video tests. The acceleration pulse was measured by using a single-axis accelerometer screwed into a threaded mount in the back of the table and captured by using computerized data acquisition software. The accelerometer data were filtered at 400Hz to eliminate high-frequency noise in the data.

Table 3.1. Design parameters for the two fabricated versions of the shock sensor.

Parameter	Description	Design 1	Design 2
H_m (mm)	height of mass	2.025	2.025
W_m (mm)	width of mass	4.0	3.1
t (µm)	sensor thickness	3.42e-7	2.65e-7
L_f (mm)	length of suspension spring	1.945	1495
W_f (mm)	width of suspension spring	12	12
w_L (µm)	width of latch cantilever	8	8
l_L (µm)	length of latch cantilever	460	460
r (µm)	latch radius	40	40
d_i (µm)	horizontal offset	15	15
y_0 (µm)	initial sensor travel to latch	150	150
$\ddot{y}_{crit}$ (g)	nominal threshold acceleration for latching	50	100

The author's test setup is shown in Figure 3.1, with a typical acceleration profile captured during the testing shown in Figure 3.2. The shock sensor wafer was attached to the shock table with thin, low-profile, double-sided tape. The setback was set to a level known not to cause latching, and the device was shocked. The wafer was inspected under a microscope to determine if any devices latched. If only one of the two latches engaged on any device, it was considered to be a non-latching event and the device was manually reset by pushing the latch out of the way by using a fine wire held in a pair of tweezers. If both latches engaged on any device, the device was considered to have latched. The setback level was increased slightly (in increments of 0.1-0.2cm) and the test was repeated until all functioning devices on the wafer had latched. This set of events constitutes a single cycle. After each cycle, the sensors were all reset by applying an out-of-plane shock sufficient to pull the masses up and over the latches to reset. The peak acceleration of the latching event as measured from the filtered accelerometer data were recorded for each device in each cycle.

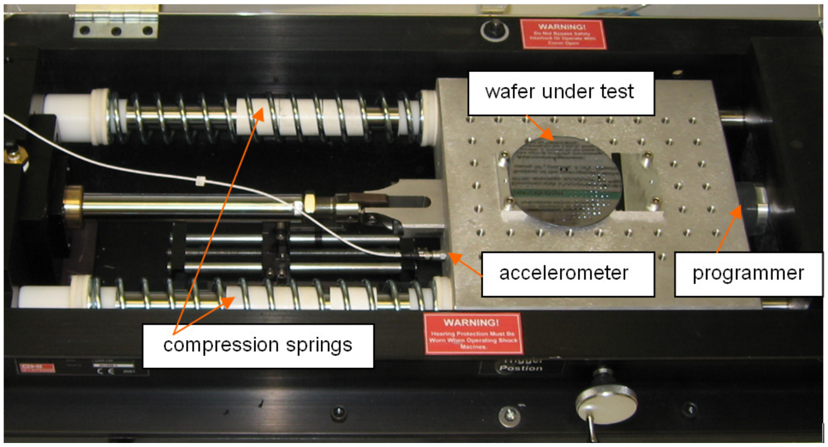

Figure 3.1. Shock table test setup for basic shock experiments.

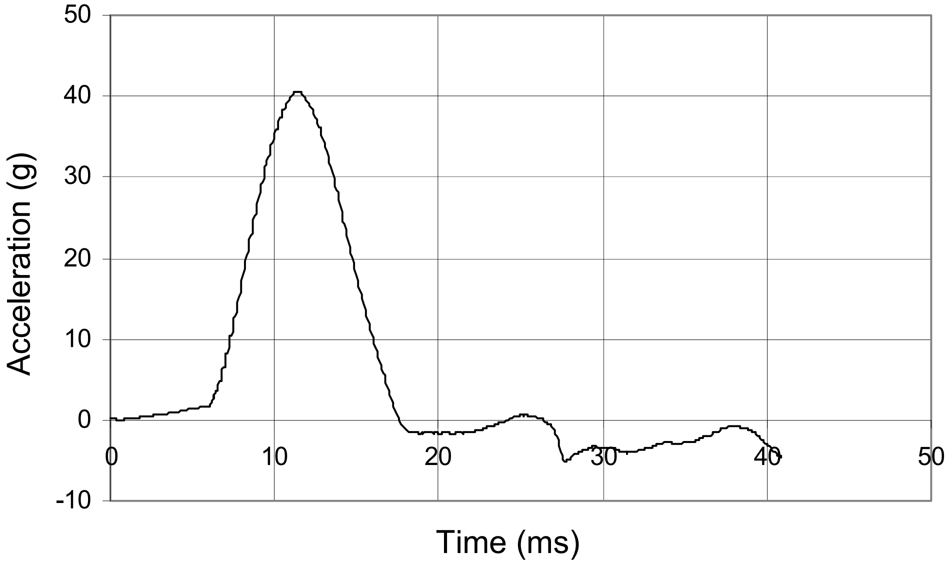

Figure 3.2. Typical acceleration time history produced by shock table, low-pass filtered at 400 Hz (acceleration units are g, or multiples of gravitational acceleration).

Twenty-nine devices on the same wafer were tested repeatedly on the shock table by using above described the full-wafer test procedure. Of these, latching thresholds were obtained in every cycle for 13 devices. Nine of the remaining devices developed stiction after several cycles, evident from manually pushing the mass with a small wire under the microscope and observing that it did not return to the designed equilibrium position. This indicates some force countering the restoring force of the springs, which is likely due to electrostatic charge buildup from the mass rubbing against the wafer during the shock events. The mass is low resistivity silicon, but silicon is known to develop a so-called "native oxide" layer when exposed to air for more than a few hours that is insulating, and the author believes that this native oxide is developing an electrostatic charge that causes the mass to stick lightly to the substrate. The mass can be moved, but there is a discernible stiction force, and hence, data from devices that exhibited this behavior were not included in the analysis. Seven other devices would not latch in the first (or first few) cycles, then started to latch thereafter. The data from these devices were also not included in the analysis.

The average acceleration required to latch the thirteen "good" devices are shown over the first ten cycles in Figure 3.3. From the minimum and maximum accelerations to latch shown for a device in each cycle (plotted as error bars), it is

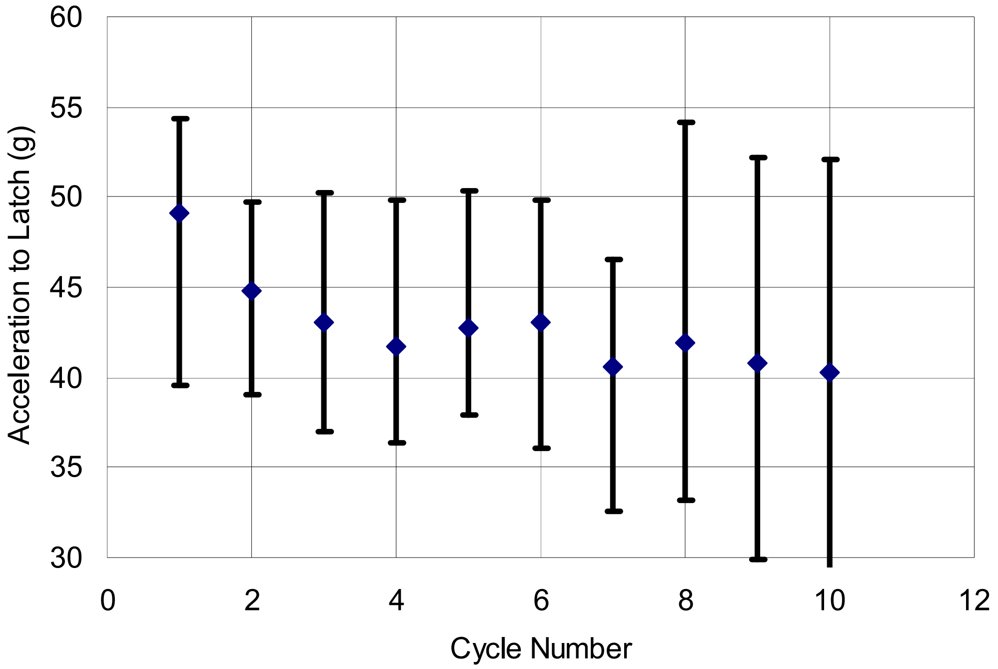

Figure 3.3. Acceleration to latch over first ten cycles for thirteen devices (Design 1). Error bars cover minimum to maximum acceleration levels.

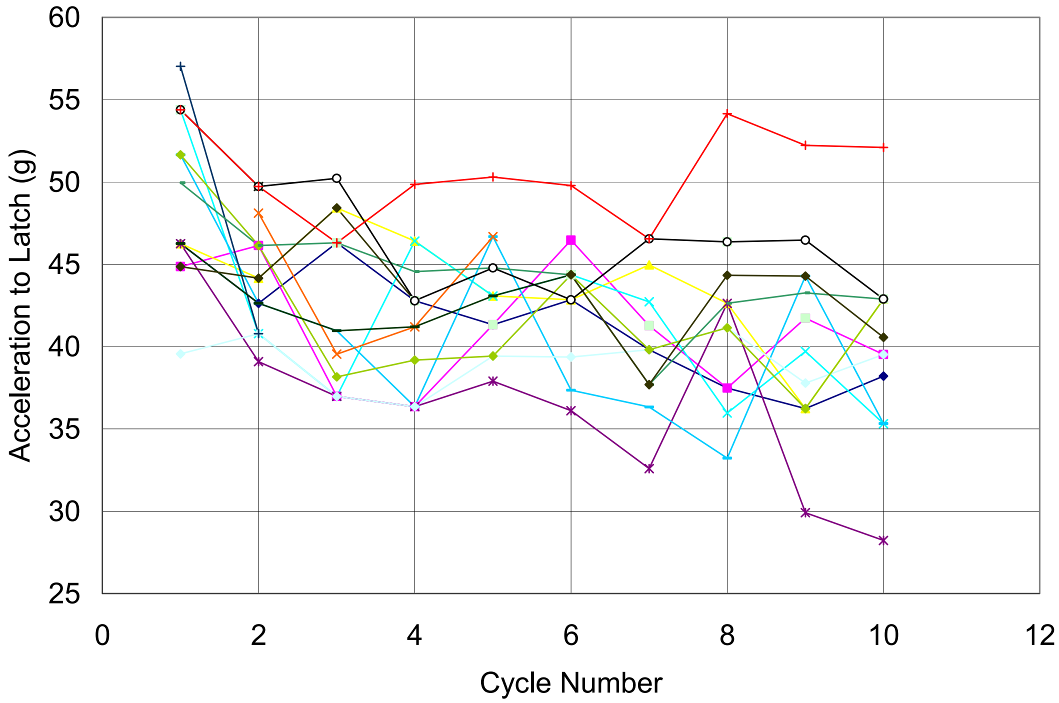

Figure 3.4. Acceleration to latch plotted for thirteen individual devices over first 10 cycles (Design 1).

readily apparent that there is a spread in the data. Nevertheless, it appears that the average latching acceleration level decreases somewhat over the first several cycles. If the latching threshold over the same number of cycles is plotted for each individual device (Figure 3.4), there is a clear downward trend visible for almost every device studied. In fact, for every individual device the acceleration to latch is lower in Cycle 10 than in Cycle 1.

The author attributes this effect to wear in the contact surfaces, smoothing asperities, and a decrease in the value of the apparent coefficient of friction. This is consistent with the findings of sidewall friction measurements on SOI devices presented in Section 3.3, and the SEMs of these cycled devices show evidence of

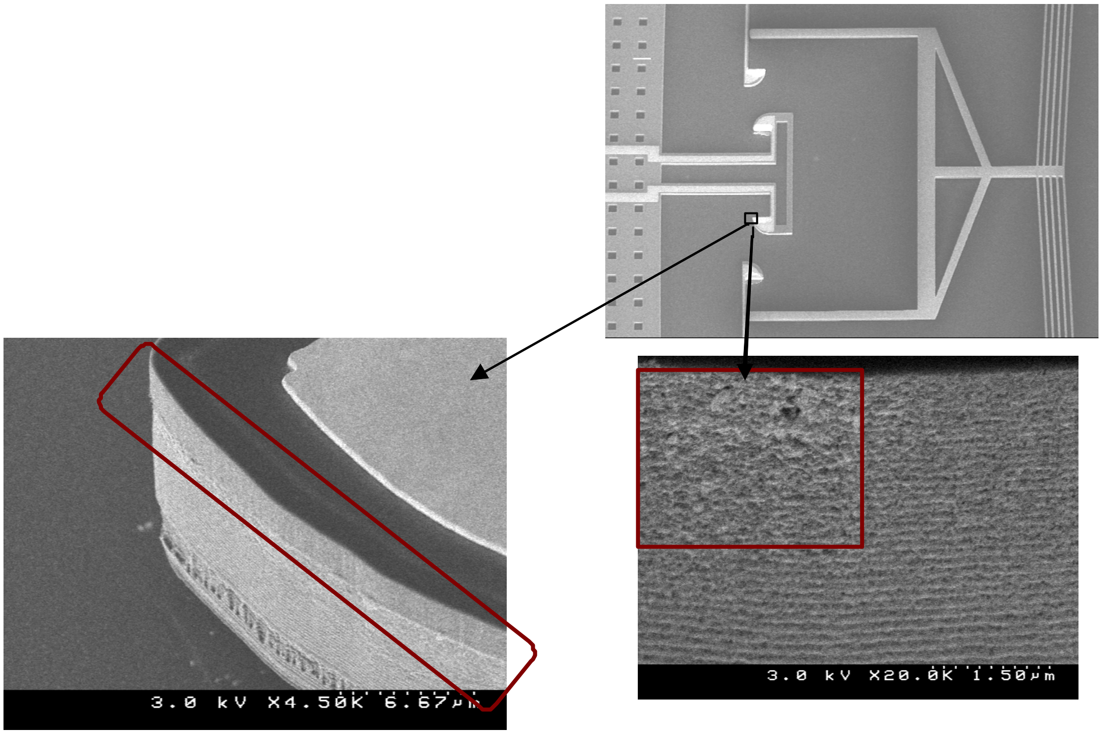

Figure 3.5. SEMs showing wear at top edge of latch contact after 10 cycles. Region of wear is outlined in red.

wear at the top edge of the latch sidewall (Figure 3.5). Contact (and therefore wear) only occurs at the top edge due to a slight taper in the sidewall from top to bottom.

To confirm that the downward trend in the latching acceleration level is due to contact wear and not softening of the springs or changes in the mass itself, the wafer was turned around and tested in the negative direction for 5 cycles. If any changes in the mass or springs were the cause, the first cycle would be expected to exhibit the lower threshold from Cycle 10 in the positive direction since the same mass and springs are used for both directions. However, the latches for the negative direction are completely separate and not affected by latching events in the positive direction, so changes in the latches would be expected to result in a return to the original (high) latching threshold in the first negative cycle.

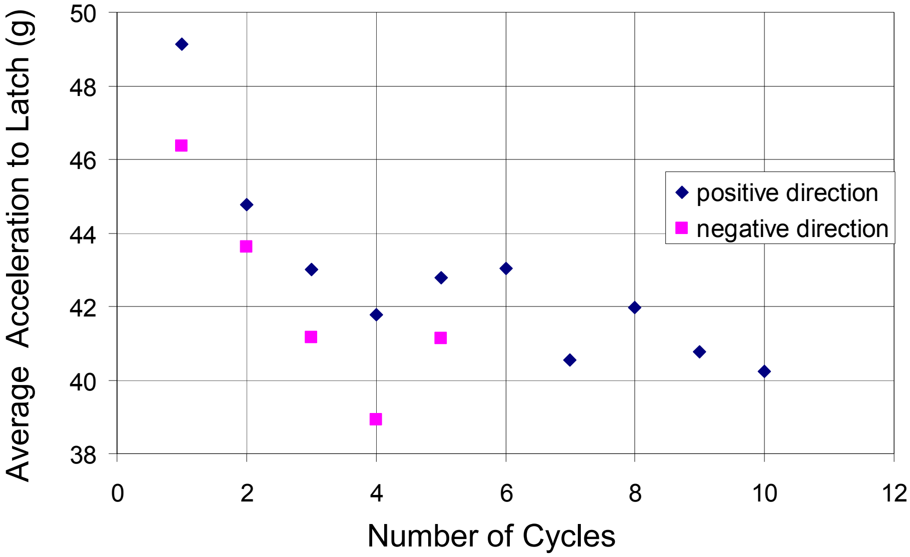

Figure 3.6. Repeated cycle testing performed first in positive direction, then, in negative direction. Data reported is averaged over 13 devices that successfully latched every time in the positive direction.

The resulting average peak acceleration to latch is shown in Figure 3.6, with the average values for the positive cycling shown for clarity. The same decreasing trend was observed in the negative direction cycling, with the average acceleration to latch jumping back up from the 40.2g level measured in the last cycle of the positive direction testing to 46.4g. This is not quite as high as the 49.1g average peak acceleration seen in the very first positive direction test. This discrepancy can be attributed to the fact that during the positive direction testing a few devices were inadvertently latched in the negative direction while attempting to free half-engaged devices. This would tend to lower the friction coefficient for a few of the devices, bringing the overall average down.

The longer term trend is shown in Figure 3.7 for a different wafer over fifty cycles of repeated shock testing. For the cycles in between the plotted data points, the acceleration was set to a sufficient level to latch all of the devices. Sixty-eight devices

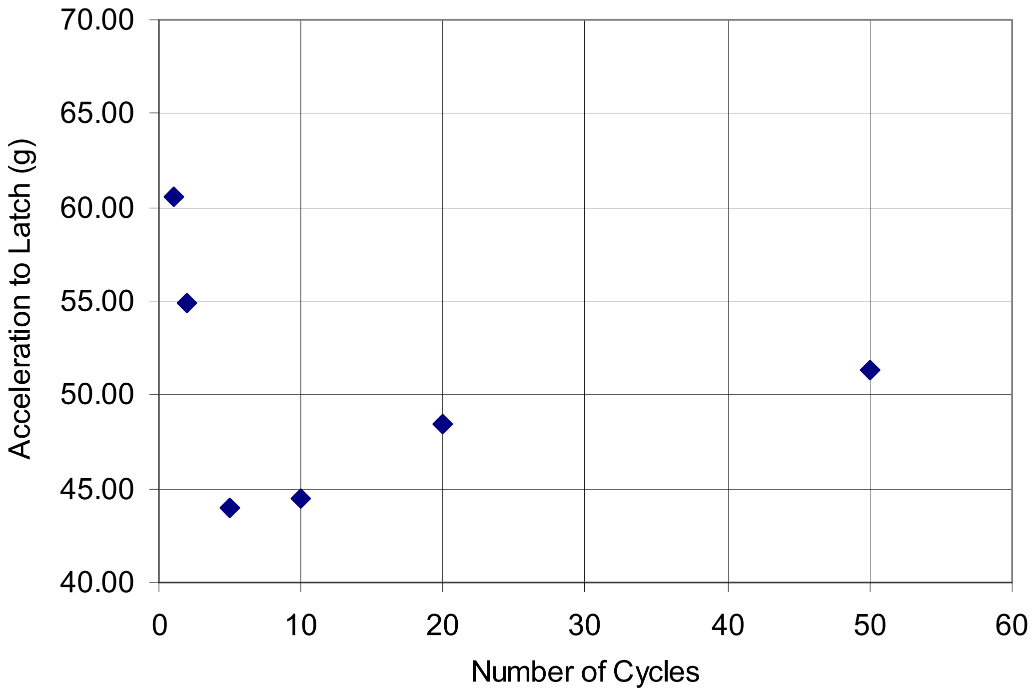

Figure 3.7. Long term repetitive shock cycling results for 36 Design 1 sensors on one wafer.

were tested on this wafer, of which 36 devices were latched at all of the cycles for which data was recorded (1, 2, 5, 10, 20 and 50 cycles). The figure shows the average acceleration to latch for these 36 devices. As seen in the previous case, a decrease in the threshold acceleration level is seen over the first ten cycles. After twenty and fifty cycles, the threshold acceleration required to latch increases again. The author attributes this phenomenon to a new resisting force arising from electrostatic stiction, which arises over time as the mass collect opposite electrostatic charges due to scraping together. Over many cycles, this begins to pull the mass down until it eventually scrapes against the substrate.

Design 2 devices from the same wafer used in Figure 3.3 were also tested over seven cycles. Out of twenty-five functional devices tested, 16 successfully latched for every cycle. The results for these 16 devices are shown in Figure 3.8. There is no

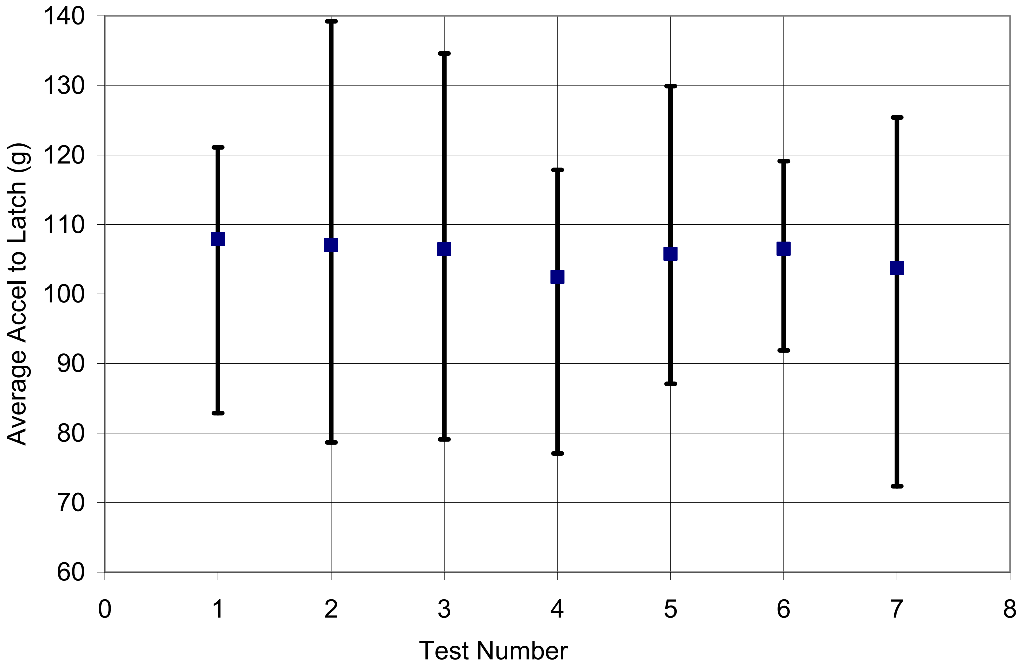

Figure 3.8. Acceleration threshold to latch for sixteen Design 2 devices over 7 cycles. The error bars indicate the maximum and minimum acceleration to latch for any one individual device.

meaningful decrease in the acceleration to latch observed over these first seven cycles. The author hypothesizes that this is because the Design 2 springs are stiffer compared to those of Design 1 (1.32 N/m as compared to 0.60 N/m for Design 1). The friction force is therefore expected to constitute a smaller percentage of the overall force resisting the motion of the mass, so slight changes in the friction coefficient would not be expected to have as large an effect on the acceleration required to latch the device.

3.1.2 High-Speed Video of Sensor Latching

To provide insight into the latch dynamics and experimental verification for the models, the latching of the shock sensor was also observed on high-speed video to follow the progression of the mass from resting, to contact, to the latched state. The experimental setup for high-speed video is shown in Figure 3.9. The acceleration applied to the shock sensor was monitored with the Dytran 3200B6T accelerometer threaded directly into the shock table. For these tests, the shock sensor was wirebonded to a dual inline package for electrical monitoring of the sensor and electrical reset in between experiments. For electrical monitoring, a voltage divider circuit was constructed. One latch of the sensor was connected to a DC power supply set to output 5 V, the other latch was connected to a 1 MΩ resistor. The opposite end of the resistor was connected to ground. When the sensor latches, the circuit is closed and a voltage is detected across the 1 MΩ resistor. A computer with a data acquisition system was set up to power the accelerometer, capture the acceleration data and the voltage sensed through the sensor.

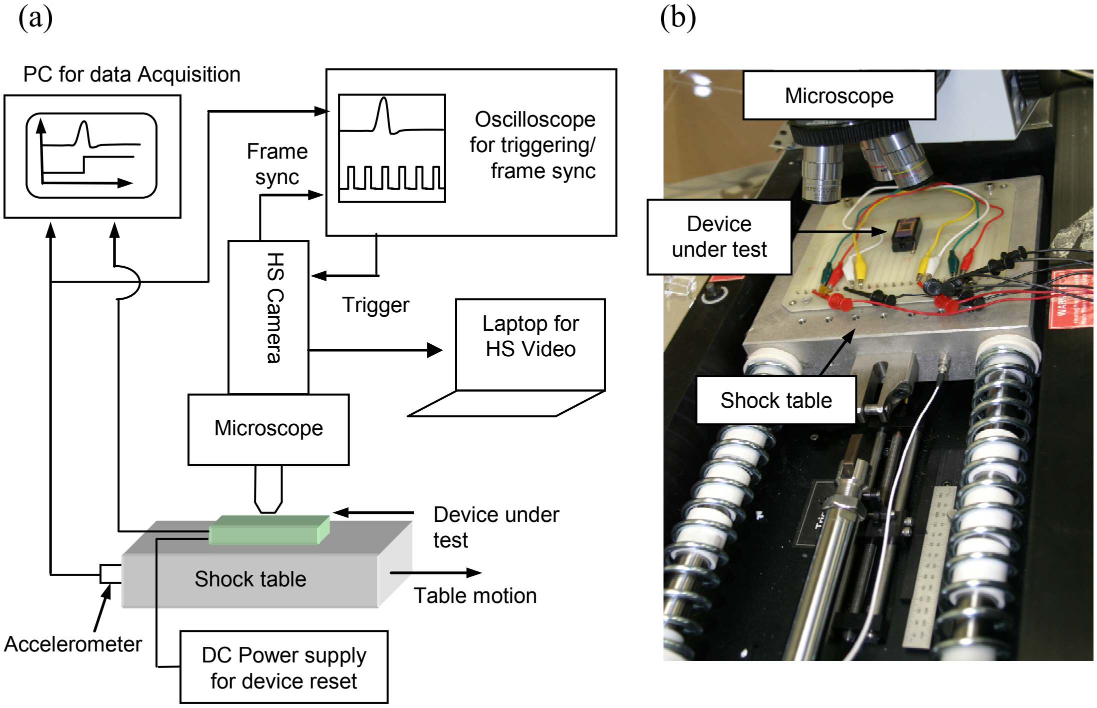

Figure 3.9. Shock table test setup for high-speed video capture. (a) Schematic of the entire test setup, and (b) photograph of the shock table with a device mounted under the microscope for testing.

The microscope setup used a 5x objective and 10x multiplier (for a total magnification of 50x) were used to image the sensors. The accelerometer output was used to trigger an oscilloscope which in turn triggered the high-speed camera. The oscilloscope captured the accelerometer output, the trigger signal sent to the camera, and the frame sync output from the high-speed camera. Because the oscilloscope used only has three channels, the voltage divider signal could not be captured on the oscilloscope. However, by matching the accelerometer trace from the data acquisition system and the oscilloscope, the trigger and frame sync can be synchronized with the voltage divider signal.

The individual frames from the high-speed video were analyzed using a simple MATLAB routine (Figure 3.10). The routine reads the image file into an array, resizes the image to exclude irrelevant parts of the frame based on user input, and sums the image brightness values (ranging from 0-255) over each column. The gold traces on the mass are significantly brighter than the background and are easy to pick out when the column sum is plotted. Because the background brightness varies with position (it is brightest in the center of the frame) and the sensor moves through the frame during the latch event, a global maximum does not necessarily suffice. Instead the frame is searched for a pair of local maximum representing the two parallel gold traces across the mass.

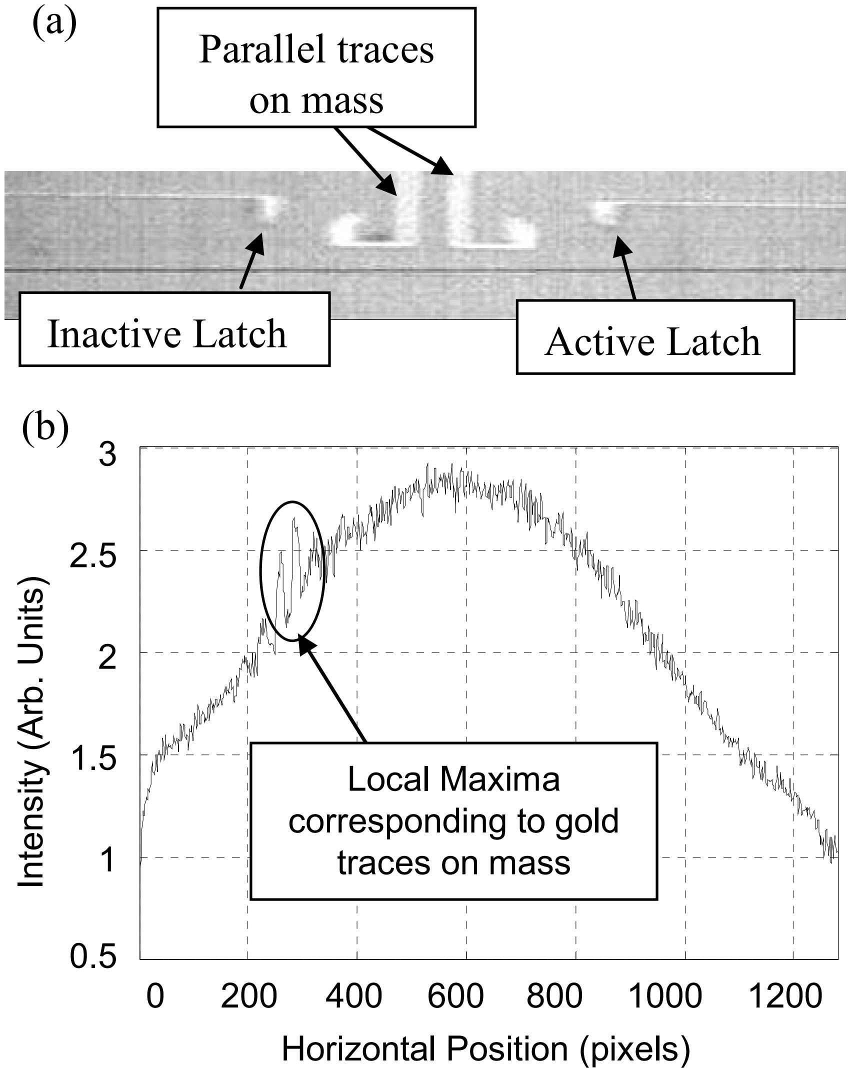

Figure 3.10. Analysis of high-speed video frame. (a) Frame from high-speed video showing parallel traces. (b) Analysis of the image - two adjacent local maxima indicate position of mass.

Similarly, the position of the chip can be tracked by assuming there is no significant deflection of the second (inactive) latch in the direction parallel to the sensor axis. By inactive, the author refers to the latch for negative deflection when the direction of the applied acceleration is such that the mass travels in the positive direction. The mass never contacts this latch and the ratio of stiffness to mass is very high, so the assumption of no deflection should be valid. Another local minima can be found, and this minima corresponds to the gold coating on top of the latch. By subtracting the motion of this local minima (and therefore the motion of the shock table under the camera) from the motion of the mass, the relative motion of the mass with respect to the translating reference frame of the chip can be found. This relative motion is the parameter tracked by the model and also indicates whether the sensor is latched. If the relative motion exceeds 150 μm, the mass has moved completely past the latch and will remain latched until the sensor is reset.

The full interaction of the shock sensor and latch is shown in Figure 3.11 for Design 1 and in Figure 3.12 for Design 2. The frame rate for both videos was 4261 frames per second, the highest frame rate available with a reasonable resolution on the high-speed camera used. Fewer frames are captured for Design 2 because the overall time to latch is lower. The position data extracted from each video are shown in Figure 3.13 for Design 1 and Figure 3.14 for Design 2. For the Design 1 video, time zero was estimated by matching the model presented in 4.2.2 to the position data from the video. To eliminate this uncertainty for the Design 2 video, a frame sync was set up from the high-speed video camera to pinpoint the exact time for each frame as well as a voltage divider to electrically monitor the contact. These are all plotted together for Design 2 in Figure 3.14.

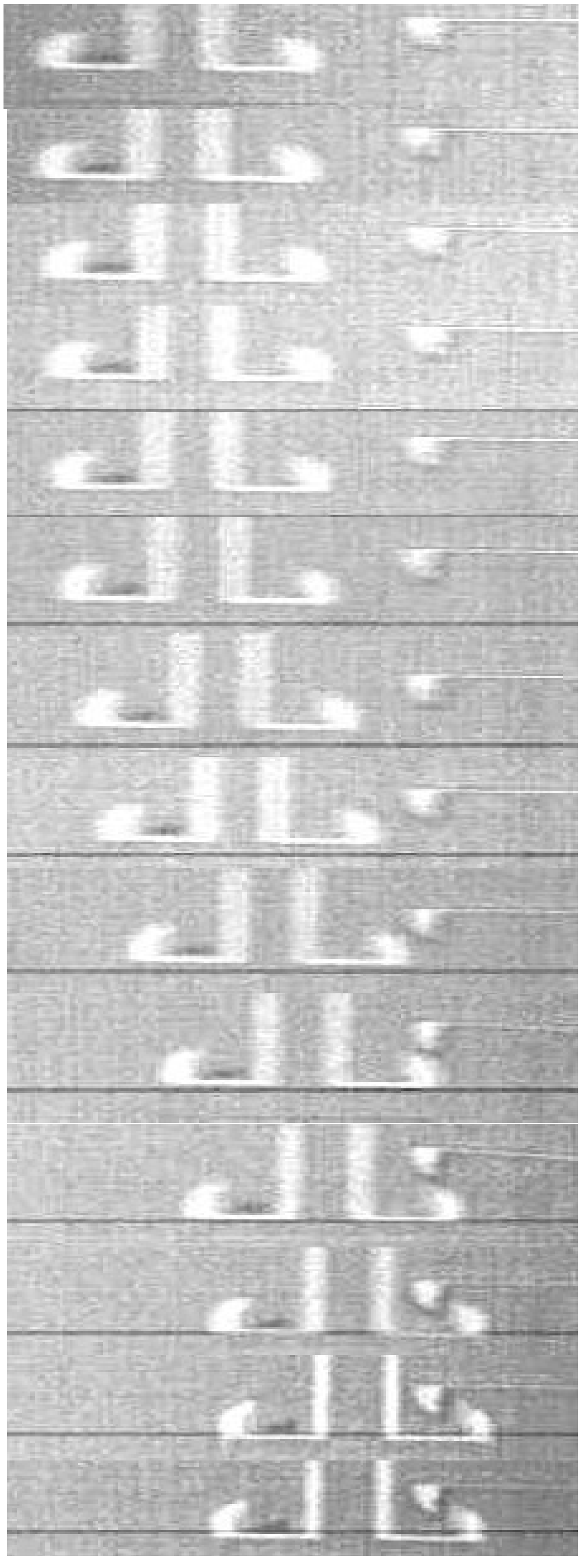

Figure 3.11. High-speed video of Design 1 sensor showing latching progression. The time between frames is 0.235 ms, and the first frame corresponds to the onset of the acceleration pulse.

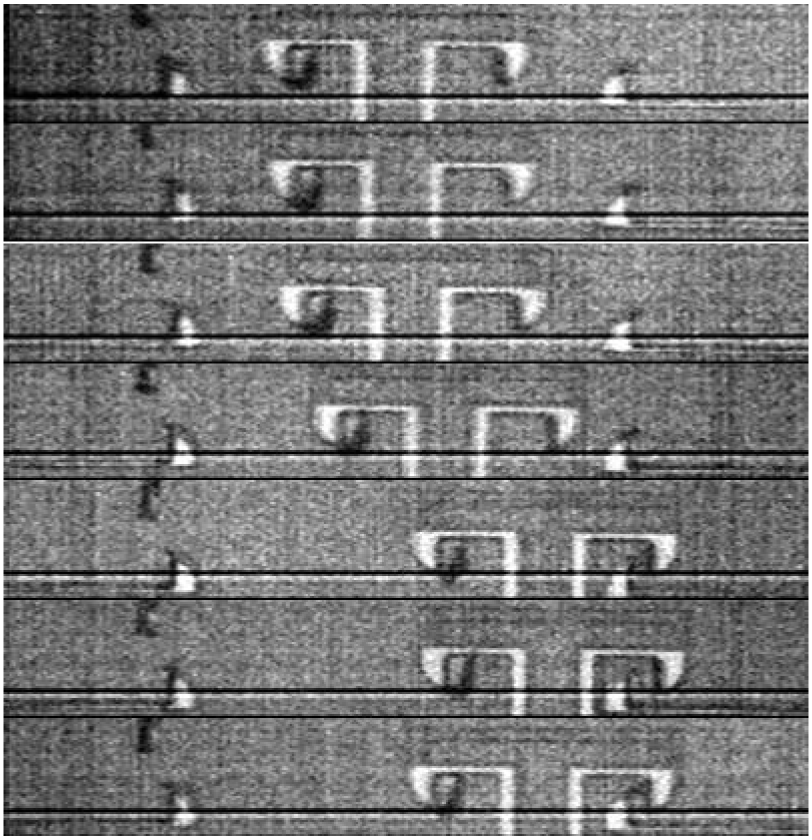

Figure 3.12. High-speed video of Design 2 sensor showing latching progression. The time between frames is 0.235 ms, and the first frame corresponds to the onset of the acceleration pulse.

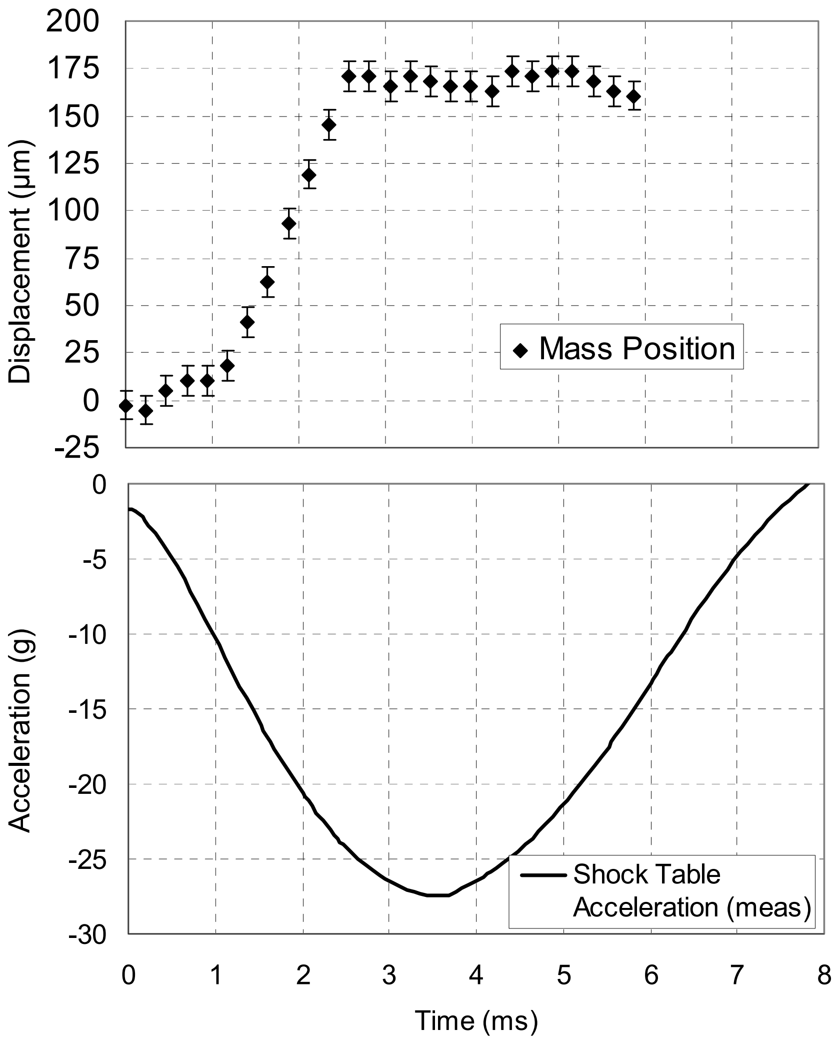

Figure 3.13. Position data extracted from Design 1 high-speed video. The error bars indicate uncertainty in the position measurements taken from the video frames due to blurring.

Examining the position versus time data, the timing of the latch event can be estimated. For both sensors, the mass must travel 92 µm before contact is made with the latch, and 150 µm before the device is fully latched. For Design 1 (Figure 3.13), contact is made after about 1.8 ms and the device is latched after about 2.6 ms. The acceleration pulse lasted approximately 8 ms in this test, so the device is latched well before the peak acceleration is even achieved. There was no electrical monitoring during this test, so the exact time when the electrical circuit closes is unknown. For the Design 2 test (Figure 3.14), a harder programmer was used to reduce blurring, so the acceleration pulse duration was approximately 2.2 ms. First contact and latching both occur sometime between 0.75 and 1 ms, and electrical closure of the switch occurs around 1.3 ms. It is also evident from the contact voltage output trace that the switch bounces several times after latching. The electrical circuit finally closes for good at 2.9 ms (outside the scale of the graph).

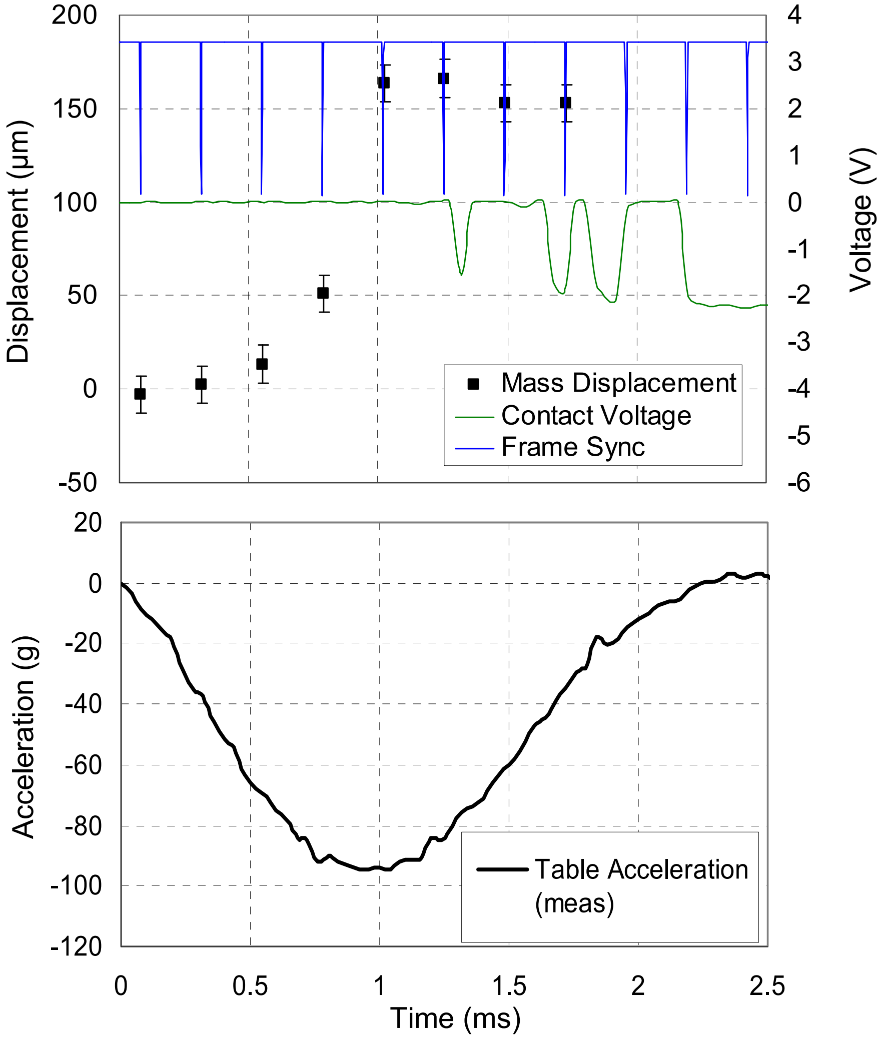

Figure 3.14. Position data extracted from Design 2 high-speed video, along with the frame synchronization signal from the camera and electrical monitoring of the latch closure.

3.1.3 Characterization of Electrical Performance of Latch

Because the sensor is intended to be electrically sensed, the author characterized the electrical performance of the sensor. The sensor was connected in series to a 1MΩ resistor during shock testing to create a switched voltage divider. One latch was connected to the positive terminal of a DC power supply set for 5V output, and the other latch was connected to one terminal of the resistor. The second terminal of the resistor was connected to the power supply ground. The voltage across the resistor was monitored during the test on one channel of the data acquisition system. The output from an accelerometer mounted on the shock table was monitored on a separate channel. The result of one such test is shown in Figure 3.15. The voltage across the resistor jumps to 4.97V after the shock sensor comes to rest against the latches and closes the circuit. Since the latch contact metallization is

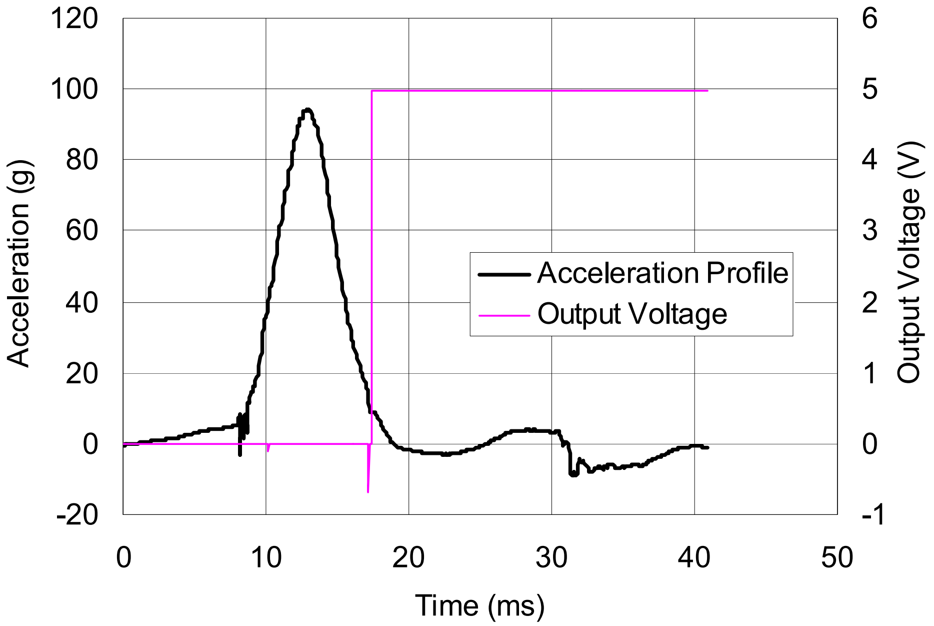

Figure 3.15. Electrical sensing of latching event. Positive voltage indicates the device is latched.

lithographically defined and only present on the flat back surface of the latches, the resistance during the sliding phase of contact is orders of magnitude higher (typically > 20MΩ), and hence, there is no false trigger before the mass pushes all the way past the latches.

The time delay between the acceleration event and the voltage output seen in Figure 3.15 is a result of the mass continuing to travel past the latch before coming back and resting against the metalized contact surface. The length of the time delay primarily depends on the time taken by the mass to move past the latch and the magnitude and duration of the applied acceleration.

In order to investigate potential degradation of the latch metallization due to repeated latch/reset events, the authors cycled the shock sensor over 100 times on the shock table, resetting the device with the integrated electro-thermal reset actuators after each cycle. During reset, as the contact metallization on the latches and mass scrape together, there is some concern that the subsequent wear might cause the contact resistance to increase dramatically after a small number of cycles. The results of the repeated cycling testing are shown in Figure 3.16. In creating this figure, data for a 6 unsuccessful latch attempts were omitted along with data for cycles one through six, which were used for the electrical confirmation of latching experiments reported above, because the contact resistance was not measured directly in these tests. The cycling was completed over the course of about an hour, eliminating the possibility of environmental degradation. It is evident from the data that the contact resistance does not change even over 100 cycles. It is also notable that the contact resistance is remarkably consistent from event to event. Even the outlier data points

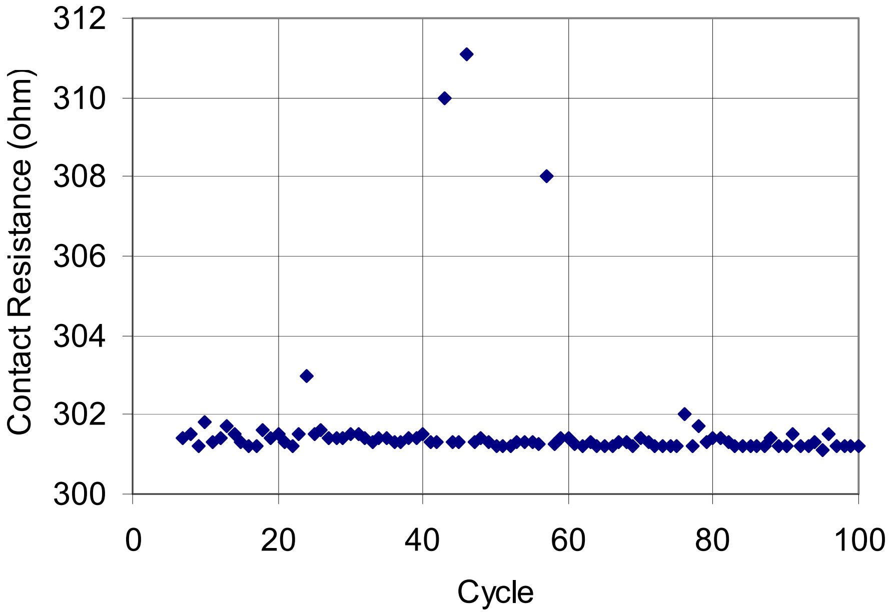

Figure 3.16. Contact resistance of latched sensor over 100 cycles.

differ from the mean by less than 4%. The standard deviation over all 93 cycles is 1.5Ω, less than 0.5% of the mean value.

The contact metallization on the latch sidewalls was examined in the SEM before and after the 100 latch-reset cycles (Figure 3.17). Despite the very good contact resistance over all 100 cycles, significant wear and flaking off of the gold contact is observed. This is most likely due to the scraping of the contact surfaces against each other during the reset actuator operation. During reset, the actuators push the latches out of the path of the mass to allow the device to reset. The excellent repeatability of the contact resistance over many cycles is even more remarkable in light of the gross degradation of the contact metallization evident in the SEM images (Figure 3.17). It is expected that this degradation will eventually lead to poor electrical contact and a higher contact resistance. However, this type of device is intended for monitoring potential damage-inducing shocks, and 100 cycles is probably much more than what would be tolerated by the system the sensor is being

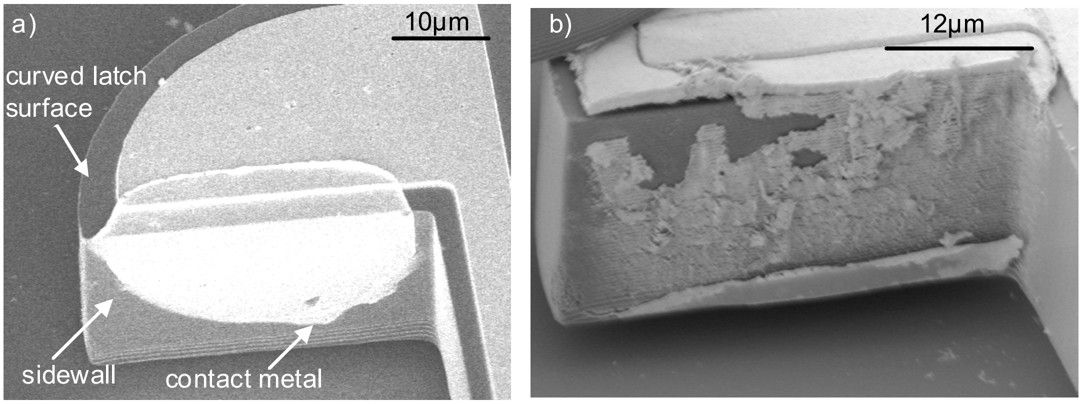

Figure 3.17. Latch contact metallization: a) before use and b) after 100 cycles. Metal shows significant degradation after cycling, but retains good contact resistance.

used to monitor. The contact wear is not expected to affect the useful life of the sensor in most applications.

3.1.4 Post-Latch Shock Testing

After the sensor has latched, it will remain latched until it is reset. However, the electrical contact between the mass and latch can be momentarily lost due to a subsequent acceleration in the latching direction, if the acceleration is large enough. To demonstrate this effect and understand the limitations of the sensor, an electrical monitoring signal was applied to a latched Design 1 shock sensor, and the sensor was shocked with progressively higher pulses until contact was lost. A constant current of 50 μA was applied across the latches, and the voltage across the latches was monitored. When the latches lose contact, a sudden increase in voltage is detected.

For the device tested, the lowest shock level observed to result in loss of contact was 53.7 g (Figure 3.18). With progressively higher acceleration pulses, the contact is lost at a similar acceleration level and remains open until the acceleration decrease below this level, with a delay of up to 300 μs at the onset and 800 μs as the

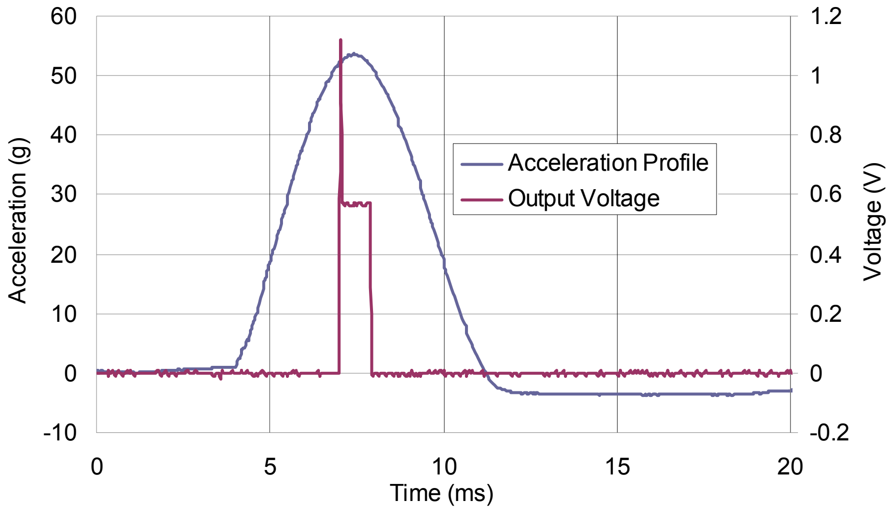

Figure 3.18. Electrical monitoring of latched shock sensor subjected to secondary shock of 53.7 g.

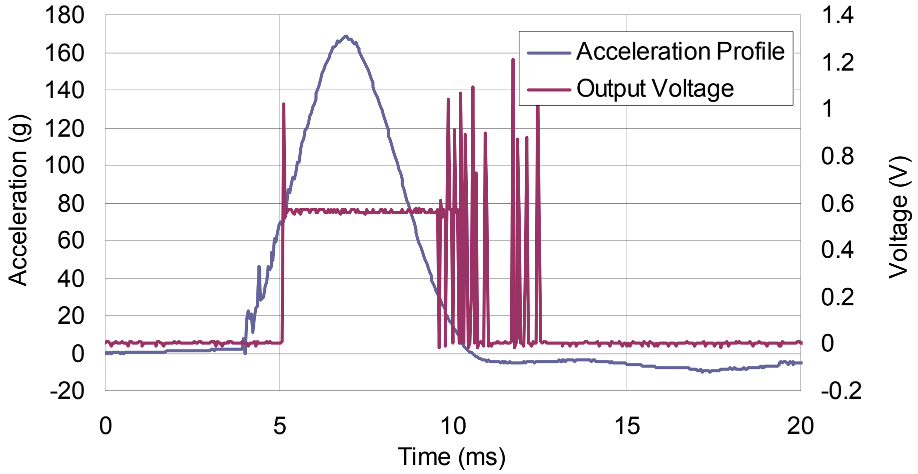

Figure 3.19. Electrical monitoring of latched shock sensor subjected to secondary shock of 168.7 g.

acceleration dissipates. The highest acceleration pulse applied was 168.7g, shown in Figure 3.19.

The implications of this loss of contact depend on how the shock sensor is integrated into a larger electronic system. The shock sensor can be used in one of three ways: the system can query the sensor at set intervals and record whether the sensor has latched in the time between intervals; it can be used as a wakeup/trigger sensor for a standard accelerometer; or it can be constantly monitored for latch contact. In the first two scenarios, the event will generally be interpreted by the system as a single event. In the last scenario, the system interpretation depends on software. In the simplest case, the software is written to log every new contact as a shock event, and both the original latching event and post-latch secondary shock will be recorded as separate events. If the software is written such that after latching, the system does not look for events until the sensor has been reset, only the original event will be recorded. The acceleration required for a latched device to lose contact will generally be smaller than the acceleration required to latch, because there is no contact force between the latch and mass to overcome. Therefore it may not be desired to record the post-latch secondary shock. This should be considered carefully in the implementation of this type of sensor.

3.1.5 Harmonic Excitation

Harmonic excitation of the shock sensor was carried out to determine the first resonance frequency of the shock sensor to verify the mass and spring constant calculated from the device dimensions. The harmonic excitation of the shock sensor was realized by using a small vibration table. The frequency response was measured using a laser Doppler vibrometer (LDV) mounted on a microscope. The microscope was in turn mounted on a boom stand and suspended above the vibration table. A laser is sent through the microscope and the LDV system is used to measure the Doppler shift in the return signal. The frequency shift is related to the velocity component parallel to the direction of the laser. This means that the measurement is well-suited for out-of-plane measurements. Since the shock sensor mass moves in-plane, the chip must be mounted perpendicular to the microscope field of view.

However, in order to provide a clear path for the laser beam to hit the mass and return, the chip was mounted perpendicular to the vibration table and the table was tilted approximately 10 degrees off of the axis of the microscope. The motion of the vibration table is therefore correctly coupled to the sensor mass, and the sensor mass moves nearly (but not exactly) parallel to the direction of the laser. The test setup is shown in Figure 3.20.

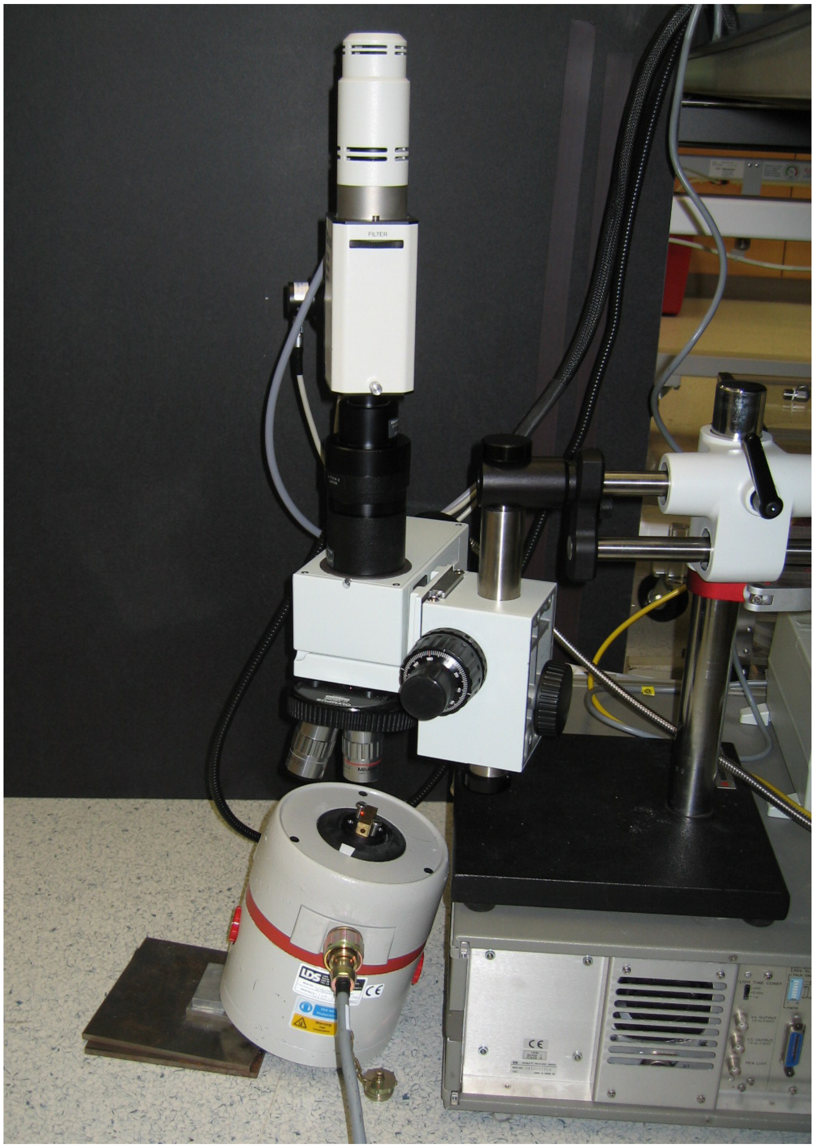

Figure 3.20. Experimental setup for harmonic excitation.

The laser Doppler vibrometer used was a Polytec MSV-300 system, with a detachable head that can mount on any microscope. The bandwidth for the measurement was set to 1 kHz, with 1600 discrete frequencies scanned. The driving signal for the vibration table was a pseudorandom (broadband) signal, with a 2 Volts rms magnitude for Design 1 and 3 Volts for Design 2.

The measurements were carried out at a single point on the device. The laser was focused on the sidewall of the beam extending from the side of the mass towards the latches because this is the point with the widest uninterrupted view of the sidewall of the mass. The test site is shown in Figure 3.21. The latches were manually broken off to prevent them from interfering with the motion of the mass. The LDV was set to perform a fast fourier transform to output the frequency response. Multiple frequency spectra (between 8 and 21) were averaged by the LDV system for each device and the resulting magnitude and phase components of the velocity, displacement, and acceleration were saved. Since the velocity measurement is a direct one, the

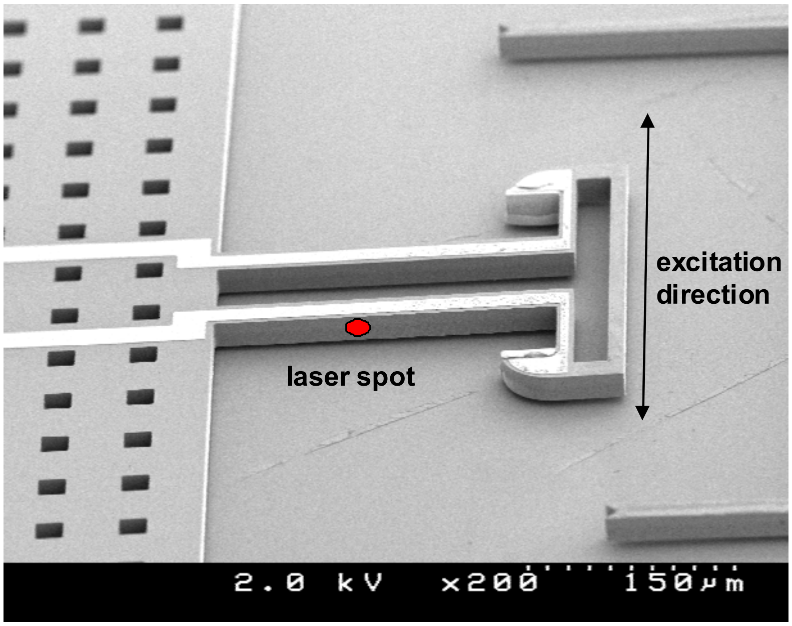

Figure 3.21. Laser query site for harmonic excitation of sensor.

acceleration and displacement are calculated from the velocity measurements.

Since the frequency-response of the vibration table itself is not flat, a spectrum was also taken off of the surface of the block on which the chip was mounted. The resulting frequency-response reference data are shown in Figure 3.22. Representative frequency responses for Designs 1 and 2 are shown in Figure 3.23 and Figure 3.24, respectively. In each case, the velocity data has been plotted since these are the actual measurements (displacement requires a numerical differentiation which can introduces an additional source of uncertainty). The rolloff between 100Hz and 200Hz in each of these device response plots is due to the frequency-dependent response of the vibration table itself.

The first resonance frequency of Design 1 was 174.8 +/- 3 Hz over 5 devices tested from one wafer. The first resonance frequency of Design 2 averages 294.8 +/- 5 Hz over 5 devices tested from one wafer. The devices were chosen in rows from the center to the edge of the wafer, since the deep reactive ion etch process which defines the features has some variation from center to edge. The resonance frequency was nearly identical in all designs, with a variation from the maximum to the minimum of less than 6 Hz for Design 1 and less than 9 Hz for Design 2.

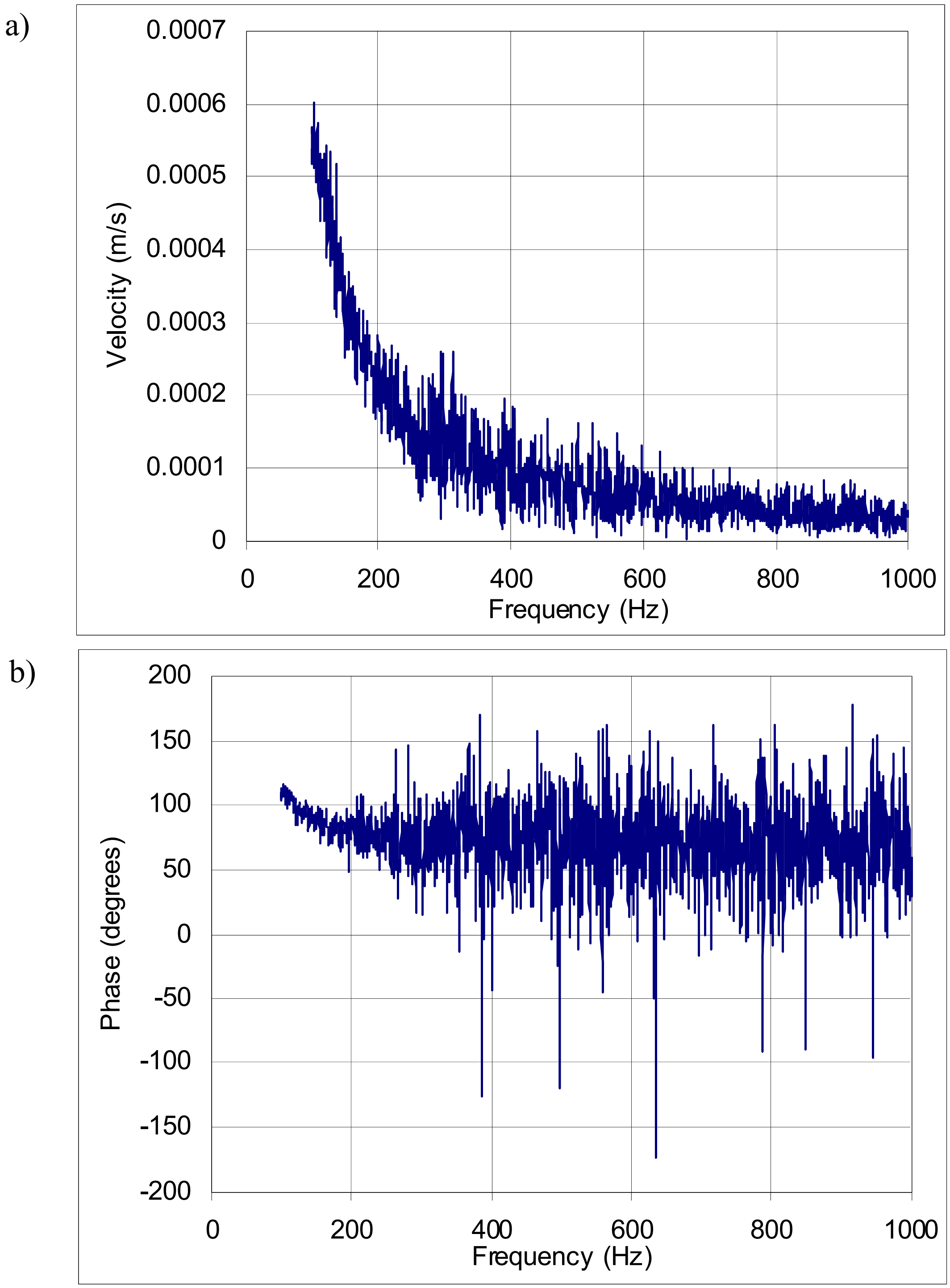

Figure 3.22. Frequency response of vibration table with 2V pseudorandom driving signal: a) magnitude and b) phase.

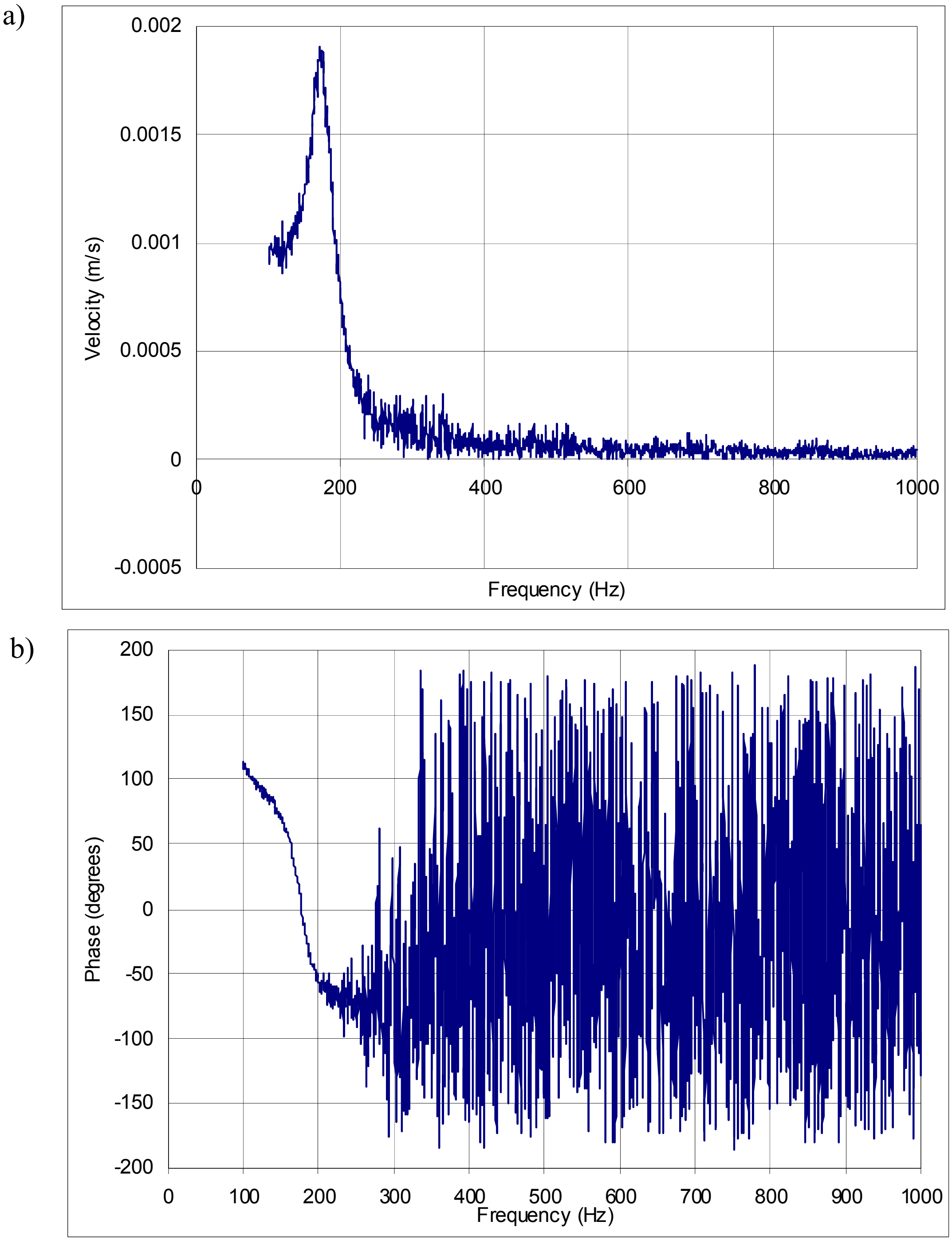

Figure 3.23. Frequency response for Design 1: a) magnitude and b) phase.

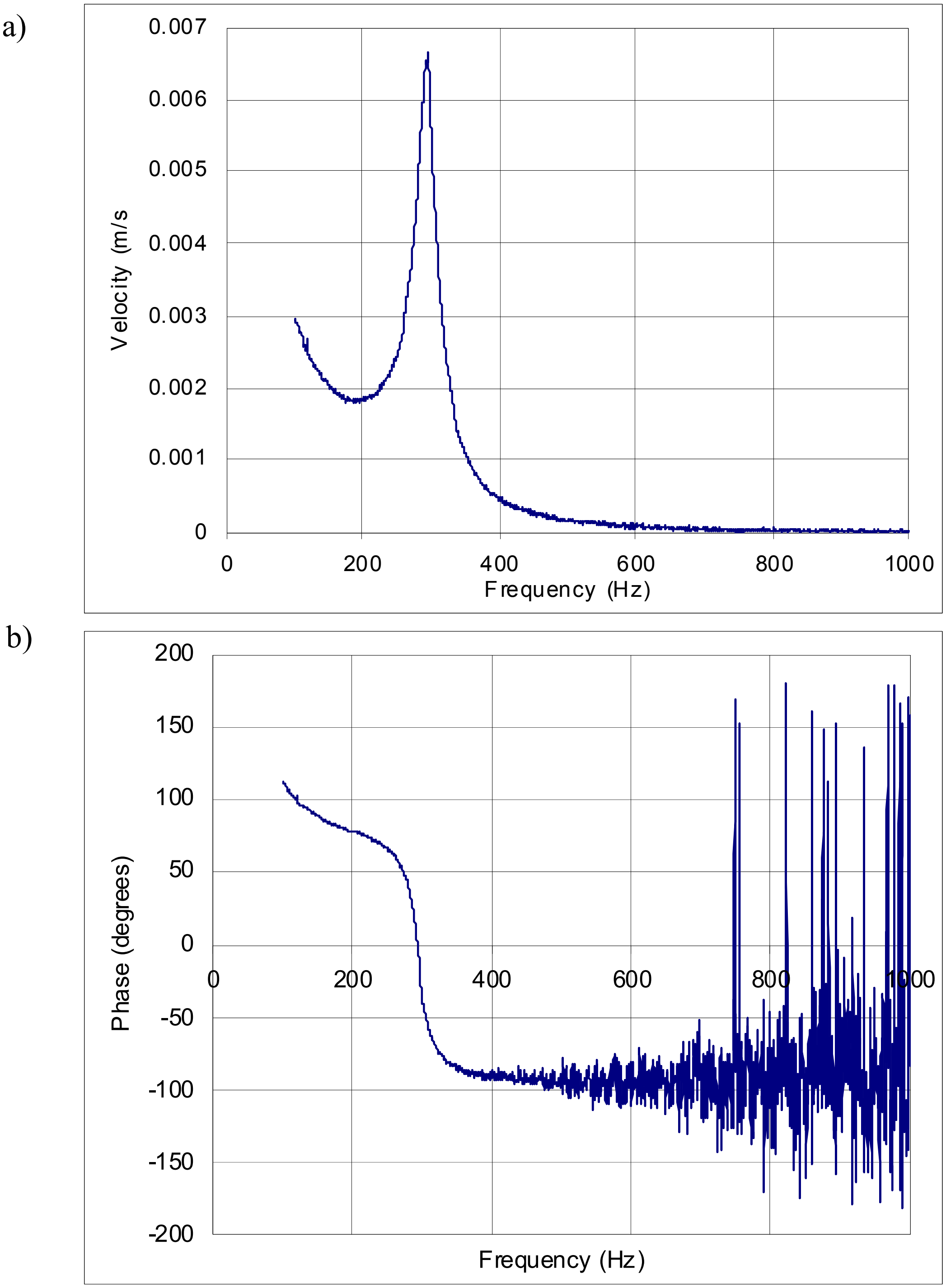

Figure 3.24. Frequency response for Design 2: a) magnitude and b) phase.

The quality factor and damping ratio can be estimated from the frequency-response data as well. The quality factor is computed as the resonance frequency divided by the bandwidth between the half-power points, or the points at which the magnitude of the response is equal to the maximum response magnitude divided the square root of two.

$$Q = \frac{F_R}{(F_{Hi} - F_{Lo})} \tag{3.1}$$

For small values of damping, the damping ratio can be estimated as [52]

$$\zeta = \frac{1}{2Q}. \tag{3.2}$$

The parameters extracted from the harmonic measurements along with the designed values are shown in Table 3.2. The measured first resonance frequency differs significantly from the values calculated by using the designed dimensions of the spring and mass, however. For Design 1, the design dimensions indicate a first natural frequency of 211 Hz and 356 Hz for Designs 1 and 2, respectively. The mass calculation is likely to be very close to accurate assuming the density value of 2.33 g/cm^3 is correct, because the dimensions of the mass are very large and small

Table 3.2. Comparison of sensor design values and those calculated from harmonic measurements.

	Design 1 (design value)	Design 1 (from harmonic measurements)	Design 2 (design value)	Design 2 (from harmonic measurements)
Resonance Frequency (Hz)	211	174.8	356	294.8
Mass (μg)	342	--	265	--
Spring Constant (N/m)	0.601	0.412	1.324	0.907
Spring Width (μm)	12	10.6	12	10.6
Quality Factor Q	--	4.9	--	11.2
Damping Ratio ζ	--	0.102	--	0.045

variations in the patterning and etching process will have minimal effect on the overall mass. The springs, however, are designed to be just 12 µm wide, and small variations in the width can cause large changes in the stiffness and correspondingly large changes in the resonance frequencies. With this in mind, the width of the spring was varied until the calculated first natural frequency matched the measured first resonance frequency for each design. The effective spring width calculated in this manner (using the average first resonance frequencies reported above) was 10.6 µm for both cases.

The frequency-response function (FRF) for each design was also obtained from the harmonic test data. The FRF is a way to decouple the uneven response of the vibration table from that of the device. The frequency-response function is determined using

$$\mathrm{FRF(dB)} = 20\log_{10}\left(\frac{\mathrm{output}}{\mathrm{input}}\right) \tag{3.3}$$

where, in this case, the output is the measured device response magnitude and the input is the measured vibration table response measurement. The resulting FRF for both designs is shown in Figure 3.25. There is quite a bit of noise introduced in the FRF plots because of the low signal-to-noise ratio in the reference measurement of the vibration table.

a)

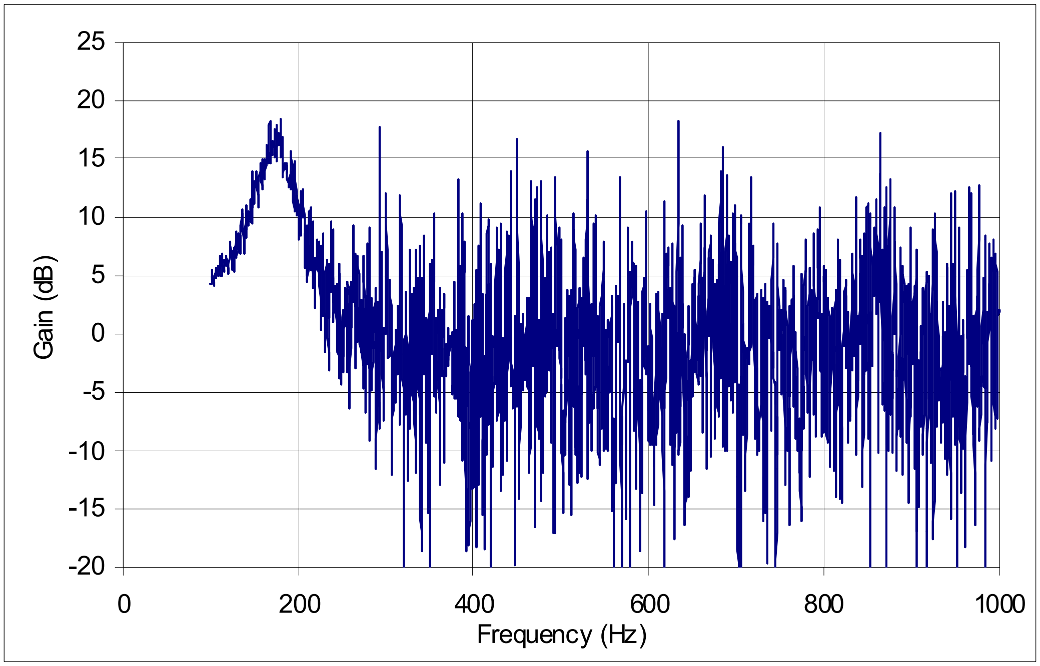

b)

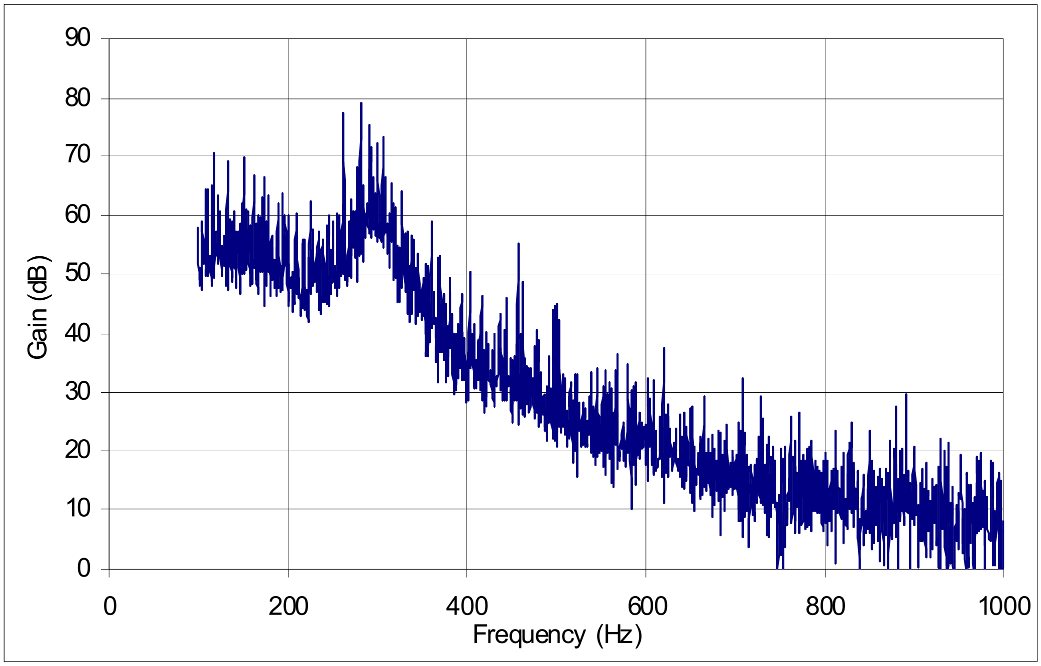

Figure 3.25. Frequency-response function: a) Design 1 and b) Design 2.

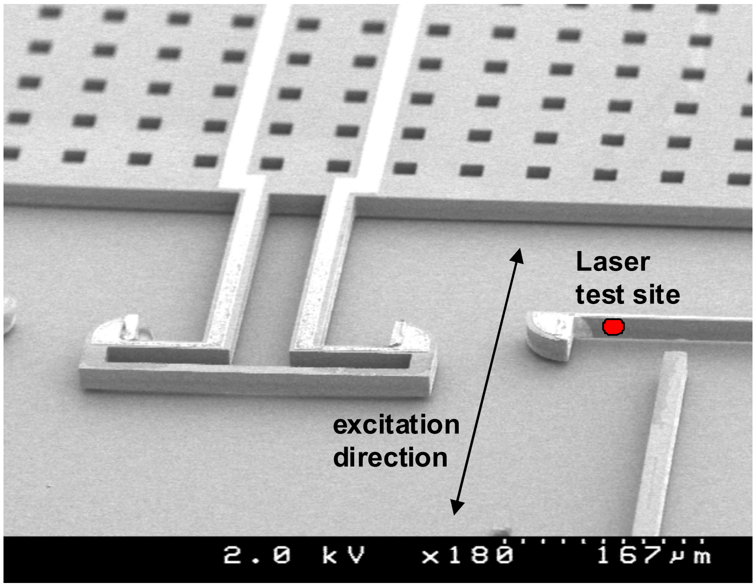

Figure 3.26. Laser query site for harmonic excitation of latch.

The harmonic responses of the latches were also characterized to verify the stiffness coefficients used in the model. The test site for the latch characterization is shown in Figure 3.26. The velocity plot of the latch response is shown in Figure 3.27. All of the resonance peaks except the largest peak (just below 19kHz) are due to the response of the vibration table, as seen in the vibration table response shown in Figure 3.28. The frequency-response function derived by comparing the latch response to the table response as described above is shown in Figure 3.29. The design parameters for the latch and the parameters extracted from the harmonic measurements are summarized in Table 3.3. Note that the effective width of the latch calculated from the harmonic measurements is only 5.5 μm, as compared to the designed latch width of 8 μm.

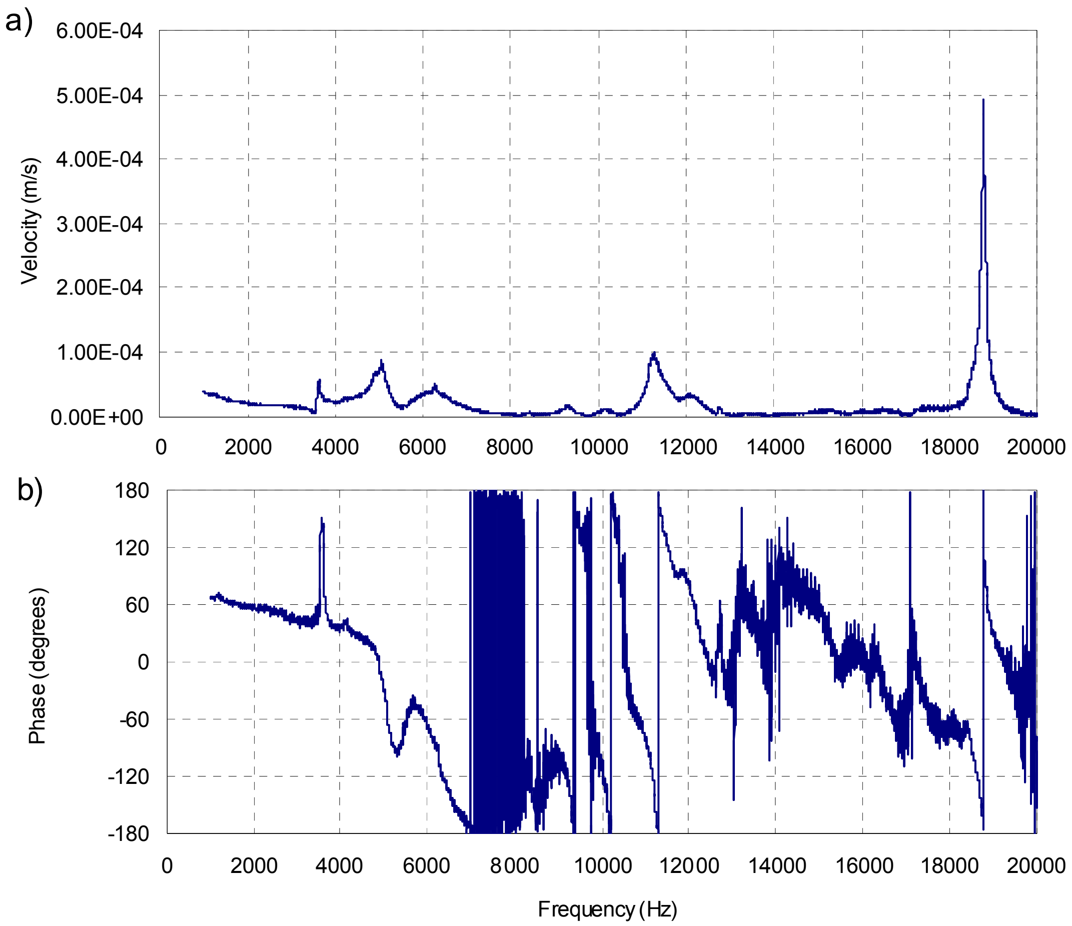

Figure 3.27. Velocity response of the latch as a function of frequency: a) magnitude and b) phase.

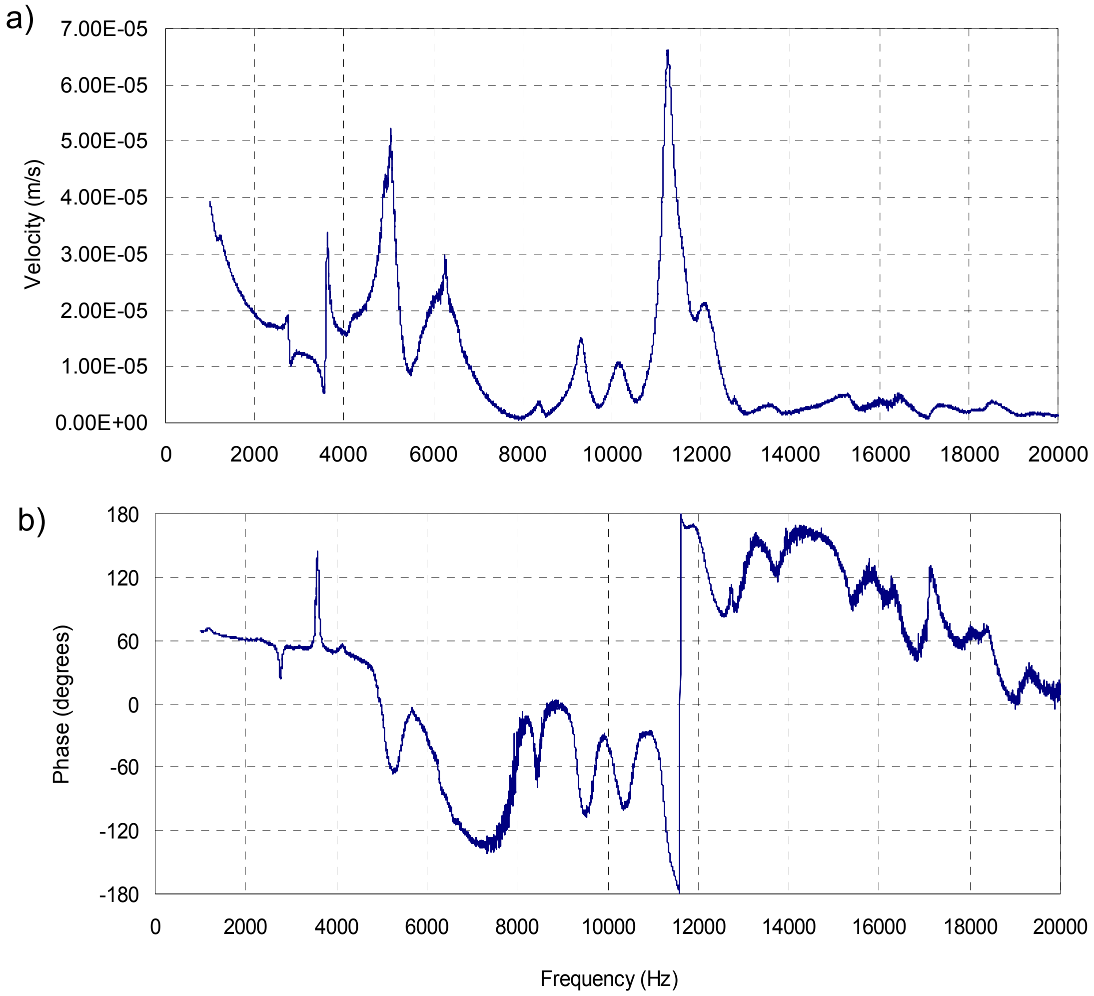

Figure 3.28. Velocity response of vibration table over frequency range used to test latch: a) magnitude and b) phase.

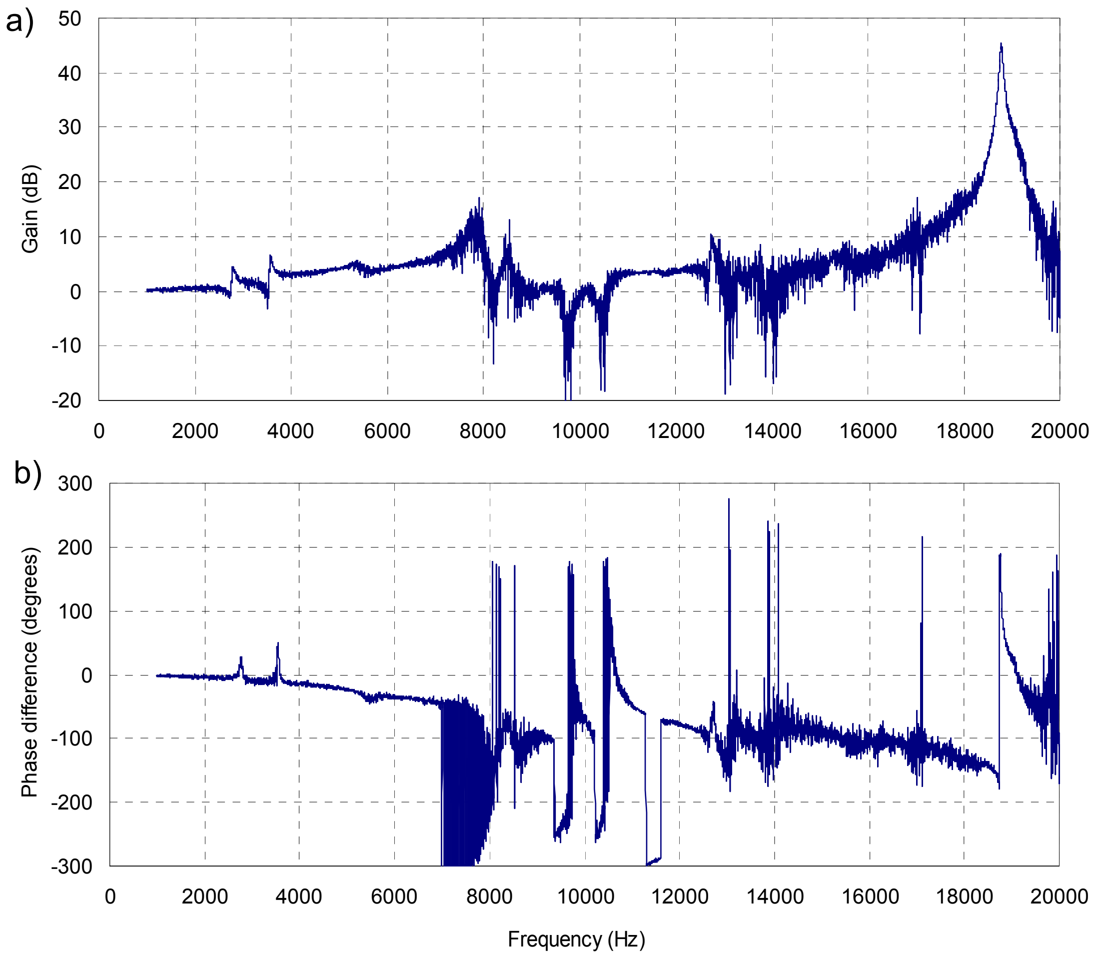

Figure 3.29. Frequency-response function of the latch: a) magnitude and b) phase.

Table 3.3. Comparison of latch design values and those calculated from harmonic measurements.

	Design value	Calculated from harmonic measurements
Resonance Frequency (kHz)	30.97	18.79
Effective Mass (μg)	0.117	0.104
Spring Constant (N/m)	4.44	1.44
Latch Width (μm)	8	5.5
Latch Length (μm)	460	460
Latch thickness (μm)	20	20
Quality Factor Q	--	332
Damping Ratio ζ	--	0.0015

3.2 Thermal Actuator Testing

3.2.1 V-Beam Actuator

In the friction studies detailed later in this dissertation, thermal actuators are used to apply the normal and transverse forces. In order to gauge the magnitudes of these forces, the actuator stiffness is required. If the actuator stiffness is constant over the deflection range, it allows extrapolation of the force exerted by the actuator with a resisting load from the measured free deflection of the actuator via the actuator loadline, or force-deflection response. The actuator stiffness is the slope of the loadline. In order to construct the actuator loadline, V-beam test structures based on the friction test structures were constructed on the same wafer. The test devices (Figure 3.30) consist of an array of V-beams connected to a resisting spring. Devices with the same size and number of drive beams with various stiffness resisting springs were used to measure multiple points on the actuator loadline. The deflection of the spring with a given drive current was measured by using an integrated vernier scale on the yoke connecting the actuator to the spring. The inherent assumption is that the

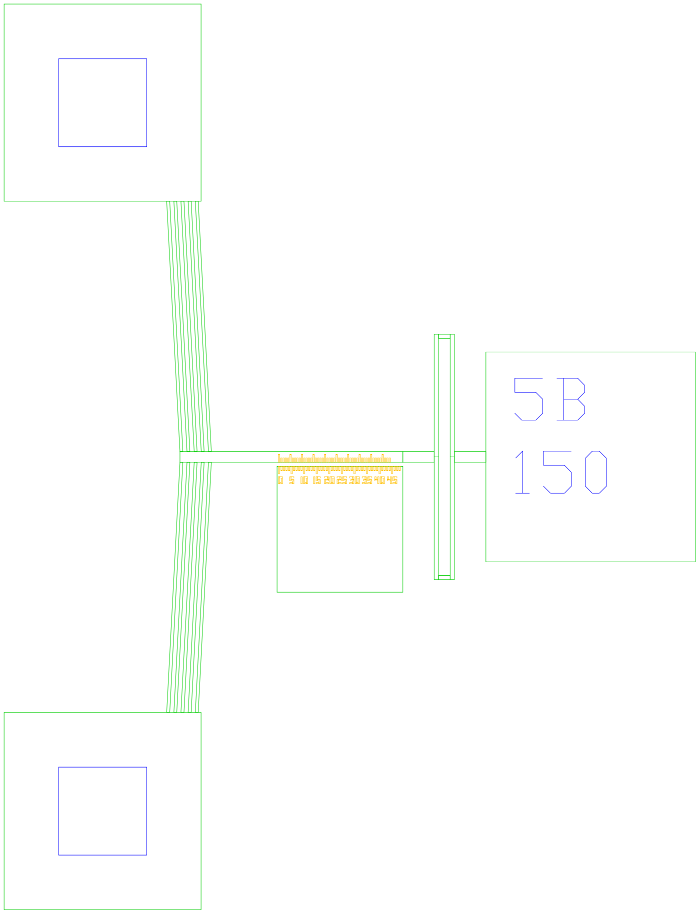

Figure 3.30. V-beam force-deflection test structure.

compression in the yoke is negligible. The exerted force was calculated by using the designed spring constant of the resisting spring.

V-beam test structures with an initial tilt angle of two to four degrees and one to five parallel beams were fabricated and tested. The resisting springs coupled to the actuators had designed spring constants of 0 (no spring), 50, 100, 150, 300, 450, and 600 N/m. A single actuator loadline is constructed by plotting measurements at a single applied current with all of the different spring constants on the same graph. The response of a single-beam actuator for each of the different angles is shown in

Figure 3.31. The response of the three degree, single actuator beam with each of the different resisting springs is shown in Figure 3.32.

A representative actuator loadline for a single, 3-degree V-beam device is shown in Figure 3.33. A linear least-squares fit has been plotted along with the data,

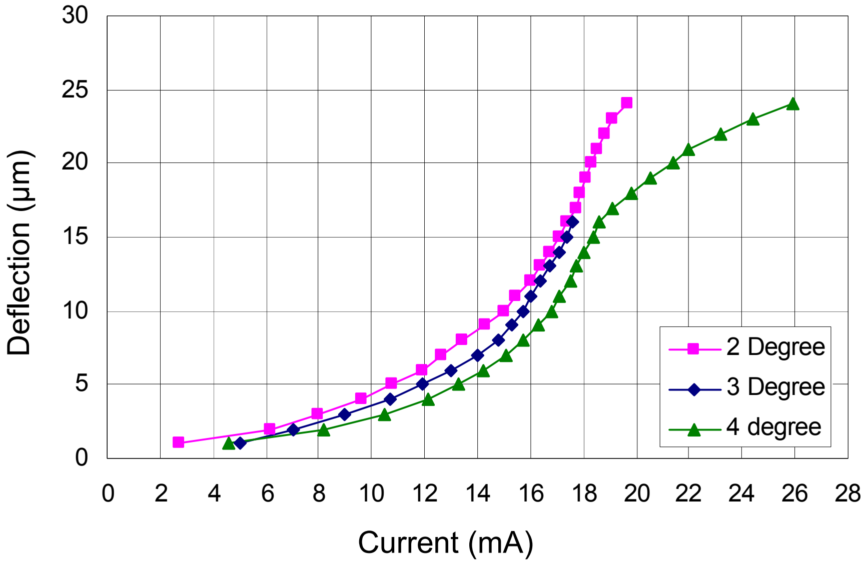

Figure 3.31. Single V-beam actuator response with no resisting spring, with different initial design angles.

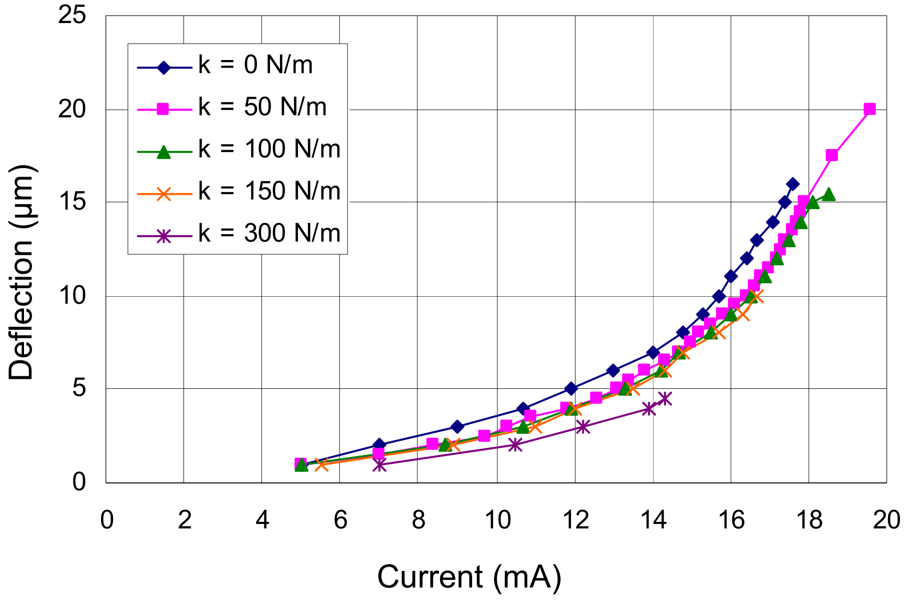

Figure 3.32. Response of a single 3 degree V-beam actuator beam with different resisting springs.

and the equation for the fit is shown on the plot as well. The slope of the fit line is the negative of the stiffness of the actuator, and the y-intercept is the predicted blocked force (the force corresponding to zero displacement). The actuator stiffness values calculated from the loadlines are summarized in Table 3.4.

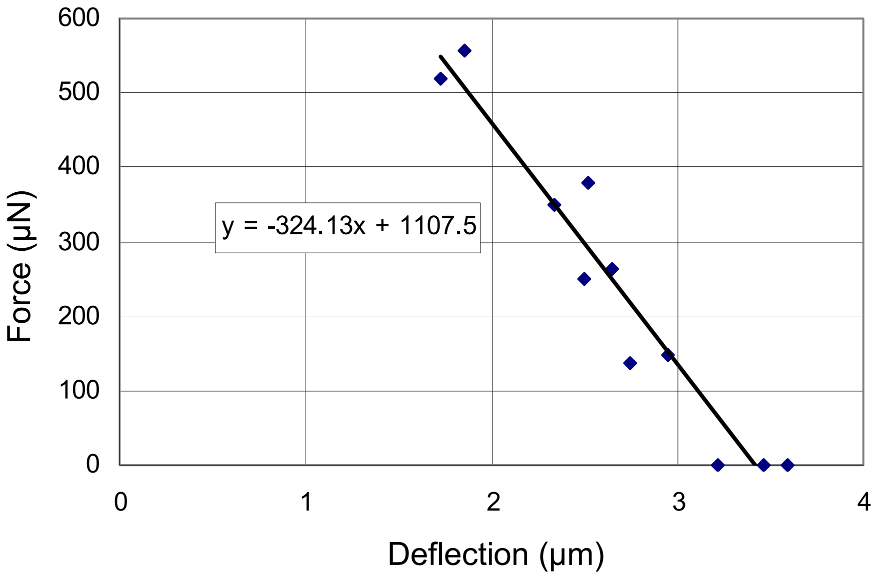

Figure 3.33. Actuator loadline for single beam, 3-degree V-beam device, using a driving current of 1mA.

Table 3.4. V-beam actuator stiffness values calculated from force testing data.

Angle (Degrees)	Beams	Total Actuator Stiffness (N/m)	Stiffness/Beam (N/m)
2	1	138.9	138.9
2	2	388.0	194.0
2	3	648.5	216.2
2	4	1014.9	253.7
3	1	324.1	324.1
3	2	736.1	368.0
3	3	1046	348.7
3	4	1355.4	338.9
4	1	211.5	211.5
4	2	313.6	156.8
4	3	319.5	106.5
4	4	790.3	197.6

The stiffness per beam is expected to be constant for each designed tilt angle, but the calculated values do not reflect this. In addition, the stiffness per beam is also expected to increase with increasing tilt angle, and the calculations also do not reflect this expectation, as the four degree devices demonstrated a lower stiffness than the three degree devices. This is likely due to variations in the fabricated dimensions across the wafer. The resisting springs were either 10 µm (for the nominal 0-300 N/m spring constants) or 15 µm wide (for the 450-600 N/m spring constants). Each individual spring constant in these two ranges was designed by modifying the spring length. Variations of as little as 2 µm in the as-fabricated spring widths can cause a 50% change in the effective stiffness of the resisting spring. This would be enough to account for the observed discrepancies in the experimental data. For future iterations of this type of device, wider and longer springs would be less sensitive to small variations in the fabricated dimensions.

Since the trends from the measurements do not make sense, the author elected to use stiffness values derived from analytical and finite element models instead when calculating the forces exerted by actuators for the purpose of friction measurements.

3.2.2 Rotational Thermal Actuator Testing

Since thermal actuators are current-driven rather than voltage-driven devices, the rotational actuator free deflection was measured as a function of applied current (Figure 3.34 and Figure 3.35). The deflection was measured by using the angular vernier scale, which has gradations of 0.15 degrees. The error in the measurement is therefore estimated as +/- 0.075 degrees. Most of the tested devices had a small initial deflection before the current was applied, in the range of 0 to 0.15 degrees. This bias

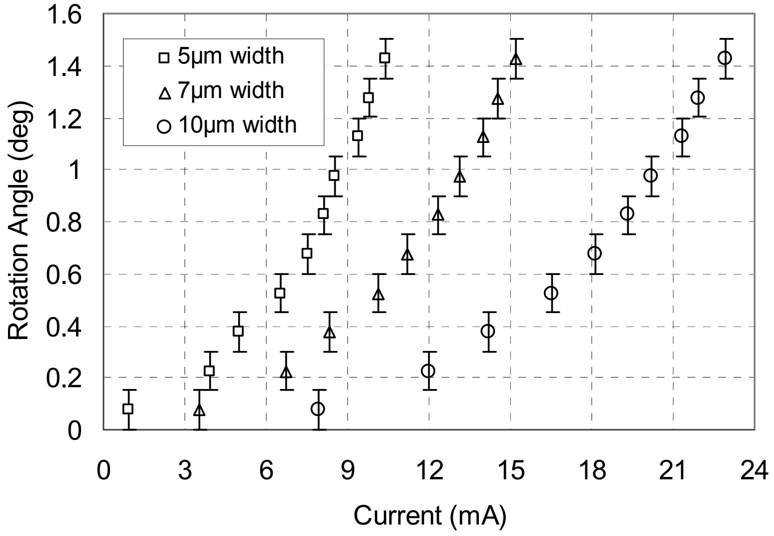

Figure 3.34. Experimental free deflection data for actuators for *L* = 400 μm and different actuator beam widths. Wider beams result in less free deflection, but should be capable of providing higher forces.

deflection was subtracted from the measurements before comparisons with the corresponding model predictions. The cause of the initial deflection is not yet known, but this could possibly be due to the compressively stressed buried thermal oxide film pushing in on the device anchors. This explanation is consistent with the fact that the initial deflection is always in the same direction as the deflection induced by thermal expansion.

The moment/angular deflection characteristics of the actuators were also examined by using a series of test structures that included resisting cantilever springs with various designed spring constants. The angular deflection was measured as a function of current for each actuator/spring combination by using an angular vernier scale patterned on the wafer adjacent to the device. The actuator moment about point *P* was calculated by using the cantilever spring constant and the measured deflection.

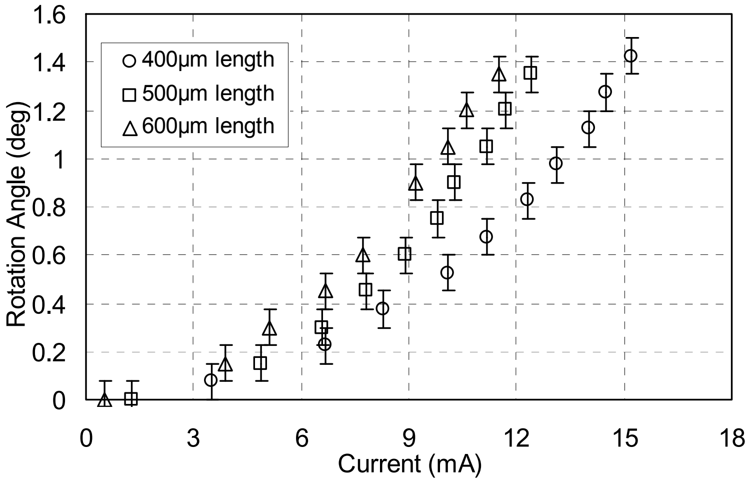

Figure 3.35. Experimental free deflection data for actuators for *w* = 7 µm and different actuator beam lengths. Longer actuators generally provide higher free deflection but generate less force.

For a single actuator design, measurements at the same applied current can be combined to get a moment-rotation angle relationship. Figure 3.36 shows three such relationships, for actuators with $L = 400$ µm and various widths. The applied current levels were chosen such that the free deflection of each of the three actuators was the same. Linear trendlines for each actuator design are plotted along with the data, and the equations describing them are also displayed on the graph. The slope of the linear trendline for each actuator beam width w is the torsion spring constant of the actuator, and the y-intercept corresponds to the actuator blocked moment. It can be seen that the actuator stiffness and blocked moment both increase with increasing beam width.

Many applications for MEMS actuators use translational motion rather than rotation as the input. The central yoke allows for near-translational motion at the actuator output for small angular deflections. The translational deflection output is proportional to the yoke length r_2, which for the considered actuators is kept constant at 485 µm. As the yoke length is increased, the free deflection at a given current will

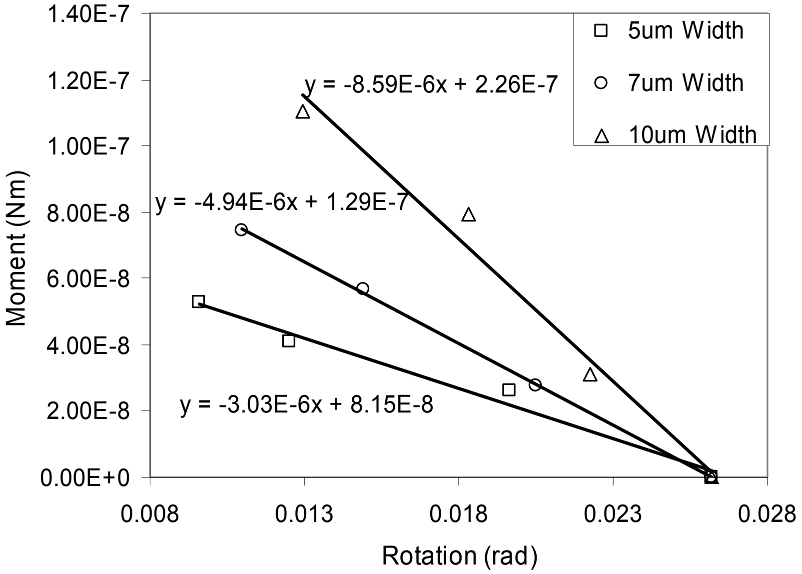

Figure 3.36. Moment-rotation angle relationships for 400 μm long rotational actuators of varying width.

increase linearly; however, the maximum output force will also decrease linearly because the available actuator moment about *P* remains the same. Stated another way, the area under the force deflection plot (which represents the feasible operation region of the actuator) remains constant, but the slope of the line can be changed simply by changing the yoke length.

With the above caveat about yoke length, some design criteria for translational output and comparisons with existing purely translational actuators is desirable. A translation force-deflection plot is given for the rotational actuators in Figure 3.37. The translational measurements were conducted with the same test structures as those used for the torsion measurements. The force is obtained by the measured deflection of the resisting cantilever spring combined with the calculated cantilever spring constant.

In Figure 3.37, a series of force-deflection profiles are shown for rotational actuators of constant length L = 400 µm and varying widths. The deflection values shown are the displacement measurements at the actuator output projected onto the x-axis. The slope of each linear trendline represents an approximate measure of the actuator linear stiffness. The actuator stiffness is observed to increase with the actuator width (the theoretical relationship is calculated in Section 4.8). The y-intercept of the trendline is an approximate measure of the actuator blocked force (zero displacement force). It can be seen from the plot that when a wider actuator beam is used, higher forces are possible for the same displacement (yielding larger actuator work). The tradeoff is increased actuator current – the voltage (and current density) remains nearly constant for a given displacement as the beam is widened.

The free deflection of a rotational actuator is also compared with the commonly-used bent-beam and hot-arm/cold-arm style thermal actuators of similar

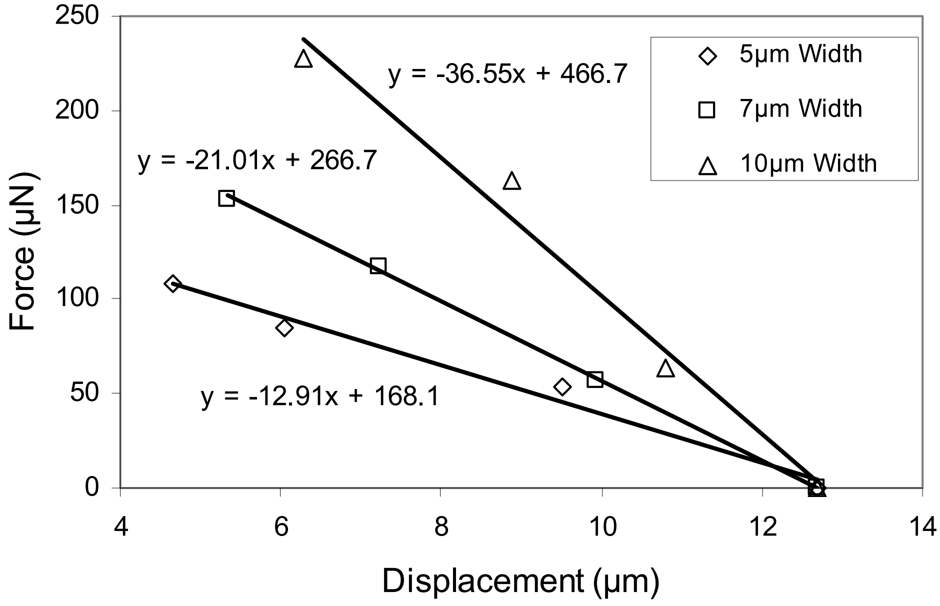

Figure 3.37. Force-deflection relationships for 400 µm long rotational actuators and different widths.

dimensions in Figure 3.38. For all of the actuators represented in this graph, 5 µm wide hot beams are used, and they are all fabricated on SOI wafers with identical 1-3 mΩ-cm resistivity device layers measuring 20 µm in thickness. The hot-arm/cold-arm actuator is 1050 µm long, the bent-beam actuator is 1200 µm long, and the rotational actuator has a 1000 µm span (L = 500 µm in Figure 2.4) with an amplification beam of r_2 = 485 µm. The rotational actuator consumes slightly more power than the hot-arm/cold-arm actuator but only about 36% as much as the bent-beam actuator for the same free deflection.

The rotational actuator provides far more force than the hot-arm/cold-arm type of actuator. While force data are not available for this hot-arm/cold-arm actuator because there were no force test structures included, this type of actuator typically is limited to a few µN of force before the actuator burns out or buckles [44-46]. The maximum measured force output from the bent-beam actuator design is 1.2mN at

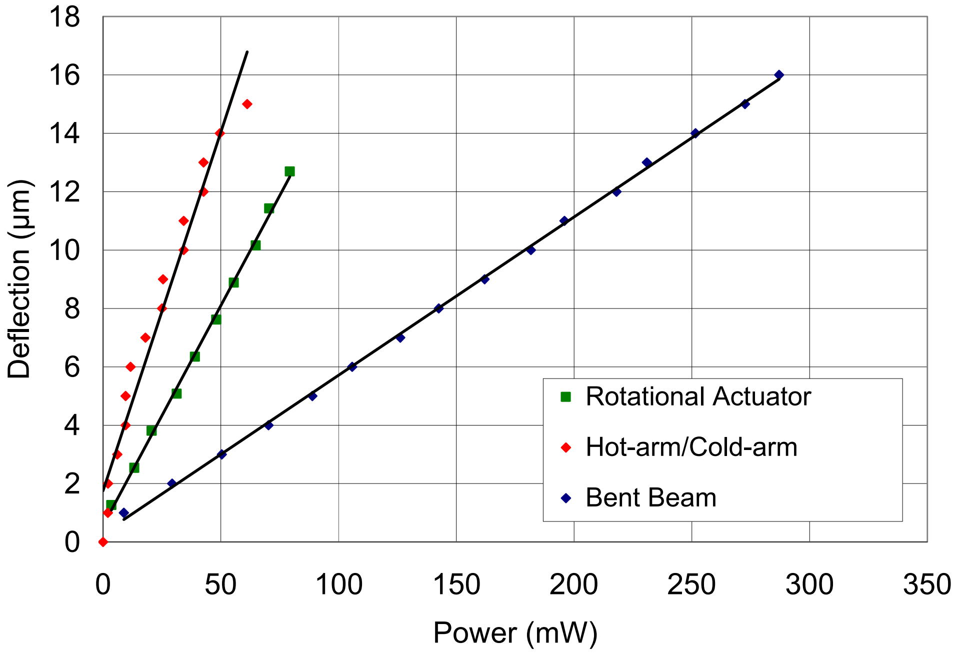

Figure 3.38. Comparison of free deflection for V-beam, U-beam, and rotational thermal actuators.

24.7 mA/18.8 V drive, pushing against a spring with a stiffness of 50 N/m. As the current is increased from this point, the actuator beams start to buckle. The maximum force measured with the rotational actuator is 0.23 mN at 15 mA/12V, pushing against a spring with a stiffness of 69.5 N/m. Therefore, the rotational actuator is a good choice for applications that require large displacements and require more force than what a hot-arm/cold-arm actuator can provide, but not all of the force available with a bent-beam actuator.

It has been shown in both simulations and testing for other types of thermal actuators that the dominant heat loss mechanism is conduction through the air to the substrate [45], followed by heat loss into the anchors. Containing these heat losses can greatly increase the actuator efficiency by increasing the equilibrium beam temperature for the same applied current. The heat loss through the air into the substrate is easily eliminated by operating the actuators under vacuum.

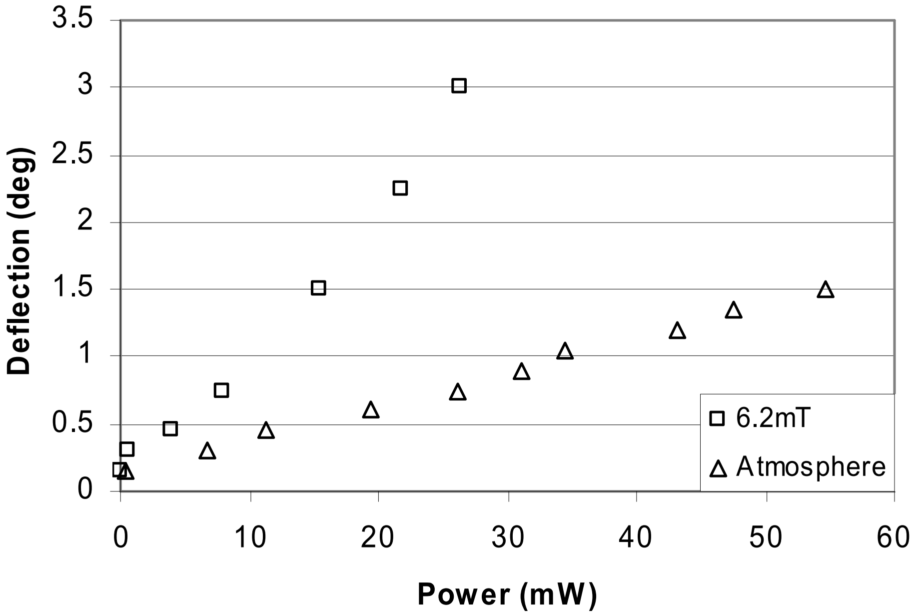

Figure 3.39. Comparison of actuator free deflection under vacuum and atmospheric conditions.

An actuator was tested both in vacuum and atmospheric (ambient) conditions. The pressure during vacuum testing varied between 5.9 mT and 6.5 mT. The results are plotted in Figure 3.39. For the same free deflection, the actuator required 50% less current and 40% less voltage, consuming 70% less overall power.

The frequency of operation for thermal actuators is generally limited by the thermal time constant of the system [41, 43, 53]. The rotational offset beam actuator is limited in the same way. The thermal time constant of the actuator depends primarily on the beam width, length, and thickness. Smaller devices have a lower thermal mass and are expected to have a larger cutoff frequency. Frequency response measurements were performed using a laser Doppler vibrometer while driving the device with a square wave input signal. The normalized frequency response in air is shown in Figure 3.40. The measurements shown correspond to actuators with L =

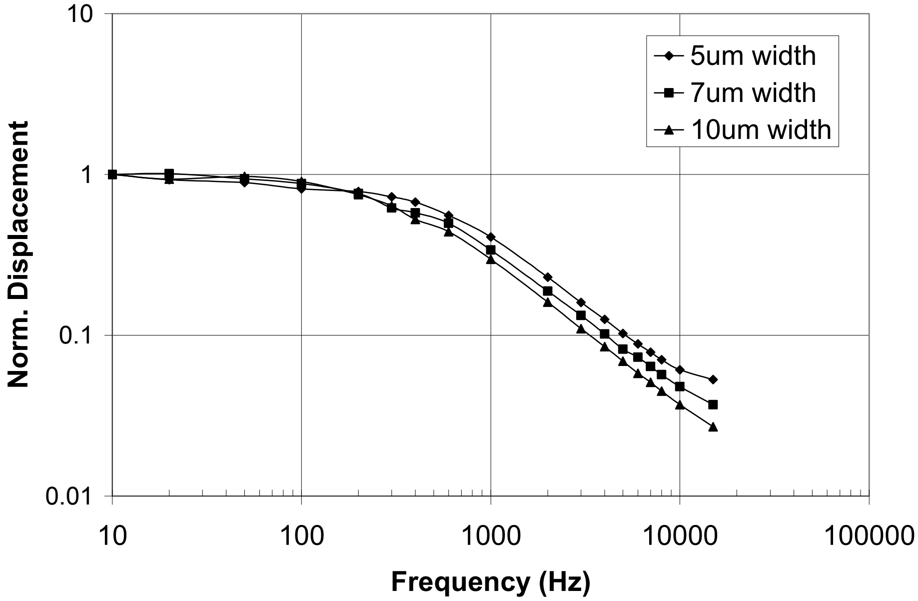

Figure 3.40. Frequency response of offset beam actuators in air for $L = 400\ \mu m$, various widths.

400 µm. The cutoff frequencies extrapolated from this data are about 350, 285, and 270 Hz for the 5 µm wide, 7 µm wide, and 10 µm wide actuators, respectively.

3.3 Friction Testing

The friction coefficient of the silicon sidewalls must be determined for the shock sensor model. A novel friction test structure has been designed for this work to perform these measurements (reported in [51]). This friction test structure makes use of V-beam thermal actuators to separately apply normal and transverse forces to test blocks of various sizes (see Figure 3.41 and Figure 3.42). A stationary fixed block provides the other surface for contact. Both contacting surfaces are deep reactive ion etched silicon, the same as the sidewalls of the contacting pieces of the shock sensor system.

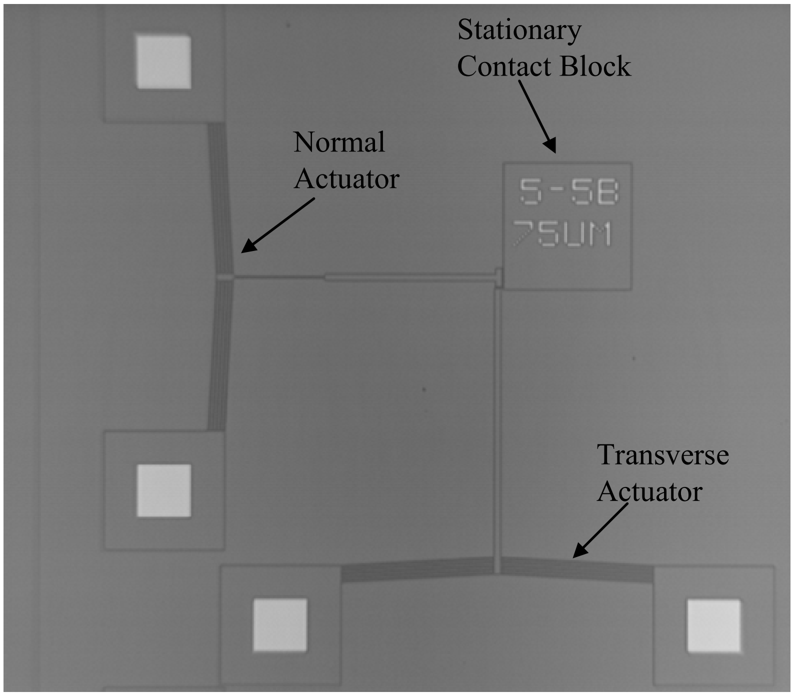

Figure 3.41. Friction test structure design.

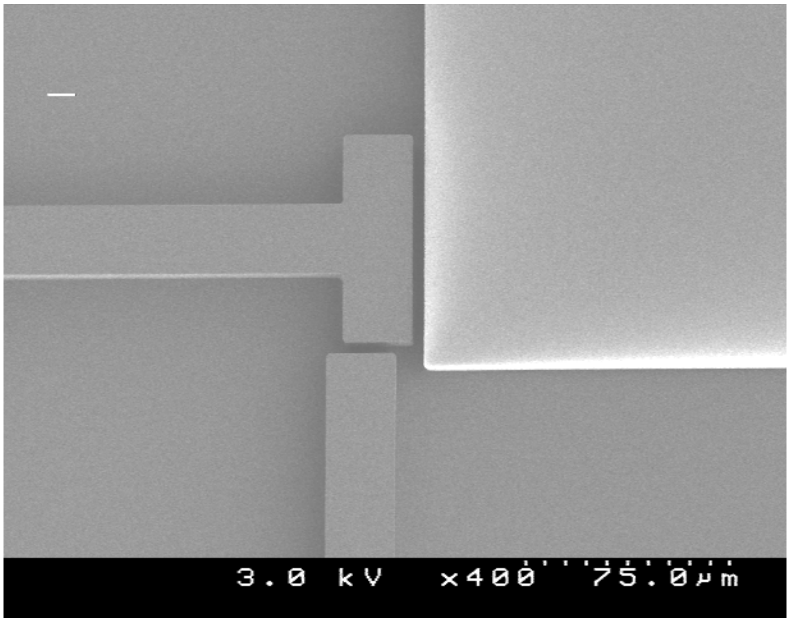

Figure 3.42. Friction test structure contact pad closeup.

The test procedure used is to apply a fixed current to the normal actuator, pushing the test block against the stationary block. The transverse actuator current is then increased until the test block is observed to slip under a microscope. The actuator stiffness and the free deflection measured from an actuator test structure are used to calculate the forces applied by each actuator, by assuming a linear force-displacement profile for an individual actuator:

$$F = k_{act}(\delta_{free} - x) \tag{3.4}$$

where x is the measured displacement of the actuator during the friction test, k_{act} is the actuator stiffness and δ_{free} is the free displacement at the given current level.

In the pictured device, each actuator has five parallel bent beams for the total force generation. The number of beams can be changed to generate a wide range of forces. The beams used in this study have been constructed by using two 600µm long segments, with a 3 degree rotation and a 25µm wide yoke in the middle. The normal

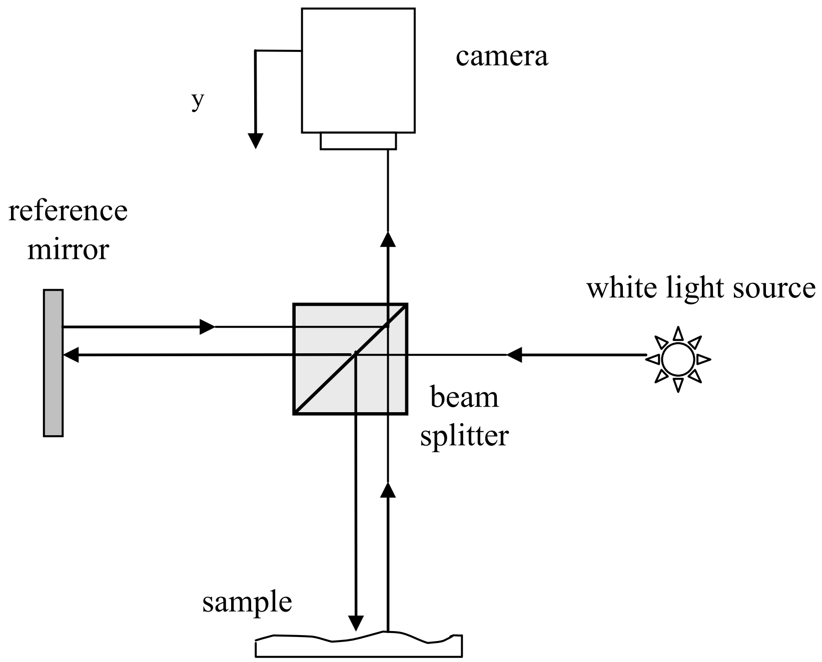

Figure 3.43. White-light optical profilometer operational principle. Camera is scanned to find position of constructive interference (where sample distance equals reference distance) for each pixel.

actuator yoke has been narrowed just beyond the actuator to be 5μm wide to provide low spring resistance for the friction measurement and additional thermal isolation between the actuator and the contact pad.

The displacement *x* for these friction test structures is fixed at 3μm in all cases for both the normal and transverse actuators. The free deflections are measured as a function of applied current on freestanding actuators fabricated on the same wafer as the friction test devices. Deflection measurements have been obtained by using a white-light optical profilometer with a lateral resolution of 162nm (see Figure 3.43). This free-deflection data was used in conjunction with the FEA derived actuator stiffness to determine the force exerted by each actuator for a particular current level.

The forces obtained depend primarily on the applied current and the number of parallel bent beams. In Figure 3.44, the force versus current profile results are

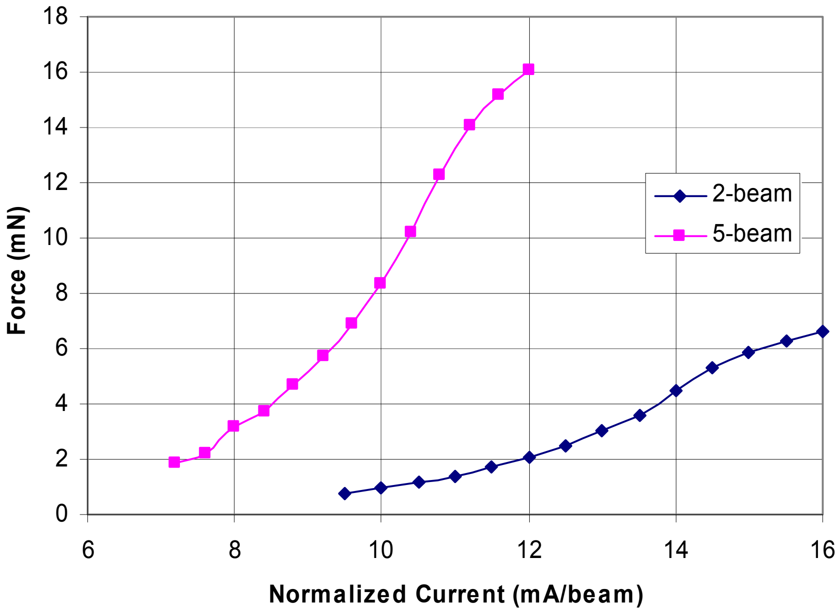

Figure 3.44. Force developed by actuators at 3 μm travel.

plotted for 2-beam and 5-beam actuator configurations. The forces developed by the thermal actuators are relatively high compared to many MEMS structures, and these forces easily extend into the mN range.

The two constraints on the high end of the applied force are overheating that can melt the actuator and buckling of the individual actuator beams or the narrowed portion of the normal actuator. For the configurations used here, the narrowed portion of the normal actuator buckled at approximately 2.55 mN, which is a bit lower than the theoretical critical buckling load of 2.84 mN. Applying a larger force than this requires stiffening of the thin portion of the normal beam, and this can be easily accomplished if desired. The maximum current applied in Figure 3.44 was limited by overheating.

It is expected that the force in Figure 3.44 should scale linearly with the number of beams in the actuator because the stiffness scales linearly, but this is clearly not the case. In practice, the displacement of a 5-beam actuator is much larger than a 2-beam actuator with the same normalized current applied. The explanation for this is the added efficiency realized when more heated beams are placed alongside the original beams – the heat losses per beam to the surrounding air decrease, so the same applied current per beam results in a larger temperature increase. This in turn leads to a larger free displacement at the same normalized current, and the larger free displacement results in a higher generated force.

Friction test structures using 5-beam normal actuators and 2-beam transverse actuators have been studied to determine the friction coefficient of the DRIE silicon sidewalls. A steady current was applied to the normal actuator, and the current input to the transverse actuator was slowly ramped up while monitoring the contact pad under the microscope until slip was observed. The test was initially performed using a current in the normal actuator just above the level required to achieve contact; this was done to keep the normal force magnitude low. The required current in the transverse actuator to achieve slip is documented, then the current input into the normal actuator is increased and the test is repeated.

Two wafers with friction test structures were fabricated with very different DRIE recipes; one of them provides fairly rough sidewalls (RMS roughness of ~275 nm as measured using white light optical profilometry) and the other provides very smooth sidewalls (RMS roughness of ~60 nm). For the wafer with smooth sidewalls, the friction coefficient measurements ranged from 0.67 to 0.76, which agrees well with the value of ~0.7 obtained in macroscale friction measurements on silicon [28].

Early tests on the rough sidewall wafer, however, appeared to indicate that the coefficient of friction was *decreasing* as the normal load was increased, to the point that a smaller transverse actuator current was needed to achieve slip after the normal actuator current was increased to a higher level than before. To sort this result out, repetitive tests were performed with a previously uncycled test structure without increasing the normal actuator current between each test. The results showed that the coefficient of friction has a high initial value, before it drops with each subsequent cycle and plateaus out to a steady-state value (see Figure 3.45). The friction measurements were repeated after a period of 90 minutes, and again several weeks later on the same device with no change from the final steady-state value. It is supposed that as the surfaces rub against one another, some asperities are broken off and the surface roughness decreases each time until nearly all asperities above a

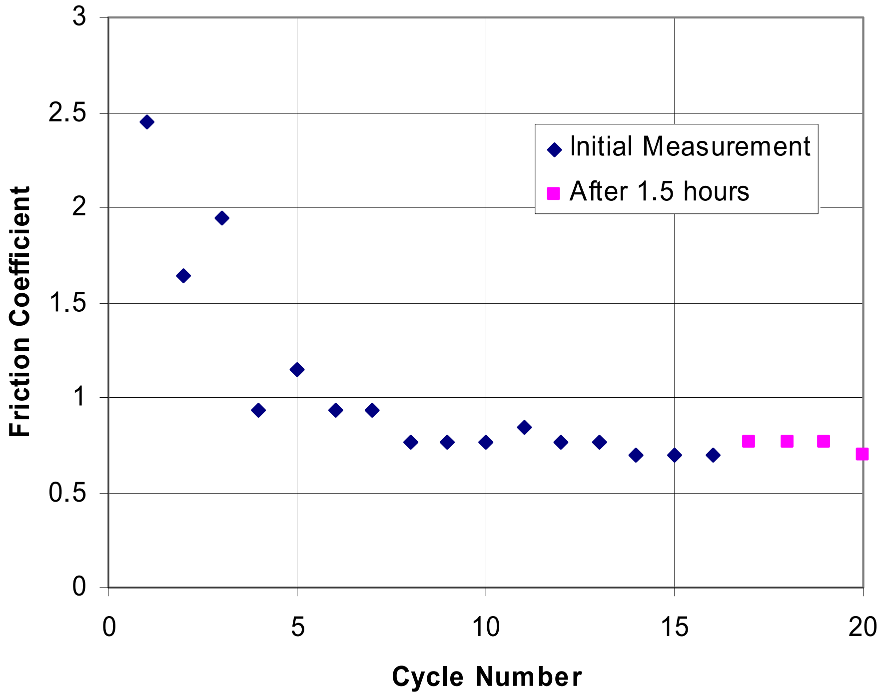

Figure 3.45. Plot of friction coefficient versus cycle number showing decrease over the first several cycles before settling to final value.

critical size are gone. After this point the roughness stays relatively constant, and the friction coefficient does not change. The initial friction coefficient seen in these particular devices is several times larger than the final steady-state value (2.45 as compared to 0.70). This suggests that rough contact surfaces should be conditioned before use by putting the sliding surfaces through several cycles (for these devices, 15 cycles was found to be enough). This ensures that the coefficient of friction will remain constant through the device's lifetime.

The contact surfaces on the rough wafer were examined after the experiments to see evidence of wear. There is a clear delineation between the area of the sidewall subjected to the sliding contact and the adjacent area not contacted (see Figure 3.46). Smoothing of the horizontal striations from the deep reactive ion etch is clearly visible in the left half of the image, which is in the contact region. The right half of the image shows the as-etched surface with the intact sharp striations, since this area

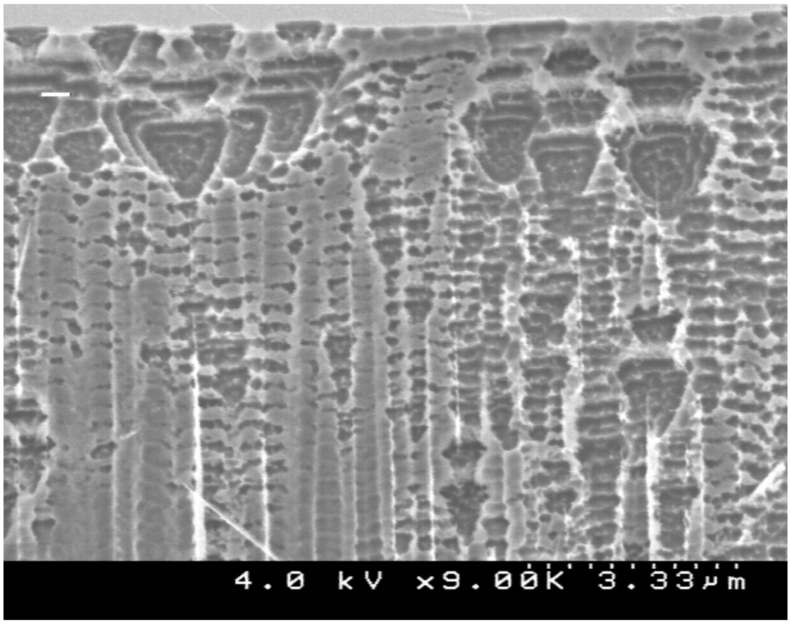

Figure 3.46. Scanning electron microscope image of plastic deformation along area of sliding contact. Right half of image does not contact friction pad, while the left half does.

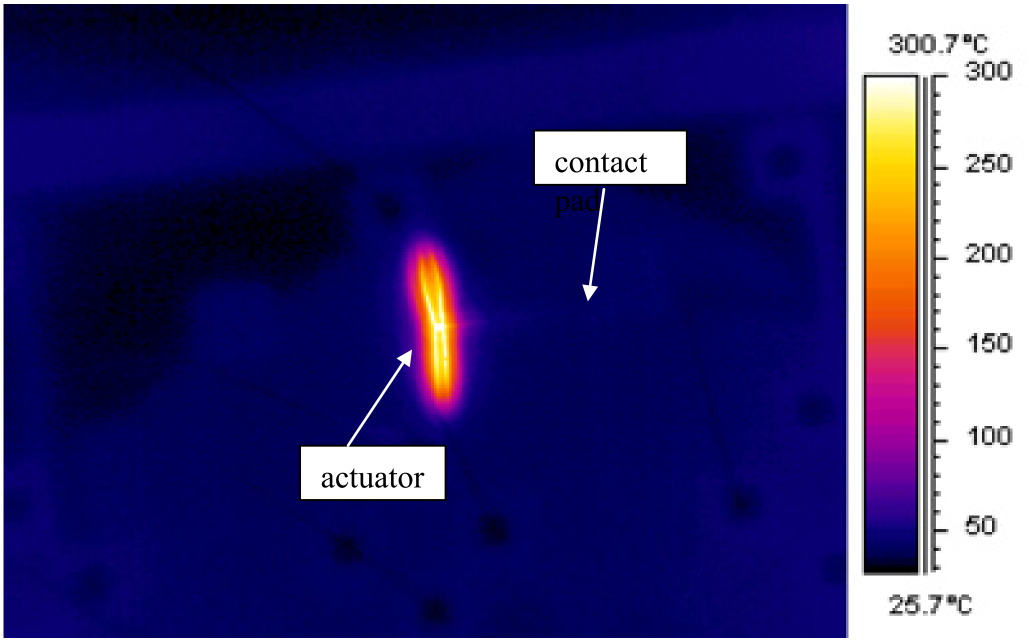

Figure 3.47. Forward-looking infrared (FLIR) measurement of temperature profile of friction device. The active area corresponding to the actuator is hot, while the contact pad is at the ambient temperature.

was not in the contact region.

To determine if heating of the contact surface occurs due to the thermal actuation technique, forward-looking infrared (FLIR) measurements were taken of the devices while the normal actuator was turned on and pressed against the contact surface. The measurements showed the contact area to be at room temperature even when the active region of the device is glowing red-hot (shown in Figure 3.47); this means that the friction measurements can be applied to room temperature contacts. Extension of the technique to allow for heated contact is possible, either by separate active heating of the contact pad or by altering the design to allow passive heating from the normal actuator. Active heating of the contact pad would be preferable, since the contact temperature could then be controlled independently from the applied force.

3.4 Summary and Contributions

The experimental techniques used to study the shock sensor and the reset actuators have been presented in this chapter. These techniques are intended to provide a framework for experimental study of this class of device, from identification of the lumped mass and spring constants, to measurement of the acceleration required to latch the device, to capturing and interpreting images of the actual latching event. A thorough experimental study of these latching shock sensors has never been reported before, and it is the author's hope that the experiments described in this chapter will aid other research efforts on this type of device, and that other researchers will build on and improve the techniques reported here. In particular, further measurements of the relative position of the mass and latch during the latching process, including other design configurations and better temporal and spatial resolution, would significantly enhance the understanding of the dynamic behavior of latching acceleration switches.

The experimental data collected have also been presented and analyzed in this chapter. Some key observations regarding latching acceleration threshold switches that are not described in previous literature include: the change in the friction coefficient over the first several cycles; the timing of the latching event ; that is, the time from the onset of the acceleration pulse to contact, to latching, and finally, to the sensor settling and closing the electrical circuit; the apparent onset of stiction due to electrostatic charge buildup in the sensor over tens to hundreds of cycles; and the surprising stability of the contact resistance over many cycles despite gross degradation in the metallization.

4. Modeling and Numerical Results

In this chapter, all of the modeling and numerical studies performed are discussed. These studies include the derivation of two distinct reduced-order models for the shock sensor operation, comparisons between the predictions of the two models, and various parametric and optimization studies intended to lend insights into the design of this class of sensor. In addition, a model is developed to calculate the force applied by a V-beam actuator (used for the friction characterization studies). A new thermal actuator model is also developed and applied to the rotational offset-beam actuator design. This new model takes into account the temperature-dependence of the thermal expansion coefficient of silicon, neglected in previous models of thermal actuators. Finally several parametric studies of the rotational actuator design are presented to gain insights into the design of these devices. Portions of this chapter have been adapted from the author's journal articles on the latching shock sensor [38, 48] and the rotational actuator [39].

4.1 Latching Progression

The latching shock sensor goes through several distinct phases during an acceleration event. These are illustrated in Figure 4.1 for the sensor under consideration here. In the first phase, the acceleration has begun and the sensor is responding, but has not yet come into contact with the latch. In the second phase, the sensor makes contact with the latch and there are some interaction forces and some resulting motion of the latch. In the third phase, the sensor has continued past the latch, possibly overshooting so that contact is again broken and there are no interaction forces. In the fourth and final stage, the sensor comes to rest against the

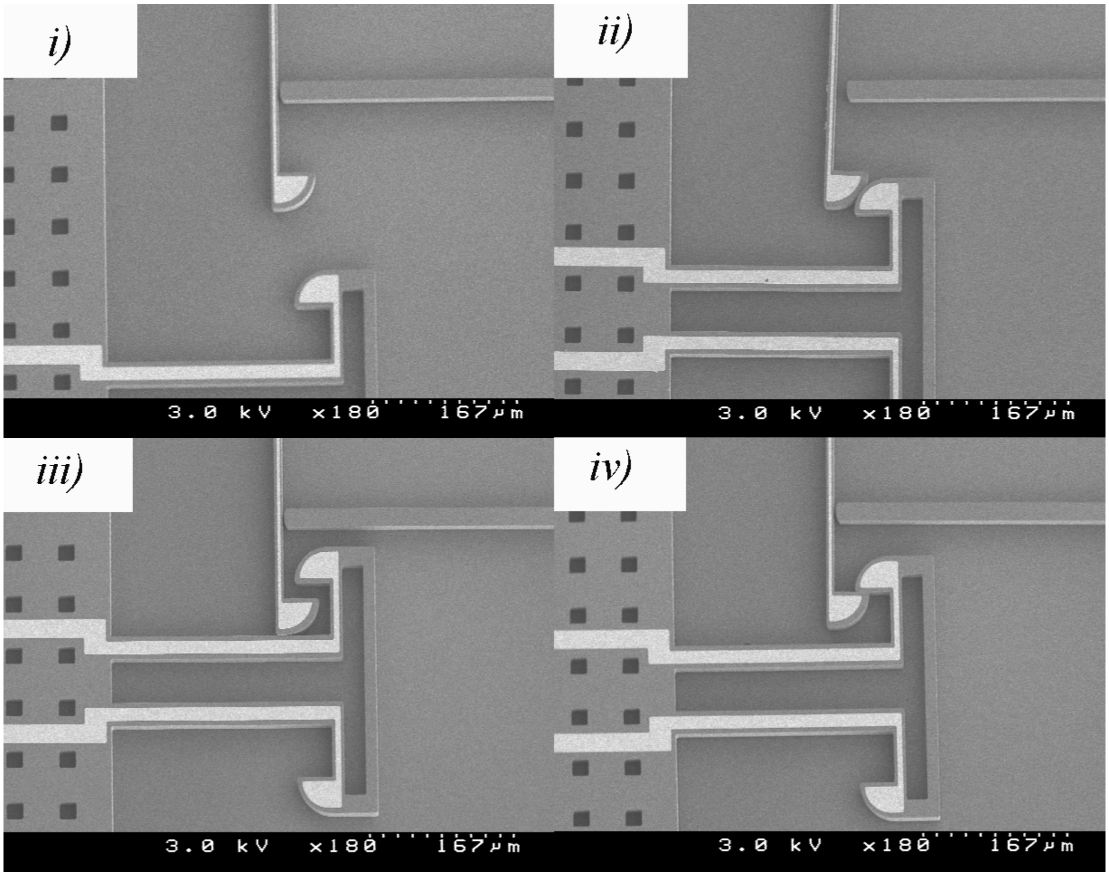

Figure 4.1. Shock sensor phases of latching: i) pre-contact, ii) during contact, iii) latched but still moving, and iv) latched and resting.

latch and the electrical circuit is closed. The following sections derive the governing equations for the sensor during the second phase, when the mass is pushing past the latch and the latch is moving. The governing equations for the first and third phase can be easily derived from these by setting the interaction forces to zero, and the governing equation for the last phase can be easily derived by setting the interaction forces to zero and adding the axial stiffness of the latch to the sensor spring constant.

4.2 Reduced-Order Latching Sensor Model

In this section, two separate models are developed to predict the response of the shock sensor. The first model developed makes use of a single degree-of-freedom (the position of the mass), and this model is based on the assumptions that contact is maintained between the mass and latch during phase ii (Figure 4.1) and that the contact force can be estimated during this phase from the spring force of the latch. It eventually became clear that these assumptions were too limiting, since the true interaction forces could not be computed. Therefore, a two-degree-of-freedom model was developed in which one degree-of-freedom is used for the mass and another for the latch (the second latch is assumed to have an identical response to the first). This allows the interaction between the mass and latch to be studied in detail, including whether contact is indeed maintained in phase ii as well as the contact forces.

The one degree-of-freedom model requires very little computation time, and it may therefore be useful for fast order-of-magnitude estimates in screening potential designs. The two-degree-of-freedom is far more computationally intensive, primarily because of the very small time steps needed for correctly capturing the onset of contact. This model is expected to provide more accurate predictions of the device response, as well as allow for a detailed study of the dynamics of the mass-latch interaction.

4.2.1 One Degree-of-Freedom Model

The simplest model of the shock sensor is a one degree-of-freedom lumped parameter representation. The suspension springs and mass are lumped into a single global mass and spring constant, and the interaction of the latch and mass is included as a nonlinear, position dependent resisting force. In order to solve for the interaction force, the assumption is made that the latch and mass remain in contact throughout the interaction period. This model may not be the most accurate, but it can be solved

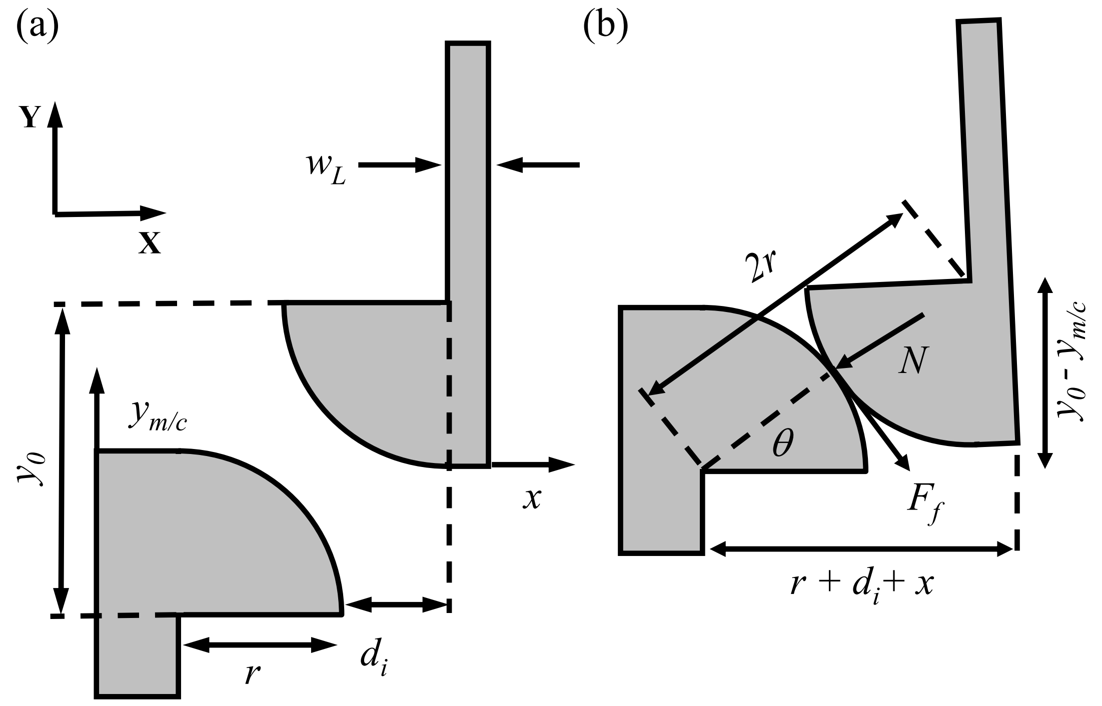

Figure 4.2. Mass and latch interaction for single DOF model: a) before contact and b) during contact.

quickly using standard numerical techniques. It may also be useful for quickly evaluating various design options in the early stages of device design. The geometry used in developing this model is shown in Figure 4.2.

We will use Lagrange's Equations to derive the basic equation of motion for the one degree of freedom case [54]. The Lagrangian is defined as

$$L = T - V, \tag{4.1}$$

where T is the kinetic energy of the system and V is the potential energy of the system. Since the mass of the latch is negligible compared to the sensor mass, the kinetic energy of the latch will be neglected. The kinetic and potential energy of the system can then be written as

$$T = \frac{1}{2} M (\dot{y}_c + \dot{y}_{m/c})^2, \tag{4.2}$$

$$V = \frac{1}{2} k y_{m/c}^2 , \tag{4.3}$$

where M is the effective mass of the sensor (including the effective mass of the suspension springs if desired), y_c is the displacement of the chip, $y_{m/c}$ is the relative displacement of the mass with respect to the chip, and k is the total effective spring constant of the suspension springs. A dot above a parameter indicates the time derivative. The complete Lagrangian can therefore be written as

$$L = \frac{1}{2} M (\dot{y}_c + \dot{y}_{m/c})^2 - \frac{1}{2} k y_{m/c}^2 . \tag{4.4}$$

The Euler-Lagrange Equations can be used to derive the equations of motion for the system from the Lagrangian expression. There is one equation for each generalized coordinate. Since we have only one generalized coordinate ($y_{m/c}$), there is only one equation of motion,

$$\frac{d}{dt}\left(\frac{\partial L}{\partial \dot{y}_{m/c}} \right) - \frac{\partial L}{\partial y_{m/c}} = Q_{ym/c} , \tag{4.5}$$

where Q represents any non-conservative forces, which in this case are the interaction forces between the mass and latch. Referring to Figure 4.2, the interaction force consists of a normal and frictional force. Both of these vary in direction and magnitude according to position of the mass.

At this stage, it is assumed that the mass and latch remain in contact throughout the interaction period and that the contact is rigid (i.e., no deformation of the mass of latch occurs in the contact region due to the contact forces). The result of this assumption is a constraint on x, wherein the deflection of the latch can be related to the displacement of the mass by simple geometry,

$$x = \sqrt{4r^2 - (y_0 - y_{m/c})^2} - (r + d_i) \tag{4.6}$$

After using static considerations for simplicity, the normal force N can be derived from a force balance on the latch in the x-direction.

$$\sum F_x = N\cos\theta - \mu N\cos(90 - \theta) - k_L x = 0 \tag{4.7}$$

Solving for N yields

$$N = \frac{k_L x}{\cos\theta - \mu\sin\theta} \tag{4.8}$$

Examining the geometry in Figure 4.2b, relations for sin θ and cos θ can be derived in terms of the generalized coordinate $y_{m/c}$ as

$$\sin\theta = \frac{y_0 - y_{m/c}}{2r} \tag{4.9}$$

$$\cos\theta = \frac{r + d_i + x}{2r} \tag{4.10}$$

The frictional force in the y-direction which resists motion is therefore

$$F_{fy} = -sign(\dot{y}_{m/c}) * \mu N\cos\theta = -sign(\dot{y}_{m/c}) * \mu N\frac{\sqrt{4r^2 - (y_0 - y_{m/c})^2}}{2r} \tag{4.11}$$

$$\begin{aligned} F_{fy} &= -sign(\dot{y}_{m/c}) * \\ &\mu\frac{k_L\left(\sqrt{4r^2 - (y_0 - y)^2} - r - d_i\right)}{\sqrt{4r^2 - (y_0 - y_{m/c})^2} - \mu(y_0 - y_{m/c})} * \sqrt{4r^2 - (y_0 - y_{m/c})^2} \end{aligned} \tag{4.12}$$

Taking the required derivatives and substituting into the Euler-Lagrange equation yields the equation of motion for the one degree-of-freedom approximation of the system dynamics.

$$
\begin{aligned}
&M\left(\ddot{y}_c + \ddot{y}_{m/c}\right) + k y_{m/c} + k_L x \frac{dx}{dy_{m/c}} = \\
&\qquad - sign(\dot{y}_{m/c}) * \mu \frac{k_L\left(\sqrt{4r^2 - (y_0 - y)^2} - r - d_i\right)}{\sqrt{4r^2 - (y_0 - y_{m/c})^2} - \mu\left(y_0 - y_{m/c}\right)} \sqrt{4r^2 - (y_0 - y_{m/c})^2},
\end{aligned}
\tag{4.13}
$$

Substituting in for x and its derivative yields the final equation of motion as a second order nonlinear differential equation in $y_{m/c}$

$$
\begin{aligned}
&M\left(\ddot{y}_c + \ddot{y}_{m/c}\right) + k y_{m/c} + 2k_L\left[\sqrt{4r^2 - (y_0 - y_{m/c})^2} - (r + d_i)\right]\frac{2\left(y_0 - y_{m/c}\right)}{\sqrt{4r^2 - (y_0 - y_{m/c})^2}} = \\
&\qquad - sign(\dot{y}_{m/c}) * 2\mu k_L \frac{\left(\sqrt{4r^2 - (y_0 - y)^2} - r - d_i\right)}{\sqrt{4r^2 - (y_0 - y_{m/c})^2} - \mu\left(y_0 - y_{m/c}\right)} \sqrt{4r^2 - (y_0 - y_{m/c})^2},
\end{aligned}
\tag{4.14}
$$

By introducing two states, y_1 an y_2, which represent the zeroth and first time derivative of $y_{m/c}$, respectively, the author converts the second order ODE into two first order ODE's.

$$
\begin{aligned}
&\frac{d}{dt}(y_1) = y_2 \\
&\frac{d}{dt}(y_2) = -\ddot{y}_c - \frac{k y_1}{m} - \frac{k_L}{m}\left[\sqrt{4r^2 - (y_0 - y_{m/c})^2} - (r + d_i)\right]\frac{2\left(y_0 - y_{m/c}\right)}{\sqrt{4r^2 - (y_0 - y_{m/c})^2}} - \\
&\qquad - sign(\dot{y}_{m/c}) * \frac{\mu k_L}{m} \frac{\left(\sqrt{4r^2 - (y_0 - y)^2} - r - d_i\right)}{\sqrt{4r^2 - (y_0 - y_{m/c})^2} - \mu\left(y_0 - y_{m/c}\right)} \sqrt{4r^2 - (y_0 - y_{m/c})^2}
\end{aligned}
\tag{4.15}
$$

Once in this form, given an initial condition and the function for the acceleration of the chip, the system can be readily solved using numerical techniques. Unless otherwise specified, we used the ode45 solver available in MATLAB which makes use of an explicit Runge-Kutta formula for the numerical integration.

The one degree-of-freedom model can be useful for quickly getting an order of magnitude estimate of the travel of the mass for a particular input acceleration function ($\ddot{y}_c$). The limitation is that this formulation does not include inertia of the latch, which may cause underestimation of the interaction forces. This also does not allow for study of the dynamics of the mass-latch interaction, so another model was created with two degrees of freedom. This model is presented next, and predictions from the two models are presented in Section 4.4.

4.2.2 Two Degree-of-Freedom Model

To avoid making the potentially erroneous assumption that the mass and latch remain in contact throughout the interaction period and to study the interaction in detail, one must include at minimum a second degree of freedom. This allows the mass and the latch to move independently, but significantly increases computation time and requires the use of very small time steps or more complex event detection during solution. The results are expected to provide more insights into the dynamics of the mass-latch interaction and to be more accurate than those obtained from the one degree of freedom model.

The two degree-of-freedom model presented in this section is the recommended model to use for detailed device design. The model is validated in Section 5.2 using the results from the high speed video measurements of the sensor position time history presented in Section 3.1.2.

The author will begin as with the one degree-of-freedom model by developing the Lagrangian and using the Euler-Lagrange equations to derive the equations of motion. For this model, however, the author will include the inertia of the latch in the kinetic energy expression and we will impose no constraint on the latch displacement x. The kinetic and potential energy for the system are

$$T = \frac{1}{2} M (\dot{y}_c + \dot{y}_{m/c})^2 + 2\frac{1}{2} m\dot{x}^2, \qquad (4.16)$$

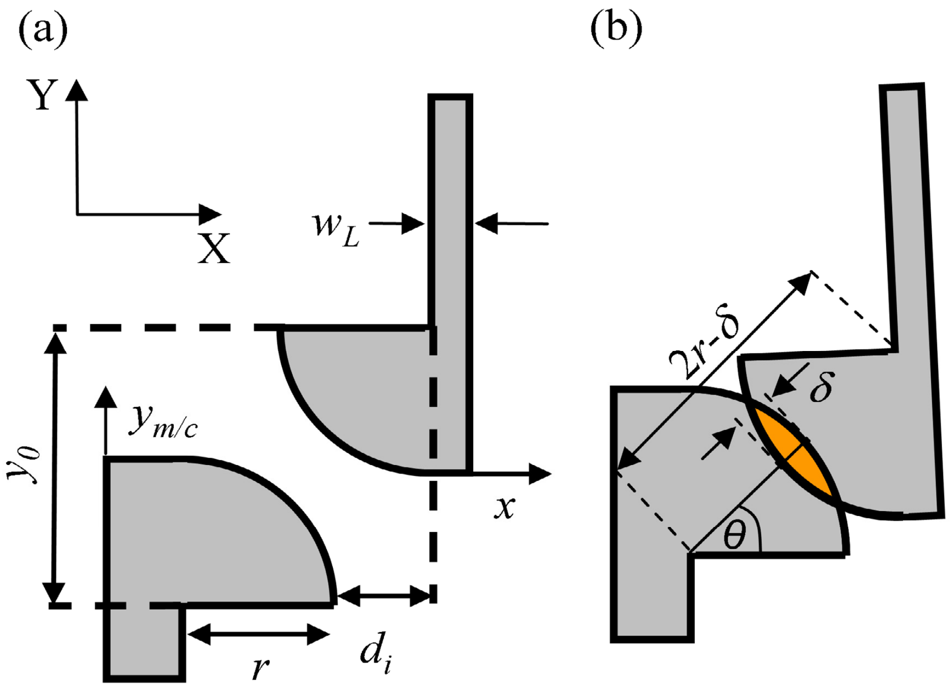

Figure 4.3. Geometry of mass-latch interaction for two DOF model: a) before contact, and b) during contact (with exaggerated contact deformation for clarity).

$$V = \frac{1}{2} k y_{m/c}^2 + 2\frac{1}{2} k_L x^2 + 2\frac{1}{2} k_c \delta^2, \tag{4.17}$$

where m is the mass of the latch, δ is the apparent penetration depth of the contact region (see Figure 4.3), and k_c is an effective spring constant of the contact interaction. The factors of two in front of the second term in the kinetic energy and the second and third terms in the potential energy result from the fact that there are two latches in the system. The implicit assumption is that both latches have the same properties and move in unison. The Lagrangian can then be written according to Eq. (4.1) as

$$L = \frac{1}{2} M (\dot{y}_c + \dot{y}_{m/c})^2 + 2\frac{1}{2} m \dot{x}^2 - \frac{1}{2} k y_{m/c}^2 - 2\frac{1}{2} k_L x^2 - 2\frac{1}{2} k_c \delta^2. \tag{4.18}$$

The equation of motion in the y-direction is found by substituting the Lagrangian into Eq. (4.6) and taking the required derivatives. There are two generalized coordinates ($y_{m/c}$ and x), resulting in two second order ODE's. With the addition of the second degree of freedom, the normal force is now conserved and the only nonconservative force Q is the friction force. The equations of motion are

$$M\left(\ddot{y}_c + \ddot{y}_{m/c}\right) + k y_{m/c} + 2k_c \delta \frac{\partial \delta}{\partial y_{m/c}} = -\mathrm{sign}(\dot{y}_{m/c}) 2\mu k_c \delta \cos\theta \tag{4.19}$$

$$2m\ddot{x} + 2k_L x + 2k_c \delta \frac{\partial \delta}{\partial x} = -\mathrm{sign}(\dot{x}) 2\mu k_c \delta \sin\theta \tag{4.20}$$

where $\sin\theta$ and $\cos\theta$ can be written as

$$\cos\theta = \frac{r + d_i + x}{2r - \delta} \tag{4.21}$$

$$\sin\theta = \frac{y_0 - y}{2r - \delta} \tag{4.22}$$

The penetration depth δ is a function of the two generalized coordinates. By examination of the geometry in Figure 4.3, the penetration depth can be derived as

$$\delta = \begin{cases} 2r - \sqrt{\left(y_0 - y_{m/c}\right)^2 + \left(r + d_i + x\right)^2}, & \sqrt{\left(y_0 - y_{m/c}\right)^2 + \left(r + d_i + x\right)^2} \le 2r \\ 0, & \sqrt{\left(y_0 - y_{m/c}\right)^2 + \left(r + d_i + x\right)^2} > 2r \end{cases} \tag{4.23}$$

The partial derivatives of δ can be obtained as

$$\frac{\partial \delta}{\partial y_{m/c}} = \frac{(y_0 - y_{m/c})}{\sqrt{(y_0 - y_{m/c})^2 + (r + d_i + x)^2}} \tag{4.24}$$

$$\frac{\partial \delta}{\partial x} = -\frac{(r + d_i + x)}{\sqrt{(y_0 - y_{m/c})^2 + (r + d_i + x)^2}} \tag{4.25}$$

Substituting δ and its partial derivatives into Eq. 4.19 and 4.20 results in the final equation of motion used in our model.

$$\begin{aligned} &M\left(\ddot{y}_c+\ddot{y}_{m/c}\right)+ky_{m/c}+2k_c\delta\frac{\left(y_0-y_{m/c}\right)}{\sqrt{\left(y_0-y_{m/c}\right)^2+\left(r+d_i+x\right)^2}}=-\mathrm{sign}(\dot{y})2\mu k_c\delta\frac{r+d_i+x}{2r-\delta} \\ &m\ddot{x}+k_Lx+k_c\delta\frac{\left(r+d_i+x\right)}{\sqrt{\left(y_0-y_{m/c}\right)^2+\left(r+d_i+x\right)^2}}=-\mathrm{sign}(\dot{x})\mu k_c\delta\frac{y_0-y}{2r-\delta} \end{aligned} \qquad (4.26)$$

The value of the contact stiffness, k_c, has not yet been addressed. For simplicity, a constant linear spring constant to represent the contact stiffness is attractive. In reference [55], Puttock and Thwaite derived expressions for the penetration depth as a function of applied force for various contact configurations with cylindrical and spherical bodies by using Hertzian contact theory. In Hertzian contact theory, the following assumptions are made: i) the contact surfaces are completely smooth, ii) the bodies are isotropic and linearly elastic, iii) the elastic limits are not exceeded, and iv) there are no friction forces in action. While these assumptions do not hold true for the silicon contact surfaces (the surfaces have roughness on the order of 60 nm, the silicon material has moderately anisotropic modulus and the sliding contact must necessarily include friction), simplifications are needed to derive a closed-form solution for the contact force-deformation relationship. According to Puttock and Thwaite, in general, the friction forces and varying elastic moduli lead to deviations of less than 10% from the ideal cases that they had studied. On this basis, for the case of two parallel cylinders in contact, the expression is

$$\delta=P(V_1+V_2)\left[1+\ln\left\{\frac{8a^2}{(V_1+V_2)P}\left(\frac{1}{D_1}+\frac{1}{D_2}\right)\right\}\right] \qquad (4.27)$$

where $2a$ is the length of contact between the cylinders, P is the compressive force per unit length applied to the cylinders, D_i is the diameter of each cylinder, and V is a material property defined as $\frac{1-\nu^2}{\pi E}$, where ν is Poisson's ratio and E is Young's modulus. For the special case of two cylinders of the same material and diameter, the relation simplifies to

$$\delta = 2PV\left[1+\ln\left\{\frac{8a^2}{VPD}\right\}\right] \tag{4.28}$$

This force deflection relationship was verified for the shock sensor dimensions by using a three-dimensional finite element model composed in ANSYS [56] (Figure 4.4). Solid95 elements (a structural element with mid-side nodes) were used to conduct a static (steady-state) analysis of the contact with a constant applied force. Half-cylinders were used to allow a uniform pressure to be applied perpendicular to a flat edge. The flat edge of one half-cylinder was fully constrained and the load applied to the flat edge of the other half-cylinder. The loads chosen are

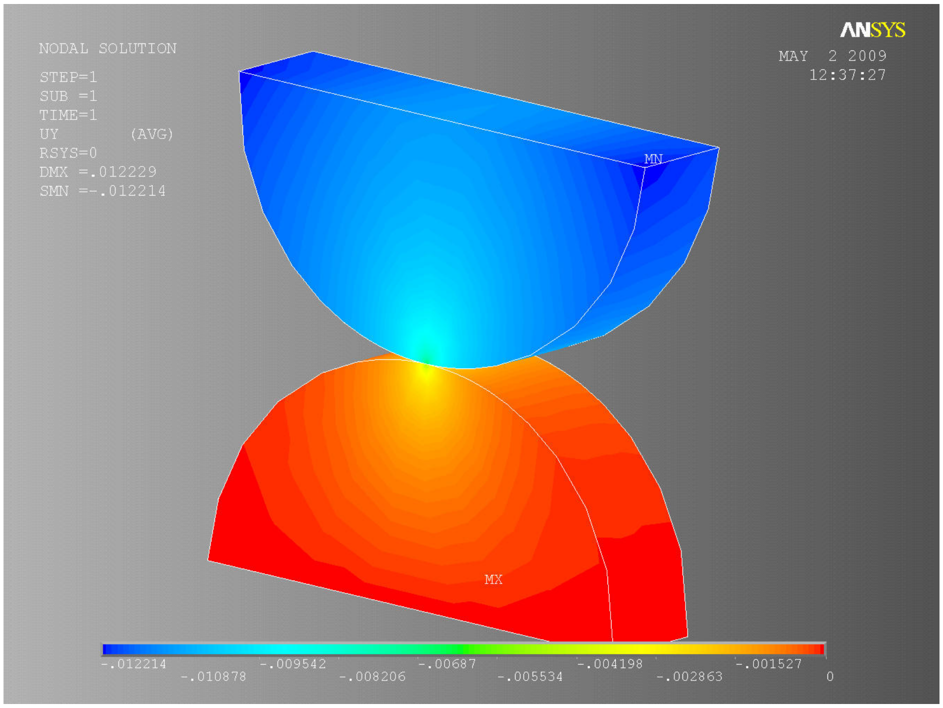

Figure 4.4. Finite element model of latch contact.

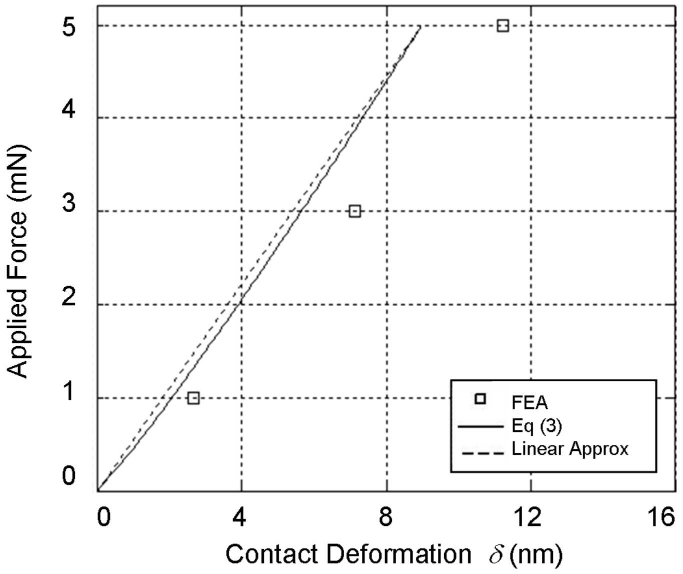

Figure 4.5. Comparison of contact forces predicted by Eq. (4.28) and finite element model over the relevant range of applied force.

in the range of the expected contact forces predicted by the dynamic shock sensor model presented above. The deflection of the edge where the load was applied is equal to the apparent interpenetration used in the model. The finite element results are compared with Eq. (4.28) in Figure 4.5.

The solutions of Eq. (4.26) are numerically determined for the chosen initial conditions and the given external acceleration profile to which the chip is subjected. The chip acceleration serves as excitation to the system. Although the model can accommodate any arbitrary function for the chip displacement y_c, in this dissertation this forcing profile is considered to be a half-sine pulse for all simulations with the magnitude and duration of the half-sine pulse as noted in each case.

The relevant parameters for the two sensor designs considered here are shown in Table 4.1. The results obtained from a representative simulation conducted for one sensor design and acceleration profile are shown in Figure 4.6. The latch initially does not undergo any motion because the mass has not contacted it. Contact is made

Table 4.1. Design parameters for shock sensor relevant to the lumped parameter model (corresponding physical dimensions are given in Table 3.1).

Parameter	Description	Design 1	Design 2
M (kg)	sensor mass	3.42e-7	2.65e-7
k (N/m)	sensor stiffness	0.601	1.324
f (Hz)	natural frequency of sensor (uncoupled)	211	356
m (kg)	latch effective mass	5.64e-11	5.64e-11
k_L (N/m)	latch stiffness	4.44	4.44
f_L (Hz)	natural frequency of latch (uncoupled)	44,700	44,700
k_c (N/m)	contact stiffness	5.57e5	5.57e5
y_0 (μm)	initial sensor travel to latch	150	150
r (μm)	latch radius	40	40
d_i (μm)	horizontal offset	15	15
$\ddot{y}_{crit}$ (g)	nominal acceleration for latching – threshold levels	50	100

at 1.1 ms in this case. At 1.4 ms, the mass has moved completely past the latch. After this event, in the simulations, the motions of the shock sensor mass and latch are treated as uncoupled. The latch undergoes free vibrations, while the mass bounces back and forth as it alternately contacts the extension frame and flat edge of the latch (see Figure 4.7). The motion of the latch in the post-contact region is treated as a free harmonic oscillation with an initial displacement equal to the position of the latch when the mass has just moved past it. As shown in Figure 4.6, the frequency of vibration of the latch (44.7 kHz) is much higher in this post-contact region than that of the mass bounce frequency (4.0 kHz). This is due to the much lower mass and higher spring constant of the latch. The frequency of the mass bouncing back and forth after latching is primarily dependent on the speed of the mass after latching.

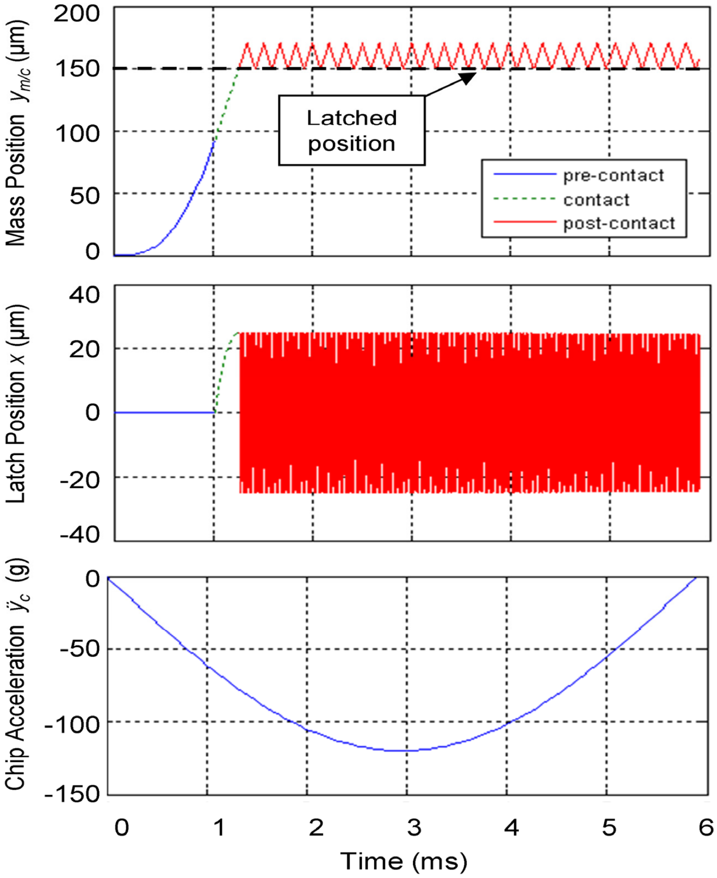

Figure 4.6. Design 2 sensor results obtained from two DOF model for displacement of mass ($y_{m/c}$) and displacement of latch (x) when μ=0.1, and acceleration pulse is 120 g for 5.9 ms.

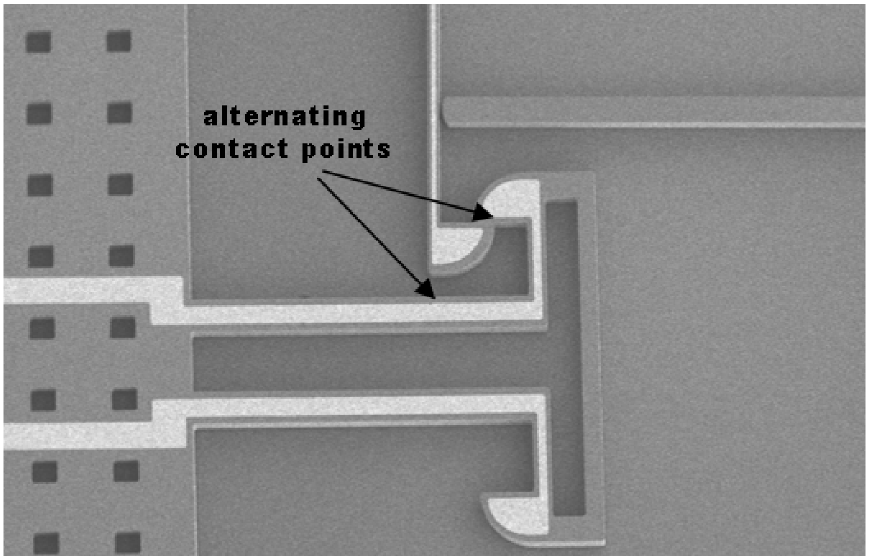

Figure 4.7. Alternating contact points which cause bouncing of mass after latching.

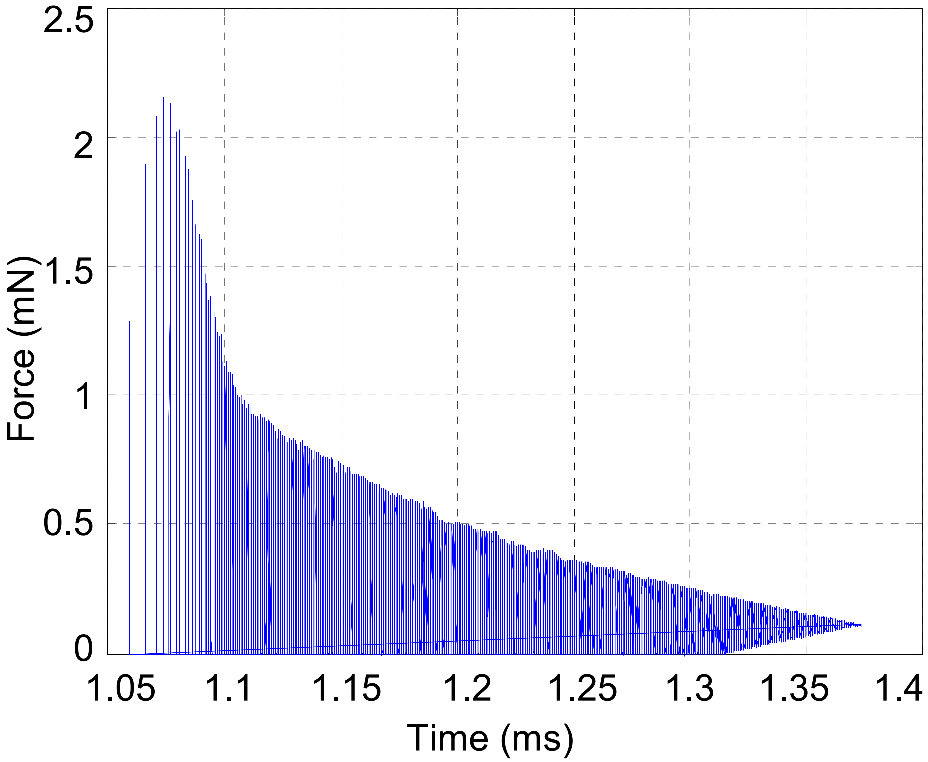

Figure 4.8. Time history of contact force for a Design 2 sensor as predicted by 2 DOF model when μ=0.1, and acceleration pulse is 120 g for 5.9 ms.

The contact force can be extracted from the 2 degree-of-freedom model at each time step to help analyze the behavior. The results for a Design 1 device are shown in Figure 4.8. Since the contact and the latch itself both have an inherent stiffness, the contact force is observed as a decaying oscillatory function. The decay is due to the changing direction of the contact normal, from just over 45 degrees from the direction of travel at the moment of first contact to 90 degrees to the direction of travel just before latching. Early on in the contact, the model predicts intermittent contact due to the latch bouncing away from the mass. This is more evident in Figure 4.9, which shows the position of the latch during the initial phase of contact. There is a clear bounce evident generated by the contact force pushing the latch away from the mass. This effect is dependent on the time steps chosen in the model solution, with

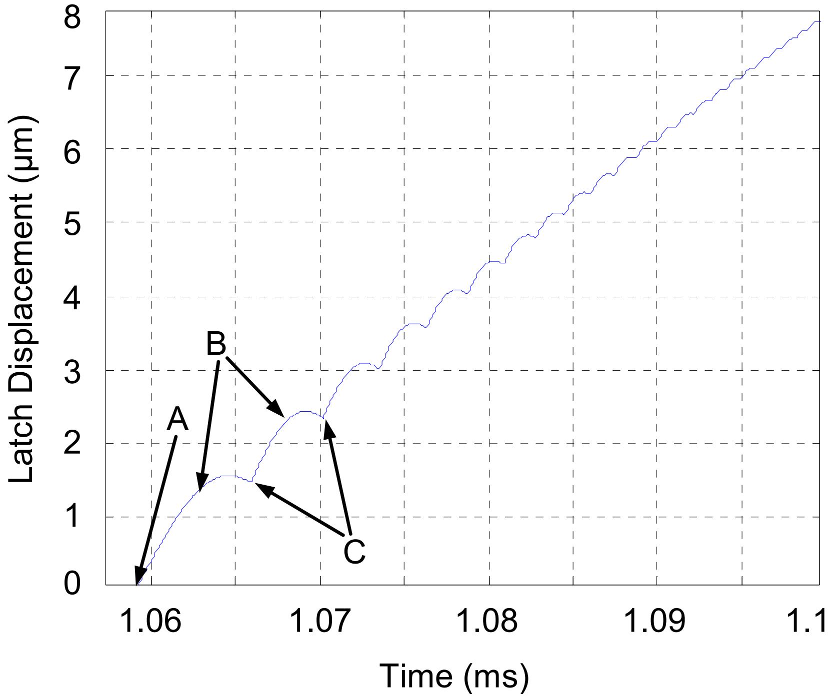

Figure 4.9. Position of latch during initial phase of contact, displaying bounce of up to 0.4 µm (blowup of the contact section in the latch position graph from Figure 4.6). Point A is where initial contact is made, points B are where contact is lost during a bounce, and points C are where contact is reestablished after a bounce.

larger bounces predicted at larger time steps. This makes sense because with a larger time step the apparent penetration when contact is first detected is larger, and therefore the contact force will be larger and the acceleration of the latch away from the mass will also be larger. However, as the time step is decreased towards zero, the magnitude of the bounce approaches a limit of about 0.5 µm – smaller time steps no longer decrease the amplitude of the bounce. For the Design 1 sensor, the initial bounce causes a loss of contact for 0.7 µs. Each successive bounce gets smaller and the loss of contact shorter until after about 40 µs there is no longer any loss of contact.

One interesting effect evident from the force time-history shown in Figure 4.8 is that the maximum contact force does not occur during the initial contact, but rather after several bounces (on the fourth bounce for the case shown in Figure 4.8). This is because the acceleration pulse applied was a half-sine pulse with a pulsewidth of 5.9 ms, and the sensor makes initial contact at 1.059ms, while the acceleration is still increasing. Figure 4.10 shows the kinetic energy of the mass and the latch during the latching event for the same case plotted in Figure 4.6 and Figure 4.8. The maximum kinetic energy for the latch is achieved at 1.070 ms, just after the third bounce. The

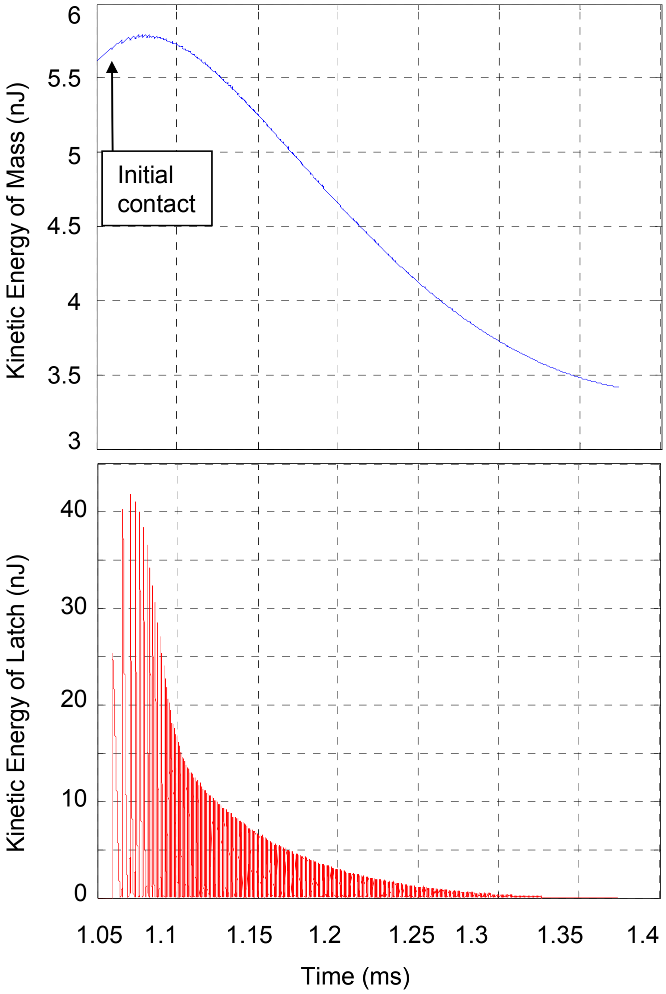

Figure 4.10. Kinetic energy of mass and latch during latching event for Design 2 sensor, when μ=0.1 and acceleration pulse is 120 g for 5.9ms.

kinetic energy for the mass reaches its maximum value at 1.079ms, just after the sixth bounce. In other words, the relative approach velocity of the mass and latch is largest for the fourth and fifth bounce. After this the relative approach velocities of each start to decrease. This explains why the contact force is highest for the fourth bounce.

4.3 Equivalent Stiffness for Suspension Springs and Latch

The reduced order model approximates the array of suspension springs as a single spring with a single stiffness value *k*. The equivalent lumped stiffness of the suspension spring is calculated by adding the four identical folded-flexure springs in parallel. The stiffness of each folded-flexure spring is in turn calculated by adding the stiffness of the individual meanders in series. The individual members are each equivalent to a clamped-guided beam, with a stiffness of $12EI/L^3$ [57], where E is the Young's modulus for the beam material, L is the length of the beam, and I is the area moment of inertia of the cross-section of the beam. The total equivalent spring constant for the sensor suspension springs can be found as

$$k = \frac{p}{n}\frac{12EI}{L^3} = \frac{p}{n}\frac{E}{L^3}tw^3, \tag{4.29}$$

where n is the number of beams in series in each folded flexure, p is the number of folded flexures in parallel, t is the device thickness, and w is the width of each folded flexure beam. The latch is approximated as a cantilever, with an equivalent spring constant of

$$k_L = \frac{3EI}{L^3} = \frac{Etw_L^3}{4L_L{}^3}. \tag{4.30}$$

4.4 Comparison of 1DOF and 2DOF Model Results

By way of comparison between the one degree-of-freedom model and the two degree-of-freedom model, the displacement time-history is plotted for one case in Figure 4.11. The difference between the two models is in the treatment of the contact force between the latch and the mass. The one degree-of-freedom model used the displacement of the mass to calculate the position of the latch (assuming contact is maintained). The position of the latch and the resultant spring force were then used to calculate the normal force on the mass. The two degree-of-freedom model does not assume a position for the latch, and the contact forces are calculated based on the relative positions of the mass and latch and the contact stiffness derived from Hertzian contact theory. The results match exactly before contact is made because the two models are functionally identical in this region.

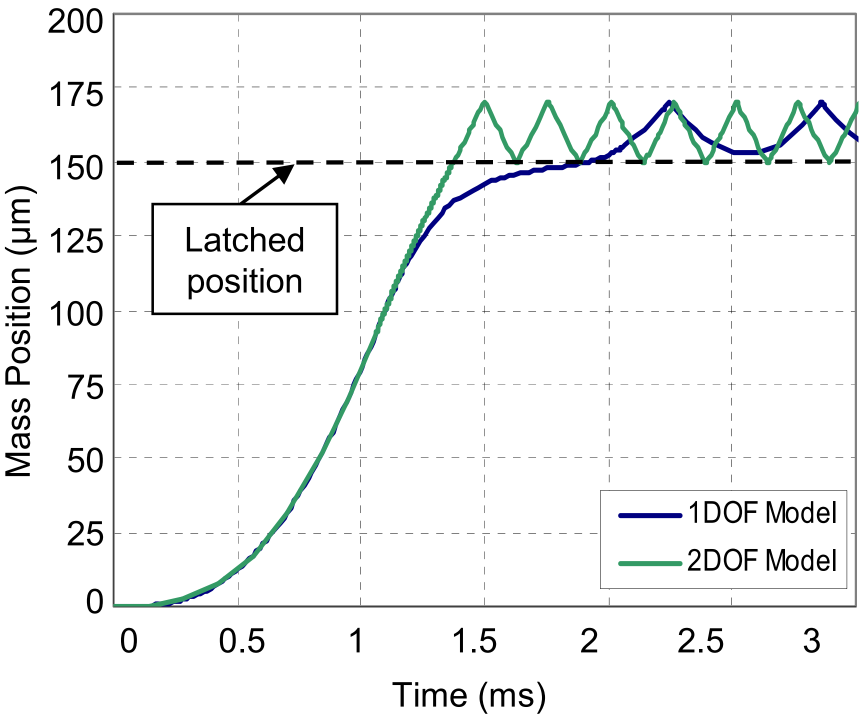

Figure 4.11. Comparison of single degree-of-freedom results from [9] to two degree-of-freedom model results for Design 2 sensor, $\mu = 0.1$, acceleration = 120 g for 5.9 ms.

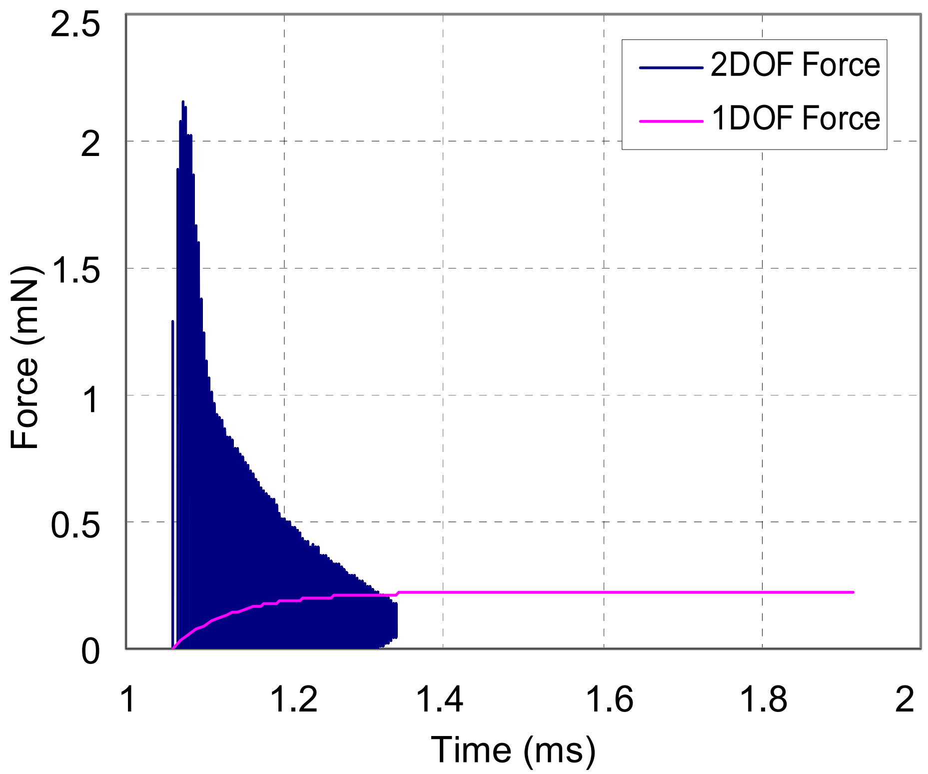

Figure 4.12. Comparison of normal forces associated with 1DOF and 2DOF models.

During contact the results diverge. The coefficient of friction affects the mass motion more strongly in the one degree-of-freedom model because the latch and mass are in constant contact, whereas in the two degree-of-freedom model the latch bounces away from the mass many times during the nominal contact period. This is even more interesting when the contact forces are compared (Figure 4.12). Although the magnitude of the contact force in the one degree-of-freedom model is only about 10% of the maximum magnitude of the contact force in the two degree-of-freedom model, the work done by the friction is higher in the one degree-of-freedom model because the distance travelled during contact is much larger.

The increased dissipation in the one degree-of-freedom model due to the larger work done by friction results in a longer time to latch and lower velocity of the mass after latching in Figure 4.11. The predicted frequency of the oscillations after

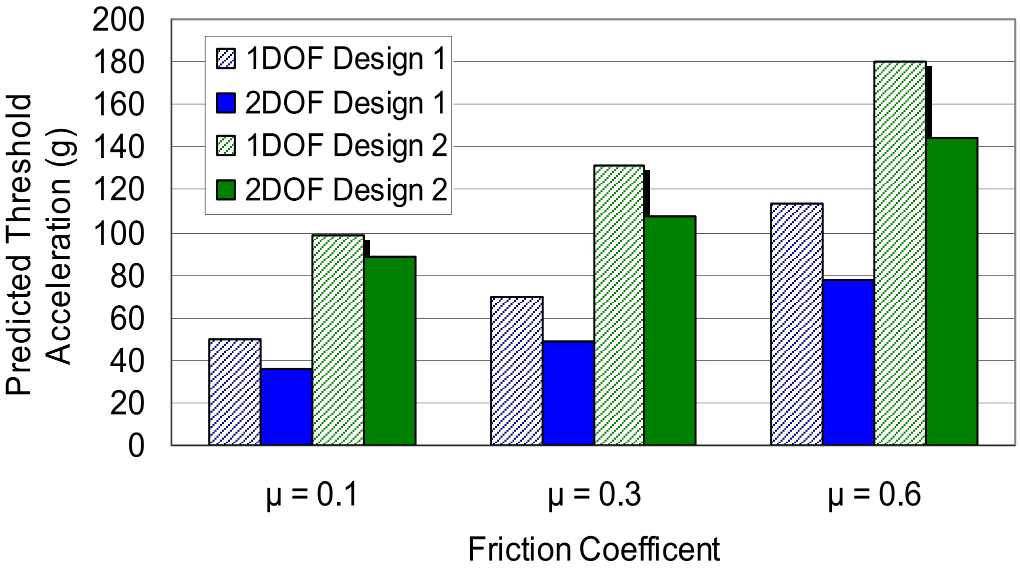

Figure 4.13. Comparison of predicted threshold acceleration to latch using one degree-of-freedom and two degree-of-freedom models for Design 1 and Design 2 devices with various friction coefficients. Applied acceleration is a half-sine pulse with duration of 8 ms for Design 1 and 5.9 ms for Design 2.

latching are therefore lower with the one degree-of-freedom model than with the two degree-of-freedom model. Perhaps more importantly, it also results in dramatically different predictions of the threshold acceleration to latch for a given design. This is illustrated in Figure 4.13, in which the predictions from both models are plotted for Design 1 and Design 2 devices with various assumed friction coefficients. In every case, the one degree-of-freedom model predicts significantly higher acceleration thresholds before a device latches. The difference is about 30% for Design 1 and ranges from 10% to 20% for Design 2.

The results presented in this section illustrate the difference in treatment of the contact interaction between the one degree-of-freedom and the two degree-of-freedom models. The implication is that while a one degree-of-freedom model may be used for rough order of magnitude calculations, at least two degrees of freedom must be used for detailed predictions of device performance. Predictions from the two degree-of-freedom model are expected to be more reliable, given the more realistic treatment of the interaction forces. The two degree-of-freedom model is validated in Section 5.2 by using the results from the high speed video measurements of the sensor position time history presented in Section 3.1.2.

4.5 Sensor Parametric Studies

To provide insights into the design of latching threshold acceleration sensors, the author undertook several parametric studies. These demonstrate the effect of one parameter on the device performance by holding all other parameters constant while varying only the parameter of interest. There are a large number of independent design parameters that can be manipulated to create designs with different latching threshold acceleration levels. For instance, the sensor mass M can be changed by modifying the length or width of the mass, or changing the size or spacing of the etch holes. The stiffness of the sensor k can be changed by modifying the length or width of the springs, the number of meanders, or the number of suspension springs used. The following studies are not intended to be exhaustive, but rather to provide a framework for understanding how the design can be manipulated to achieve the desired latching threshold. The baseline case used was the Design 2 sensor, which nominally latches around 100 g. The baseline values for each design parameter along with the mass and stiffness values calculated from these parameters are shown in Table 4.2.

Table 4.2. Baseline parameters used for parametric studies (taken from Design 2 sensor).

Parameter	Units	Description	Baseline Value for Parametric Studies
H_m	mm	height of mass	2.025
W_m	mm	width of mass	3.1
t	μm	thickness of device	20
M	kg	equivalent mass of sensor (including flexures)	2.65e-7
L_f	mm	length of suspension flexure	1.495
W_f	μm	width of suspension flexure	12
k	N/m	total suspension stiffness	1.324
w_L	μm	width of latch cantilever	8
l_L	μm	length of latch cantilever	460
r	μm	radius of latch and mass contact surfaces	40
d_i	μm	horizontal offset between latch and mass contact surfaces	15
m	kg	equivalent mass of latch	5.64e-11
k_L	N/m	bending stiffness of latch cantilever	4.44
k_c	N/m	contact stiffness	5.57e5
y_0	μm	initial sensor travel required to latch	150

The first parameters examined are the height of the mass and the length of a flexure. The mass of the sensor varies linearly with the height of the mass, which causes the acceleration to latch to decrease with increasing H_m as shown in Figure 4.14. The length of the flexure is a little more complicated, because the stiffness k is proportional to the inverse cubed length, and the width of the mass is also linked to the length of the flexure. In the design and in the model, the width of the mass is equal to

$$W_m = 2L_f + 110\,\mu\text{m} \tag{4.31}$$

The result is that as the length of the flexure increases, the stiffness k decreases and the effective mass of the sensor M also increases. Since both of these effects contribute to decrease the acceleration to latch as the length of the flexure increases, the dependence shown in Figure 4.15 is far more pronounced than when the mass alone was varied.

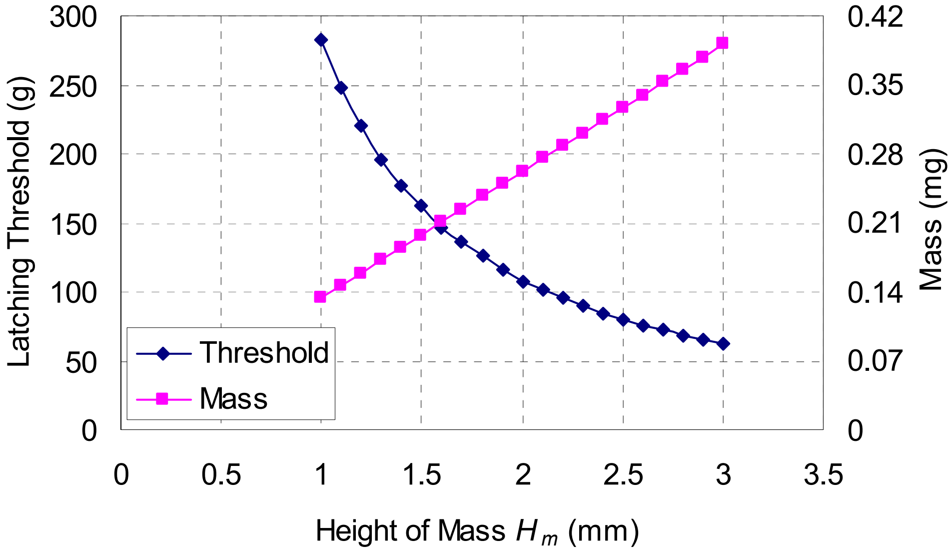

Figure 4.14. Effect of vertical mass dimension on acceleration to latch. All other parameters are the same as those for the Design 2 sensor.

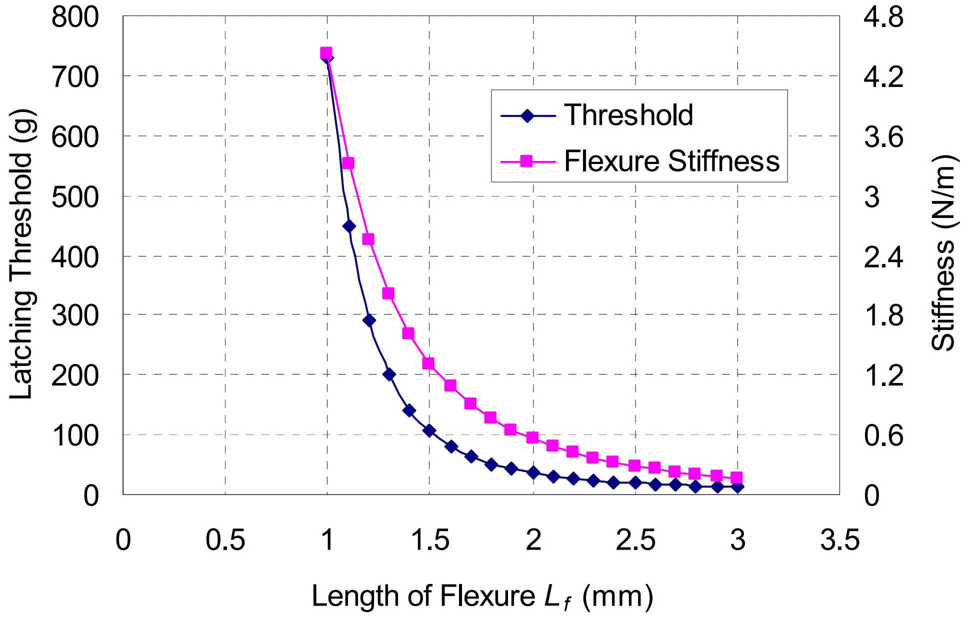

Figure 4.15. Effect of suspension spring length on acceleration to latch. All other parameters are the same as those for the Design 2 sensor.

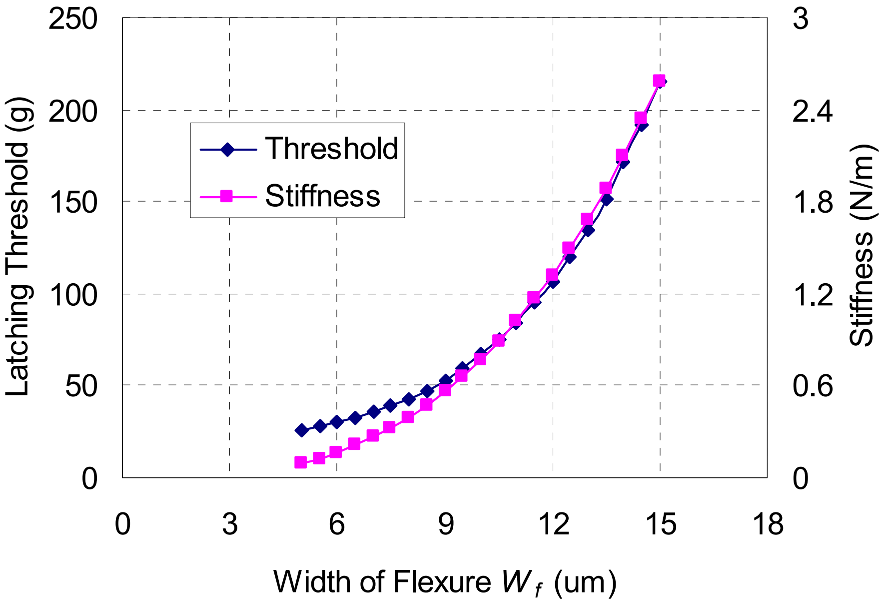

Figure 4.16. Effect of flexure width on acceleration to latch. All other parameters are the same as those for the Design 2 sensor.

The stiffness of the flexures can also be changed by modifying the flexure width W_f. The stiffness changes with the cube of the flexure width, so the acceleration to latch increases as the flexure width increases, as shown in Figure 4.16.

The acceleration to latch is not only affected by the mass and stiffness of the sensor; the characteristics of the latch must also be considered since the interaction forces are non-trivial in magnitude. The stiffness of the latch is affected primarily by the length and width of the latch cantilever. As the stiffness of the latch decreases, the interaction forces decrease and the threshold acceleration consequently also decreases. Therefore, as the latch cantilever gets longer the threshold acceleration decreases (Figure 4.17). Similarly, as the latch cantilever width decreases the threshold acceleration decreases (Figure 4.18).

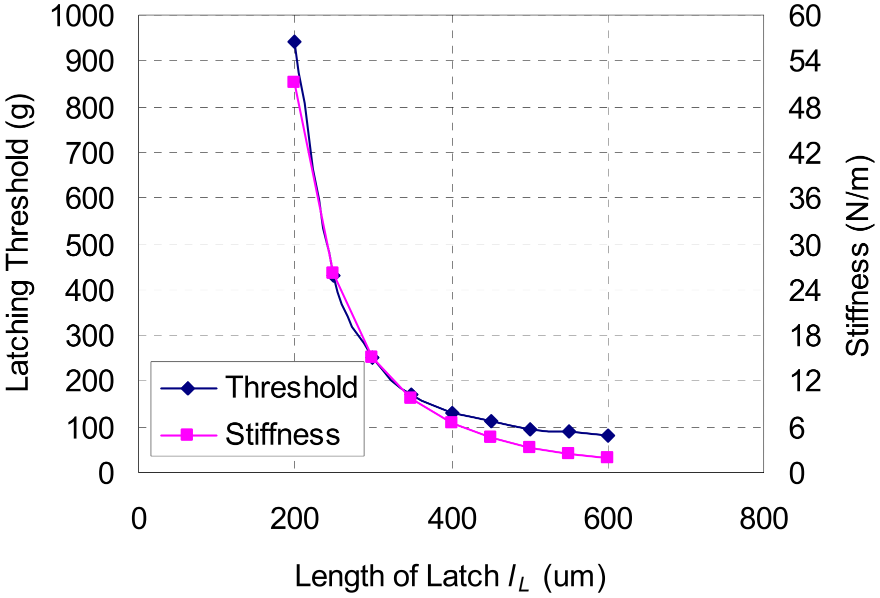

Figure 4.17. Effect of latch length on acceleration to latch. All other parameters are the same as those for the Design 2 sensor.

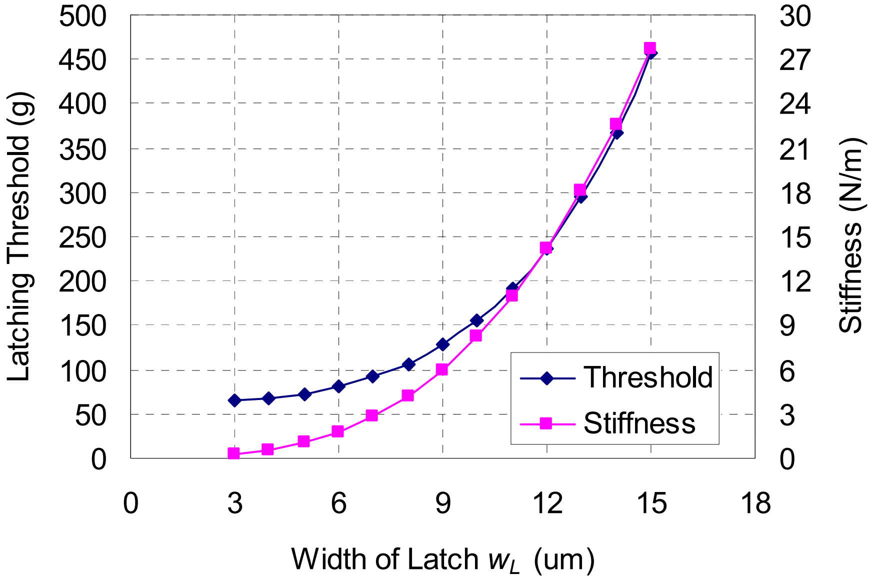

Figure 4.18. Effect of latch width on acceleration to latch. All other parameters are the same as those for the Design 2 sensor.

Each of the trends presented here are obvious to the casual observer (e.g., as stiffness increases, the acceleration required to latch should also increase), but the exact relationships are not easily found by inspection or simple calculations. The parametric studies presented so far shed some light on the exact relationships of the design parameters, as well as the relative importance of one parameter as compared to the others. This is intended to aid in the design process – in attempting to design a device that meets a certain threshold, one can refer to these relationships and determine which parameters to change. Some modeling will clearly still have to be undertaken for the best results, but the parametric studies should help decide where to start.

Because the coefficient of friction can vary somewhat due to the fabrication process and over a number of cycles (see Section 3.3), the acceleration required to latch the device is plotted over a range of friction coefficients in Figure 4.19. The acceleration required to latch shows a strong dependence on friction coefficient, more than doubling over the range of $0.1 \leq \mu \leq 0.8$ (from 89 to 183 g). Because the friction coefficient can depend on the sidewall roughness (see Section 3.3 or [51]), good control over the fabrication process is critical with this particular shock sensor design

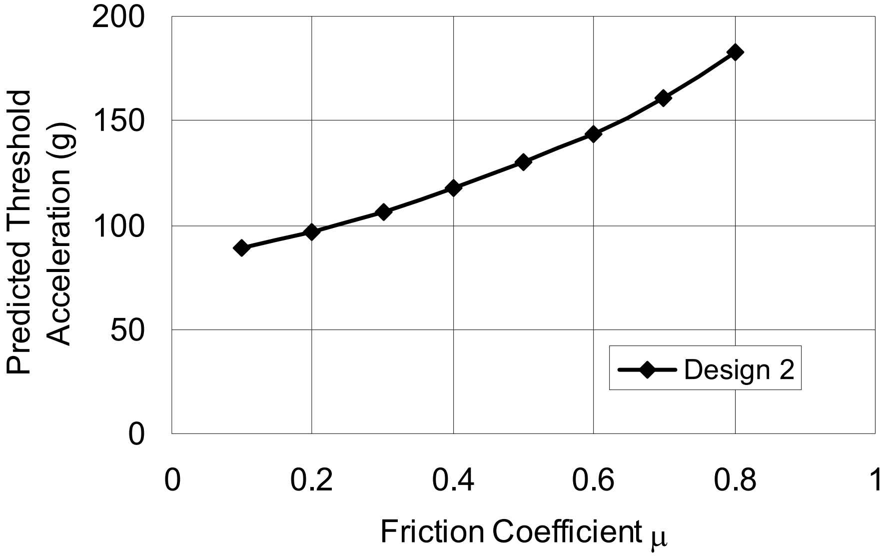

Figure 4.19. Effect of friction coefficient on latching level for Design 2 sensor.

to ensure that every device latches at the same threshold level.

The bounce of the latch is an important aspect never reported before for latching shock sensors. The two degree-of-freedom model allows further study of the latch bounce phenomenon. The bounce dynamics are determined by the stiffness of the latch, the effective mass of the latch and the velocity of the mass when it hits the latch. Figure 4.20 shows how the magnitude of the first bounce (which is also the larrgest bounce) changes with changing stiffness and mass of the latch. The stiffness of the latch was changed by varying the width of the latch. The effective mass was calculated from the latch dimensions and the density of silicon, and assuming vibration in the first natural modeshape of a cantilever. The mass of the latch was changed directly to match each of the total effective masses calculated by changing the latch width (equivalent to adding a point mass at the end of the latch). When the

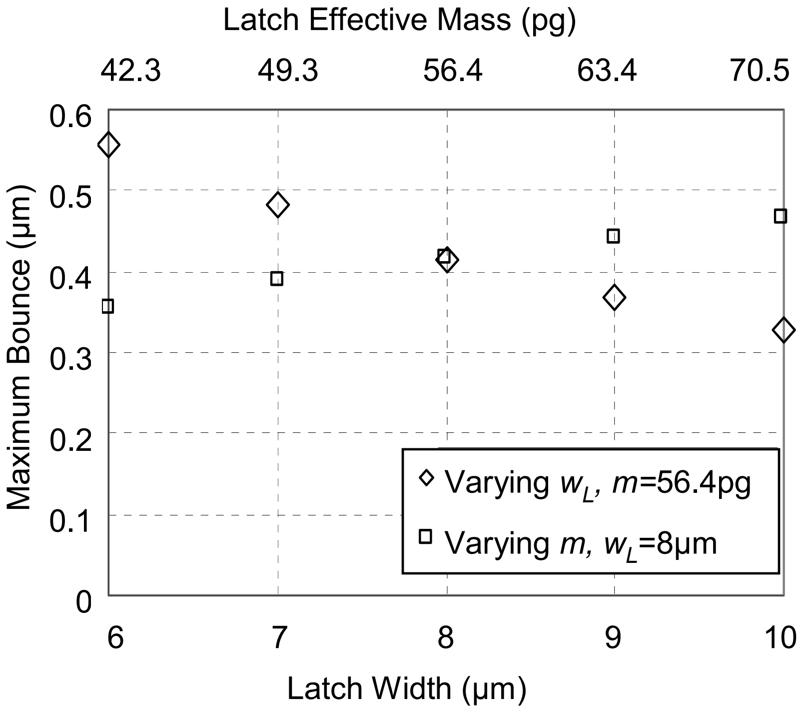

Figure 4.20. Effect of varying latch width and effective mass of latch on magnitude of bounce for Design 2 sensor. Applied acceleration pulse is 140 g for 5.9 ms.

latch width increases, the stiffness increases with the cube of the width and the mass increases linearly with the width. The result is that the bounces get smaller as the width of the latch decreases because the inertia decreases more slowly than the force keeping the latch in contact with the mass. When the mass of the latch increases while keeping the latch stiffness constant, the inertia increases and the force keeping the latch in contact with the mass remains the same, so the magnitude of the bounce increases.

The model results outlined so far have assumed the only dissipative force is the friction in the contact between the mass and latch. There may in fact be some viscous damping due to air resistance or material damping due to stretching of the springs present throughout the entire sensor operation. This can be considered in the model by adding a constant damping term into the equation of motion for the mass (Eq. (4.26)):

$$\begin{aligned} M\left(\ddot{y}_c + \ddot{y}_{m/c}\right) + c\dot{y}_{m/c} + k y_{m/c} + 2k_c\delta\frac{\partial\delta}{\partial y_{m/c}} \\ = -\mathrm{sgn}(\dot{y})2\mu k_c\delta\cos\theta \end{aligned} \tag{4.32}$$

The effect of constant damping on the response of the mass is shown in Figure 4.21. As expected, the time to latch increases as the damping factor increases, and the acceleration required to latch also increases as the damping factor increases. The bouncing of the mass after latching is also dissipated when damping is added. The oscillations after latching decrease in frequency with increased damping because the velocity of the mass after latching decreases.

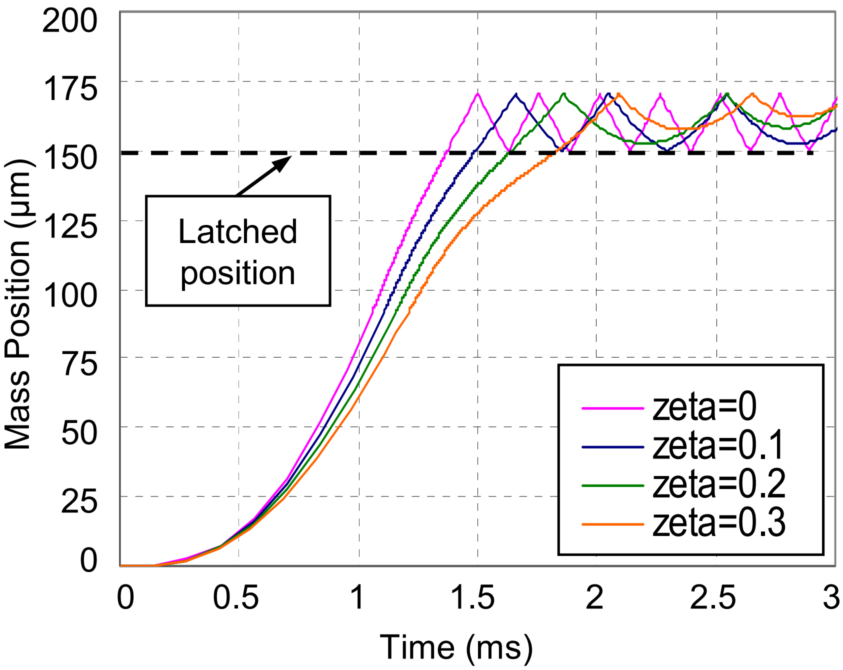

Figure 4.21. Modeled response of shock sensor with various damping factors.

4.6 Sensor Optimization Studies and Robust Design

Various uncertainties in the properties of the fabricated devices can have a significant effect on the device performance. These uncertain properties can take the form of small deviations from the designed dimensions, uncertainty in the precise material properties, or in the case of the friction coefficient, variations in the surface roughness from device to device, wafer to wafer, or even changes over time due to wear, as illustrated by the measurements made with the friction test structure in Section 3.3 and the repetitive shock cycling tests of the sensor itself discussed in Section 3.1.1. The ideal way to account for variations and uncertainty is to create a robust design that exhibits very little variations in the performance over an expected range of a given parameter. This can be done through optimization of the design, with sensitivity to a particular parameter or set of parameters defined as the objective function.

Given the observed dependence of latching threshold accelerometers on friction, and the variability in roughness (and therefore friction coefficients) of the sidewalls in the shock sensor design under consideration, optimization of the design so that it is relatively insensitive to variations in the friction coefficient is examined in a case study. Similar optimizations can be performed with respect to other parameters, such as the width of the springs or latches.

The optimization problem for friction sensitivity can be stated as a minimization of the slope of the latching threshold as a function of the friction coefficient, subject to the constraint that the latching threshold for a particular friction coefficient should not vary from the target threshold by more than an acceptable error. In mathematical terms, this can be written as:

$$\begin{aligned} &\min_{\mu} && \Delta[\mathrm{Thresh}(\mu)] \\ &\mathrm{s.t.} && \mathrm{abs}\left(\mathrm{Thresh}(\mu_0) - \mathrm{Target}\right) \le \varepsilon \end{aligned} \tag{4.33}$$

where the friction sensitivity is defined as:

$$\Delta[\mathrm{Thresh}(\mu)] = \frac{\mathrm{Thresh}(0.6)}{\mathrm{Thresh}(0.3)} - 1 \tag{4.34}$$

To simplify the problem somewhat, the slope was evaluated by using only two different friction coefficients, 0.3 and 0.6. The constraint was evaluated using $\mu_0 = 0.3$. The acceptable error ε between the target threshold and the actual threshold in an individual design was defined as 3% of the target threshold, or 3g for a target threshold of 100 g. For designs that differ by more than 3%, the constraint is not satisfied and the design is not considered feasible.

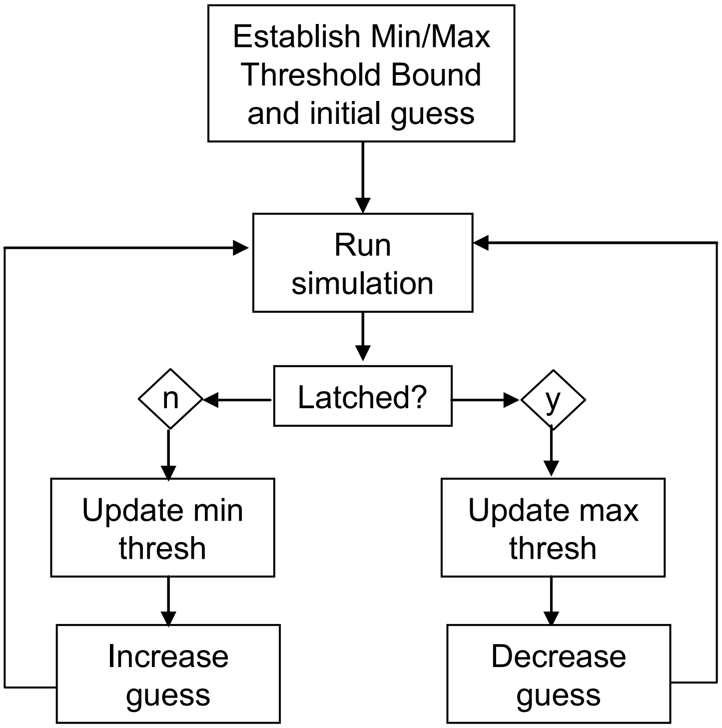

Figure 4.22. Algorithm to find the acceleration threshold required to latch any individual design.

Finding the threshold for an individual design is in itself an optimization problem. It is not tractable to come up with a closed form expression, and when the sensor either latches or does not latch, the gradient is undefined. Therefore a simple guess-and-test search algorithm was written to find the latching threshold. The algorithm is shown as a block diagram in Figure 4.22. Bounds on the search space are established, and the position/time response of the device is calculated by using the two degree-of-freedom model presented in Section 4.2.2. If the model predicts that the device will latch at the guessed acceleration value, the guess value is decreased and the simulation is run again. If the model predicts that the device will not latch, the guess value is increased and the simulation is run again. This process is repeated iteratively, updating the minimum and maximum bounds on the search at each step until the difference between the minimum bound and maximum bound reaches an acceptable value (0.1g for the studies presented here). The final value of the maximum bound is used as the threshold acceleration required to latch, since the device is predicted to latch at this value and predicted not to latch just below this value.

The independent design parameters used are as shown in Table 4.3. There are 6 independent design variables here. Some other variables could be chosen, including the radius of the latch r, the initial horizontal offset d_i, and the total distance to latch y_0. Only six parameters were chosen to keep the problem somewhat tractable without limiting the results any more than necessary. Even so, this represents a tremendous number of potential designs, far more than could ever be experimentally investigated. This of course is the point of numerical optimization studies – to identify potentially promising designs in a large design space without having to make and experimentally study each design.

The difficulty of the latching shock sensor optimization problem is that finding the latching threshold is an iterative process that requires guessing an acceleration and solving the model to determine whether the sensor will latch. The

Table 4.3. Design parameters used for optimization studies. All other parameters are the same as that for Design 2.

Optimization Parameter	Description	Units	Lower Bound	Upper Bound
t	device thickness	μm	1	50
L_f	length of flexure	mm	1	2
W_f	width of flexure	μm	3	20
H_m	height of mass	mm	1	3
w_L	width of latch	μm	3	18
l_L	length of latch	μm	200	600

result is binary: either the sensor latches or it does not. If it latches, the guessed acceleration is lowered and the process is repeated. If it does not latch, the guess is raised and the process is repeated, until the latching threshold is found within an acceptable error range. This is essentially a line-search technique where the gradient is zero everywhere except right at the latch threshold, where it is infinite. On a typical desktop computer, each guess/test iteration of the model takes on the order of 40 seconds, so the process of finding the latching threshold for any one design can take several minutes. Additionally, this optimization problem requires finding the latching threshold for two different friction coefficients. The computational time can therefore quickly become prohibitive on a desktop computer. Parallel processing, wherein multiple designs are evaluated simultaneously on separate processors, relieves this problem somewhat.

Two MATLAB [58] optimization tools are used to solve the optimization problem, fmincon (function call: “fmincon”) and the genetic algorithm tool (function call “gatool”). Fmincon attempts to find the minimum of a nonlinear multivariable problem subject to linear and/or nonlinear constraints. Fmincon is a gradient-based technique, but the gradient of the objective function does not need to be known before beginning the optimization. The MATLAB function begins by changing each of the variables slightly to calculate the gradient, then moves in the most promising direction. With each step, the gradient is updated. Unfortunately, if the search reaches the boundary of the parameter space, the minimization is terminated rather than searching in another direction. This makes the success of the Fmincon optimization for this problem highly dependent on the user-specified initial point. This led to

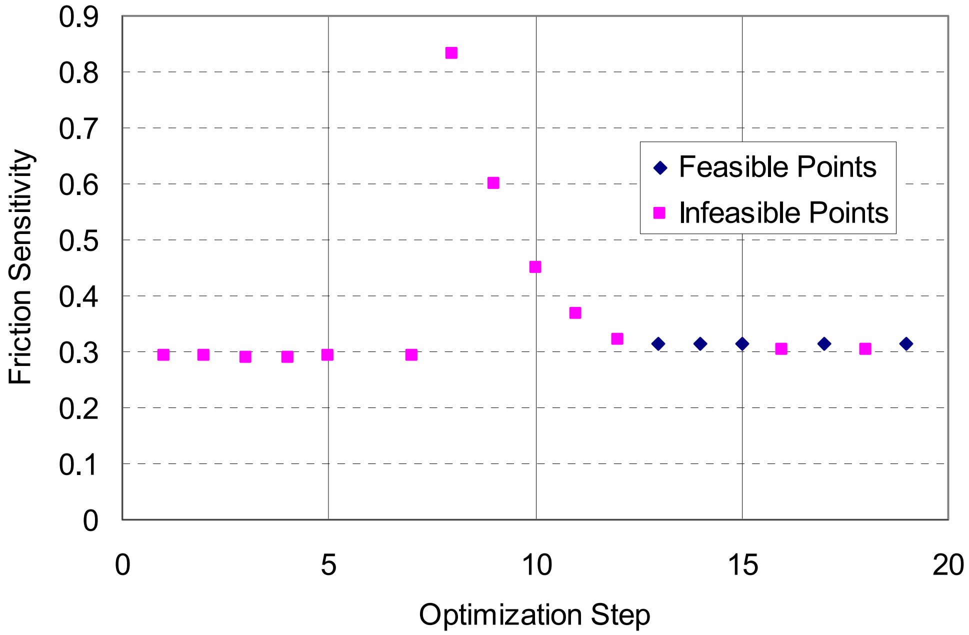

Figure 4.23. Fmincon optimization run using Design 2 as the initial point.

several unsuccessful optimization runs which took several hours to complete but did not significantly improve on the initial design. This is illustrated by the optimization run in Figure 4.23, solved by fmincon by using the Design 2 parameters as the initial point. Each successive point attempted by the fmincon solver is plotted in sequence. It is clear that the friction sensitivity does not improve, and the optimization terminated after trying 19 different points and reaching the edge of the parameter space. Most of the points attempted are not feasible (that is, the acceleration to latch with a friction coefficient of $\mu = 0.3$ is not within 3g of the target acceleration to latch, 100 g) and not a single point has measurably lower friction sensitivity than the initial design.

Genetic algorithms are pseudo-evolutionary models used for optimization in cases when the gradient cannot easily be determined [59]. They are more of a brute-force technique, and very computationally intensive compared to gradient-based techniques. Bounds are applied on the design variables and a population of multiple points is chosen inside the bounds. The objective function (and any constraints) must be calculated for every member of the population. The results are used to create a new population through mutation and cross-breeding. Each successive population is called a generation. The mutation and cross-breeding favor the fittest members of the population, theoretically improving the population with each successive generation. The quality of the results depends strongly on the population size and the number of generations used. The randomness of the cross-breeding and mutation help ensure that the optimization does not get stuck at local minima.

Given a sufficiently high number of points in the population and enough generations, a genetic algorithm stands a very good chance of success even for problems (like this one) that are challenging for gradient-based techniques. The genetic algorithm was initially more successful than fmincon, although each generation of the genetic algorithm can take several hours to evaluate the constraints and objective function. The genetic algorithms were run using the vectorized population option, in which the genetic algorithm function passes the entire population to the objective function at once rather than in sequence. This allows the use of the MATLAB parallel for loop construct, in which multiple processing cores can be used to independently and simultaneously evaluate different members of the population. These simulations were run on the Army Research Laboratory's (ARL) high performance computing center's supercomputer. ARL's MATLAB license has a limit of 8 processors, so this effectively speeds up the computations by a factor of 8. Even so, with a population of 100 (which may even be low given the 6 different

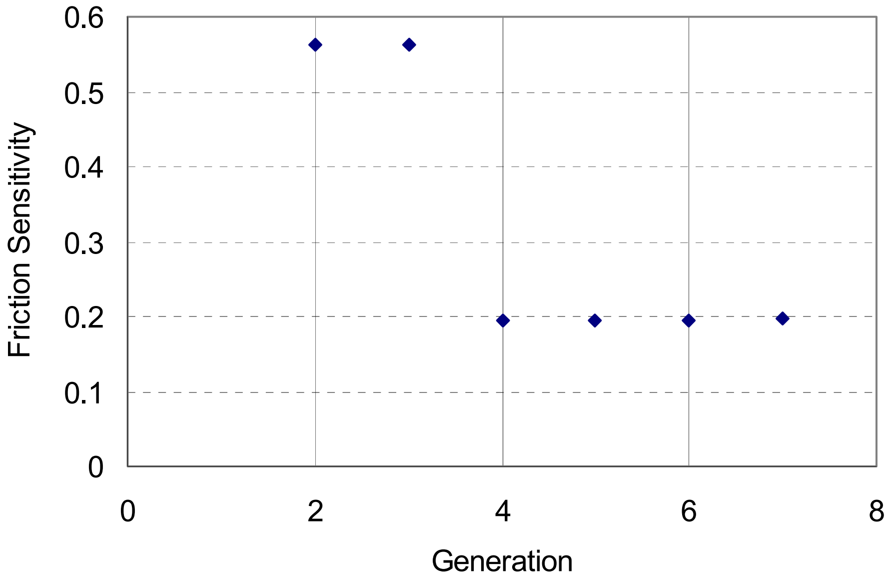

Figure 4.24. Best value of objective function (friction sensitivity) from first 7 generations of genetic algorithm by using 100 points in population. The first generation had no feasible points.

independent design parameters used) each generation took over 12 hours to evaluate on the supercomputer.

The results obtained for the first seven generations, with the initial population generated by the random uniform distribution function provided by MATLAB (genetic algorithm option CreationFcn set to @gacreationuniform), are shown in Figure 4.24. There was essentially one step improvement in friction sensitivity, from about 0.56 in generation 3 to about 0.19 in generation 4. This is somewhat of an improvement on the 0.3 friction sensitivity of the Design 2 sensor and that found by the first fmincon optimization run.

Given the time required for the genetic algorithm runs, the author decided to try using the best point from the genetic algorithm as a starting point for another fmincon optimization rather than run the genetic algorithm for more iterations. (While it was unknown to the author at the time of running the simulations, the use of a

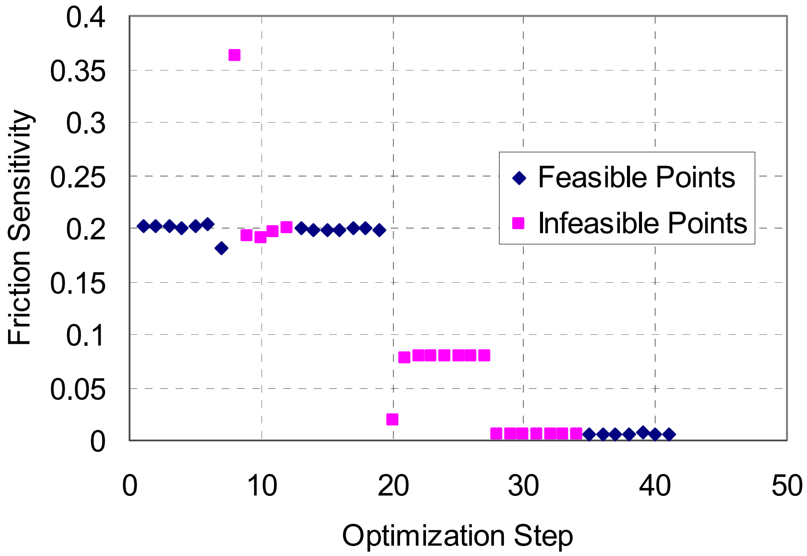

Figure 4.25. Fmincon optimization run using best point found from genetic algorithm as starting point.

genetic algorithm to find promising directions and then following it with the gradient-based fmincon tool is now an automated option (beginning with MATLAB R14 service pack 3). This is available by setting the Hybrid Function option of the genetic algorithm solver to fmincon). It had also become clear from studying the genetic algorithm results that the thickness of the sensor had no effect on the latch threshold or the friction sensitivity (this is because both the mass and stiffness scale linearly with thickness and effectively cancel each other out), so that parameter was removed from consideration. The results are shown in Figure 4.25. This time, the fmincon function succeeded at improving the friction sensitivity dramatically, from 0.19 to 0.006. The final design is feasible and has almost negligible change in the latching threshold when the friction coefficient changes from 0.3 to 0.6 (98g to 98.6g).

The parameter values for this optimized design are given in Table 4.4. The obvious change from Design 2 is the width and length of the latch cantilever – both are taken to the edge of the defined parameter space to minimize the stiffness of the

Table 4.4. Optimized Design for low sensitivity to friction-coefficient changes.

Optimization Parameter	Description	Units	Design 2 value	Optimum Value
t	device thickness	µm	20	20
L_f	length of flexure	mm	1.495	2
W_f	width of flexure	µm	12	20.5
H_m	height of mass	mm	2.025	2.25
w_L	width of latch	µm	8	3
l_L	length of latch	µm	500	600
M	equivalent mass of sensor	µg	265	396
k	equivalent stiffness of flexures	N/m	1.324	2.76
m	equivalent mass of latch	ng	56.4	80
k_L	equivalent stiffness of latch	N/m	4.44	0.1

latch. This minimizes the interaction forces, including the frictional force, as compared to the restoring force of the spring. The stiffness of the suspension springs also increases even though the flexures get longer, because they also get wider. This increases the restoring force at a given deflection, further diluting the effect of the frictional forces on the latching threshold. The size of the mass is increased, which compensates for the increase in stiffness of the flexures and increases the inertia of the sensor before it hits the latches, making it more difficult for the latches to stop the sensor during the contact phase. Each of these changes to the design makes sense, but all of them combine to produce a design that has virtually no dependence on friction. The tradeoff is that the optimized design is about 30% wider and 10% taller than the Design 2 device. Also, the changes in the latch dimensions will make the latch more fragile and more likely to fracture during operation. Notably, neither the genetic algorithm nor the fmincon gradient-based optimization approach arrived at this design on their own – it was only when the two approaches were combined that the optimization study led to a successful completion.

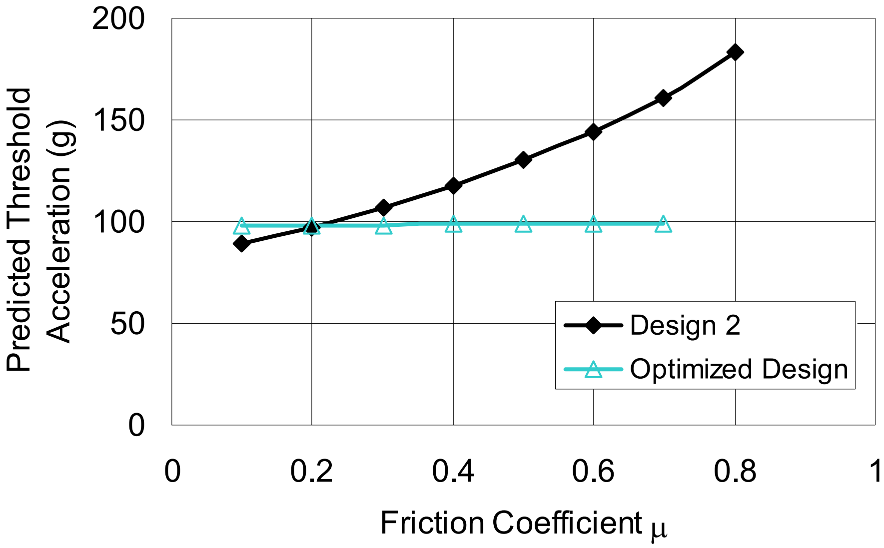

Figure 4.26. Comparison between the sensitivity of Design 2 and optimized design to changes in the friction coefficient. Note that optimized design has almost no change in threshold acceleration over a wide range of friction coefficients.

The changes in the threshold acceleration to latch were calculated for the optimized design over a wide range of friction values and compared to those for Design 2 as a baseline. The results are shown in Figure 4.26. It is clear from the graph that Design 2 is highly sensitive to changes in the friction coefficient, with the acceleration threshold changing by more than a factor of two over the range of $0.1 \leq \mu \leq 0.8$. The threshold for the optimized design changes by less than 2% (increasing from 98.2 to 99.8 g) over the same range. This optimized design will be fabricated and evaluated experimentally in future work.

4.7 V-Beam Actuator Model

The V-beam structure can be modeled by using the same basic procedure as that used for the offset beam actuator, by using the transverse component of the developed force and the actuator stiffness to find the actuator displacement. To develop an analytical expression for the actuator transverse stiffness, Castigliano's

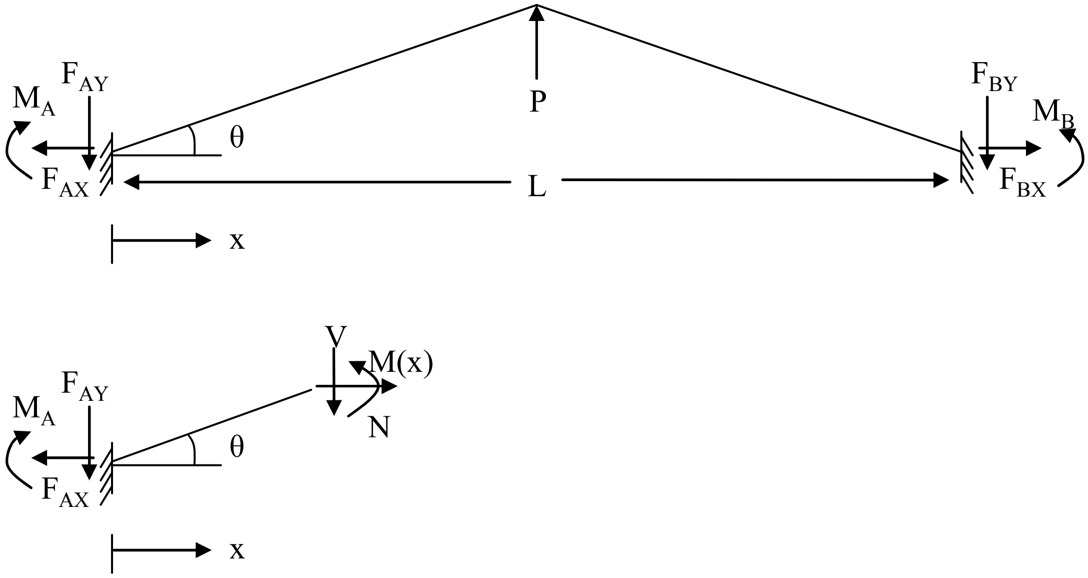

Figure 4.27. Notation and geometry used for V-beam actuator stiffness model.

theorem [60] is employed because the structure is statically indeterminate. Castigliano's theorem can be summarized as the displacement at the point of application of a force in the direction of that force is equal to the partial derivative of the structure's complementary energy with respect to the force. For Hookean materials, the strain energy is equal to the complementary energy, so the relationship becomes

$$u_F = \frac{\partial U}{\partial F} \tag{4.35}$$

where F is the applied force and u_F is the displacement at the point of application of F in the direction of F. Referring to Figure 4.27, the reactions can be solved by recognizing that the displacement and rotation at the clamped ends of the structure are equal to zero:

$$u(0) = \frac{\partial U}{\partial F_{AX}} = 0 \tag{4.36}$$

The general form for the strain energy in a beam is:

$$U = 2\int_0^{L/2} \left(\frac{M^2}{2EI} + \frac{N^2}{2AE} + \frac{(6/5)V^2}{2GA} \right) dx \tag{4.37}$$

where M, N, and V are the internal moment, normal force, and shear in the beam, respectively, E is the Young's modulus of the beam material, A is the cross-sectional area, I is the moment of inertia of the cross-section about the bending axis centroid, and G is the shear modulus of the material. Differentiating Eq. (4.37) with respect to the reaction force F_{AX} leads to

$$\frac{\partial U}{\partial F_{AX}} = 2\int_0^{L/2} \left(\frac{M}{EI}\frac{\partial M}{\partial F_{AX}} + \frac{N}{AE}\frac{\partial N}{\partial F_{AX}} + \frac{(6/5)V}{GA}\frac{\partial V}{\partial F_{AX}} \right) dx \tag{4.38}$$

The internal forces and moments can be determined as

$$\begin{aligned}
V(x) &= \begin{cases} -\dfrac{P}{2} & 0 \le \text{x} \le \text{L/2} \\ \dfrac{P}{2} & \text{L/2} \le \text{x} \le \text{L} \end{cases} \\
N(x) &= F_{AX} \\
M(x) &= \begin{cases} M_A - \dfrac{P}{2}x + F_{AX}x\tan\theta & 0 \le \text{x} \le \text{L/2} \\ M_A - \dfrac{P}{2}(L-x) + F_{AX}(L-x)\tan\theta & 0 \le \text{x} \le \text{L/2} \end{cases}
\end{aligned} \tag{4.39}$$

The derivatives of the internal forces and moments can then be written as:

$$\frac{\partial N}{\partial F_{AX}} = 1, \quad \frac{\partial M}{\partial F_{AX}} = x\tan\theta, \quad \frac{\partial V}{\partial F_{AX}} = 0. \tag{4.40}$$

After substituting these relations into Eq. (4.38), and taking advantage of symmetry to avoid the discontinuity at $x = L/2$, it is found that

$$\frac{\partial U}{\partial F_{AX}} = 2\int_0^{L/2} \left(\frac{1}{EI}\left(M_A - \frac{P}{2}x + F_{AX}x\tan\theta \right) x\tan\theta + \frac{F_{AX}}{AE} \right) dx = 0 \tag{4.41}$$

Integrating and setting (4.41) equal to zero, a relation between the reaction moment and x-direction component of the reaction force can be obtained in terms of the applied axial force P.

$$0 = \frac{1}{EI}\left(\frac{M_A L^2}{8}\tan\theta - \frac{PL^3}{48}\tan\theta + \frac{F_{AX}L^3}{24}\tan^2\theta\right) + \frac{F_{AX}L}{2AE} \tag{4.42}$$

The second equilibrium equation is obtained using the fact that the slope of the deflection profile must be zero at the clamped end. Applying Castigliano's theorem again, leads to

$$\phi(0) = \frac{\partial U}{\partial M_A} = 0 \tag{4.43}$$

The derivative of the strain energy with respect to the reaction moment can be written as:

$$\frac{\partial U}{\partial M_A} = 2\int_0^{L/2}\left(\frac{M}{EI}\frac{\partial M}{\partial M_A} + \frac{N}{AE}\frac{\partial N}{\partial M_A} + \frac{(6/5)V}{GA}\frac{\partial V}{\partial M_A}\right)dx \tag{4.44}$$

From Eq. (4.38), the partial derivatives on the right-hand side of Eq. (4.44) are determined as

$$\frac{\partial N}{\partial M_A} = 0,\quad \frac{\partial M}{\partial M_A} = 1,\quad \frac{\partial V}{\partial M_A} = 0 \tag{4.45}$$

On substituting Eq. (4.45) into Eq. (4.44), and solving Eq. (4.44) results in

$$0 = \frac{M_A L}{2} - \frac{PL^2}{16} + \frac{F_{AX}L^2\tan\theta}{8} \tag{4.46}$$

Combining the two equilibrium equations (4.46) and (4.42), the reactions can be obtained as

$$F_{AX} = \frac{PL^2 \tan\theta}{2L^2 \tan^2\theta + \frac{96I}{A}} \tag{4.47}$$

$$M_A = \frac{PL}{8} - \frac{L\tan\theta}{4}\left(\frac{PL^2 \tan\theta}{2L^2 \tan^2\theta + \frac{96I}{A}}\right) \tag{4.48}$$

Next, the transverse stiffness of the actuator is defined as

$$k = \frac{P}{w\left(L/2\right)} \tag{4.49}$$

Now, Castigliano's theorem can be used one more time to obtain

$$w\left(L/2\right) = \frac{\partial U}{\partial P} = 2\int_0^{L/2}\left(\frac{M}{EI}\frac{\partial M}{\partial P} + \frac{N}{AE}\frac{\partial N}{\partial P} + \frac{(6/5)V}{GA}\frac{\partial V}{\partial P}\right)dx \tag{4.50}$$

After substituting the reaction force and moment into the relations for the internal forces and moments, the partial derivatives on the right hand side can be written as:

$$\begin{gathered}\frac{\partial M}{\partial P} = \frac{L}{8} - \frac{L^3 \tan^2\theta}{8L^2 \tan^2\theta + \frac{384I}{A}} - \frac{1}{2}x + \frac{L^2 \tan^2\theta}{2L^2 \tan^2\theta + \frac{96I}{A}}x, \\ \frac{\partial N}{\partial P} = \frac{L^2 \tan\theta}{2L^2 \tan^2\theta + \frac{96I}{A}}, \\ \frac{\partial V}{\partial P} = -\frac{1}{2}\end{gathered} \tag{4.51}$$

After substituting, integrating, and solving, Eq. (4.50) becomes:

$$\begin{aligned}w\left(L/2\right) = \frac{\partial U}{\partial P} = \frac{PL^3}{48EI}\left(\frac{1}{2} - \frac{L^2 \tan^2\theta}{2L^2 \tan^2\theta + \frac{96I}{A}}\right)^2 + \\ \frac{PL}{AE}\left(\frac{L^2 \tan\theta}{2L^2 \tan^2\theta + \frac{96I}{A}}\right)^2 + \frac{6PL}{20GA}\end{aligned} \tag{4.52}$$

Solving for the stiffness from Eq. (4.49) leads to

$$k = \frac{1}{\left(\frac{1}{2} - \frac{L^2 \tan^2\theta}{2L^2 \tan^2\theta + \frac{96I}{A}}\right)^2 \frac{L^3}{48EI} + \frac{L}{AE}\left(\frac{L^2 \tan\theta}{2L^2 \tan^2\theta + \frac{96I}{A}}\right)^2 + \frac{6L}{20GA}} \tag{4.53}$$

For slender beams, the shear term can be neglected without substantially changing the results. For a straight beam (θ = 0), if the shear term is neglected, this formula converges to the stiffness formula for a traditional clamped-clamped beam [57]:

$$k = \frac{192EI}{L^3} \tag{4.54}$$

By using typical parameters for the V-beam actuators used in this research (Table 4.5), the analytical stiffness values obtained from Eq. (4.53) closely match the finite-element predictions of the stiffness along the entire range of theta from 0 to 4 degrees, and both converge to the clamped-clamped value as the angle is decreased to zero, as shown in Figure 4.28. The match is very good, with a maximum difference between the analytical predictions and finite-element stiffness calculations of 1.2%. Therefore Eq. (4.53) is validated over this range. This is the first reported analytical expression for the stiffness of these common actuators, and may help maximize efficiency.

Table 4.5. Parameters used in FEA and numerical calculations

Parameter	Value
P	100μN
L	1200μm
E	169e9
b	20μm
t	5μm

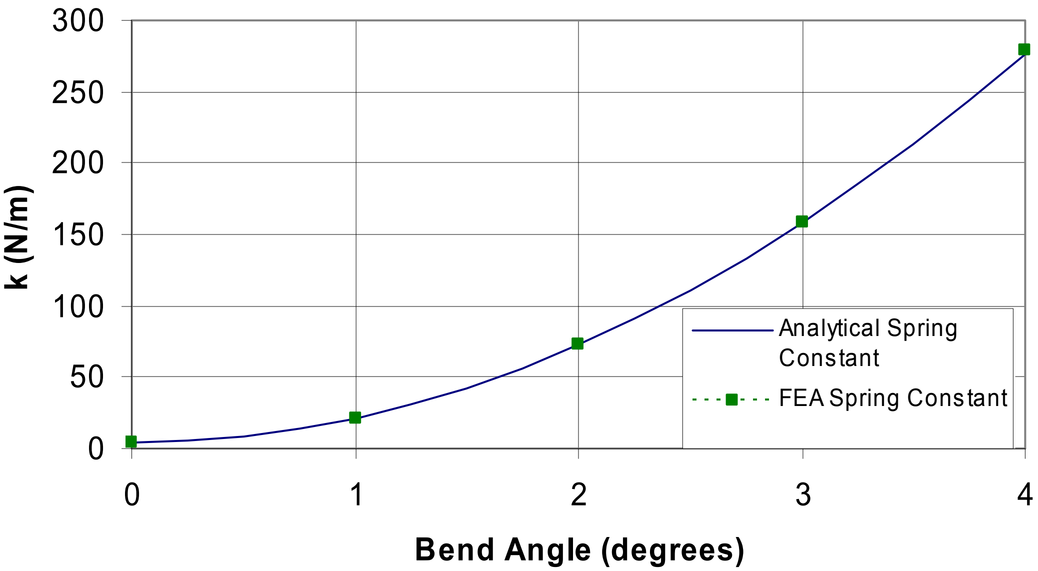

Figure 4.28. Comparison of analytical and finite element spring constants for V-beam actuator.

4.8 Offset-beam Rotational Thermal Actuator Model

The actuators under consideration for this dissertation work are electro-thermal actuators. Current driven through the conductive actuator beams causes Joule heating, which induces thermal expansion. Through geometric constraints, the thermal expansion is amplified and converted into usable motion. The thermal actuators are to be modeled by using an analytical electro-thermal model to calculate the expected free thermal expansion followed by the use of a mechanical strain-displacement model to convert this thermal expansion into actuator displacement.

The electro-thermal model for the offset-beam rotational actuator is developed in a similar manner as in reference [42]. The geometry is shown in Figure 4.29. For the electro-thermal model, it is assumed that there is no temperature variation through the beam cross-section and that convection and radiation effects are negligible effects compared to conduction as has been demonstrated for other microscale thermal

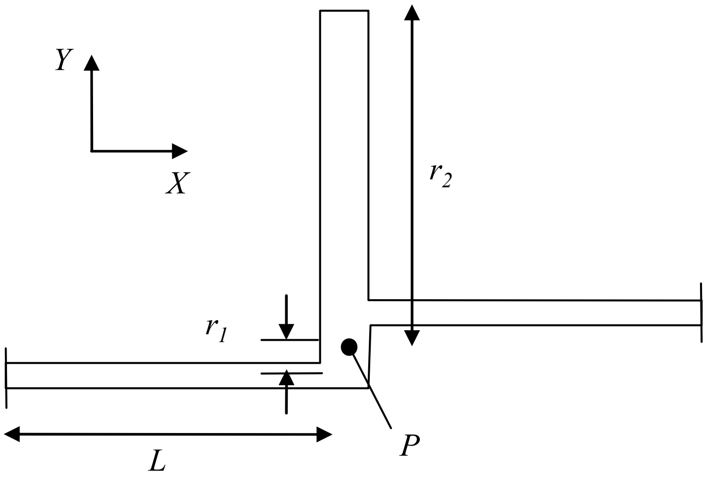

Figure 4.29. Offset beam rotational thermal actuator parameter definition.

actuators [45]. It is further assumed that the anchors remain at the substrate temperature. The rotational actuator is modeled as a beam suspended over a substrate, for which the one-dimensional steady-state heat equation is given by

$$k_s \frac{d^2T(x)}{dx^2} + J^2\rho - Sk_a \frac{T(x)-T_\infty}{gh} = 0 \tag{4.55}$$

where x is the variable along the direction of heat flow. The first term in Eq. (4.55) corresponds to heat flow into the element from the adjacent elements, the second corresponds to heat generation in the element via joule heating, and the final term corresponds to conductive heat flow from the element through the surrounding air into the substrate. The parameters in this equation are as defined in Table 4.6.

The shape factor S in equation (4.55) describes the ratio of heat loss from the bottom of the beam to the sides of the beam. Examining a cross-section of a thermal actuator, the shape factor can be expressed in terms of the geometric parameters, the applied current and resistivity, and the temperature difference between the substrate and the beam cross-section as

Table 4.6. Electro-thermo-mechanical model parameter definition

Parameter	Definition
α	thermal expansion coefficient of silicon
ρ	electrical resistivity of silicon
g	Air gap between beam and substrate
h	height of beam
J	current density in beam
k_a	thermal conductivity of air
k_s	thermal conductivity of silicon
L	length of actuator
S	thermal shape factor
T_∞	ambient temperature
w	width of beam

$$S_{FEA} = \frac{J^2 \rho h}{g\left(T - T_\infty\right)} \tag{4.56}$$

An empirical expression for shape factor was extracted from finite element simulations by Lin and Chiao for a polysilicon beam suspended over a substrate in [61], but this does not scale up to beam heights of 10 μm or more. Maloney used a similar technique to derive the following expression for shape factor for 50 μm thick SOI beams [43]:

$$S = \frac{4}{w}\left(g + 1\times 10^{-6}\right) + 1 \tag{4.57}$$

This expression does not include the beam height, and is therefore only useful for beams exactly 50 μm height. The same technique has been applied in this dissertation work to develop a more general relationship that can be used for many different beam heights. Beam heights of 10-50 μm were used, along with gaps from 0.25-3 μm and beam widths of 2-20 μm. The new shape factor approximation derived from this parametric study includes the beam height, and reduces to Maloney's shape factor when a beam height of 50 μm is used:

$$S = \frac{4}{w}\left(g + \frac{h}{50}\right) + 1 \qquad (4.58)$$

This relationship approximates the shape factor calculated from the finite-element analysis to within 5% for beam height to gap ratios in the range of 7 to 40 with less than 5% error (see Figure 4.30).

Equation (4.55) must be solved iteratively because the thermal conductivity of silicon, the thermal conductivity of air, and the electrical resistivity of silicon are all temperature dependent. The thermal conductivity of silicon has previously been as a function of temperature is approximated in reference [62] as

$$k_s(T) = e^{-1.28\ln T + 12.28} \quad \text{[W/mK]} \qquad (4.59)$$

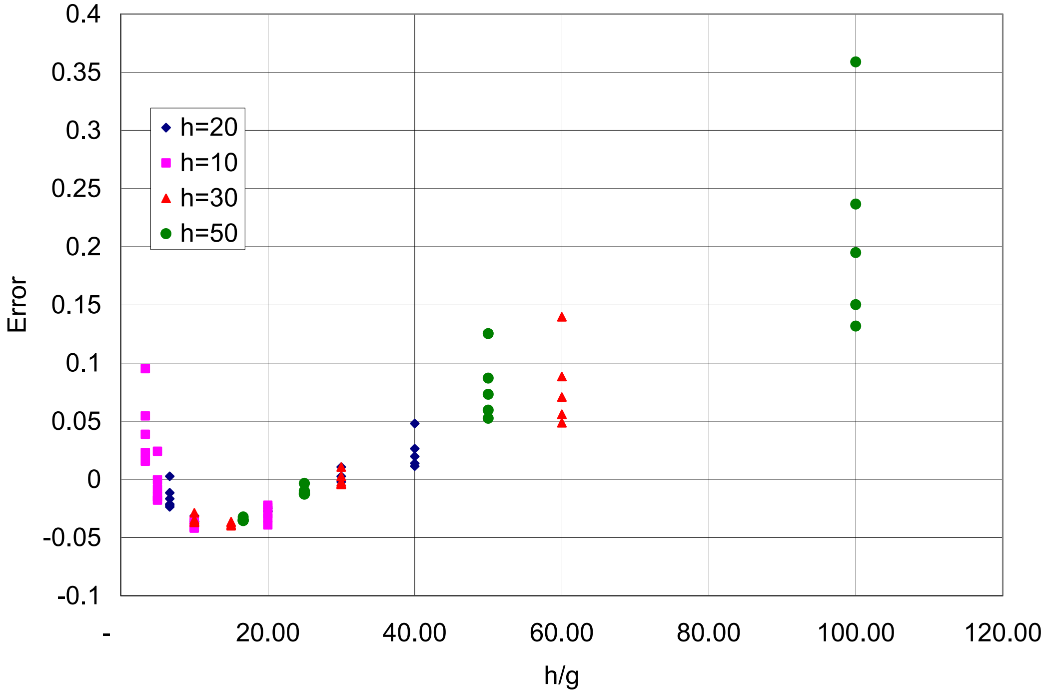

Figure 4.30. Error in shape factor approximation with respect to finite-element calculations.

A table with thermal conductivity of air at various temperatures is given in reference [63]. Applying a second-order polynomial fit to these values, the thermal conductivity of air can be approximated within 1% over the range of 100K to 950K as

$$k_a(T) = -3.06 \times 10^{-8}\,\mathrm{T}^2 + 9.62 \times 10^{-5}\,\mathrm{T} + 1.05 \times 10^{-4} \ \ [\mathrm{W/mK}] \tag{4.60}$$

The temperature dependence of the electrical resistivity of the low resistivity silicon used to make the actuators was measured using an offset-beam actuator. The device was wirebonded to an electronic package and placed on a hotplate. The temperature of the hotplate was increased gradually and the resistance of the device was measured at various temperatures. Because the temperature of the hotplate and the silicon are not the same, a thermocouple with digital readout was placed in contact with the top of the silicon chip. The temperature/resistance profile is shown in Figure 4.31. As can be seen from the chart, the first cycle displays a resistance drop

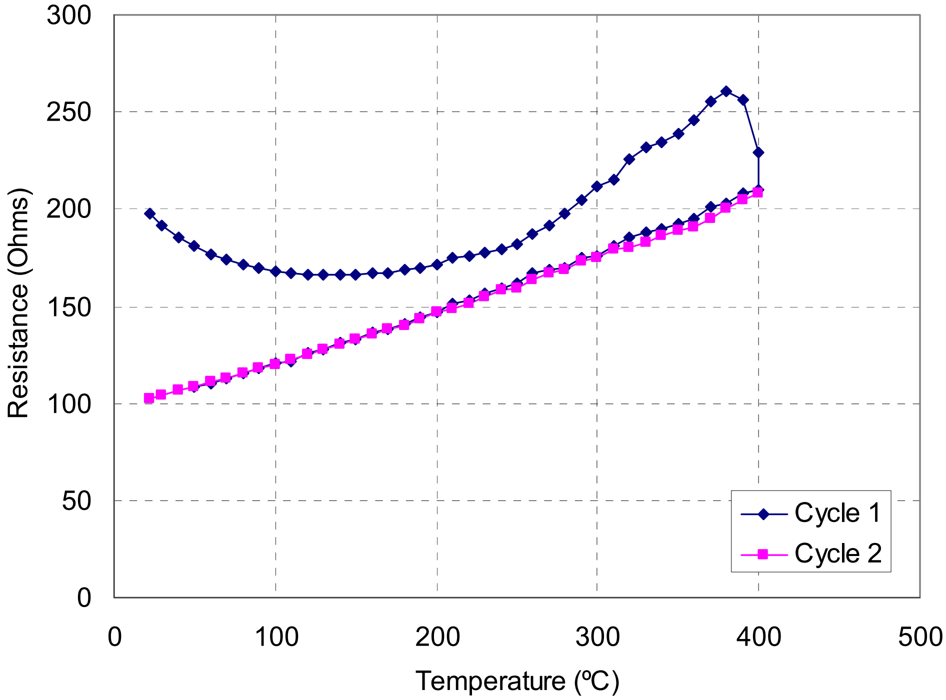

Figure 4.31. Temperature dependence of resistance for an offset beam actuator.

as the temperature increases up to 150ºC, then the resistance begins to increase as expected for silicon. This is due to annealing of the contacts, decreasing the contact resistance. The resistance was measured during cooling of the hotplate as well, and the cooling trend follows a linear slope. A second cycle of heating and cooling follows the cooling trend of the first cycle very closely. The temperature coefficient of resistivity is found by using the device dimensions to convert the data to resistivity, then finding the slope of the temperature-resistivity plot. While the resistivity may vary somewhat from wafer to wafer, the temperature coefficient of resistivity is expected to be relatively stable. The temperature coefficient of resistivity found from this data was $4.7\text{x}10^{-8}$ Ω-m/K.

Without knowledge of the final temperature distribution, the precise values of the thermal conductivity of air and silicon as well as the electrical resistivity of silicon are unknowns; hence, equation (4.55) cannot be solved directly. An iterative solution procedure must be used by assuming an initial temperature distribution and corresponding values for the thermal conductivities, then calculating the temperature distribution by using those thermal conductivity values, updating the thermal conductivity values, and repeating this process until the temperature change from step to steps is negligible. A finite difference approximation to equation (4.55) which allows such an iterative solution procedure can be written as

$$\frac{T_{i+1}+T_{i-1}-2T_i}{(\Delta x)^2}-\frac{Sk_a}{k_s gh}T_i=-\frac{J^2\rho}{k_s}-\frac{Sk_a}{k_s gh}T_\infty \tag{4.61}$$

where the subscript i, i-1, and i+1 correspond to the current element, the previous element, and the adjacent elements. Equation (4.61) can be solved using the matrix inversion technique presented in reference [63] with the material properties updated at each element based on the temperature calculated for that element in the previous iteration. A uniform temperature of 298K can be assumed for the first iteration. The convergence criteria is subjective, but a maximum temperature change of any element of less than $1\text{x}10^{-3}$ K from one step to the next is a reasonable criterion, and this is typically achieved in 6 to 8 iterations.

The thermal expansion over an actuator beam is then calculated as

$$\delta = \alpha \int_0^L \left[T(x) - T(\infty) \right] dx, \tag{4.62}$$

where the thermal expansion coefficient of silicon, α, is also a temperature-dependent material property that can be approximated as [64]

$$\alpha(T) = 3.725 \times 10^{-6} \left(1 - e^{-5.88\times10^{-3}(T-124)} \right) + 5.548 \times 10^{-10} T \quad \left[\text{K}^{-1} \right] \tag{4.63}$$

Because the temperature distribution is discrete due to the approximation of the beam as a set of elements, a trapezoidal rule approximation is used to evaluate the integral (4.62). The temperature of each element is used to assign an element-specific thermal expansion coefficient. Once the thermal expansion is known, an equivalent force which would produce the same increase in length can be determined as

$$F = \frac{\delta E A}{L} \tag{4.64}$$

The actuator stiffness can be derived, and this force can be applied to determine the actuator displacement. For the rotational actuator, the stiffness is obtained by approximating the structure as two clamped-pinned beams connected at the pinned end. An additional stiffness term is used to account for the extension of each beam due to the vertical offset r_1 (see Figure 4.32). The actuation of this device

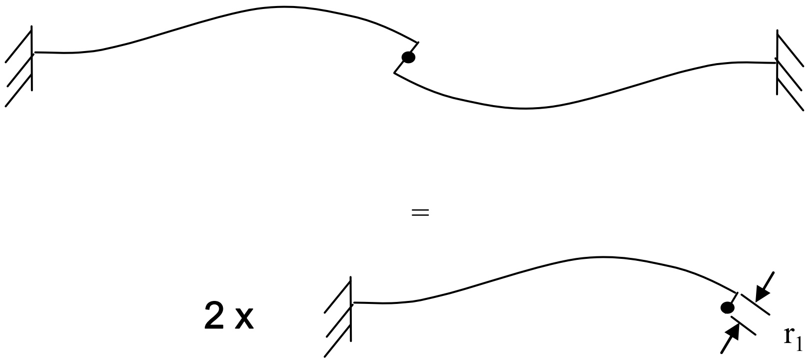

Figure 4.32. Spring constant model for rotational actuator.

is assumed to be due to a pure moment due to symmetry; so the torsion stiffness is used. The torsion stiffness of a clamped-pinned beam is given by

$$k_{cp} = \frac{4EI}{L} \tag{4.65}$$

The torsion stiffness term due to the extension of each beam segment is

$$k_{ext} = \frac{EA}{L} r_1^{\,2} \tag{4.66}$$

The full actuator spring constant is obtained by taking the two spring constants in parallel for each segment, and realizing that the segments are also in parallel with each other the total torsion spring constant is

$$k_\theta = 2k_{cp} + 2k_{ext} = \frac{2E}{L}\left(4I + Ar_1^{\,2}\right) \tag{4.67}$$

If used as a translational actuator, the equivalent spring constant is given by

$$k = \frac{F}{x} = \frac{M}{r_2^2 \theta} \tag{4.68}$$

$$k = \frac{k_\theta}{r_2^2} = \frac{2E}{Lr_2^2}\left(4I + Ar_1^2\right) \tag{4.69}$$

The electro-thermal model can be modified for the vacuum case by eliminating the term representing the heat loss through the air into the substrate. Equation (4.55) then becomes

$$k_s \frac{d^2T(s)}{ds^2} + J^2\rho = 0. \tag{4.70}$$

The solution to (4.70) can be found by separating variables and applying the boundary conditions $T = T_\infty$ at $s = 0, L$.

$$T(s) = -\frac{J^2\rho}{2k_s}s^2 + \frac{J^2\rho L}{k_s}s + T_\infty \tag{4.71}$$

The resulting thermal expansion and free angular deflection in each actuator beam under vacuum conditions become

$$\delta = \frac{\alpha J^2 \rho}{k_s}\left(\frac{L^3}{6}\right) \tag{4.72}$$

$$\theta = r_1 \frac{2E^2 A\alpha J^2 \rho L}{3k_s}\left(4I + Ar_1^{\,2}\right) \tag{4.73}$$

For comparison, the temperature profiles for an actuator with L = 400 µm, w = 5 µm are shown in Figure 4.33 under vacuum and atmospheric conditions. The predicted maximum temperature is nearly 90 °C higher in vacuum than at atmospheric pressure with the same applied current. This clearly will result in much larger actuator displacement if the actuator is used at low pressure (for instance, in a vacuum-sealed electronic package).

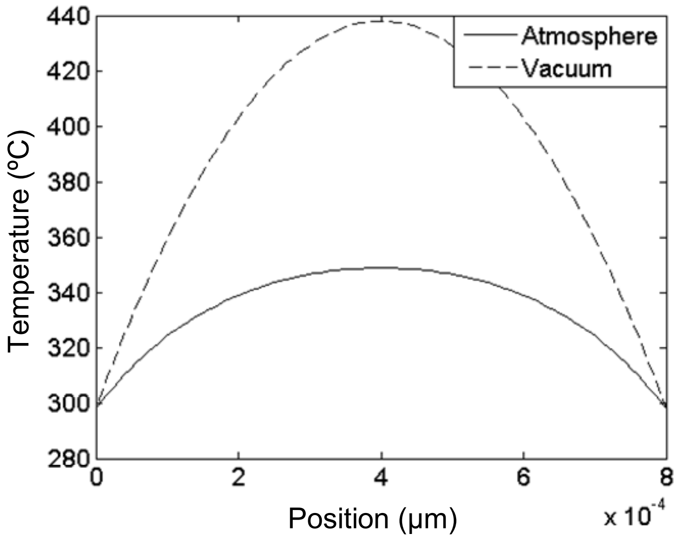

Figure 4.33. Vacuum and atmosphere temperature profiles for an actuator with *L* = 400 μm, *w* = 5 μm, and an applied current of 5 mA.

4.8.1 Parametric Studies of Rotational Thermal Actuator

To aid in device design, parametric studies were undertaken using the electrothermo-mechanical model developed above, including the temperature dependent material properties. The geometric parameters h, w, l, and r_1 were each varied, and the results are presented here in terms of free rotation and blocked moment for a constant power consumption of 50mW. Figure 4.34 shows the effect of actuator width w and neutral axis offset r_1 on the free rotation of the actuator. It can be seen that the actuator width w should be minimized within the constraints of the fabrication process in order to maximize the free deflection. This is expected because smaller widths correspond to lower actuator stiffness. There is also clearly an optimum value of the offset r_1 once the actuator width w has been determined. This optimum value of r_1 does not depend on the height or length of the actuator beams, and the optimum can be represented by a linear relationship between r_1 and w (see Figure 4.35):

$$r_1 = 0.577w + 0.00105 \qquad (4.74)$$

There is no optimum length or height which maximizes free deflection for a given input power found within the parameter range used (Figure 4.36). *L* was varied from 100 µm to 800 µm and *h* was varied from 10 µm to 50 µm (corresponding to the

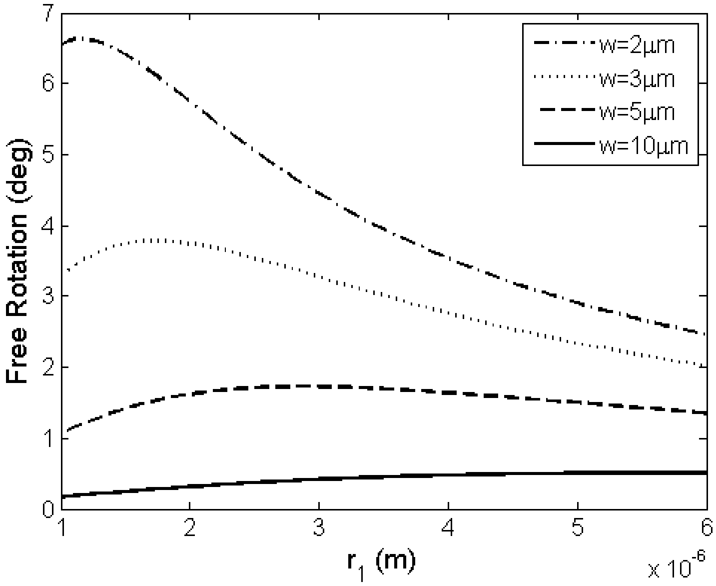

Figure 4.34. Optimization of r_1 for maximum free rotation, with h = 20 µm and L = 400 µm.

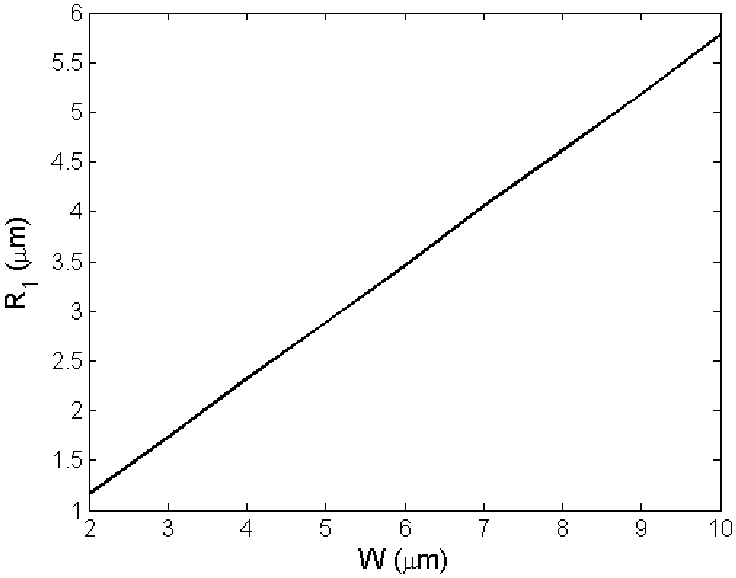

Figure 4.35. Optimum value of netrual axis offset r_1 vs beam width w.

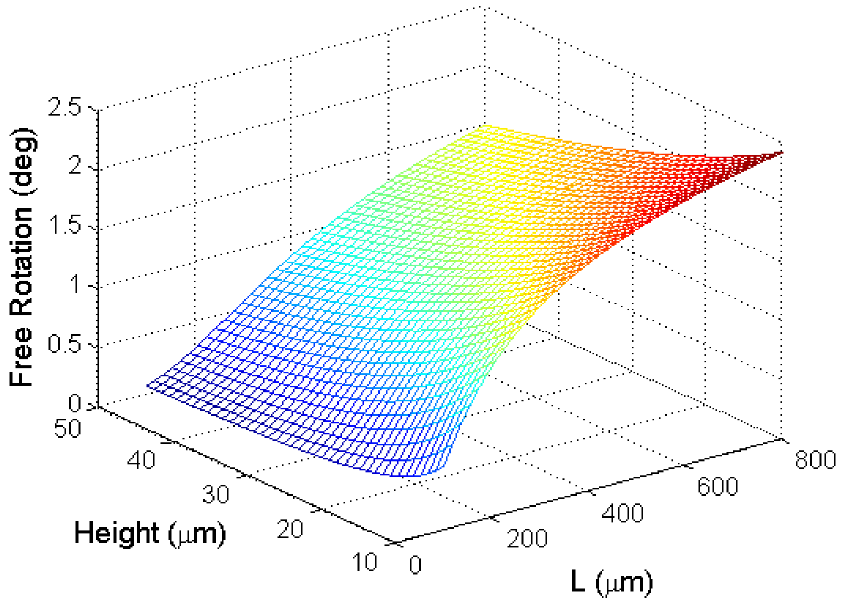

Figure 4.36. Effect of *L* and *h* on free deflection, at constant 50 mW power.

height range over which the shape factor approximation was found to be valid). From anywhere in the parameter space, increasing the actuator length or decreasing the actuator height gives a corresponding increase in free deflection. These trends correspond primarily to decreasing the actuator stiffness, which is expected to result in larger free deflections.

When optimizing for maximum blocked moment at constant driving power, the results are somewhat more complicated. An optimum length to height relationship is found which can be fit with a quadratic curve, but the optimum length/height relationship changes when the width is varied. The relationship is shown for one particular width value in Figure 4.37 and Figure 4.38. The blocked moment is also found to increase linearly with r_1, which directly results from the increase in the moment arm of the actuator.

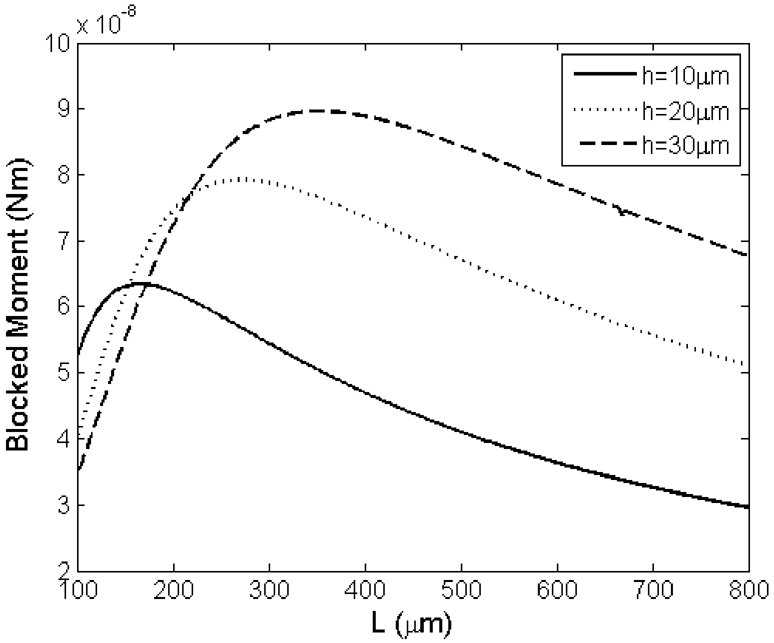

Figure 4.37. Optimization of *L* and *h* for maximum blocked moment, with r_1 = 5 μm and *w* = 5 μm.

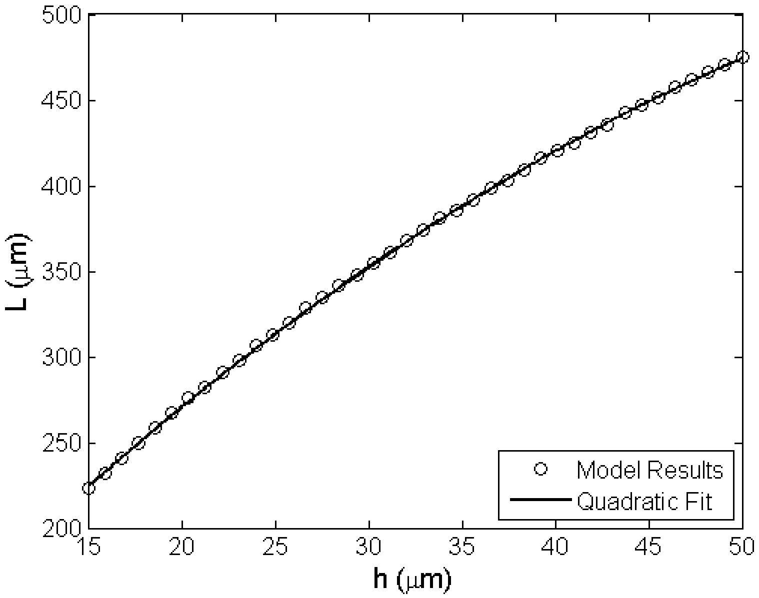

Figure 4.38. Optimum relationship between *L* and *h* for *w* = 5 μm, r_1 = 5 μm.

The possible failure modes of the actuator when overdriven are buckling (as if both beams are in line), fracture of the actuator beam due to exceeding the fracture stress, or plastic deformation at temperatures above about 550ºC [65, 66]. In testing, free deflection was generally limited by buckling, as shown in Figure 4.39. Some

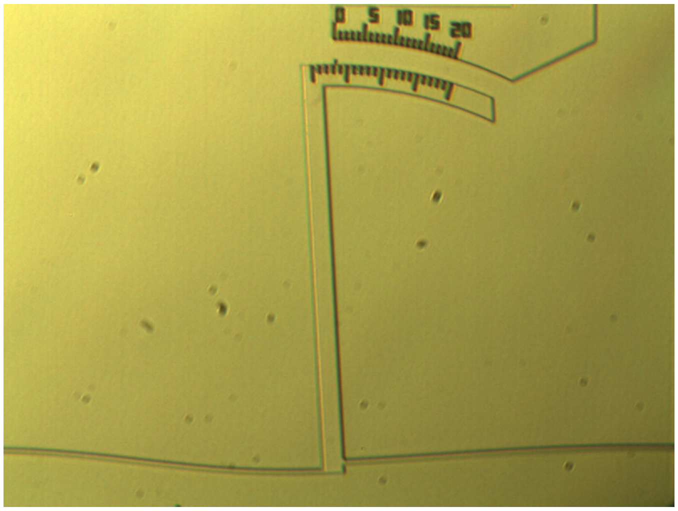

Figure 4.39. Rotational actuator limited by buckling.

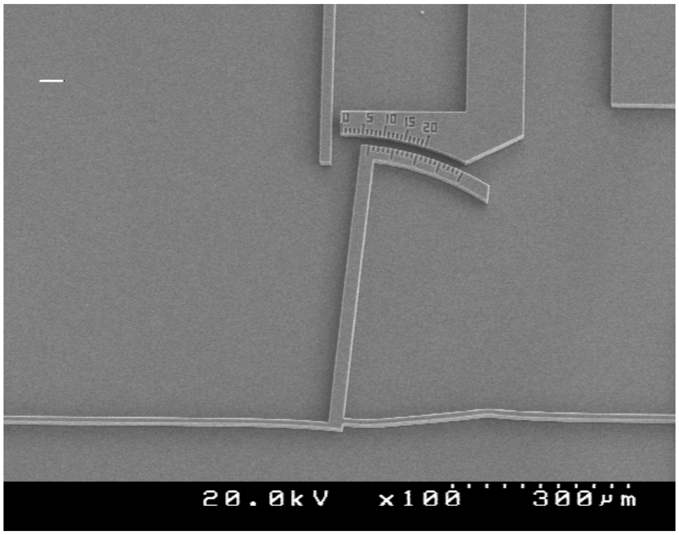

Figure 4.40. Plastically deformed rotational actuator.

devices did fail with plastic deformation, as shown in Figure 4.40, but this typically occurred when the actuator was driven past the current required for maximum deflection.

The maximum deflection that can be achieved as a function of beam width and length is shown in Figure 4.41. The fracture strength of silicon is taken to be 7 GPa [67]. Plastic deformation is not considered because there is no reliable relationship between yield stress and temperature available. Fracture is expected to

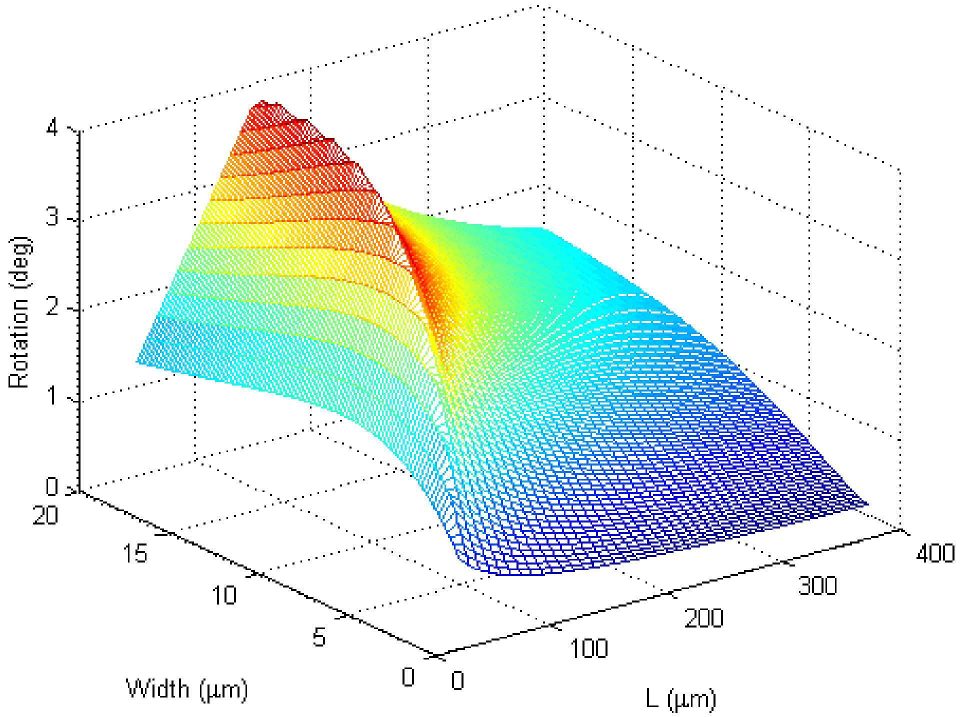

Figure 4.41. Maximum deflection achievable from a rotational actuator as a function of *L* and *w*, with r_1 = 5 µm and *h* = 20 µm.

dominate over buckling at shorter actuator lengths and larger actuator widths, which are less susceptible to buckling. There is an optimum line on the plot that allows maximum deflection before failure if power is not a consideration.

The maximum deflection that can be achieved is also plotted as a function of actuator width and beam offset r_1 in Figure 4.42. *L* and *h* are held constant in this plot, and the predicted failure mode for the entire range of *w* and r_1 is buckling. The optimum ratio of r_1 to *w* is found to be 0.578.

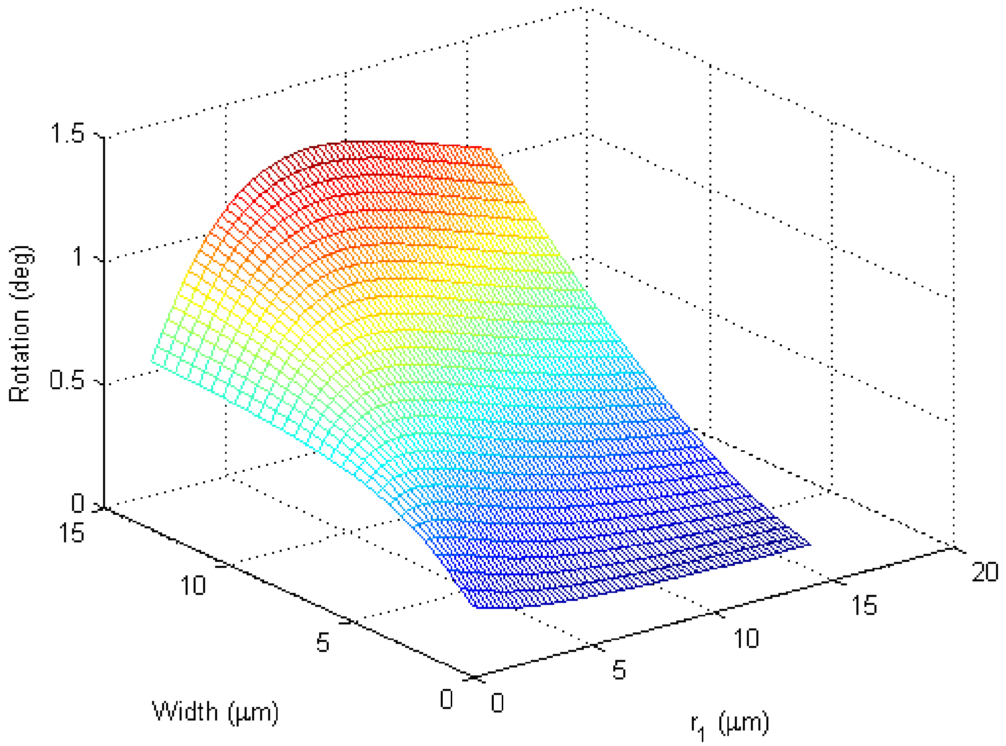

Figure 4.42. Maximum deflection achievable from a rotational actuator as a function of r_1 and w, with L = 500 μm and h = 20 μm.

4.9 Summary and Contributions

In this chapter, reduced-order models have been developed for the shock sensor, the reset actuators, and the friction measurement device. Two models have been presented for the shock sensor, a one degree-of-freedom model that is very efficient to solve, but one which is based on the assumption that the sensor moves smoothly past the latch without losing contact, and a more computationally intensive two degree-of-freedom model that allows for inertia of the latch and loss of contact. Both models attempt to account for interaction forces between the mass and latch, which have been neglected in the previous studies of this class of device [18-24]. Comparisons between the models illustrate that the single degree-of-freedom model, while more realistic than models used in previous work, does not allow for a full representation of the dynamics of latching and the interaction forces. The prediction of loss of contact due to the inertia of the latch by the two degree-of-freedom model is an illustration of an aspect that cannot be captured with the one degree-of-freedom model.. This phenomenon has not been predicted before in latching acceleration switches because of the limitations of the single degree-of-freedom approach.

Parametric studies of the effect of changing various design parameters on the two degree-of-freedom model predictions were also presented as a quick-reference tool for future designs of latching acceleration switches. An optimization approach was presented and used to optimize the design to reduce the sensitivity to changes in friction coefficient that can result from variations in the sidewall roughness of fabricated devices. The optimized design is predicted by the model to result in negligible changes in the acceleration threshold over a wide range of friction coefficients. This is expected to result in significantly more repeatable experimental results, which has been one of the barriers to carry out a wide study of latching MEMS devices.

An electro-thermomechanical model was also presented for the rotational thermal actuator proposed in Section 2.2. This builds on previous models of thermal actuators by accounting for the temperature dependence of thermal expansion coefficient of silicon and by presenting a more general estimate of the shape factor that describes the loss of heat through the sides and bottom of the thermal actuators than presented in previous work [43, 61]. Parametric studies of the actuator design were also presented as a design tool for future versions of this type of actuator.

Finally, a closed-form expression for the stiffness of a bent-beam actuator has been presented. Since optimal actuator performance occurs when the stiffness of the actuator is matched to the stiffness of the resisting load, this is a valuable design tool. While these actuators are quite common in MEMS devices, a simple closed-form expression for the stiffness has never been reported before.

Taken together, the models, parametric design and optimization studies presented in this chapter provide a complete framework for the design of MEMS latching shock sensor systems.

5. Results and Discussion

In this chapter, comparisons between the experimental measurements and model predictions are made for the shock sensor and the thermal actuator for the purpose of verifying the proposed models. Portions of this section have been adapted from the author's journal articles on the latching MEMS shock sensor [38, 48] and the rotational actuator [39].

5.1 Shock Testing Model Fit

To explore the changes in the sensor response observed over multiple cycles, the average acceleration to latch measured over the first 50 cycles was compared to model results. There are no position time-histories for these measurements, and only the minimum acceleration required to latch the sensor was measured. The effective friction coefficient (μ) in the model was changed to obtain the same threshold acceleration values observed in the experiments. All other parameters were kept fixed from cycle to cycle in the model, and the parameters used in the model are shown in Table 5.1. The two degree-of-freedom reduced-order model presented in Section

Table 5.1. Parameter values used in simulations of reduced-order model.

Geometric Parameters		**Calculated Parameters**	
t	20 µm	k (Design 1)	0.529 N/m
w	11 µm	k (Design 2)	
w_L	7 µm	k_L	2.98 N/m
L_f (Design 1)	1945 µm	M (Design 1)	342 µg
L_f (Design 2)	1495 µm	M (Design 2)	265 µg
L_L	460 µm	m	97 ng
r	40 µm	**Material Properties**	
d_i	15 µm	E	169 GPa
y_o	150 µm	density	2.33 g/cm^3
n	5		
p	4		

4.2.2 was used to obtain the results presented in this section.

The widths of the springs and latches is an important parameter because deviations have a significant effect on the results. The average width was found by matching the first cycle results for Design 1 and Design 2 devices from the same wafer, and was about 1μm narrower than the designed values. All of the other parameters values correspond to the design values. The resulting friction coefficient fits using these parameters are shown in Figure 5.1.

For wafer 1, the effective friction coefficient fit using the Design 1 devices (average threshold data from Figure 3.7) decreased from 0.77 to 0.58 over the first ten cycles (a 25% decrease), and then increased to 0.65. The fit obtained by using the Design 2 devices from the same wafer (average threshold data from Figure 3.8) started at 0.76 and decreased to 0.72 after seven cycles (Design 2 devices were not tested beyond seven cycles because no change was observed in the average threshold acceleration). For Design 1 devices from wafer 2 (acceleration data from Figure 3.6),

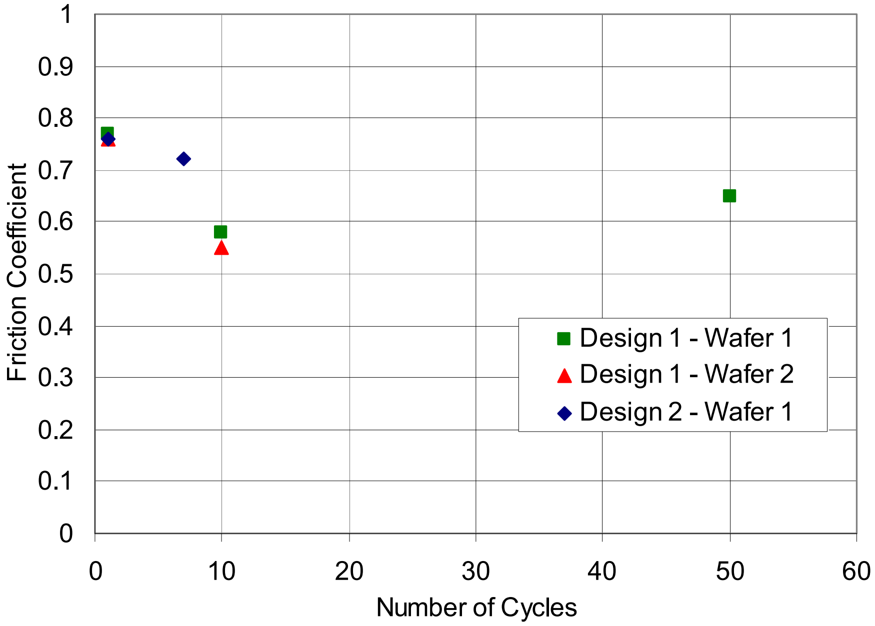

Figure 5.1. Friction coefficients found from model fit.

the effective friction coefficient fit decreased from 0.76 to 0.55 over the first ten cycles.

It is notable that the friction coefficients obtained in this way are nearly identical for Design 1 devices on wafers 1 and 2, indicating good repeatability from wafer to wafer. The values obtained for all devices also match reasonably well with the friction coefficient of 0.7 measured by using the friction test devices discussed in Section 3.3. The friction test devices were produced by using the same fabrication process, and hence, it is expected that the friction coefficients would match. The fact that they actually do match is encouraging for verification of the model.

The 25% decrease in the effective friction coefficient over the first ten cycles for Design 1 devices suggests that contact conditioning of about ten cycles might be required for consistent results from cycle to cycle with this design. This is not as important for Design 2 devices, which are less sensitive to changes in the friction coefficient. Furthermore, measures to eliminate the effect of stiction might be necessary for consistent results after 10 cycles. Since the stiction is most likely precipitated by electrostatic attraction, these could include increasing the gap between the device and the substrate, increasing the thickness of the device layer to increase the out-of-plane stiffness of the springs, or minimizing the effective substrate area under the mass by etching through holes in the substrate.

5.2 Comparison of High-Speed Video Images with Model Predictions

The primary validation of the proposed two degree-of-freedom shock sensor model involved matching the high speed video measurements of the position time-history of the sensor presented in Section 3.1.2. Two different sensors were tested and filmed on high-speed camera, representing two different nominal threshold levels – 50 g (Design 1) and 100 g (Design 2). The only differences between the two designs are the length of the springs and the size of the mass. The width of the springs, the size and stiffness of the latches, and the travel required to latch the sensor are all identical. The video was captured at 4261 frames per second, which is the maximum framerate of our camera with a reasonable pixel resolution.

The parameters used in the model predictions are the same as those used in Section 5.1 to extract the friction coefficients from the repetitive shock cycling experiments. The same 1μm spring narrowing was used for both the springs and the latch, with all other parameters kept as designed. The damping coefficients for the sensor and latch extracted from the harmonic measurements were also used in the model predictions. The friction coefficients extracted in Section 5.1 did not give a reasonable match to the experimental data, perhaps because the high speed video measurements were performed on devices from a different wafer. The model response was therefore obtained using different values of the friction coefficient for Design 1, and the closest match was obtained with a friction coefficient of $\mu = 0.1$. This value was then also used for the Design 2 comparison of the model prediction to experimental results.

The various frames from one high-speed video capture for the Design 1 sensor are shown in Figure 5.2 along with line drawings of the latch interaction generated using the two degree of freedom model results at the same timesteps. The timesteps are shown on the line drawings and correspond to the framerate of the high-speed video capture. An examination of the line drawings and the high-speed video frames shows a very good qualitative agreement between the two, including an identical number of frames with the mass contacting the latch (frames 9-11) before pushing past.

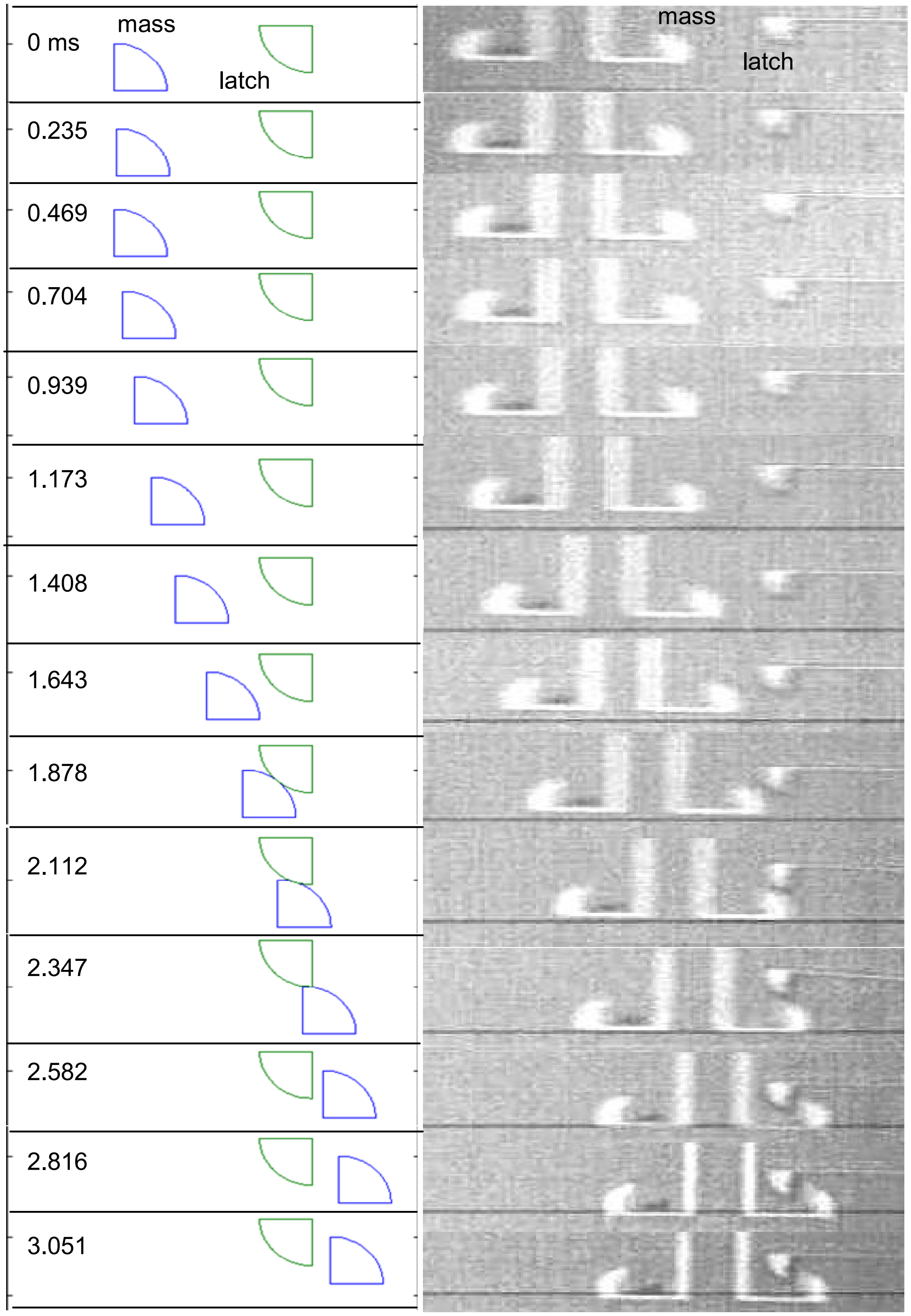

Figure 5.2. Time-stamped images generated from model results and from high-speed video for Design 1 sensor.

For a quantitative measure of the model performance, the model results were also compared with the relative motion of the mass extracted from the high-speed video. The results are shown in Figure 5.3 and Figure 5.4 for the Design 1 sensor and the Design 2 sensor, respectively. A friction coefficient of $\mu = 0.1$ was used for the comparison. The model of the Design 1 sensor matches the high-speed video measurements very well. There are not as many data points from the high-speed video for the Design 2 sensor because the response is faster, and the match is not quite as good as the Design 1 sensor. However, the overall time to latch matches well and the predicted position before latching is fairly close to the high-speed video results, although outside the error bars for the third and fourth frames. Altogether this confirms that the model predicts the device performance very well.

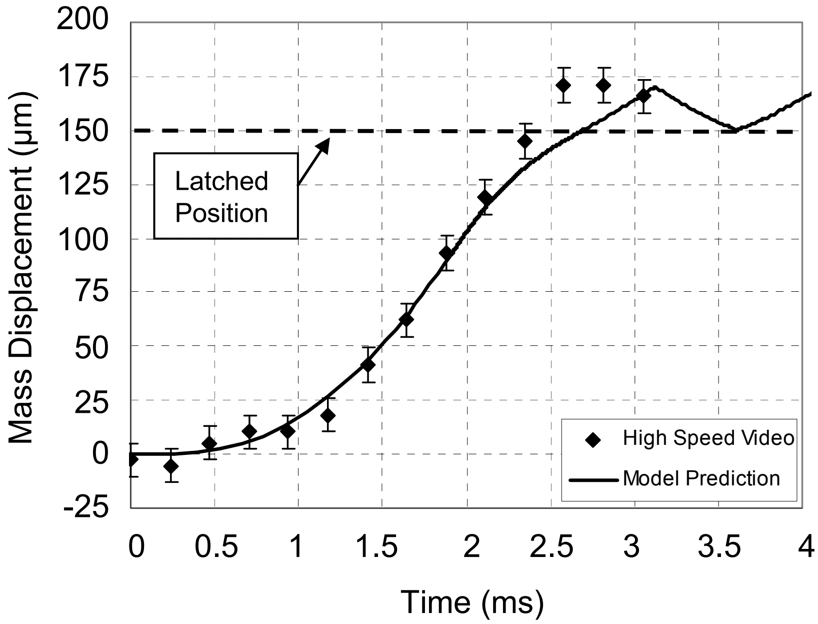

Figure 5.3. Comparison of model with high-speed video for Design 1 sensor.

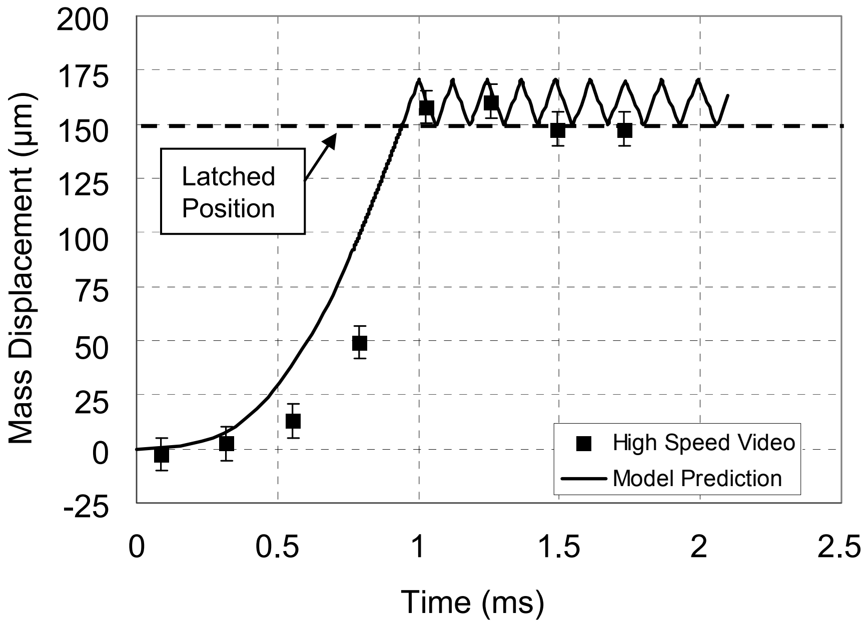

Figure 5.4. Comparison of model with high-speed video for Design 2 sensor.

5.3 Experimental Confirmation of Latch Bounce Effect Observed in Model

Regarding the loss of contact, or bounce of the latch predicted by the two degree of freedom model in Section 4.2.2, there is no confirmation of this in the high-speed video measurements because the magnitude and duration of the bounces are too small to be captured (0.5 µm and 7 µs for the Design 1 sensor). The video resolution is about 2.5 µm/pixel and the time between frames is 0.23 ms, both of which are much too large to enable visualization of any bouncing that might be occurring.

It is possible to confirm bouncing electrically, however. Recall that in the standard design, the flat surface of the latch is coated with metal to give a low resistance contact after the device has latched (see Figure 3.17). The rounded surface is typically uncoated to ensure that the electrical circuit does not close until the device has fully latched. By switching this metallization scheme and coating the rounded latch surface with metal instead of coating the flat latch surface, physical contact can be electrically monitored during the phase when the mass is sliding past the latch. This was accomplished by constructing a voltage divider circuit similar to that used for the electrical characterization of the latch performance in Section 3.1.3. This time a 10kΩ resistor was used in place of the 1MΩ resistor. The resistor was connected to one latch and grounded at the other end. The other latch was connected to a 5V DC power supply and the voltage across the 10kΩ resistor was monitored on an oscilloscope at 10MHz sampling frequency. When the two curved surfaces of the latch and mass come into contact, the 5V source is connected to ground through the contact resistance of the latches and the 10kΩ resistor. The voltage drop across the 10kΩ resistor depends on the latch resistance. The lower value resistor (10kΩ as opposed to 1MΩ) makes the output voltage more sensitive to contact resistance changes, to illustrate variations in the contact pressure.

One representative result showing the measured acceleration pulse (low-pass filtered at 400Hz) and the output voltage from the contact monitoring signal is shown in Figure 5.5. In this plot, the acceleration profile is from the data acquisition system provided with the shock table because there is included signal conditioning for lower noise. The output voltage is taken from an oscilloscope because the sampling rate of the data acquisition system is only 40kHz. To reduce the amount of data from the contact monitoring circuit, the periods before first contact and after the last contact have been reduced to the zero in the plot. The arrows in Figure 5.5b indicate times where contact is established/re-established after a bounce. At least 6 events are detected, with two other possible events where the voltage is only slightly above the noise floor. In addition, two of the events (at 2.35 ms and 2.4 ms) contain multiple

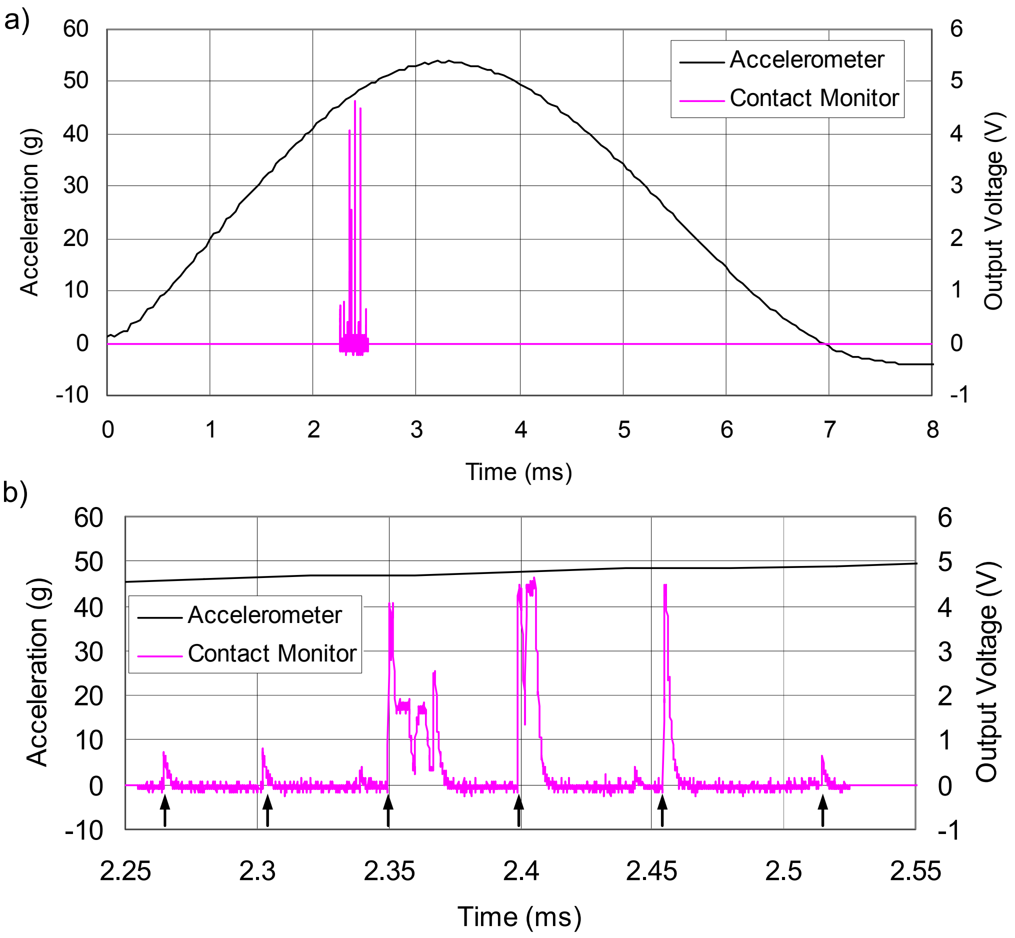

Figure 5.5. Electrical monitoring of contact of latch for a Design 1 sensor: a) full time history, and b) expanded view of contact period. Positive spikes in voltage indicated the latch is in contact with the mass, zero voltage indicates no contact. Arrows indicate contact is reestablished after a bounce.

voltage oscillations even though the voltage never goes to zero in between. Qualitatively, these results confirm both the model predictions of latch bounce with loss of contact and contact force oscillations without loss of contact.

5.4 Rotational Thermal Actuator Results

The electro-thermal model predictions determined on the basis of Eqs. (4.62) and (4.68-4.69) are plotted along with the experimental data in Figure 5.6 and Figure 5.7, and there is good agreement in all cases. The model predictions are compared

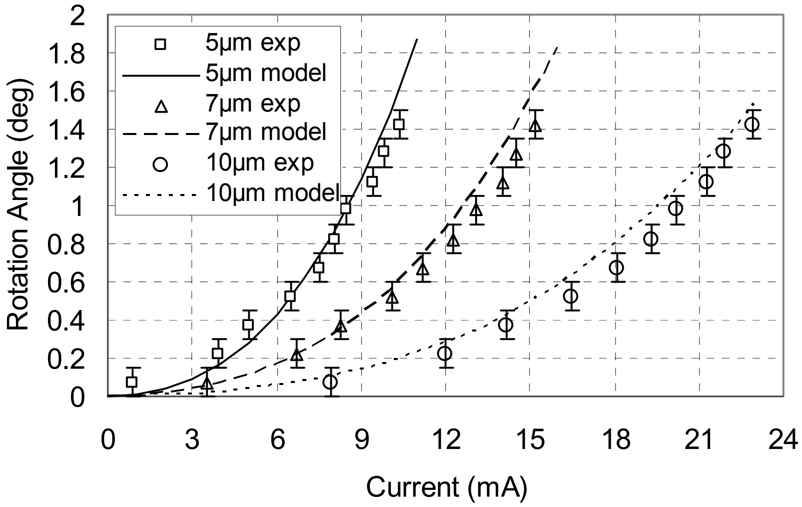

Figure 5.6. Comparison of model free deflection predictions with experimental data: Actuators with *L* = 400 µm and varying actuator beam widths.

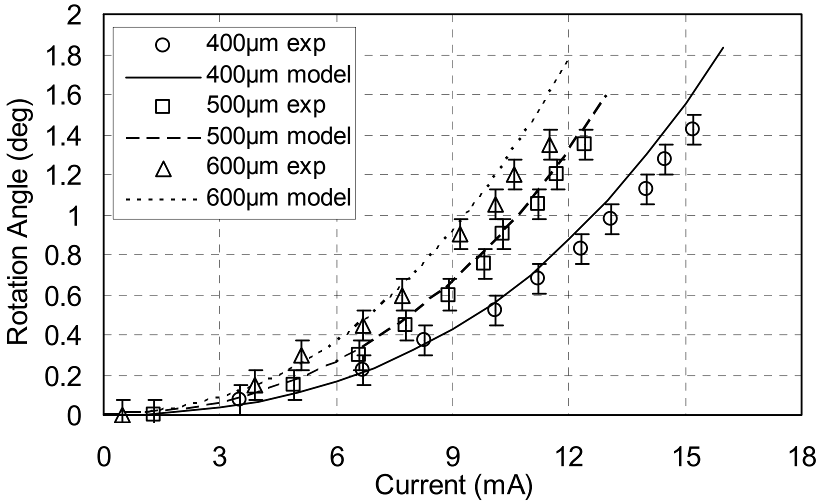

Figure 5.7. Comparison of model free deflection predictions with experimental data for actuators with *w* = 7 µm and varying actuator beam lengths.

with experimental results for 400 µm actuator beam lengths with the three different actuator beam widths in Figure 5.6. The data for different actuator beam lengths with a fixed beam width of 7 µm are compared to the model predictions in Figure 5.7. The experimental error is assumed as one-half of a vernier gradation, or 0.075 degrees of rotation.

The measurements match the model predictions fairly well. The experimental results deviate most from the model for the case when the beam width *w* is 10 µm. This is likely because the measured actuator stiffnesses for 10 µm beams do not match very well with the analytically determined spring constants (see Figure 5.8). The trends in Figure 5.6 and Figure 5.7 illustrate that, for a given applied current, the actuator rotation angle increases with decreasing beam width and increasing beam length. Both of these trends are tied to the decreasing actuator stiffness; this means that to minimize power and maximize deflection performance for low resisting loads, the actuator stiffness should be low. For the tested devices, the free deflection benefit of a less wide actuator is much larger than the benefit of a longer actuator.

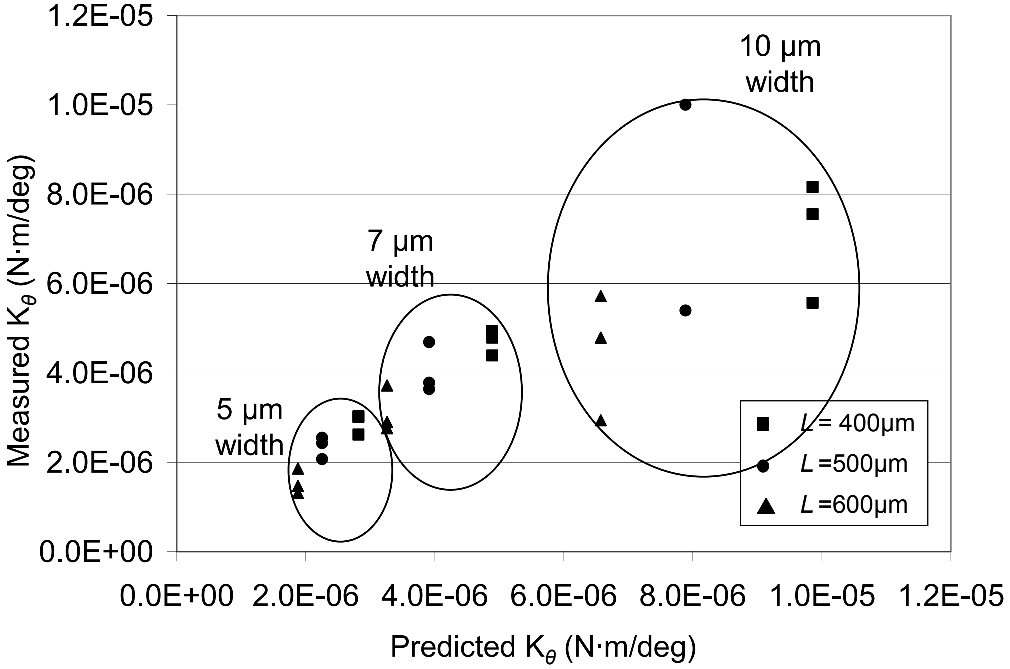

Figure 5.8. Predicted versus measured torsional stiffness for the rotational offset-beam thermal actuators.

5.5 Summary and Contributions

Comparisons between experiments and model predictions have been presented in this chapter. First, the two degree-of-freedom model was validated by using repetitive shock cycling data and effective friction coefficients extracted from the model. The results showed good agreement between the effective friction coefficients for Design 1 and Design 2 devices on the same wafer, and between Design 1 devices from two different wafers.

Next the high-speed video experiments were compared to model predictions with a good match for Design 1, and a reasonable match for Design 2 devices. The caveat is that the friction coefficients extracted by fitting the repetitive cycling acceleration threshold data were significantly higher than those that give a good fit to the high speed video measurements. It is possible that the surface roughness on the wafer used for the high speed video measurements was lower, resulting in a smaller effective friction coefficient. More work is needed to fully understand this discrepancy and whether it indicates variations in the fabricated devices or a limitation of the model itself.

A qualitative experimental verification of the latch bounce/chatter effect predicted by the two degree-of-freedom model was also presented. Electrical monitoring of contact resistance on devices with metallization on the round contact surfaces was performed, and showed several successive contact/loss of contact events during the latching progression. This phenomenon, previously unreported in this class of device, was first predicted by the two degree-of-freedom reduced order model. Experimental verification provides justification for using at least two degrees of freedom in modeling latching acceleration threshold switches, because a one-degree-of-freedom model simply cannot account for this type of behavior, nor the effect it has on the interaction forces and latching threshold levels.

Finally, the measured free deflection of the novel rotational actuator design was compared to the prediction of the electro-thermomechanical model presented in Section 4.8. The model predictions agree very well with the experimental results.

6. Concluding Remarks

In this chapter, a summary of the work is presented, along with the contributions made to the field and suggestions for future research directions.

6.1 Summary

A uniaxial, bidirectional, latching, resettable microelectromechanical acceleration threshold switch has been studied in depth in this work. Rather than a device, this actually comprises a small-scale system with a sensor, latching mechanism, and reset actuators. Each component of the system has been studied experimentally and theoretically. Models for the operation of the various parts of the system have been developed and used to gain insight into the design and operation of this class of device. The body of literature on MEMS latching acceleration threshold switches is fairly thin, with only a handful of device reported in the literature. The literature that does exist contains very limited experimental data and overly simplistic models that neglect the interaction of the sensor with the mass in every case.

The primary goal of this work has been to advance the understanding of the design and operation of this type of device. This has included extensive characterization of fabricated latching acceleration threshold switches, including the acceleration required to latch, changes to this threshold due to wear, and high-speed images of the latching event. It has also included lumped parameter models that capture the dynamics of the latching event and allow for insight into the contact forces and possibility of loss of contact during the latching event. The lumped parameter models have also been used in various parametric and optimization studies to gain insight into the design of latching acceleration threshold switches. As a byproduct of this work, a new type of rotational thermal actuator and a new friction measurement device suitable for friction measurements on deep reactive ion etched sidewalls have also been developed.

6.2 Contributions

The primary scholarly contribution of this work is a more in-depth understanding of latching shock sensors, with more thorough experimental data than ever presented before and a reduced-order model which for the first time allows detailed study of the shock sensor dynamics, including interactions with the latch. Along the way, the author has made various contributions to fabrication, design, testing, metrology, and modeling. The author's detailed contributions in each of these areas are as follows:

In the area of fabrication, the author's contributions include the following:

- Selectively patterned metallization on sidewalls of MEMS structures, used here to ensure high contact resistance before latching and low contact resistance after latching. This is a challenging process but the use of a thick negative photoresist, slow spin speeds, and increasing the exposure time by about 15% enabled photo-defined openings on 20μm sidewalls for sputter-coating with metal.
- A wafer level packaging process suitable for high aspect ratio structures while allowing wirebonding to the device contacts. This is a new idea which eliminates the need for filling of through-wafer vias for electrical contact to a devices encapsulated by wafer-bonding.

In the area of actuator design and modeling, the author's contributions include the following:

- Derivation of a closed-form expression for the stiffness of bent-beam actuators
- Developing a novel rotational thermal actuator design and publication of experimental performance data
- Parametric studies of the rotational thermal actuator design to show design tradeoffs and opportunities for improved performance
- Developing a model for the rotational thermal actuator which incorporates temperature dependent thermal expansion coefficients and a new shape factor expression that fits a wider set of beam heights than previously published approximations, both of which can be applied to other types of thermal actuators

In the area of MEMS metrology, the author's contributions include the following:

- Developing a novel thermally-actuated MEMS friction test structure for measurement of friction on sidewalls of MEMS devices at high normal forces and demonstration of friction coefficient change due to wear of sidewall asperities from repetitive cycling

In the area of latching acceleration sensor testing, the author's contributions include the following:

- Publication of shock testing data of latching accelerometers for the first time, including acceleration thresholds required to latch sensors and changes to the thresholds over many cycles. These data enhance the understanding of the limitations of the device that can be used to improve the robustness of performance. For instance, the contacts should be conditioned by latching and unlatching the sensor a minimum of 10 times to allow the effective friction coefficient to settle in before the sensor is used.
- High-speed video derived images of the sensor progression from resting state to latched under a shock pulse. This enhances the understanding of the dynamics of the mass/latch interaction, as well as the timing of the progression from resting, to contact, to latched, to closed electrical circuit (phases *i-iv* in Figure 4.1).

Finally, in the area of latching acceleration sensor modeling, the author's contributions include the following:

- Development of a two degree-of-freedom reduced order model for a latching acceleration threshold sensor which includes a separate degree of freedom for the mass and the latch, allowing in-depth study of the interaction of the mass and latch and the contact forces. Previously published papers either had no model at all or ignored the interaction forces for a very rough estimate of latching levels.
- Use of the two degree-of-freedom model to predict "bouncing" effect causing intermittent loss of contact between the mass and latch during latching. This is

a new observation made possible by the two degree-of-freedom model, and subsequently the author experimentally confirmed this phenomenon by electrically monitoring a device with contact metallization on the rounded surface of the latches.

- Use of the two degree-of-freedom model to optimize the design for reduced sensitivity to the friction coefficient.

This work has also led to a total of seven conference and journal publications. In particular, two journal articles have been published in a leading MEMS journal, *Sensors and Actuators A*. In the first article [38] (published in 2008), the authors described the sensor design and fabrication process, introduced the single degree of freedom lumped model, and compared the model results to latching threshold measurements taken using a shock table. This was the first publication in the open literature of a model for this type of sensor which took into account the interaction forces between the sensor and the latch, albeit with a limiting assumption prohibiting loss of contact between the sensor and the latch. In the second paper [48], (accepted for publication in March 2010), the authors introduced the two degree of freedom model, eliminating this assumption and allowing study of the dynamics of the contact between the latch and sensor. The second paper also presented for the first time pictures of the progression from resting to latched state for this type of sensor, and compared the progression to that predicted by the 2DOF model. The author also published an article in the journal *Advances In Science and Technology* [39] on the rotational thermal actuator, presenting the design, numerical model, and test results from various configurations of the design. The author has also presented this research at 5 conferences, including the ASME International Mechanical Engineering Conference and Exposition, the International Workshop on Structural Health Monitoring, the Shock and Vibration Symposium, and the 3rd International Conference on Smart Materials, Structures and Systems (CIMTEC 2008). Each of these presentations was also accompanied by a manuscript published in the respective proceedings [39, 51, 49, 50, 68].

6.3 ***Possible Improvements and Future Directions***

The shock sensor itself may be improved in a few ways. Most notably, stiction failures are common if the sensor is exposed to moderate or high humidity levels for extended periods of time. This can be alleviated either by including a hermetic seal, as in the packaging process presented in Section 0, or by coating the sensor with a hydrophobic material. While the packaging process has been developed, the hermeticity has not been tested, nor has the influence of the package on the operation of the sensor (if there is any). For instance, the amount of gas in the package and the confinement might affect the damping factors for the sensor and/or latch. Coating with a hydrophobic material has been done for many other MEMS devices [69], and is fairly well understood, but this device is more susceptible to stiction given the large surface area of the mass, the small gap between the mass and the substrate, and the long, compliant suspension springs.

The reset operation of the shock sensor makes use of thermal actuators. These could be replaced by in-plane piezoelectric actuators, which draw far less current (nA as compared to mA). The fabrication challenges with integrating a piezoelectric material are nontrivial in general, and compounded in this case by the hydrofluoric acid release process. Hydroflouric acid aggressively attacks the most attractive piezoelectric actuator material, PZT. ARL has demonstrated fabrication and release of piezoelectric actuators on SOI in a process compatible with the shock sensor, but the shock sensor release process is much longer and this will make protecting the PZT more challenging [70].

Shock sensor designs for other acceleration threshold levels should also be studied. The dynamics of the latching event are likely to be qualitatively different for much higher or much lower acceleration levels.

The response of the shock sensor to different shape acceleration pulses is also an avenue of future research. Impulse, half-sine, step function, or triangular acceleration profiles could be studied experimentally and through the sensor model. Modifying the shape of the acceleration profile for the model is very simple; although possible, it is considerably more involved to obtain different acceleration profiles with a shock table [71].

This work has treated the acceleration pulses as being applied precisely along the axis of the sensor. How the sensor responds to both cross-axis shocks and slight variations in the angle of the applied shock from the sensor axis is an important topic to investigate because the sensor is likely to encounter both of these in real-world use. The model could be extended to include two or even three degrees of freedom for the mass and for the latch to study these effects from a theoretical perspective. From an experimental perspective, variable angle jigs or mounting blocks could be constructed to change the angle of the sensor with respect to the shock table.

Further experimental study of latch bouncing can be conducted by using the devices with the metallization on the rounded edge of the latch, monitoring the resistance between the mass and latch during an acceleration event. Variations in the contact resistance are expected to track the contact pressure, and when contact is actually lost, the contact resistance increases dramatically. Further study of the time in contact, the time between bounces, and the contact pressure as it relates to the contact resistance could yield further insight into the validity of the model predictions. The metal coating on the latch will change the contact stiffness and friction coefficient, however, so the results may not be conclusive.

Finally, another useful optimization study would be a constrained multi-objective optimization of the friction sensitivity and the area footprint of the sensor, since it was found in Section 4.6 that the changes that reduce the friction sensitivity tend to increase the physical size of the sensor. Understanding the tradeoff completely requires knowledge of the Pareto front for these two objectives, with the constraint of latching threshold level being within some acceptable range.

A. Appendix

The fabrication process flow and detailed recipes to make the device is presented as Appendix A.1. The various MATLAB scripts used to run models and simulations throughout this work are provided in Appendix A.2. The ANSYS scripts used for the shape factor calculation for the rotational thermal actuator model and the contact stiffness calculation for the two degree-of-freedom sensor model are presented as Appendix A.3.

A.1 Fabrication Details

A.1.1 Detailed Fabrication Process Flow

The following is the fabrication process flowsheet used to track the fabrication process. It includes every step used in the fabrication of the shock sensors, as discussed in Section 2.3.

Device Wafer Process:

▪ **Bondpad Metal:**	**Completed by:**	**Date:**
1. **Wafer lot number:** ______________ **Wafer number (scribe on back):**_______		
2. Measure: **Resistivity** (thickness = 20um): _______________**Ω-cm**		
3. Photo 1 (**Bondpad metal**) AZ 5214 resist *Reverse Image* - Basic Wafer Flat Alignment		
4. Descum in Metroline M4L oxygen plasma (5214.RGP.descum.5min)		
5. 1 minute 6:1 buffered oxide etch immediately before loading into evaporator		
6. E-beam evaporation for bondpads in CHA SEC-600-RAP (400Å Cr/ 1000Å Pt/ 4000Å Au)		
7. Liftoff in Baker PRS-3000 photoresist stripper at 80°C		

- **Waferbond Ring:**

8. Photo 2 (**Bondring metal**) Futurex NR5-8000 negative resist (1000rpm spin, 6.8s exposure time, ~40sec develop) – **alignment to layer 1**		
9. Descum in Metroline M4L oxygen plasma (5214.RGP.descum.5min)		
10. E-beam evaporation for bondrings in CHA SEC-600-RAP (200Å Cr/ 1.5um Au)		
11. Liftoff in Futurex RR4 photoresist stripper at 110°C		

- **Device DRIE etch**

12. Photo 3 (**Device DRIE etch**) AZ 5214 – **alignment to layer 1**		
13. Descum in Metroline M4L oxygen plasma (5214.RGP.descum.5min)		
14. DRIE in VLR-700 (ARL_Via for ~14+ min)		
15. Strip P/R with Acetone/IPA/DI water and finish with Metroline M4L 5214.RGP.5min ash		

- **Cleave Assist Streets Etch**

16. Photo 5 (Cleave streets DRIE) Futurex NR5-8000 resist on backside of wafer (*front/back alignment*) **align to layer 1**		
17. Etch in VLR for 110 minutes (ARL_Via_Hold)		
18. Strip photoresist in Acetone/IPA/DI rinse		
19. Metroline M4L oxygen plasma ash to remove residue if necessary (5214.RGP.10min)		

- **Latch metallization**

20. Photo 4 (**Latch metal**) Futurex NR5-8000 resist – **align to layer 1**		
21. Sputter Cr/Au in CVC (200A/4000A) – 2.8min for Cr, 34 min for Au		
22. Liftoff in Acetone – do not use ultrasonic agitation		
23. Oxygen plasma strip – 5min to get rid of any photoresist residue		
24. Anneal on hotplate to improve contact resistance – ramp to 400C and hold for 1min on hotplate		
25. Keep in nitrogen drybox and in conductive wafer carrier from this point on		

- **Vapor HF release**

26. Release in Primaxx MEMS-CET Vapor HF Etcher –start with ARL Clear4 & UC4 recipe, continue with more undercut steps if necessary		

27. Inspect under infrared microscope for full release		

Wafer Bonding Process:

- **Wafer Standoff:**

	Completed By:	**Date:**
1. Begin with double-side polished silicon wafer		
2. Deposit isolation oxide in Plasmatherm 790 PECVD reactor (12:30 ~ 5000A)		
3. Photo 6 (**bond ring**) with Futurex NR5-8000 photoresist)		
4. Descum in Metroline M4L Oxygen plasma (5214.RGP.descum.5min)		
5. E-beam evaporation of bondring in CHA evaporator (200Å Cr/ 500Å Au/1.5um AuSn, 500Å Au)		
6. Liftoff in Futurex RR4 photoresist stripper at 110°		

- **Silicon Cap Wafer Via:**

7. Photo 7 (**Via step 1**) Futurex NR5-8000 resist on backside of cap wafer (front/back alignment) align to layer 1		
8. DRIE in Unaxis VLR-700 (ARL_Via) for 70min (timed etch – approx 200um)		
9. Strip Resist (Acetone/IPA/DI water, followed by Metroline M4L oxygen plasma 5214.RGP.5min if necessary)		
10 Spin AZ9245 photoresist on backside of capwafer (2500 rpm) and softbake, then spin AZ9245 on front of capwafer (2500rpm) and softbake ***supported by scrap pieces to keep backside resist from sticking to hotplate***		
11 Photo 8 (**Via step 2**) AZ9245 resist, 2500rpm process, expose for 12sec (align to layer 1)		
13 DRIE (VLR – ARL_Via) for 50min (3,000s) – check for through etch completion under microscope		
14 Strip resist – Acetone and IPA, followed by Metroline M4L oxygen plasma (5214.RGP.5min) if necessary		

- **Wafer Bonding**

15 Align patterned silicon cap wafer to SOI device wafer in Karl Suss MA/BA6 – silicon/silicon program (device wafer loaded first, then cap wafer)		
16 Bond patterned silicon cap wafer to top of SOI device wafer in Karl Suss SB6 Wafer Bonder (AuSn_315C_10min_50vac.rcp)		

A.1.2. Process Recipe Details

- Photolithography Recipes:
    - AZ 5214 (~2 µm thick)
        - Positive Tone
          Spread: 500rpm for 5 seconds
          Spin: 2000 rpm for 40 seconds
          Softbake: 110 C for 60 seconds on hotplate
          Exposure: 2.3 seconds at 1000mJ/cm^2
          Develop: 80 seconds in AZ300 developer
        - Negative Tone
          Spread: 500rpm for 5 seconds
          Spin: 2000 rpm for 40 seconds
          Softbake: 110 C for 60 seconds on hotplate
          Exposure: 2.3 seconds at 1000mJ/cm^2
          Post-Exposure Bake: 30 seconds at 120C on hotplate
          Flood Exposure (no mask): 2.8 seconds at 1000mJ/cm^2
          Develop: 80 seconds in AZ300 developer

    - Futurex NR5-8000 (~15 µm thick)
        - Standard Process
          Spread: 500rpm for 5 seconds
          Spin: 1000rpm for 40 seconds
          Softbake: 110C for 20 sec, followed by 150C for 60 sec
          Exposure: 6.8 seconds at 1000mJ/cm^2
          Post-exposure bake: 110C for 120 seconds on hotplate
          Gradual cool: 120 seconds on pyrex dish (to keep resist from cracking if it cools too fast
          Develop: 40 seconds in Futurex RD6 developer

        - Latch Metallization (over 20 µm topography)
          Same as above except use 7.8 second exposure

- Etch Recipes:
    - Primaxx MEMS-CET Vapor HF etch recipe

Clear Cycle	Undercut Cycle
(to remove exposed oxide slowly)	(to undercut quickly)
Pressure: 125 T	Pressure: 125 T
HF flowrate: 250 sccm	HF flowrate: 600 sccm
Methanol flowrate: 500 sccm	Methanol flowrate: 450 sccm
N2 flowrate: 1050 sccm	N2 flowrate: 1000 sccm

- Unaxis VLR-700 ICP DRIE

Etch Step	Deposition Step
Pressure: 25 mT	Pressure: 20 mT
SF6 flowrate: 100 sccm	C4F8 flowrate: 70 sccm
Ar flowrate: 40 sccm	Ar flowrate: 40 sccm
Plasma power: 850 W	Plasma Power: 850 W
Platen Power: 16W	Platen Power: 1 W

- Silicon Dioxide RIE
  Pressure: 5 mT
  CHF3 flowrate: 5 sccm
  CF4 flowrate: 15 sccm
  He flowrate: 28.3 sccm
  Plasma Power: 500 W
  Platen Power: 5 W

- Deposition Recipes:
  - CHA SEC-600-RAP E-beam evaporator:
    - Metal evaporation rates:
      Chromium: 1 Å/s
      Platinum: 2.5 Å/s
      Gold: 4 Å/s
      AuSn (80/20): 5 Å/s
  - CVC Sputtered gold (3” target)
      Power Ramp: 100W/minute
      Power: 100W
      Ar flow: 45sccm
      Rotation: 6 rpm

- Wafer-bonding recipe:
  Pump/purge chamber 3x
  Backfill with H_2N_2 (forming gas) to 50 Torr
  Remove spacers to place wafers in contact
  Tool Pressure: 4000 N
  Heat to 315C for 10 minutes
  Cool to <200C before removing from chamber

A.2 MATLAB Scripts

A.2.1 Rotational Actuator MATLAB Model

```
%therm_rot_iter2.m
%12/29/09
%calculates temperature profiles and free deflections for rotational
%offset actuator, updating thermal conductivity and iterating

clear all
curr=linspace(0,12e-3,13);  %input current
p=(5.00e-3)/100;            %room-temp resistivity

%geometric properties
L=600e-6;               %length of one beam - total length = 2L
x=linspace(0,2*L);      %define grid of nodes
g=2e-6;                 %gap between beam and substrate
w=7e-6;                 %width of beam
h=20e-6;                %height of beam (i.e., thickness of SOI)
A=w*h;                  %cross-sectional area of beam
I=1/12*h*w^3;           %bending moment of inertia
offset=5e-6;            %offset between each beam and pivot point

%material properties
E=169e9;                %Young's modulus

%S=4/w*(1e-6+g)+1;       %Maloney's shape factor
S=4/w*(g+h/50)+1;        %Currano's shape factor
T_inf=298;              %boundary temperature

%calculate spring constant of actuator
k=2*E/L*(4*I+A*offset^2);

%convert current to current density in A/m^2
J=curr/A;

%Step through various current densities
for j=1:length(J)
    N=length(x)/2;      %N = number of elements in single beam
    T=ones(N,1)*T_inf;  %initialize temperature of each element
    Told=zeros(N,1);
    %initialize matrix
    B=2*eye(N);
    for r=1:N-1
        B(r,r+1)=-1;
        B(r+1,r)=-1;
    end
    B(N,N-1)=-2;

    dx=max(x)/(length(x)-1);
    %loop through iterative solution procedure
    iter=0;
    while abs(max(T-Told))>1e-3
        iter=iter+1
```

```
        Told=T;
        %element-wise temp-dependent coefficients of thermal
        %conductivity:
        ks=exp(-1.28*log(T)+12.28);
        ka=-3.06e-8*T.^2+9.62e-5*T+1.05e-4;
        %element-wise temp-dependent resistivity
        rho=p+4.7e-8*(T-T_inf);
        %finite difference soln to heat Eq
        C=B.*repmat(ks,1,N)/dx^2+S*diag(ka)/g/h;
        D=S*ka*T_inf/g/h+J(j)^2*rho;
        D(1)=D(1)+T_inf*ks(1)/dx^2;
        T=C\D;      %solve for temperature distribution
    end
    average_resistivity=mean(rho)
    max_temp=max(T);

    %calculate thermal expansion in beam, summing over all elements
    delta=0;
    total_resistance=0;
    for s=2:N
        %temperature in element assumed to be average of temperature
        % at the nodes:
        avg_T=(T(s)+T(s-1))/2;
        %temperature dependent coefficient of thermal expansion
        alpha=(3.725*(1-exp(-5.88e-3*(avg_T-124)))+…
            5.548e-4*avg_T)*1e-6;
        delta=delta+alpha*(x(s)-x(s-1))/2*((T(s)-T_inf)+…
            (T(s-1)-T_inf));
        elem_resistance=(p+4.7e-8*(avg_T-T_inf))*dx/A;
        total_resistance=total_resistance+elem_resistance;
    end

    %Calculate force/moment from thermal expansion
    F=delta*E*w*h/L;
    M=2*F*offset;

    %calculate rotation angle in degrees
    theta(j)=M/k*180/pi;
end
theta'
```

A.2.2. 1DOF Shock Sensor MATLAB Model

```
%predicts transient response of latching shock sensor to steady
%acceleration beginning at time = 0
%does not handle impulse acceleration (i.e., acceleration pulse
%lasts for shorter than 1/2 of device period
function shock_sensor
clear all
format short e;
hold off;

global chip_accel k m kl ybar r di mu yc;

%initialize global variables to describe system
%75g sensor
```

```
%chip_accel=-103.7*9.81;
%k=1.324;
%m=2.65e-7;

%37.5g sensor
chip_accel=-63*9.81;
k=0.601;
m=3.42e-7;

kl=4.44;
ybar=150e-6;
r=40e-6;
di=15e-6;
%no friction
%mu=0;
%best fit friction coefficient
mu=0.29;

yc=91.9e-6;          %distance to initial contact
yc2=ybar;            %distance to latch/distance till contact is lost

%define the frequency and period of the basic spring-mass system
freq=sqrt(k/m)/(2*pi);
period=1/freq;

%Solve differential equation for period before contact
%set options to find where contact occurs and stop integration
refine=20;
options=odeset('Events',@events,'Refine',refine);
initial=[0;0]
[T1,Y1,TE1,YE1,IE]=ode45(@shock_init,[0 period],initial,options)
subplot(2,1,1),plot(T1,Y1(:,1));
%subplot(2,1,2),plot(T1,zeros(length(T1),1)*chip_accel/9.81);

hold on;

%Solve differential equation for period while mass is in contact
%with latch
%find where contact ends and stop integration
yc=yc2;
options=odeset('Events',@events,'Refine',refine);
initial2=[YE1(1,1);YE1(1,2)];
[T2,Y2,TE2,YE2,IE2]=ode45(@latchfr,[TE1
period+TE1],initial2,options)
subplot(2,1,1),plot(T2,Y2(:,1),'g:');
%subplot(2,1,2),plot(T2,ones(length(T2),1)*chip_accel/9.81);

%Solve differential equation for period after mass breaks contact
%with latch
initial3=[YE2(1,1);YE2(1,2)]
[T3,Y3]=ode45(@shock_init,[TE2 period+TE2],initial3);
subplot(2,1,1),plot(T3,Y3(:,1),'r');
%subplot(2,1,2),plot(T3,ones(length(T3),1)*chip_accel/9.81);

%Labels and legends for graph of data
```

```
title('Displacment vs. Time of Shock Sensor')
xlabel('Time (s)')
ylabel('Displacement (m)')
legend('pre-contact','contact','post-contact')

%-------------------------------------------------------------------
function dy=shock_init(t,y)

%this function defines the differential equation before the shock
%sensor makes contact with the latch
%y(1) is the displacement, y(2) is the velocity
%ypp is the acceleration function, F is the mass-latch interaction
%(friction & normal force)

global chip_accel k m;

F=0;
ypp=-chip_accel-k*y(1)/m-2*F/m;

dy=[y(2);ypp];

%-------------------------------------------------------------------
function dy=latchfr(t,y)

%this function defines the differential equation while the shock
%sensor is in contact with the latch
%y(1) is the displacement, y(2) is the velocity
%ypp is the acceleration function, F is the mass-latch interaction
%(friction & normal force)


global chip_accel k m kl ybar r di mu yc;

yl=ybar-y(1);                     %remaining travel
theta=asin(yl/(2*r));            %contact angle
F=2*kl*(2*r*cos(theta)-r-di)*(sin(theta)+…
   mu*cos(theta))/(cos(theta)-mu*sin(theta));

ypp=-chip_accel-k*y(1)/m-2*F/m;

dy=[y(2);ypp];

%-------------------------------------------------------------------

function dy=shock_final(t,y)

global chip_accel k m;

%this function defines the differential equation after the shock
%sensor leaves contact with the latch
%y(1) is the displacement, y(2) is the velocity
%ypp is the acceleration function, F is the mass-latch interaction
%(friction & normal force)
```

```
F=0;
ypp=-chip_accel-k*y(1)/m-2*F/m;

dy=[y(2);ypp];

%-------------------------------------------------------------------

function [value,isterminal,direction]=events(t,y)
global yc;
    %this function compares the distance the device has travelled to
    %a critical distance (either distance to contact or
    %distance to loss of contact) to determine when to switch the
    %differential equation used
    value=abs(y(1))-abs(yc);
    isterminal=1;
    direction=1;
```

A.2.3. 2DOF Shock Sensor MATLAB Model

```
% 2DOF shock sensor model with deflection of latch included
%predicts transient response of latching shock sensor to half-sine
%acceleration function beginning at time = 0
function [state]=shock_sensor_contact3()
%clear all
format short e;
hold off;

global chip_accel duration k kaxial M m kl ybar r di mu yc ca_fn…
            Fymon1 Fymon2 Fymon3 Fmon;
%Fymon2=0; Fymon3=0;
E=169e9;    %Young's Modulus
wl=8e-6;    %width of latch
ll=460e-6;  %length of latch
tl=20e-6;   %thickness of latch
%stiffness of a single latch - multiplied by 2 in force function –
%nominal 4.44
kl=3*E*(1/12*tl*wl^3)/ll^3;
kaxial=E*wl*tl/ll;          %axial stiffness of latch
dens=2300;                  %density of silicon
m=1/3*ll*wl*tl*dens;        %mass of latch
freql=sqrt(kl/m)/(2*pi)     %natural frequency of latch

%initialize global variables to describe system 100 g sensor
chip_accel=-120*9.81;    %103.72 for hs video
duration=5.9e-3;
k=0.887;
M=2.65e-7;

%50 g sensor chip_accel=-62.56*9.81;
%duration=8.24e-3;
%k=0.601;

ybar=150e-6;        %total travel to latched position
r=40e-6;            %radius of latch
di=15e-6;          %initial horizontal offset between latch and mass
```

```
mu=0.1;             %friction coefficient
yc=91.9e-6;         %distance to initial contact
yc2=ybar;           %distance to latch/distance till contact is lost

%define the frequency and period of the basic spring-mass system
freq=sqrt(k/M)/(2*pi);
period=1/freq;

%Solve differential equation for period before contact set options
%to find where contact occurs and stop integration
refine=20;
options=odeset('Events',@events,'Refine',refine);
initial=[0;0;0;0];
[T1,Y1,TE1,YE1,IE]=ode45(@shock_init,[0 period],initial,options);
subplot(3,1,1),plot(T1,Y1(:,1));
hold on
subplot(3,1,2),plot(T1,Y1(:,3));
hold on;

%Solve differential equation for period while mass is in contact
%with latch find where contact ends and stop integration
refine=1;
yc=yc2;
maxstep=1e-7;
initstep=0.5e-9;
%full version - includes storage of force information at each
%timestep, but runs slowly
%options=odeset('Events',@events,'Refine',refine,'MaxStep'…
%,maxstep,'OutputFcn',@Fstore,'Stats','on','InitialStep',initstep);

%simple version - no storage of force data - much faster execution
options=odeset('Events',@events,'Refine',refine,'MaxStep',maxstep,'I
nitialStep',initstep);
initial2=[YE1(1,1);YE1(1,2);YE1(1,3);YE1(1,4)];
[T2,Y2,TE2,YE2,IE2]=ode45(@latchfr,[TE1 duration],initial2,options);
%if desired, code can be interrupted here to simply report whether
%the device latched or not
%if IE2==2
    %this corresponds to the velocity going to zero (didn't latch)
%    state=0; return;
%else state=1;
    %otherwise the device did latch
%    return;
%end
subplot(3,1,1),plot(T2,Y2(:,1),'g:');
subplot(3,1,2),plot(T2,Y2(:,3),'g:');
%Solve differential equation for period after mass breaks contact
%with latch
initial3=[YE2(1,1);YE2(1,2);YE2(1,3);YE2(1,4)]
[T3,Y3]=ode45(@shock_final,[TE2 duration],initial3);
subplot(3,1,1),plot(T3,Y3(:,1),'r');
%Labels and legends for graph of data
title('Displacment vs. Time of Shock Sensor')
xlabel('Time (s)')
ylabel('Displacement (m)')
legend('pre-contact','contact','post-contact')
```

```
grid on
axis([0 .006 0 200e-6])
subplot(3,1,2),plot(T3,Y3(:,3),'r');
axis([0 .006 -50e-6 50e-6])
%Labels and legends for graph of data
title('Latch Displacement')
xlabel('Time (s)')
ylabel('Displacement (m)')
grid on
%plot x displacement
figure
plot(T2,Y2(:,3))              %plot x-displacement of latch
title('Latch Displacement')
xlabel('Time (s)')
ylabel('Displacement (m)')
grid on
figure
plot(Fmon(:,1),Fmon(:,5))     %plot y force on latch
title('Normal Force on Latch')
xlabel('Time (s)')
ylabel('Force (N)')
grid on
%write out position/time data for animation
%fid=fopen('T_data.txt','wt');
%T=[T1;T2;T3]; fprintf(fid,'%15.6e\n',T); fclose(fid);
%fid=fopen('Y_data.txt','wt'); Y=[Y1(:,1);Y2(:,1);Y3(:,1)];
%fprintf(fid,'%15.6e\n',Y); fclose(fid);
%fid=fopen('X_data.txt','wt');
%X=[Y1(:,3);Y2(:,3);Y3(:,3)]; fprintf(fid,'%15.6e\n',X);
%fclose(fid);

%-------------------------------------------------------------------
function dy=shock_init(t,y)

%this function defines the differential equation before the shock
%sensor
%makes contact with the latch y(1) is the displacement, y(2) is the
%velocity ydd is the Eq of motion for the mass, F is the mass-latch
%interaction (friction & normal force)

global chip_accel duration k m M Fymon1;

F=0;
Fy=F;
Fx=F;
if t<=duration
    ydd=-chip_accel*sin(t/duration*pi)-k*y(1)/M-2*F/M;
else
    ydd=-k*y(1)/M-2*F/M;
end
xdd=0;
dy=[y(2);ydd;y(4);xdd];

%-------------------------------------------------------------------
function dy=latchfr(t,y)
```

```
%this function defines the differential equation while the shock
%sensor is
%in contact with the latch y(1) is the displacement, y(2) is the
%velocity
%ypp is the acceleration function, F is the mass-latch interaction
%(friction & normal force)

global chip_accel duration k m kl kaxial ybar r di mu yc M Fymon2 Fx
Fy F_normal;

yl=ybar-y(1);                        %remaining travel

%calculations of surface deflection using various equations for
%cylinders
%reasonable range for normal force 0-5mN
L=20e-6;
P=linspace(1e-6,5e-3);
r=40e-6;
v=0.28;
E=169e9;
%Eq. 4 - for two cylinders in contact
V4=(1-v^2)/(pi*E);
P4=P/L;
a=L/2;
d=2*P4.*V4.*(1+log((4*a^2)./(V4*P4*2*r)));

int2=2*r-sqrt((ybar-y(1))^2+(r+di+y(3))^2);
theta=asin(yl/(2*r-int2));              %contact angle
if int2<0
    int2=0;
end

%approx. stiffness of contact
kc=P(100)/d(100);
%effective latch stiffness in direction of contact
kl_eff=1/(cos(theta)^2/kl+sin(theta)^2/kaxial);
keff=kl_eff+kc;

F_normal=keff*int2;

Fx=F_normal*cos(theta);
Fy=F_normal*sin(theta)*2+2*mu*F_normal*cos(theta);

%equation of motion for mass, ydd means y double dot
if t<=duration
    ydd2=-chip_accel*sin(t/duration*pi)-k*y(1)/M-2*F_normal*(ybar-
y(1))/sqrt((ybar-y(1))^2+(r+di+y(3))^2)/M-
sign(y(2))*2*mu*F_normal*(r+di+y(3))/(2*r-int2)/M;
else
    ydd2=-k*y(1)/M-2*F_normal*(ybar-y(1))/sqrt((ybar-
y(1))^2+(r+di+y(3))^2)/M-sign(y(2))*2*mu*F_normal*(r+di+y(3))/(2*r-
int2)/M;

end
```

```
%equation of motion for latch, xdd means x double dot

xdd2=(-kl*y(3)+kc*int2*(r+di+y(3))/sqrt((ybar-
y(1))^2+(r+di+y(3))^2)-sign(y(4))*mu*F_normal*sin(theta))/m;
%return state for each time step
dy=[y(2);ydd2;y(4);xdd2];

%-------------------------------------------------------------------
function dy=shock_final(t,y)

global chip_accel ca_fn duration k kaxial kl m M ybar Fymon3 mu;

%this function defines the differential equation after the shock
%sensor
%leaves contact with the latch y(1) is the displacement, y(2) is the
%velocity ypp is the acceleration function, F is the mass-latch
%interaction
%(friction & normal force)
zm=0;
cm=2*zm*sqrt(k/M);
if y(1)>ybar&&y(1)<170e-6
    F=0;
elseif y(1)>170e-6
    F=kaxial*(y(1)-170e-6);
else
    F=kaxial*(y(1)-ybar);
end
if t<=duration
    ydd=-chip_accel*sin(t/duration*pi)-k*y(1)/M-cm*y(2)/M-2*F/M;
else
    ydd=-k*y(1)/M-cm*y(2)/M-2*F/M;
end
zeta=0;
cl=2*zeta*sqrt(kl*m);
%equation of motion for latch, xdd means x double dot
%xdd=-kl*y(3)/m-sign(y(4))*mu*F/m;
xdd=-kl*y(3)/m-cl*y(4)/m;
dy=[y(2);ydd;y(4);xdd];

%-------------------------------------------------------------------

function [value,isterminal,direction]=events(t,y)
global yc;
    %this function compares the distance the device has travelled to
a
    %critical distance (either distance to contact or distance to
loss of
    %contact) to determine when to switch the differential equation
used
    value=[abs(y(1))-abs(yc);y(2)];
    isterminal=[1;1];
    direction=[1;-1];

%-------------------------------------------------------------------
function status=Fstore(t,y,flag)
```

```
  global Fx Fy Fmon F_normal;
if strcmp(flag,'init')
  Fmon=[Fmon;t(1) y(1) Fx Fy F_normal];
elseif strcmp(flag,'') Fmon=[Fmon;t(1) y(1) Fx Fy F_normal];
end
  status=0;
```

A.2.4. Shock Sensor Parametric Study Code

```
%self-contained code to vary design paprameters and solve for
%corresponding latching thresholds
function [thresh_array]=find_thresh_param()
    %define baseline parameter values
    t=20e-6;
    Lf_baseline=1495e-6;
    Wf_baseline=12e-6;
    Hm_baseline=2.025e-3;
    wl_baseline=8e-6;
    ll_baseline=460e-6;

    %define range to vary each parameter and array to store results
    Hm=linspace(1e-3,3e-3,21);
    Hm_thresh=zeros(length(Hm),1);
    Lf=linspace(1e-3,3e-3,21);
    Lf_thresh=zeros(length(Lf),1);
    Wf=linspace(5e-6,15e-6,21);
    Wf_thresh=zeros(length(Wf),1);
    wl=linspace(3e-6,15e-6,13);
    wl_thresh=zeros(length(wl),1);
    ll=linspace(200e-6,600e-6,9);
    ll_thresh=zeros(length(ll),1);

    %define initial guess for threshold acceleration for each array
    Hm_guess=500;
    Lf_guess=500;
    Wf_guess=50;
    wl_guess=80;
    ll_guess=350;
    mu=0.3;

    %step through array of parameter values and solve for threshold
    %comment out all but parameter being currently investigated
    for i=1:length(ll)
        %assemble full parameter to pass
        %Hm_pass=[Hm_guess mu t Lf_baseline Wf_baseline Hm(i) wl ll]
        %Hm_thresh(i)=find_thresh(Hm_pass)
        %Hm_guess=Hm_thresh(i);

        %Lf_pass=[Lf_guess mu t Lf(i) Wf_baseline Hm_baseline wl ll]
        %Lf_thresh(i)=find_thresh(Lf_pass)
        %Lf_guess=Lf_thresh(i);

        %Wf_pass=[Wf_guess mu t Lf_baseline Wf(i) Hm_baseline wl ll]
        %Wf_thresh(i)=find_thresh(Wf_pass)
        %Wf_guess=Wf_thresh(i);
```

```
        %wl_pass=[wl_guess mu t Lf_baseline Wf_baseline Hm_baseline
            %wl(i) ll_baseline];
        %wl_thresh(i)=find_thresh(wl_pass)
        %wl_guess=wl_thresh(i);
        ll_pass=[wl_guess mu t Lf_baseline Wf_baseline Hm_baseline
wl_baseline ll(i)];
        ll_thresh(i)=find_thresh(ll_pass)
        ll_guess=ll_thresh(i);
    end
    %print out results
    ll'
    ll_thresh

%-------------------------------------------------------------------
%Uses internal version of ssc3_optim to find threshold acceleration
%for a given design
function [thresh]=find_thresh(ft)
   %set parameters of particular design
   guess=ft(1);
   mu=ft(2);
   t=ft(3);
   Lf=ft(4);
   Wf=ft(5);
   Hm=ft(6);
   wl=ft(7);
   ll=ft(8);
    global chip_accel
    incr=20;    %initial adjustment increment
    chip_accel=-guess     %apply initial guess
    ca_low=0;              %apply initial bounds
    ca_hi=5000;
%loop through until threshold is found within 1g
    while (ca_hi-ca_low)>=1
      latched=ssc3_optim(t,Lf,Wf,Hm,wl,ll,mu) %test if latches
        if latched==0            %if doesn't latch, increase accel
            ca_low=-chip_accel;    %update lower bound on search
            if abs(chip_accel-incr)>=ca_hi         %don’t overshoot
                incr=incr/2;     %decrease increment
            end
            chip_accel=chip_accel-incr;        %adjust guess
            continue            %and retry

        else                        %if it did latch, decrease
            ca_hi=-chip_accel;            %modify upper bound
            if abs(chip_accel+incr)<=ca_low         %don’t overshoot
                incr=incr/2;     %decrease increment if you would
            end
            chip_accel=chip_accel+incr        %adjust guess
            continue            %and retry
        end
    end     %end while loop
    mu
    thresh=ca_hi      %set threshold to lowest accel resulting in
%latched event
```

```
%-------------------------------------------------------------------
% 2DOF shock sensor model with deflection of latch included
%predicts transient response of latching shock sensor to steady
%acceleration beginning at time = 0
%also predicts steady state maximum deflection
%does not handle impulse acceleration (i.e., acceleration pulse
%lasts for shorter than 1/2 of device period
function [state]=ssc3_optim(t,Lf,Wf,Hm,wl,ll,mu_pass)
%clear all
format short e;
hold off;

global chip_accel duration k kaxial M m kl ybar r di mu yc ca_fn
Fymon1 Fymon2 Fymon3 Fmon max_bounce;
E=160e9;
radius=40e-6;
%define wl,ll,t outside this m-file
%calculate mass and stiffness of latch
kl=3*E*(1/12*t*wl^3)/ll^3;       %stiffness of a single latch -
%multiplied by 2 in force function -nominal 4.44, 3.66 for 7.5um
%wide latch
kaxial=E*wl*t/ll;
dens=2330;
m=33/140*(ll+40e-6)*wl*t*dens+pi*radius^2/4*t*dens;
freql=sqrt(kl/m)/(2*pi);

%initialize global variables to describe system
%chip_accel=-120*9.81;       %chip_accel comes from input at runtime
duration=5.9e-3;                 %
Np=4;
Ns=5;

%define t,Lf,Wf,Hm outside of this m-file
%calculate mass and stiffness of springs and mass of Mass
k=E*t*Wf^3/(Lf^3*Ns)*Np;
Wm=Lf*2+110e-6;
num_holes=ceil((Hm-40e-6)/(60e-6))*ceil((Wm-40e-6)/(60e-6));
Mm=dens*t*(Hm*Wm-120e-6*120e-6-num_holes*20e-6*20e-6);  %mass of
%sensor
Mf=Lf*Wf*t*dens*Ns*Np/3;                                 %equivalent
%mass of springs
M=Mm+Mf;

ybar=150e-6;
r=40e-6;
di=15e-6;

mu=mu_pass;            %mu defined by input at runtime
yc=91.9e-6;         %distance to initial contact
yc2=ybar;           %distance to latch/distance till contact is lost
k2=kl;                %axial stiffness of latch

%define the frequency and period of the basic spring-mass system
freq=sqrt(k/M)/(2*pi);
period=1/freq;
```

```
%Solve differential equation for period before contact
%set options to find where contact occurs and stop integration
options=odeset('Events',@events);
initial=[0;0;0;0];
[T1,Y1,TE1,YE1,IE]=ode45(@shock_init,[0 period],initial,options);
if IE==2
    state=0;    %unlatched
    return;
end

%Solve differential equation for period while mass is in contact
%with latch
%find where contact ends and stop integration
yc=yc2;
maxstep=10e-7;      %1e-8 used for model match
initstep=5e-8;     %0.5ns for model match
refine=1;

options=odeset('Events',@events,'Refine',refine,'MaxStep',maxstep,'S
tats','off','InitialStep',initstep);
initial2=[YE1(1,1);YE1(1,2);YE1(1,3);YE1(1,4)];
[T2,Y2,TE2,YE2,IE2]=ode45(@latchfr,[TE1
duration+period],initial2,options);
%max_bounce
if IE2==2
    state=0;    %unlatched
    return;
else state=1;   %latched
    return;
end

%-------------------------------------------------------------------
function dy=shock_init(t,y)

%this function defines the differential equation before the shock
%sensor makes contact with the latch
%y(1) is the displacement, y(2) is the velocity
%ydd is the Eq of motion for the mass, F is the mass-latch
%interaction (friction & normal force)

global chip_accel duration k m M Fymon1;

F=0;
Fy=F;
Fx=F;
if t<=duration
    ydd=-chip_accel*9.81*sin(t/duration*pi)-k*y(1)/M-2*F/M;
else
    ydd=-k*y(1)/M-2*F/M;
end
xdd=0;
dy=[y(2);ydd;y(4);xdd];

%-------------------------------------------------------------------
```

```
function dy=latchfr(t,y)

%this function defines the differential equation while the shock
%sensor is in contact with the latch
%y(1) is the displacement, y(2) is the velocity
%ypp is the acceleration function, F is the mass-latch interaction
%(friction & normal force)

global chip_accel duration k m kl kaxial ybar r di mu yc M Fymon2 Fx
Fy F_normal max_bounce;

yl=ybar-y(1);                         %remaining travel

%calculations of surface deflection using various equations for
%cylinders
%reasonable range for normal force 0-5mN
L=20e-6;
P=linspace(1e-6,5e-3);
r=40e-6;
v=0.28;
E=169e9;
%Eq. 4 - for two cylinders in contact
V4=(1-v^2)/(pi*E);
P4=P/L;
a=L/2;
d=2*P4.*V4.*(1+log((4*a^2)./(V4*P4*2*r)));

int2=2*r-sqrt((ybar-y(1))^2+(r+di+y(3))^2);
theta=asin(yl/(2*r-int2));            %contact angle

if int2<0
    if abs(int2)>max_bounce
        max_bounce=abs(int2);
    end
    int2=0;
end

%approx. stiffness of contact
kc=P(100)/d(100);
%effective latch stiffness in direction of contact
kl_eff=1/(cos(theta)^2/kl+sin(theta)^2/kaxial);
keff=kl_eff+kc;

F_normal=keff*int2;

Fx=F_normal*cos(theta);
Fy=F_normal*sin(theta)*2+2*mu*F_normal*cos(theta);

if t<=duration
    ydd2=-chip_accel*9.81*sin(t/duration*pi)-k*y(1)/M-
2*F_normal*(ybar-y(1))/sqrt((ybar-y(1))^2+(r+di+y(3))^2)/M-
sign(y(2))*2*mu*F_normal*(r+di+y(3))/(2*r-int2)/M;
else
```

```
    ydd2=-k*y(1)/M-2*F_normal*(ybar-y(1))/sqrt((ybar-
y(1))^2+(r+di+y(3))^2)/M-sign(y(2))*2*mu*F_normal*(r+di+y(3))/(2*r-
int2)/M;
end
zeta=.1;
cl=2*zeta*sqrt(kl*m);
%equation of motion for latch, xdd means x double dot
%xdd=(-kl*y(3)-cl*y(4)+Fx)/m
xdd2=(-kl*y(3)+Fx)/m;
xdd2=(-kl*y(3)+kc*int2*(r+di+y(3))/sqrt((ybar-
y(1))^2+(r+di+y(3))^2)-sign(y(4))*mu*F_normal*sin(theta))/m;
%return state for each time step
dy=[y(2);ydd2;y(4);xdd2];

%--------------------------------------------------------------------

function dy=shock_final(t,y)

global chip_accel ca_fn duration k kaxial kl m M ybar Fymon3 mu;

%this function defines the differential equation after the shock
sensor leaves contact with the latch
%y(1) is the displacement, y(2) is the velocity
%ypp is the acceleration function, F is the mass-latch interaction
(friction & normal force)
zm=3e-7;
cm=2*zm*sqrt(k/M);
if y(1)>ybar&&y(1)<170e-6
    F=0;
elseif y(1)>170e-6
    F=kaxial*(y(1)-170e-6);
else
    F=kaxial*(y(1)-ybar);
end
if t<=duration
    ydd=-chip_accel*9.81*sin(t/duration*pi)-k*y(1)/M-cm*y(2)/M-
2*F/M;
else
    ydd=-k*y(1)/M-cm*y(2)/M-2*F/M;
end
zeta=0.1;
cl=2*zeta*sqrt(kl*m);
%equation of motion for latch, xdd means x double dot
%xdd=-kl*y(3)/m-sign(y(4))*mu*F/m;
xdd=-kl*y(3)/m-cl*y(4)/m;
dy=[y(2);ydd;y(4);xdd];

%--------------------------------------------------------------------

function [value,isterminal,direction]=events(t,y)
global yc;
    %this function compares the distance the device has travelled to
%a critical distance (either distance to contact or
    %distance to loss of contact) to determine when to switch the
%differential equation used
```

```
    value=[abs(y(1))-abs(yc);y(2)];     %returns 2 if velocity is 
%zero, returns 1 if moves past latch dist
    isterminal=[1;1];
    direction=[1;-1];

%---------------------------------------------------------------------
```

A.2.5. Genetic Algorithm Codes

```
%----------------------run_ga.m----------------------
%requires the following m-files: ssc3_optim.m GA_frict_thresh_obj.m, 
thresh_err_calc.m

datestr(now)
tic

global THRESH_P3 TARGET_THRESH
TARGET_THRESH=100;

matlabpool local 8
format('shorte');
% Start with the default options
options = gaoptimset;
% Modify options setting
options = gaoptimset(options,'PopulationSize', 100);
options = gaoptimset(options,'EliteCount', 2);
options = gaoptimset(options,'CreationFcn', @gacreationuniform);
options = gaoptimset(options,'Display', 'iter');
options = gaoptimset(options,'PlotFcns', { @gaplotscores });
options = gaoptimset(options,'Vectorized', 'on');
options = gaoptimset(options,'UseParallel', 'never');
options = gaoptimset(options,'SelectionFcn',@selectionstochunif);
lb=[20e-6 1000e-6 3e-6 1e-3 8e-6 460e-6]
ub=[20e-6 2000e-6 20e-6 3e-3 8e-6 460e-6]
[x,fval,exitflag,output,population,score] = ...
      ga(@GA_frict_thresh_obj,6,[],[],[],[],lb,ub,…
      @thresh_err_calc,options);
matlabpool close
toc
datestr(now)

%-----------GA_frict_thresh_obj.m----------------------
%vectorized single-objective optimization
%uses find_thresh, ssc3_optim to perform constrained single-
objective optimization
%objective is: Low friction sensitivity
% uses ndsort to assign fitness values at the end of each generation
%intended as objective function in an optimization routine

function fitness=GA_frict_thresh_obj(x)
    %x is the vector of independent variables for the optimization
    %definition of x=[t Lf Wf Hm wl ll]

    global TARGET_THRESH
    TARGET_THRESH=100;
```

```
    persistent GEN pop_results
    if isempty(GEN)
        GEN=1;
        PARETO=[];
    else GEN=GEN+1;
    end
    if isempty(pop_results)
        pop_results=zeros(1,10)
    end
    pop_size=size(x,1)
    %initialize results array
    %array elements will be:
    %[generation# x-values thresh_p3 thresh_p6]
    current_results_p3=zeros(pop_size,1);
    current_results_p6=zeros(pop_size,1);

%step through population:
parfor i=1:pop_size
    %find low friction threshold for current design
    mu_pass=0.3;
    quick_test=1000;
    guess=TARGET_THRESH;
    par=[guess mu_pass x(i,1) x(i,2) x(i,3) x(i,4) x(i,5) x(i,6)];

latched=ssc3_optim(x(i,1),x(i,2),x(i,3),x(i,4),x(i,5),x(i,6),mu_pass
,quick_test);
    if latched==1
        thresh_p3=quick_test;
    else
        thresh_p3=find_thresh(par)
   end
    %compare to target
    thresh_err=abs(thresh_p3-TARGET_THRESH);

     %find high friction threshold for current design
    if (thresh_p3<1000)
        mu_pass=0.6;
        guess=thresh_p3;
        par=[guess mu_pass x(i,1) x(i,2) x(i,3) x(i,4)…
             x(i,5) x(i,6)];
        thresh_p6=find_thresh(par)
    else thresh_p6=10000
    end
    %compare to thresh_p3
    frict_sens=abs(thresh_p6/thresh_p3-1);

    %update current_results array
    current_results_p3(i)=thresh_p3;
    current_results_p6(i)=thresh_p6;
end
thresh_err_array=abs(current_results_p3-…
      TARGET_THRESH*ones(pop_size,1));
frict_sens_array=abs(current_results_p6./current_results_p3-1);

%assign final fitness values to current results
%just using friction sensitivity
```

```
fitness=frict_sens_array;

%assemble current results array
current_results=cat(2,GEN*ones(pop_size,1),x,current_results_p3,curr
ent_results_p6,fitness)

%update the persistent results array
    pop_results=cat(1,pop_results,current_results)
    save('frict_thresh_results.mat','pop_results')

%---------------find_thresh.m----------------------
%Uses ssc3_optim to find threshold acceleration for a given design
function [thresh]=find_thresh(ft)
   %set parameters of particular design
   guess=ft(1);     %guess should be positive
   mu=ft(2);
   t=ft(3);
   Lf=ft(4);
   Wf=ft(5);
   Hm=ft(6);
   wl=ft(7);
   ll=ft(8);
    global chip_accel
    %t=20e-6;
    %Lf=1495e-6;
    %Wf=12e-6;
    %Hm=2.025*1e-3;
    %wl=8e-6;
    %ll=460e-6;
    incr=2;    %initial adjustment increment
quick_test=1000;
   latched=ssc3_optim(t,Lf,Wf,Hm,wl,ll,quick_test,mu);
if latched==0
   thresh=1000
   return;
else
    ca_low=0;              %apply initial bounds
    ca_hi=1000;

%loop through until threshold is found within 1g
    while (ca_hi-ca_low)>=0.1
      %test to see if sensor latches at this level
       latched=ssc3_optim(t,Lf,Wf,Hm,wl,ll,guess,mu);
       %if doesn't latch, increase chip accel
       if latched==0
       ca_low=guess;    %update lower bound on search
        %make sure not to overshoot past bounds...
            if abs(guess+incr)>=ca_hi
                incr=incr/2;     %decrease increment if you would
            end
            guess=guess+incr;         %adjust guess
            continue            %and retry

      %if it did latch, decrease chip_accel
      else
            ca_hi=guess;            %modify upper bound on search
```

```
            if abs(guess-incr)<=ca_low       %don’t overshoot
                incr=incr/2;     %decrease increment if you would
            end
            guess=guess-incr;         %adjust guess
            continue            %and retry
        end
    end     %end while loop
end
    mu
    %set threshold to lowest accel resulting in latched event
    thresh=ca_hi;
end

%-------------------ssc3_optim.m----------------------
% 2DOF shock sensor model with deflection of latch included
%predicts transient response of latching shock sensor to steady
%acceleration beginning at time = 0
function [state]=ssc3_optim(t,Lf,Wf,Hm,wl,ll,guess,mu_pass)
%clear all
format short e;
hold off;

global chip_accel duration k kaxial M m kl ybar r di mu yc ca_fn
Fymon1 Fymon2 Fymon3 Fmon max_bounce;
E=160e9;
%wl=8e-6;        %design width is 8um
%ll=460e-6;
%t=20e-6;
radius=40e-6;
%define wl,ll,t outside this m-file
kl=3*E*(1/12*t*wl^3)/ll^3;       %stiffness of a single latch -
%multiplied by 2 in force function -nominal 4.44, 3.66 for 7.5um
%wide latch
kaxial=E*wl*t/ll;
dens=2330;
m=33/140*(ll+40e-6)*wl*t*dens+pi*radius^2/4*t*dens;
freql=sqrt(kl/m)/(2*pi);

%initialize global variables to describe system
%75g sensor
chip_accel=-guess;         %chip_accel comes from input at runtime
duration=5.9e-3;                 %
%k=1.324;                          %design value 1.324, value with
10.5um wide spring is 0.887
%define t,Lf,Wf Ns outside of this m-file
Np=4;
Ns=5;
k=E*t*Wf^3/(Lf^3*Ns)*Np;
%M=2.65e-7;                          %design value 2.65e-7
%define Hm outside this m-file
Wm=Lf*2+110e-6;
num_holes=ceil((Hm-40e-6)/(60e-6))*ceil((Wm-40e-6)/(60e-6));
%mass of sensor
Mm=dens*t*(Hm*Wm-120e-6*120e-6-num_holes*20e-6*20e-6);
%equivalent mass of springs
Mf=Lf*Wf*t*dens*Ns*Np/3;
```

```
M=Mm+Mf;

%50 g sensor
%chip_accel=-60*9.81;     %27.5g for hs video
%duration=6e-3;   %7.52ms for hs video, 8.24ms for standard testing
%k=0.601;    %actual value=0.601 - 0.529 for 11.5um wide spring,
%0.403 for 10.5um wide spring
%M=3.42e-7;

ybar=150e-6;
r=40e-6;
di=15e-6;

mu=mu_pass;            %mu defined by input at runtime
yc=91.9e-6;         %distance to initial contact
yc2=ybar;           %distance to latch/distance till contact is lost
k2=kl;                %axial stiffness of latch

%define the frequency and period of the basic spring-mass system
freq=sqrt(k/M)/(2*pi);
period=1/freq;
%Solve differential equation for period before contact
%set options to find where contact occurs and stop integration
options=odeset('Events',@events);
initial=[0;0;0;0];
[T1,Y1,TE1,YE1,IE]=ode45(@shock_init,[0
duration+period],initial,options);
if isempty(IE)
    state=0;
    return;
elseif IE==2
    state=0;    %unlatched
    return;
end

max_bounce=0;
%Solve differential equation for period while mass is in contact
%with latch
%find where contact ends and stop integration
yc=yc2;
maxstep=10e-7;      %1e-8 used for model match
initstep=5e-8;     %0.5ns for model match
refine=1;
%options=odeset('Events',@events,'Refine',refine,'MaxStep',maxstep,'
%OutputFcn',@Fstore,'Stats','on','InitialStep',initstep);
options=odeset('Events',@events,'Refine',refine,'MaxStep',maxstep,'S
tats','off','InitialStep',initstep);
initial2=[YE1(1,1);YE1(1,2);YE1(1,3);YE1(1,4)];
if length(TE1)>1
    TE1
        YE1
    TE1=max(TE1)
end
[T2,Y2,TE2,YE2,IE2]=ode45(@latchfr,[TE1
duration+period],initial2,options);
%max_bounce
```

```
if isempty(IE2)
    state=0;
    return;
elseif IE2==2
    state=0;    %unlatched
    return;
else state=1;   %latched
    return;
end

clear global F*

%--------------------------------------------------------------------
function dy=shock_init(t,y)

%this function defines the differential equation before the shock
%sensor makes contact with the latch
%y(1) is the displacement, y(2) is the velocity
%ydd is the Eq of motion for the mass, F is the mass-latch
%interaction (friction & normal force)

global chip_accel duration k m M Fymon1;

F=0;
Fy=F;
Fx=F;
if t<=duration
    ydd=-chip_accel*9.81*sin(t/duration*pi)-k*y(1)/M-2*F/M;
else
    ydd=-k*y(1)/M-2*F/M;
end
xdd=0;
dy=[y(2);ydd;y(4);xdd];

%--------------------------------------------------------------------
function dy=latchfr(t,y)

%this function defines the differential equation while the shock
%sensor is in contact with the latch
%y(1) is the displacement, y(2) is the velocity
%ypp is the acceleration function, F is the mass-latch interaction
%(friction & normal force)

global chip_accel duration k m kl kaxial ybar r di mu yc M Fymon2 Fx
Fy F_normal max_bounce;

yl=ybar-y(1);                     %remaining travel

%calculations of surface deflection using various equations for
%cylinders
%reasonable range for normal force 0-5mN
L=20e-6;
P=linspace(1e-6,5e-3);
r=40e-6;
v=0.28;
```

```
E=169e9;
%Eq. 4 - for two cylinders in contact
V4=(1-v^2)/(pi*E);
P4=P/L;
a=L/2;
d=2*P4.*V4.*(1+log((4*a^2)./(V4*P4*2*r)));

int2=2*r-sqrt((ybar-y(1))^2+(r+di+y(3))^2);
theta=asin(yl/(2*r-int2));            %contact angle

if int2<0
    if abs(int2)>max_bounce
        max_bounce=abs(int2);
    end
    int2=0;
end

%approx. stiffness of contact
kc=P(100)/d(100);
%effective latch stiffness in direction of contact
kl_eff=1/(cos(theta)^2/kl+sin(theta)^2/kaxial);
keff=kl_eff+kc;

F_normal=keff*int2;

Fx=F_normal*cos(theta);
Fy=F_normal*sin(theta)*2+2*mu*F_normal*cos(theta);

if t<=duration
    ydd2=-chip_accel*9.81*sin(t/duration*pi)-k*y(1)/M-
2*F_normal*(ybar-y(1))/sqrt((ybar-y(1))^2+(r+di+y(3))^2)/M-
sign(y(2))*2*mu*F_normal*(r+di+y(3))/(2*r-int2)/M;
else
    ydd2=-k*y(1)/M-2*F_normal*(ybar-y(1))/sqrt((ybar-
y(1))^2+(r+di+y(3))^2)/M-sign(y(2))*2*mu*F_normal*(r+di+y(3))/(2*r-
int2)/M;
end
zeta=.1;
cl=2*zeta*sqrt(kl*m);
%equation of motion for latch, xdd means x double dot
%xdd=(-kl*y(3)-cl*y(4)+Fx)/m
xdd2=(-kl*y(3)+Fx)/m;
xdd2=(-kl*y(3)+kc*int2*(r+di+y(3))/sqrt((ybar-
y(1))^2+(r+di+y(3))^2)-sign(y(4))*mu*F_normal*sin(theta))/m;
%return state for each time step
dy=[y(2);ydd2;y(4);xdd2];

%------------------------------------------------------------------
function dy=shock_final(t,y)

global chip_accel ca_fn duration k kaxial kl m M ybar Fymon3 mu;

%this function defines the differential equation after the shock
%sensor leaves contact with the latch
%y(1) is the displacement, y(2) is the velocity
```

```
%ypp is the acceleration function, F is the mass-latch interaction
%(friction & normal force)
zm=3e-7;
cm=2*zm*sqrt(k/M);
if y(1)>ybar&&y(1)<170e-6
    F=0;
elseif y(1)>170e-6
    F=kaxial*(y(1)-170e-6);
else
    F=kaxial*(y(1)-ybar);
end
if t<=duration
    ydd=-chip_accel*9.81*sin(t/duration*pi)-k*y(1)/M-cm*y(2)/M-
2*F/M;
else
    ydd=-k*y(1)/M-cm*y(2)/M-2*F/M;
end
zeta=0.1;
cl=2*zeta*sqrt(kl*m);
%equation of motion for latch, xdd means x double dot
%xdd=-kl*y(3)/m-sign(y(4))*mu*F/m;
xdd=-kl*y(3)/m-cl*y(4)/m;
dy=[y(2);ydd;y(4);xdd];

%-------------------------------------------------------------------

function [value,isterminal,direction]=events(t,y)
global yc;
    %this function compares the distance the device has travelled to
%a critical distance (either distance to contact or
    %distance to loss of contact) to determine when to switch the
%differential equation used
    value=[y(1)-yc;y(2)];    %returns 2 if velocity is zero, returns
%1 if moves past latch dist
    isterminal=[1;1];
    direction=[1;-1];

%-------------------------------------------------------------------
function status=Fstore(t,y,flag)
  global Fx Fy Fmon F_normal;
if strcmp(flag,'init')
  Fmon=[Fmon;t(1) y(1) Fx Fy F_normal];
elseif strcmp(flag,'') Fmon=[Fmon;t(1) y(1) Fx Fy F_normal];
end
  status=0;
```

A.2.6. Fmincon Optimization Routine

Note: this optimization routine also requires the ssc3_optim.m and find_thresh.m files from section A.2.5

```
%----------fmin_frict_thresh_opt.m-----------
%define overall program flow here
%requires the follwoing m-files:
%ssc3_optim.m, fmin_frict_thresh_obj.m, thresh_err_constraint.m
```

```
    global THRESH_P3 TARGET_THRESH
    TARGET_THRESH=100;

    %definition of x=[t Lf Wf Hm wl ll]
    x0=[20e-6 1869e-6 18.4e-6 2.607e-3 6.36e-6 379e-6];
    lb = [20e-6 1000e-6 3e-6 1e-3 3e-6 200e-6];   %lower bounds on x
    ub = [20e-6 2000e-6 20e-6 3e-3 18e-6 600e-6]; %upper bounds on x
    options = optimset('DiffMinChange',.1);
    options = optimset('TypicalX',[20e-6 1500e-6 12e-6 2.6e-3 8e-6
400e-6])
    options = optimset('Algorithm','internal-point')

[x,fval,exitflag]=fmincon(@fmin_frict_thresh_obj,x0,[],[],[],[],lb,u
b,@thresh_err_constraint)

%-----------fmin_frict_thresh_obj.m-------------
%FMINCON optimization
%uses files: ssc3_optim to perform constrained optimization
%objective is: Low friction sensitivity
%constraint is: less than 3g variation from target acceleration
%intended as objective function in an optimization routine

%---------------OBJECTIVE FUNCTION--------------------
function frict_sens=fmin_frict_thresh_obj(x)
    %x is the vector of independent variables for the optimization
    %definition of x=[t Lf Wf Hm wl ll]
    global THRESH_P3 TARGET_THRESH
    x
    persistent gen compiled_results
    if isempty(gen)
        gen=1;
    else gen=gen+1;
    end
    if isempty(compiled_results)
        compiled_results=zeros(1,11)
    end

    %initialize results array
    %array elements will be:
    %[generation# x-values THRESH_P3 thresh_p6]

    %find low friction threshold for current design
    mu_pass=0.3;
    guess=TARGET_THRESH;
    par=[guess mu_pass x(1) x(2) x(3) x(4) x(5) x(6)];
    THRESH_P3=find_thresh(par)
    disp(['x-values are: ',num2str(x)]);
    disp(['THRESH_P3 found from objective function is
',num2str(THRESH_P3)]);
    %compare to target
    thresh_err=abs(THRESH_P3-TARGET_THRESH);

     %find high friction threshold for current design
    if (THRESH_P3<1000)
```

```
        mu_pass=0.6;
        guess=THRESH_P3;
        par=[guess mu_pass x(1) x(2) x(3) x(4) x(5) x(6)];
        thresh_p6=find_thresh(par)
    else thresh_p6=10000
    end
    %compare to THRESH_P3
    frict_sens=abs(thresh_p6/THRESH_P3-1);

%assemble current results array
current_results=[gen x THRESH_P3 thresh_p6 thresh_err frict_sens]
compiled_results=[compiled_results;current_results]
end


%---------thresh_err_constraint.m------------------
function [c,ceq]=thresh_err_constraint(x)
    global THRESH_P3 TARGET_THRESH
    ceq=[];
    disp(['x-values are: ',num2str(x)]);
    disp(['THRESH_P3 used in constraint function is
',num2str(THRESH_P3)]);
    c=abs(THRESH_P3-TARGET_THRESH)-3
end
```

A.3. ANSYS Scripts

A.3.1. Shape Factor Code

```
!Ansys model for
!Thermal actuator
!shape factor calculation
!
/show,win32c
/contour,all,128

/prep7
et,1,plane77
et,2,infin110
keyopt,2,1,2    !set infin element dof to temp

rho=5.868e-3/100        !resistivity of beam

gap=2e-6                !gap between beam and substrate
h=20e-6                         !height of beam
w=10e-6                         !width of beam
diam=2*h                !location of infinite boundary elements

J=1e8                   !current density
```

```
!silicon material properties
mp,kxx,1,148            !thermal conductivity of silicon

!air material properties
mp,kxx,2,0.026                  !thermal conductivity of air

!define geometry
cyl4,0,0,diam,0,,90     !air circle
blc4,0,gap,0.5*w,h      !silicon rectangle
blc4,0,0,diam,-gap      !substrate
cyl4,0,0,diam,0,2*diam,90     !infinite element domain
blc4,diam,0,diam,-gap!infinite element domain

!glue areas together
asba,1,2,,delete,keep
asel,all
aglue,all

!assign material properties and element types to air volume
asel,s,,,8
aatt,2,0,1
!assign material properties and element types to silicon volumes
asel,s,,,2,3,1
aatt,1,0,1
!assign material properties and element types to infinite domain
asel,s,,,1
aatt,1,0,2
asel,s,,,7
aatt,2,0,2

!size elements and mesh
asel,all
lsel,s,loc,x,0
lsel,s,loc,y,gap/2
lesize,all,,,3

!infinite domain is one element thick
lsel,s,length,,diam
lsel,u,loc,x,diam/2
lesize,all,,,1

!number of infinite elements around the boundary
lsel,s,radius,,diam
lsel,a,radius,,2*diam
lesize,all,,,60
```

```
lsel,s,loc,x,diam,2*diam
lsel,r,loc,y,-gap/2
lesize,all,,,2

asel,s,type,,2
mshkey,1
amesh,all

asel,all
mshkey,0
esize,1e-6
amesh,all

!apply boundary conditions
asel,s,loc,y,-gap,0
asel,r,loc,x,0,diam
da,all,temp,0
lsel,s,loc,x,0
dl,all,,symm

asel,s,,,2
bfa,all,hgen,J*J*rho

lsel,s,radius,,2*diam
lsel,a,loc,x,2*diam
nsll,s,1
sf,all,inf

allsel
/solution
solve

/expand,2,rect,half

/post1
plnsol,temp
```

A.3.2. Latch Contact Force/Deflection Code

```
!ansys contact force/displacement model

/prep7
et,1,solid95

mp,ex,1,169e3
mp,prxy,1,0.28
```

```
radius=40
depth=20
cyl4,0,0,radius,0,,180,depth
cyl4,0,2*radius,radius,0,,-180,depth

vmesh,all

asel,s,loc,y,0
da,all,all,0

P=5000
pressure=P/(2*radius*depth)
asel,s,loc,y,80
sfa,all,,pres,pressure
allsel

!define contact pair and solve through GUI
```

Bibliography

[1] H. Van der Auweraer and B. Peeters, “International Research Projects on Structural Health Monitoring: An Overview,” *Structural Health Monitoring*, vol. 2, Dec. 2003, pp. 341-358.

[2] J.P. Lynch and K.J. Loh, “A Summary review of wireless sensors and sensor networks for structural health monitoring,” *Shock and Vibration Digest*, vol. 38, 2006, pp. 91-128.

[3] S.J. Prosser, “Automotive sensors: past, present and future,” *Journal of Physics: Conference Series*, vol 76, Institute of Physics Publishing, 2007, p. 012001.

[4] Military Standard 1389-D, *Design Requirements for Standard Electronic Modules*, U.S Department of Defense, .

[5] S. Jean-Michel, I. Sensing, S.A. Colibrys, and S. Neuchatel, “Market opportunities for advanced MEMS accelerometers and overview of actual capabilities vs. required specifications,” *Proc. of Position Location and Navigation Symposium*, Monterey, CA, April 26-29, 2004, pp. 78-82.

[6] W. Frobenius, S. Zeitman, M. White, D. O'Sullivan, and R. Hamel, “Microminiature ganged threshold accelerometers compatible with integrated circuit technology,” *IEEE Transactions on Electron Devices*, vol. 19, Jan. 1972, pp. 37-40.

[7] Y. Loke, G.H. McKinnon, and M.J. Brett, “Fabrication and characterization of silicon micromachined threshold accelerometers,” *Sensors and Actuators A: Physical*, vol. 29, 1991, pp. 235-240.

[8] J. Noetzel, T. Tonnesen, T.W. Benecke, J. Binder, and G. Mader, “Quasianalog Accelerometer using Microswitch Array,” *Sensors and Actuators A*, vol 54, 1996, pp. 574-578.

[9] S. McNamara and Y.B. Gianchandani, “LIGA fabricated 19-element threshold accelerometer array,” *Sensors and Actuators A: Physical*, vol. 112, 2004, pp. 175-183.

[1] P.F. Man and C.H. Mastrangelo, “Surface micromachined shock sensor for impact detection,” *Proc. of the Solid-State Sensor and Actuator Workshop,* Hilton Head, SC, June 13-16, 1994, pp. 156-159.

[11] A. Selvakumar, N. Yazdi, and K. Najafi, “A wide-range micromachined threshold accelerometer array and interface circuit,” *Journal of Micromechanics and Microengineering*, vol. 11, 2001, pp. 118-125.

[12] Z. Yang, G. Ding, W. Chen, S. Fu, X. Sun, and X. Zhao, “Design, simulation and characterization of an inertia micro-switch fabricated by non-silicon surface micromachining,” *Journal of Micromechanics and Microengineering*, vol. 17, 2007, pp. 1598-1604.

[13] M. Jia, X. Li, Z. Song, M. Bao, Y. Wang, and H. Yang, “Micro-cantilever shocking-acceleration switches with threshold adjusting and 'on'-state latching functions,” *Journal of Micomechanics and Microengineering*, vol. 17, 2007, pp. 567-575.

[14] J.S. Go, Y. Cho, B.M. Kwak, and K. Park, “Snapping microswitches with adjustable acceleration threshold,” *Sensors and Actuators A: Physical*, vol. 54,

1996, pp. 579 -583.

[15] B.J. Hansen, C.J. Carron, B.D. Jensen, A.R. Hawkins, and S.M. Schultz, “Plastic latching accelerometer based on bistable compliant mechanisms,” *Smart Materials and Structures*, vol. 16, 2007, pp. 1967-1972.

[16] J.W. Wittwer, M.S. Baker, D.S. Epp, and J.A. Mitchell, “MEMS Passive Latching Mechanical Shock Sensor,” *Proceedings of the ASME 2008 International Design Engineering Technical Conference & Computers and Information in Engineering Conference*, New York, NY, Aug. 3-6, 2008.

[17] J. Zhao, J. Jia, H. Wang, and W. Li, “A Novel Threshold Accelerometer With Postbuckling Structures for Airbag Restraint Systems,” *IEEE Sensors Journal*, vol. 7, 2007, p. 1102.

[18] D.R. Ciarlo, “A latching accelerometer fabricated by the anisotropic etching of (110) oriented silicon wafers,” *Journal of Micromechanics and Microengineering*, vol. 2, 1992, pp. 10-13.

[19] M.R. Whitley, M. Kranz, R. Kesmodel, and S. Burgett, “Latching shock sensors for health monitoring and quality control,” *Proceedings of SPIE 5717*, 2005, pp. 185-194.

[20] D. Jean, “Integrated MEMS Mechanical Shock Sensor,” *Proc. of 48th Annual NDIA Fuze Conference*, Charlotte, NC, Apr. 26-28, 2004.

[21] G.L. Smith, L. Fan, R. Balestrieri, and D. Jean, “Micromechanical Shock Sensor,” U.S. Patent 6737979, 2004.

[22] D. Jean, “MEMS multi-directional shock sensor,” U.S. Patent 7159442 .

[23] Z.Y. Guo, Q.C. Zhao, L.T. Lin, H.T. Ding, X.S. Liu, J. Cui, Z.C. Yang, H. Xie, and G.Z. Yan, “An acceleration switch with a robust latching mechanism and cylindrical contacts,” *Journal of Micromechanics and Microengineering*, vol. 20, 2010, p. 055006.

[24] Z.Y. Guo, Z.C. Yang, L.T. Lin, Q.C. Zhao, H.T. Ding, X.S. Liu, X.Z. Chi, J. Cui, and G.Z. Yan, “A Latching acceleration switch with multi-contacts independent to the proof-mass,” *Proceedings of IEEE Microelectromechanical Systems*, Sorrento, Italy: 2009, pp. 813-816.

[25] J. Walraven, “Failure mechanisms in MEMS,” *Proceedings of the International Test Conference*, Charlotte, NC:, Sept. 28-Oct. 3, 2003, pp. 828-833.

[26] B. Bhushan and C. Dandavate, “Thin-film friction and adhesion studies using atomic force microscopy,” *Journal of Applied Physics*, vol. 87, Feb. 2000, pp. 1201-1210.

[27] E. Yoon, R.A. Singh, H. Oh, and H. Kong, “The effect of contact area on nano/micro-scale friction,” *Wear*, vol. 259, 2005, pp. 1424-1431.

[28] W. Wang, Y. Wang, H. Bao, B. Xiong, and M. Bao, “Friction and wear properties in MEMS,” *Sensors and Actuators A: Physical*, vol. 97, 2002, pp. 486-491.

[29] M.P. de Boer, J.M. Redmond, and T.A. Michalske, “A hinged-pad test structure for sliding friction measurement in micromachining,” *Proc. SPIE*, vol. 3512, 1998, pp. 241–50.

[30] E.E. Flater, A.D. Corwin, M.P. de Boer, and R.W. Carpick, “In situ wear studies of surface micromachined interfaces subject to controlled loading,” *Wear*, vol. 260, 2006, pp. 580-593.

[31] M.G. Lim, J.C. Chang, D.P. Schultz, R.T. Howe, and R.M. White, “Polysilicon microstructures to characterize static friction,” *Proc. IEEE Micro Electro Mechanical Systems Workshop*, Napa Valley, CA, Feb. 11-14, 1990, pp. 82–88.

[32] S.L. Miller, J.J. Sniegowski, G. LaVigne, and P.J. McWhorter, “Friction in surface-micromachined microengines,” *Proceedings of SPIE*, 1996, p. 197.

[33] N.R. Tas, C. Gui, and M. Elwenspoek, “Static friction in elastic adhesive MEMS contacts, models and experiment,” *Proceedings of IEEE Microelectromechanical Systems*, pp. 193-198.

[34] Z. Guo, Y. Meng, H. Wu, C. Su, and S. Wen, “Measurement of static and dynamic friction coefficients of sidewalls of bulk-microfabricated MEMS devices with an on-chip micro-tribotester,” *Sensors & Actuators: A. Physical*, vol. 135, 2007, pp. 863-869.

[35] J. Wu, S. Wang, and J. Miao, “A MEMS device for studying the friction behavior of micromachined sidewall surfaces,” *Journal of Microelectromechanical Systems,* vol. 17, 2008, pp. 921-933.

[36] I. Hwang, Y. Lee, and J. Lee, “A micromachined friction meter for silicon sidewalls with consideration of contact surface shape,” *Journal of Micromechanics and Microengineering*, vol. 16, 2006, pp. 2475-2481.

[37] S.J. Timpe and K. Komvopoulos, “The effect of adhesion on the static friction properties of sidewall contact interfaces of microelectromechanical devices,” *Journal of Microelectromechanical Systems* vol. 15, 2006, pp. 1612-1621.

[38] L.J. Currano, S. Bauman, W. Churaman, M. Peckerar, J. Wienke, S. Kim, M. Yu, and B. Balachandran, “Latching ultra-low power MEMS shock sensors for acceleration monitoring,” *Sensors and Actuators A: Physical*, vol. 147, 2008, pp. 490 -497.

[39] L.J. Currano, D. Gee, W.A. Churaman, M. Dubey, P. Amirtharaj, M. Yu, and B. Balachandran, “MEMS Rotational Actuator for High Force and Large Displacement,” *Advances in Science and Technology*, vol. 54, 2008, pp. 372-377.

[1] R.C. Hibbeler, *Mechanics of Materials*, Upper Saddle River, NJ: Prentice Hall, 1997, pp. 653-673.

[41] L. Que, J.S. Park, and Y.B. Gianchandani, “Bent-beam electrothermal actuators-Part I: Single beam and cascaded devices,” *Journal of Microelectromechanical Systems*, vol. 10, 2001, pp. 247-254.

[42] J.M. Maloney, D.S. Schreiber, and D.L. DeVoe, “Large-force electrothermal linear micromotors,” *Journal of Micromechanics and Microengineering*, vol. 14, 2004, pp. 226-234.

[43] J.M. Maloney, “Fabrication and thermal actuation of three-dimensional micro electro mechanical systems,” Masters Thesis, University of Maryland, 2001.

[44] J.R. Reid, V.M. Bright, and J.H. Comtois, “Force measurements of polysilicon thermal microactuators,” *Proceedings of SPIE*, vol. 2882, 1996, p. 296.

[45] R. Hickey, M. Kujath, and T. Hubbard, “Heat transfer analysis and optimization of two-beam microelectromechanical thermal actuators,” *Journal of Vacuum Science & Technology A: Vacuum, Surfaces, and Films*, vol. 20, 2002, p. 971.

[46] Q.A. Huang and N.K.S. Lee, “Analysis and design of polysilicon thermal flexure actuator,” *Journal of Micromechanics and Microengineering*, vol. 9,

1999, pp. 64-70.
[47] S. Heo and Y.Y. Kim, "Optimal design and fabrication of MEMS rotary thermal actuators," *Journal of Micromechanics and Microengineering*, vol. 17, 2007, pp. 2241-2247.
[48] L.J. Currano, M. Yu, and B. Balachandran, "Latching in a MEMS shock sensor: modeling and experiments," *Sensors and Actuators A: Physical*, vol. (in revision), 2010.
[49] L. Currano, "A No-Power MEMS Shock Threshold Sensor," *Structural Health Monitoring 2005: Advancements and Challenges for Implementation*, Stanford, CA: 2005, pp. 647-653.
[50] L. Currano, D. Gee, M. Yu, and B. Balachandran, "Characterization of a No-Power Latching Acceleration Threshold Sensor," *Proceedings of 79th Annual Shock and Vibration Symposium*, 2009.
[51] L.J. Currano, M. Yu, and B. Balachandran, "Novel friction test structures for microelectromechanical systems," *Proceedings of the ASME International Mechanical Engineering Congress and Exposition*, 2006, p. 14054.
[52] S.S. Rao, *Mechanical Vibrations, 3rd Edition*, Prentice Hall, 1995.
[53] L.L. Chu, L. Que, A.D. Oliver, and Y.B. Gianchandani, "Lifetime studies of electrothermal bent-beam actuators in single-crystal silicon and polysilicon," *Journal of Microelectromechanical Systems,* vol. 15, 2006, pp. 498-506.
[54] D.T. Greenwood, *Principles of Dynamics*, Englewood Cliffs, NJ: Prentice Hall, 1988.
[55] M.J. Puttock and E.G. Thwaite, *Elastic compression of spheres and cylinders at point and line contact*, National Standards Laboratory Technical Paper, Commonwealth Scientific and Industrial Research Organization, Melbourne, Australia, 1969.
[56] *ANSYS Multiphysics*, Canonsburg, PA: ANSYS, Inc., .
[57] R.D. Blevins, *Formulas for Natural Frequencies and Mode Shapes*, New York: Van Nostrand Reinhold Co, 1979.
[58] *MATLAB*, Natick, MA: The MathWorks, .
[59] M. Mitchell, *An Introduction to Genetic Algorithms*, The MIT press, 1998.
[60] J.N. Reddy, *Energy Principles and Variational Methods in Applied Mechanics*, Hoboken, NJ: John Wiley & Sons Inc, 2002.
[61] L. Lin and M. Chiao, "Electrothermal responses of lineshape microstructures," *Sensors & Actuators: A. Physical*, vol. 55, 1996, pp. 35-41.
[62] Y.S. Touloukian, R.W. Powell, C.Y. Ho, and P.G. Klemens, "Thermophysical Properties of Matter (IFI/Plenum, New York, 1970)," vol. 2, p. 166.
[63] D.P. DeWitt and F.P. Incropera, *Fundamentals of Heat and Mass Transfer*, John Wiley and Sons, 2002.
[64] Y. Okada and Y. Tokumaru, "Precise determination of lattice parameter and thermal expansion coefficient of silicon between 300 and 1500 K," *Journal of Applied Physics*, vol. 56, 1984, p. 314.
[65] J. Fruhauf, E. Gartner, and E. Jansch, "Silicon as a plastic material," *Journal of Micromechanics and Microengineering*, vol. 9, 1999, pp. 305-312.
[66] K. Yasutake, J. Murakami, M. Umeno, and H. Kawabe, "Mechanical properties of heat-treated CZ-Si wafers from brittle to ductile temperature range,"

Japanese Journal of Applied Physics, vol. 21, 1982, pp. L288-L290.

[67] G.T.A. Kovacs, *Micromachined Transducers Sourcebook. 1998*, McGraw-Hill, .

[68] L.J. Currano, M. Yu, and B. Balachandran, "Modeling, testing and evaluation of a latching MEMS shock sensor," *Structural Health Monitoring 2009: From System Integration to Autonomous Systems,* Fu-kuo Chang, Ed., pp. 1027-1033.

[69] W.R. Ashurst, C. Carraro, R. Maboudian, and W. Frey, "Wafer level anti-stiction coatings for MEMS," *Sensors & Actuators: A. Physical*, vol. 104, 2003, pp. 213-221.

[70] D. Gee, W.A. Churaman, L.J. Currano, and E. Zakar, "Design and Fabrication of MEMS Piezoelectric Rotational Actuators," *Mater. Res. Soc. Symp. Proc.*, vol. 1139, pp. GG03-01 pp.1-6.

[71] C. Lalanne, *Mechanical Vibration & Shock: Mechanical Shock*, Hermes, 2002.